ALMA MATER STUDIORUM
UNIVERSITÀ DI BOLOGNA

DOTTORATO DI RICERCA IN

ASTROFISICA

Ciclo 36

Settore Concorsuale: 02/C1 - ASTRONOMIA, ASTROFISICA, FISICA DELLA TERRA E DEI PIANETI

Settore Scientifico Disciplinare: FIS/05 - ASTRONOMIA E ASTROFISICA

ACCRETION PROPERTIES OF SUPERMASSIVE BLACK HOLES ACROSS COSMIC TIME AND LUMINOSITIES

Presentata da: Iván Ezequiel López

Coordinatore Dottorato:

Andrea Miglio

Supervisore:

Marcella Brusa

Co-supervisore:

Silvia Bonoli

ESAME FINALE ANNO 2024

ACCRETION PROPERTIES OF SUPERMASSIVE BLACK HOLES ACROSS COSMIC TIME AND LUMINOSITIES

IVÁN EZEQUIEL LÓPEZ
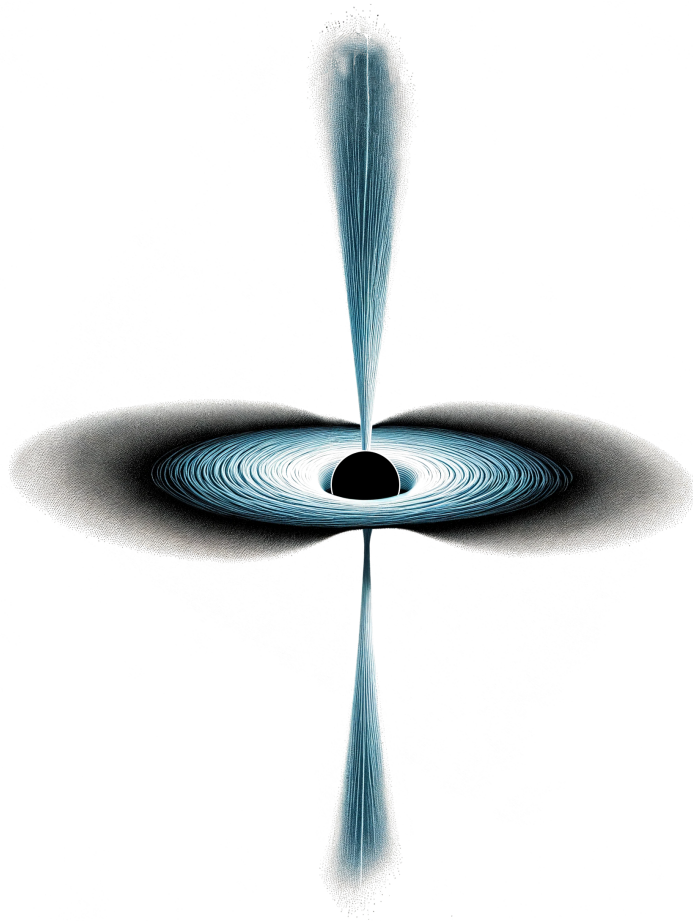
Tesi di Dottorato

January 2024

A mi abuela Emma,
para charlar del cielo un poco más...

ABSTRACT

This thesis comprehensively explores Active Galactic Nuclei (AGN) since cosmic noon and down to the lowest luminosities, utilizing a multiwavelength approach spanning X-ray to radio wavelengths. A key contribution is a method leveraging narrowband data from the miniJPAS survey, enabling the characterization of AGN properties while constraining their host galaxies. Robust physical parameters for X-ray-selected AGN up to $z \sim 2.5$ are derived. The analysis includes the examination of accretion ratios, a comparison with their proxies, and a forward modeling approach for assessing coevolution scenarios relative to local relations.

Another significant contribution is a novel SED fitting module tailored for Low-Luminosity AGN (LLAGN), accurately characterizing their properties. Validated with diverse AGN samples, this module proves effective even in scenarios with galaxy contamination. The derived X-ray bolometric correction and exploration of UV-X-ray relations for LLAGN are presented. We further explore the host galaxy contamination problem and the possible impact of LLAGN on the specific star formation rate of their host galaxies.

The thesis concludes with a case study on how an LLAGN influences the interstellar medium of its host galaxy. High-resolution observations of the spiral galaxy M58 unveil H_2 emission from warm molecular gas, indicating suppressed star formation in the inner kiloparsecs. Dust molecules remain unaffected compared to more luminous AGN. Optical forbidden line ratios suggest heating by low-velocity shocks caused by low-power radio-jet, highlighting the significant impact of LLAGN feedback on their host galaxies.

DECLARATION

Portions of this work have appeared (or are to appear) in the following papers:

- **López I.E.**, Brusa M., Bonoli S., Shankar F., et al., 2023, A&A, 672, A137; *The miniJPAS survey: AGN and host galaxy coevolution of X-ray-selected sources*

- Ogle P., **López I.E.**, Reynaldi V., Togi A., Rich M., et al., 2024, ApJ, 962, 196; *Radio Jet Feedback on the inner of Virgo Spiral Galaxy Messier 58*

- **López I.E.**, Yang G., Mountrichas G, Brusa M., et al. (submitted to A&A); *A tailored CIGALE module for Low-Luminosity AGN*

In addition to the work presented in this thesis, the author has contributed to the following projects during the period of their PhD. Most of these contributions were done within the BiD4BEST ITN and align with the network science objectives:

- Andonie C., Alexander D.M., Greenwell C., Puglisi A., Laloux B., Alonso-Tetilla, A.V., Calistro Rivera G., Harrison C., Hickox R.C., Kaasinen M., Lapi A., **López I.E.**, Petter G., Ramos Almeida C., Rosario D.J., Shankar F., Villforth C., 2023, MNRAS, 527, 1; *Obscuration beyond the nucleus: infrared quasars can be buried in extreme compact starbursts*

- Marchesini E.J., Reynaldi V., Vieyro F., Saponara J., Andruchow I., **López I.E.**, Benaglia P., Cellone S.A., Masetti N., Massaro F., Peña-Herazo H.A., Chavushyan V., et al., 2023, A&A 670, A91; *Disentangling the nature of the prototype radio weak BL Lac: Contemporaneous multifrequency observations of WISE J141046.00+740511.2*

- Alonso-Tetilla A.V., Shankar F., Fontanot F., Menci N., Valentini M., Buchner J., Laloux B., Lapi A., Puglisi A., Alexander D.M.,

Allevato V., Andonie C., Bonoli S., Hirschmann M., **López I.E.**, Raimundo S.I., Ramos Almeida C., 2024, MNRAS, 527, 4; *Probing the roles of orientation and multiscale gas distributions in shaping the obscuration of active galactic nuclei through cosmic time*

- Avirett-Mackenzie M.S., Villforth C., Huertas-Company M., Wuyts S., Alexander D.M., Bonoli S., Lapi A., **López I.E.**, Ramos Almeida C., Shankar F., 2024, MNRAS, 528, 4; *A post-merger enhancement only in star-forming Type 2 Seyfert galaxies: the deep learning view*

- Speranza G., Ramos Almeida, C., Acosta-Pulido J.A., Audibert A., Holden L.R., Tadhunter C.N., Lapi A., González-Martín O., Brusa M., **López I.E.**, Musiimenta B., Shankar, F., 2024, A&A 681, A63; *Multiphase characterization of AGN winds in five local type-2 quasars*

- Acharya N., Bonoli S., Salvato M., Cortesi A., González Delgado R.M., **López I.E.**, Marquez I., Martínez-Solaeche G., et al., (accepted for publication in A&A); *The miniJPAS Survey: The radial distribution of star formation rates in faint X-ray active galactic nuclei*

- Baldini P., Lanzuisi G., Brusa M., Merloni A., Gkimisi K., Perna M., **López I.E.**, Bertola E., Igo Z., et al.; (accepted for publication in A&A); *Winds of change: the nuclear and galaxy-scale outflows and the X-ray variability of 2MASS 0918+2117*

- Musiimenta B., Speranza G., Urrutia T., Brusa M., Ramos Almeida C., Perna M., **López I.E.**, Alexander D., Laloux B., Shankar F., Lapi A.; (accepted for publication in A&A); *Ionised AGN outflows in the Goldfish galaxy - The illuminating and interacting red quasar eFEDS J091157.4+014327 at $z \sim 0.6$*

- Bertola E., Circosta C., Ginolfi M., Mainieri V., Vignali C., Calistro Rivera G., Ward S.R., **López I.E.**, Pensabene A., Alexander D.M., et al.; (submitted to A&A); *KASHz+SUPER: Evidence for cold molecular gas depletion in AGN hosts at cosmic noon*

- Sengupta D., Torres-Albà N., Pizzetti A., **López I.E.**, Barchiesi L., Marchesi S., Vignali C., Ajello M.; (submitted to A&A); *Multi-Wavelength Overview of the AGN Torus: I. NGC 6300*

- Vito F., Brandt W.N., Comastri A., Gilli R., Ivison J.R., Lanzuisi G., Lehmer B.D., **López I.E.**, Tozzi P., Vignali C.; (submitted to A&A); *Fast SMBH growth in the SPT2349−56 protocluster at $z = 4.3$*

CONTENTS

LIST OF FIGURES

LIST OF TABLES

ACRONYMS

ADAF   Advection-dominated accretion flows

AGN   Active Galactic Nuclei

BBB   Big Blue Bump

BHAR   Black hole accretion rate

BiD4BEST   Big Data Applications for Black Hole Evolution Studies

BLR   Broad-line Region

CIGALE   Code Investigating GALaxy Emission

CSP   Complex Stellar Population

EGS   Extended Groth Strip

EHT   Event Horizon Telescope

HMXB   High-mass X-ray binaries

IMF   Initial Mass Function

IR   Infrared

ISCO   Innermost Stable Circular Orbit

ISM   Interstellar medium

J-PAS   Javalambre Physics of the Accelerating Universe
            Astrophysical Survey

LF   Luminosity Function

LINER   Low-ionization Nuclear Emission Line Region

LLAGN   Low-Luminosity AGN

LMXB   Low-mass X-ray binaries

MOHEG   Molecular Hydrogen Emission Galaxy

NLR   Narrow-line Region

PAH   Polycyclic Aromatic Hydrocarbon

PDR   Photodissociation Region

PDF   Probability Density Function

QSO   Quasar

RM   Reverberation Mapping

SINGS   Spitzer Infrared Nearby Galaxies Survey

SDSS   Sloan Digital Sky Survey

SED   Spectral Energy Distribution

SFH   Star Formation History

SFR   Star Formation Rate

SMBH   Supermassive Black Hole

SMC   Small Magellanic Cloud

SSP   Simple Stellar Population

UV   Ultraviolet

Part I

SETTING THE STAGE

1 | BACKGROUND

Our Universe is filled with captivating objects that challenge our understanding of reality. From asteroids adorned with rings to nebulas in fantastical shapes, from starquakes that reverberate through the stars to supernovae that mark the end of stellar lives, the cosmos is a realm of constant transformation and discovery. Among these cosmic curiosities, *black holes* stand out as some of the most enigmatic and fascinating entities in the Universe.

Black holes represent the ultimate consequence of gravity's immense power. They arise when a massive star collapses under its own weight, compressing its matter into an unimaginably small volume. Picture the entire mass of the Moon condensed to the size of a dot on this page, and you begin to grasp the essence of a black hole: a point of infinite density where gravity reigns supreme.

The conceptual foundations of black holes trace back to the 18th century with John Michell's idea of a "*dark star*," a massive object possessing a gravitational force so intense that not even light, the fastest entity in the Universe, can break free (Schaffer, 1979). However, it wasn't until the 20th century that Schwarzschild (1916) derived the first exact solution to the field equations of general relativity, describing a non-rotating black hole. This solution unveiled the existence of an event horizon: a spherical region around the black hole from which no information, including light, could escape. The event horizon is defined by the Schwarzschild radius $r_S = 2GM_{BH}/c^2$, scaling linearly with the black hole mass (M_{BH}). Beyond this boundary lies a domain of mystery and uncertainty, where the familiar laws of physics may unravel.

Observational evidence supporting the existence of extragalactic black holes emerged in 1963 when Schmidt (1963) discovered a quasi-stellar object, commonly known as a *quasar*. This celestial entity exhibited extraordinary luminosity and a notably high redshift. The prevailing hypothesis proposed that these quasars derived their energy from accretion disks surrounding supermassive black holes situated at the centers of galaxies. A significant milestone in 1971 was the identification of Cygnus X-1, a binary star system within our galaxy housing a compact object presumed to be a black hole. Subsequently, the field of astrophysics has thrived, progressively unraveling the mysteries surrounding black holes.

In 2019, the Event Horizon Telescope (EHT), a global collaboration of radio telescopes, achieved a groundbreaking milestone by capturing the first direct images of the black hole located at the center of the

galaxy M87. This accomplishment provided unequivocal proof of the existence of black holes and facilitated detailed studies of their structure and behavior. In subsequent years, the EHT successfully obtained a similar image for Sgr A*, the black hole at the center of the Milky Way. The EHT's images depicted a dark, featureless region surrounded by a luminous ring—a visual representation of the event horizon and the swirling accretion material around it (see Figure 1.1).
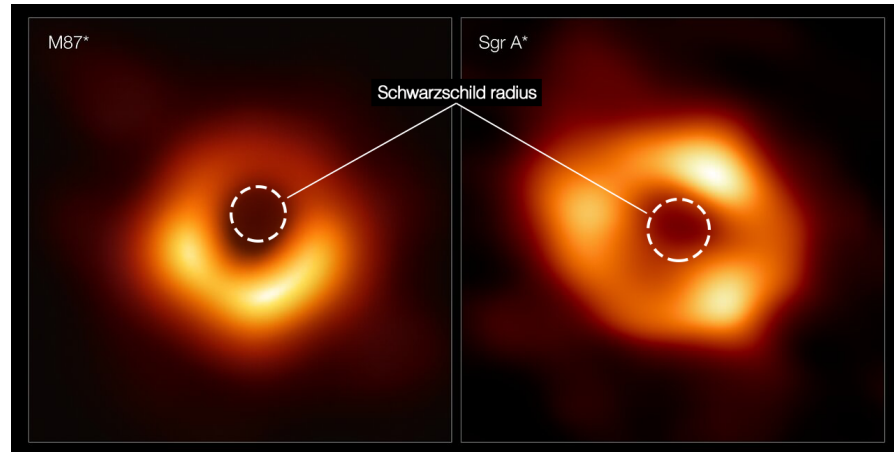
Figure 1.1: Images of the supermassive black holes M87* and Sgr A* observed with the Event Horizon Telescope. The dashed circles have a Schwarzschild radius for black holes of 4.3×10^6 and $6.5 \times 10^9 \, M_\odot$. Credits: EHT Collaboration.

Black holes exhibit a diverse range of masses, spanning from stellar-mass black holes, weighing hundreds of times the mass of the Sun ($\sim 10^2 \, M_\odot$), to the *supermassive black holes* (SMBHs) dominating the cores of galaxies (Lynden-Bell, 1969; Soltan, 1982). SMBHs can accumulate masses ranging from hundreds of thousands to billions of times that of the Sun (10^5 to $10^{10} \, M_\odot$).

While the formation of stellar-mass black holes is relatively well understood—resulting from the collapse of massive stars at the end of their life cycles—the genesis of SMBHs remains veiled in uncertainty. These black holes must have experienced substantial growth in the early Universe, a period when the cosmos was in its infancy and abundant material was accessible for accretion. Recent discoveries of supermassive black holes with high masses at high redshifts between $z = 6 - 8$ add a layer of complexity to the puzzle (Bogdán et al., 2023; Larson et al., 2023; Zappacosta et al., 2023).

Beyond mass, black holes are characterized by two fundamental parameters: charge and spin. While astrophysical black holes are generally assumed to be neutral in charge, spin significantly influences their surroundings. The black hole's spin can profoundly alter the spacetime metric, affecting how it accretes material through a surrounding accretion disk and giving rise to powerful jets.

Despite the notion that black holes, by their very nature, trap light and prevent any information from escaping, astronomers have found ingenious ways to glean insights into these enigmatic entities by studying their surroundings. SMBHs exhibiting high accretion activity manifest as an *Active Galactic Nuclei* (AGN), observable from vast distances. During periods of activity, matter falls into the black hole, emitting copious radiation across the electromagnetic spectrum. Notably, only 5–10% of galaxies host an AGN, making them a distinctive and captivating subset for observation. Although they are relatively rare, AGN stand out as the most luminous and energetic objects in the Universe, capable of outshining entire galaxies by factors of up to a trillion.

1.1 ACTIVE GALACTIC NUCLEI

Historically, galaxies are considered *active* when the luminosity in their nuclear regions surpasses that which conventional sources, such as star clusters, supernovae, or regions of star formation, can account for. The observed bolometric luminosity, i.e., the integrated luminosity over the full electromagnetic spectrum, in the cores of active galaxies, ranges from around 10^{42} erg s^{-1} to an extraordinary 10^{48} erg s^{-1} (equivalent to solar luminosity levels of approximately 10^5 to 10^{11} L$_\odot$). This is several orders of magnitude higher than the luminosity produced by the entire galaxy[1]. The heightened luminosity is often accompanied by rapid time variability, implying extremely compact emission regions (Ulrich et al., 1997).

1.1.1 Spherical Accretion

A key point supporting the notion of accreting black holes as compact emissions is the consideration of radiative pressure on accreting material. In a basic approach, a radiative source applies pressure on the accreting material, and in the most unfavorable limit, this radiation pressure opposes gravity, preventing further accretion. Assuming a simplistic scenario where a) the accretion flow is steady and spherically symmetric, b) the accreting material is mainly fully ionized hydrogen, and c) all accretion energy is converted into radiation, the acceleration from radiative pressure is given by:

$$a_{\mathrm{rad}} = \frac{\sigma_{\mathrm{T}}}{\mu_{\mathrm{p}}} \frac{\mathcal{L}}{4\pi c r^2},$$

---

[1] For reference, the integrated luminosity of the Andromeda galaxy is 5×10^{43} erg s^{-1}

where $\mathcal{L}$ is the source luminosity, σ_T is the Thomson cross-section of the electron, and μ_p is the proton mass[2]. The ratio of accelerations from radiation pressure and gravity ($g = \frac{GM_{BH}}{r^2}$) is then:

$$\frac{a_{rad}}{g} = \frac{\sigma_T \mathcal{L}}{4\pi c \mu_p G M_{BH}} = \frac{\mathcal{L}}{L_{Edd}},$$

where L_{Edd} is the Eddington luminosity, then:

$$L_{Edd} = \frac{4\pi c G \mu_p M_{BH}}{\sigma_T} \approx 1.26 \times 10^{38} \frac{M_{BH}}{M_\odot} \text{ erg s}^{-1}. \tag{1.1}$$

The Eddington luminosity represents the maximum luminosity an accreting source can achieve when the outward radiation pressure of the accreting matter balances the inward gravitational pull of the black hole. For a SMBH with a mass of $10^8\,M_\odot$, the Eddington luminosity is $L_{Edd} \approx 10^{46}$ erg/s. This means that such a black hole, accreting at its Eddington limit, can produce the luminosities observed in the center of active galaxies.

Moreover, keeping these basic assumptions, we can calculate the mass the black hole needs to accrete to produce such luminosities. Assuming a central accreting spherical body of mass M and radius R, the gravitational potential energy released by accretion of a mass m (falling freely from infinity) onto its surface is given by:

$$\Delta E_{acc} = \frac{GMm}{R},$$

where G is the gravitational constant. If, instead of a single particle of mass m, accretion occurs at a rate $\dot{m}$ and all mechanical energy is eventually radiated, the resultant luminosity is given by:

$$L_{acc} = \frac{GM\dot{m}}{R},$$

and for a given object with a given value of M/R, the accretion luminosity depends only on the infall accretion rate ($\dot{m}$). However, there is no hard surface at a given radius R for black holes. Alternatively, there is a region at $r < r_s^4$ where matter could fall in without losing its mechanical energy, not contributing to the total radiated energy. This uncertainty is usually parameterized by the introduction of a dimensionless quantity η, which represents the process efficiency. Then, for accretion in a SMBH, the luminosity equation becomes:

$$L_{acc} = \dot{m}\eta c^2 \tag{1.2}$$

A typical efficiency value for accretion processes onto black holes is $\eta \approx 0.1$ (Shapiro, 2005), surpassing the efficiency of thermonuclear

---

2 For ionized hydrogen plasma, the dominant mechanism is Thomson scattering, acting primarily on electrons. These electrons, in turn, drag protons along due to the Coulomb force. If the plasma contains heavier elements than hydrogen, the cross-section may increase due to photon absorption in spectral lines.

fusion ($\eta_{\mathrm{fus}} \approx 0.007$). Returning to our example, a non-rotating black hole with a luminosity close to the Eddington limit ($L_{\mathrm{Edd}} \approx 10^{46}$ erg/s) would only need to accrete at a rate of $\dot{m} \approx 2.5\,\mathrm{M_\odot}/\mathrm{yr}$. Thus, from an energy perspective, generating such colossal luminosities does not require a significant amount of matter, making it cost-effective for black holes to consume.

These calculations were simplified to illustrate the successful theoretical foundation of these sources as the primary engines behind AGN. In a realistic scenario, infalling gas is expected to carry a non-zero angular momentum component, resulting in an orbital motion around the black hole that creates an accretion disk. Additionally, black holes are not restricted to accreting at the Eddington limit, and rotating black holes are even more efficient than the example shown. Further exploration of different accretion modes will be discussed in Section 1.1.3.

1.1.2 The Unified Model

The history of AGN detection dates back to the early 20th century, with the recording of nebular emission lines in the optical spectra of nearby galaxies (Seyfert, 1943). Carl Seyfert identified peculiar galaxies, now named Seyfert galaxies, characterized by a significant fraction of their total luminosity in their nuclear regions and diverse emission lines spanning a wide range of ionization states.

In the early 1960s, the advent of radio astronomy facilitated the detection of extremely powerful sources dominated by non-thermal processes, followed by the identification of their point-source-like optical counterparts (Schmidt, 1963). These quasi-stellar objects, called quasars (QSOs), revealed unprecedented distances and luminosities, surpassing ordinary galaxies by factors of hundreds or even thousands. Between them, two populations were defined using their radio-to-optical ratio (Sandage, 1965): the bright radio sources ("radio loud") and the radio faint ("radio quiet").

These distinct yet simultaneous paths in observing active galaxies led to a classification based on observed phenomenology that persists for historical reasons. Consequently, the contemporary taxonomy can be highly intricate (Padovani et al., 2017), with boundaries that may appear blurred (Merloni et al., 2014; Mountrichas et al., 2021). Moreover, the complexity is compounded by the diverse observational characteristics across the electromagnetic spectrum, often necessitating multi-wavelength studies to better understand these puzzling objects (Netzer, 2015).

In the following decades, surveys defined the AGN typical properties (Weedman, 1977). Seyfert galaxies were categorized into two types based on their optical spectra. Seyfert 1 galaxies displayed broad permitted emission lines, indicative of high-velocity gas ($> 1000\,\mathrm{km\,s^{-1}}$)

around the central SMBH. In contrast, Seyfert 2 galaxies exhibited both permitted and forbidden lines with similar widths of low-velocity dispersion ($\sim 100\,\mathrm{km\,s^{-1}}$). Some galaxies also showed weaker nuclear luminosities with low-ionization nuclear emission-line regions (LINERs; Heckman, 1980). These sources are usually associated with the lowest luminosity AGN. Like other AGN, LINERs can be classified into type 1 and type 2 sources, although the great majority of the discovered LINERs are type 2 (Ho, 2008; Netzer, 2013).

Beyond a particular wavelength band, AGN emissions span the entire electromagnetic spectrum, from radio waves to high-energy radiation. However, not all emissions are necessarily generated by the same physical processes. Significant contributions from thermal processes are observed in wavelengths such as ultraviolet (UV), optical, and infrared (IR). In contrast, at both ends of the spectrum, the energy distribution is dominated by non-thermal processes[3]. While these processes can be related, they do not necessarily occur in the same physical space or at the same physical timescale. Therefore, an AGN is not merely an object but a complex *engine* with different components interacting.

Active galaxies also share a common trait: a powerful central emission accompanied by temporal variability, i.e., their optical magnitudes can change at the 0.3–0.5 level over timescales of a few days. The temporal variations suggest that the emission source is spatially confined, with a size smaller than a cubic parsec. This implies that a region comparable to the size of the Solar System emits more radiation than an entire galaxy (Peterson, 1997).

The pivotal moment in AGN understanding arrived with the unification model (Antonucci, 1993; Urry and Padovani, 1995). This framework proposed that observed differences between Seyfert 1 and Seyfert 2 were due to orientation effects rather than intrinsic disparities. At its core lies a central torus, a geometrically thick structure of dust and gas surrounding the central SMBH and its accretion disk. The torus obscures inner regions based on the observer's line of sight and orientation. Support for the unification model emerged from mid-1980s polarization measurements, revealing polarized broad emission lines in some Seyfert 2 galaxies (Antonucci and Miller, 1985). X-ray observations further confirmed the model, associating unabsorbed and absorbed X-ray AGN with optical Seyfert 1 and 2, respectively (Awaki et al., 1991).

The modern understanding of AGN is anchored in the unified model, which provides a coherent framework to explain the diversity of their properties. The model highlights the crucial role of orientation

---

3 The distinction between thermal and non-thermal processes lies in the former's dependence on temperature (e.g., blackbody radiation, emission lines from a gas in thermodynamic equilibrium, bremsstrahlung, etc.). On the other hand, non-thermal processes lack this temperature dependence (e.g., synchrotron radiation, inverse Compton effect, Cherenkov radiation, production of photo-mesons, etc.).

effects in shaping the observed characteristics of these enigmatic objects. This standard model of AGN comprises the following structures:

- Supermassive black hole
- Accretion disk
- Hot corona
- Regions of low and high-density clouds
- Toroid of dust and gas
- Bipolar relativistic jet
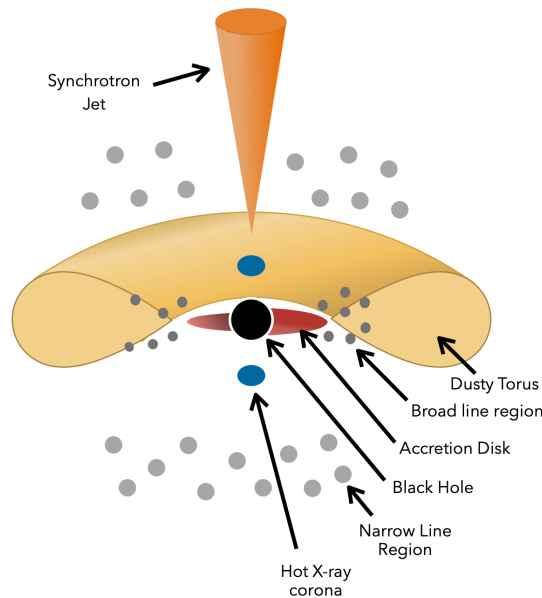
Figure 1.2: A simple diagram of the core of an active galaxy and its key structures. Credits: Thorne et al. (2022)

As depicted in Fig. 1.2, at the core of the system, an SMBH accretes material from an accretion disk formed in its vicinity. This accretion disk is a flattened, circular structure formed when material falls towards the strong gravitational pull of the SMBH and can extend until 200 AU[4]. The material in the disk spirals inwards, losing energy and angular momentum as it does so. This energy loss causes the disk to heat up, and the hot gas in the disk emits radiation that peaks at the UV. The balance between gravity and the pressure of the gas in the disk determines the structure of an accretion disk. If gravity is too strong, the disk will simply fall into the central object. If the pressure is too high, the disk will be disrupted, and the material will not be able to accrete onto the central object. The commonly assumed theory is that this disk is optically thick and geometrically thin (Shakura and

---

4 Distances are considering a SMBH with a mass of $10^8 \ M_\odot$

Sunyaev, 1973). The disk is assumed to be in a steady state, meaning that the rate at which material is falling into the disk is equal to the rate at which it is being accreted onto the central object. The high efficiency discussed earlier ($\eta \sim 0.1$) implies that the accretion rate remains relatively low even for the most powerful AGN. The details on the accretion are discussed in Section 1.1.3.

Surrounding the accretion disk, there is the so-called hot corona of relativistic electrons (Fig. 1.2). The exact way in which the corona is heated is still not fully understood, but it is thought to be due to a combination of magnetic reconnection, turbulence, and Inverse Compton. The hot corona is a key component of AGN, and it plays an important role in the production of X-ray radiation. The simplest model considers hot ($T \sim 10^8 - 10^9$ K) optically thin gas placed above or within the inner part of the accretion disk (Haardt and Maraschi, 1991; Fabian et al., 2015).

In a parsec scale from the center, there is a toroidal structure of gas and dust called a dusty torus or molecular torus (Fig. 1.2). This highly dense dust absorbs UV-optical radiation at some angles and thermally reprocesses it in the mid-IR. The torus can also absorb X-ray emissions. The toroidal structure is debated between being smooth or clumpy and its shape since it is not static; it constantly interacts with the surrounding environment. The intense radiation from the accretion disk can heat and ionize the gas in the toroid, causing it to expand and become more diffuse. The molecular toroid is also thought to play a role in the fueling of the AGN. As gas from the toroid falls inward towards the accretion disk, it can provide a fresh supply of material to power the SMBH. Observational data indicate that the size of this structure is compact (less than 1 parsec, see Elitzur, 2006, for a review). This size scales with luminosity and is uncorrelated with the black hole mass (Suganuma et al., 2006), demonstrating that the torus inner boundary is ruled by dust sublimation. On the other hand, determining its outer edge proves challenging. An anticipated outer boundary may correspond broadly to the gravitational sphere of influence of the SMBH, estimated at a radius of approximately 10 parsecs (Hickox and Alexander, 2018).

The SMBH affects the gas clouds at sub-pc distances ($10^3 - 10^4$ AU). The movement of the closer ones is dominated by SMBH gravity, and this region is home to clouds of gas swirling around the black hole at incredibly high speeds, reaching up to a few thousand kilometers per second ($10^3 - 10^4$ km s^{-1}; Peterson, 1997). The emission of these clouds with high velocities and high density produces Doppler-induced broadening of their emission lines, giving the name to the broad-line region (BLR). The intense radiation from the accretion disk and the hot corona bombard the gas in the BLR, stripping away electrons and leaving behind ions. Since the width of these emission lines directly reflects the high velocities of the gas clouds, the BLR is a

powerful tool for measuring the gravitational forces near the black hole (more on that in Chapter 2). The outer boundary of this region is believed to be the physical transition to the dusty torus (Elitzur, 2008).

At the outskirts of the AGN structure, at the 0.3-30 parsec scale, lies a more serene and extended region known as the narrow-line region (NLR). Unlike the BLR, where gas clouds are subjected to intense gravitational forces and high velocities, the NLR is characterized by lower temperatures, lower densities, and slower gas motions ($300 - 1000\,\mathrm{km\,s^{-1}}$, Padovani et al., 2017). This gas is ionized by the intense radiation from the AGN's central engine, causing it to emit emission lines at specific wavelengths. However, due to the lower velocities of the gas in the NLR, these emission lines are much narrower than those observed in the BLR. The NLR provides valuable insights into the overall structure and extent of AGN. By measuring the size and brightness of the NLR, astronomers can estimate the total amount of gas surrounding the black hole and gain a better understanding of the AGN's fueling mechanism (Osterbrock and Ferland, 2006). Additionally, the NLR can be used to study the winds that are ejected from AGN, which can significantly impact the evolution of galaxies (more about that in Chapter 2).

Finally, the AGN can have a pair of highly collimated jets perpendicular to the accretion disk formed by relativistic particles. These jets can extend into the intergalactic medium for the most powerful AGN. The main emission of the jets is through synchrotron emission and the Compton inverse mechanism, based on the synchrotron-self-Compton model that can cover from gamma to radio bands. The mechanisms that drive the formation and collimation of relativistic jets are still not fully understood, but they are thought to involve magnetic fields and the rotational energy of the black hole (Blandford and Znajek, 1977; Lu et al., 2023). The intense gravitational forces near the black hole twist and stretch the magnetic field lines, creating a funnel-like structure that guides the jet particles along a narrow path. Relativistic jets are characterized by their extremely high speeds, approaching the speed of light. This high speed is due to the relativistic effects that become significant at such velocities. As the jet particles interact with the interstellar medium, they can shock-heat the gas, trigger star formation, and even disrupt the evolution of entire galaxies (for a review, see Hardcastle and Croston, 2020).

The strength of the unified model lies in its axisymmetric nature, capable of explaining observed differences based on the orientation of the system relative to the observer. As shown in Figure 1.3, the anisotropy of the model, along with variations in jet power, explains the different classifications of AGN. When observed in the direction of the jet, a *blazar* is detected. These sources are strongly dominated by the non-thermal emission from its jets and amplified for relativistic effects. If the observer maintains a close but non-aligned direction with
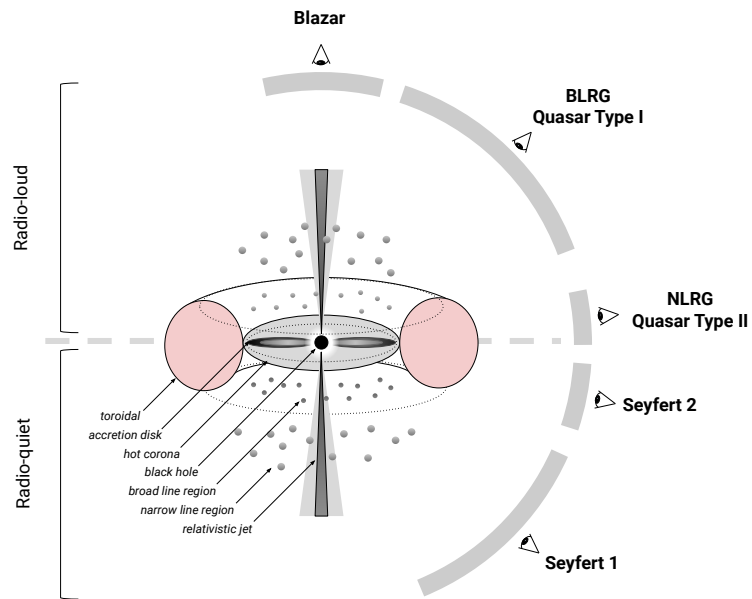
Figure 1.3: *Unified model:* Different classifications of AGN can be explained by their radio emission and the observer's inclination. Adapted from: Beckmann and Shrader (2012).

the symmetry axis, the jet's emission is attenuated, and both broad and narrow emission lines are observed (BLRG or QSO). A higher inclination will cause the toroid to obscure the high-density regions near the SMBH, and only narrow lines will be observed (NLRG). In cases where no radio jet is detected or it is very weak, the source will be classified as Seyfert I or II, using the same criterion for emission lines as for BLRG and NLRG.

Cumulatively, each of these structures imparts a distinctive signature across the broad electromagnetic spectrum emission of AGN. The hot corona plays a pivotal role in X-ray emission, while the accretion disk explains the observed UV-optical emission. The obscuration of the accretion disk at certain angles and reemission in the infrared is done by the dusty torus. The radio properties, on the other hand, are generally explained by the jet. The NLR and BLR elucidate the high-ionization lines observed in UV-optical spectra. The Spectral Energy Distribution (SED) produced by each component is depicted in Fig. 1.4. Understanding the diverse SED that an AGN can produce and fitting observations can provide valuable insights into the physical properties of an AGN, a methodology that will be explained in detail in Chapter 3.
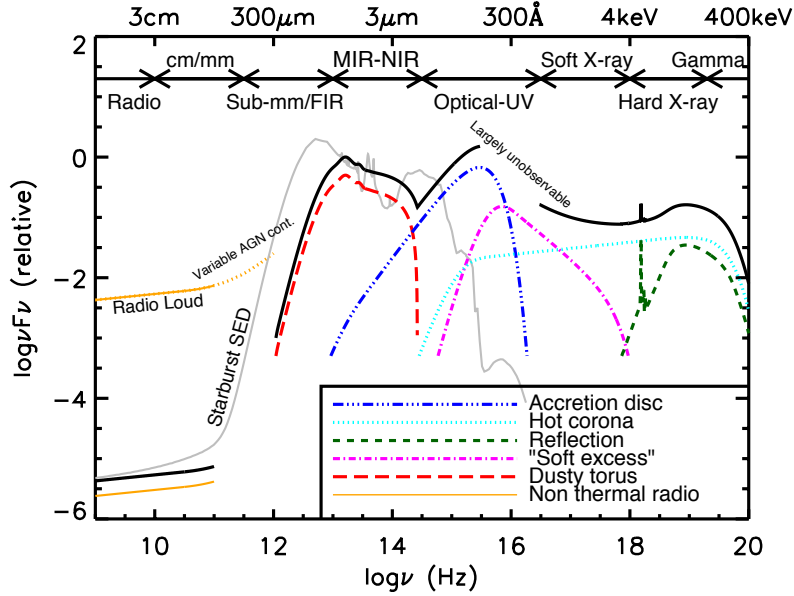
Figure 1.4: Schematic representation of the SED of an AGN (black curve)
and its main components (as indicated by the colored curves).
A SED from a star-forming galaxy is shown in light grey for
comparison. Credit: Harrison (2014).

1.1.3 Accretion on SMBH

1.1.3.1 Standard accretion disk

As previously discussed, the prevailing theory explaining the UV-
optical emission from AGN involves the accretion disk model. Ac-
cording to this model, SMBHs are enveloped by a flattened disk of
hot and dense gas spiraling inward due to gravitational forces. The
strong gravitational pull of the SMBH accelerates the gas, leading
to heating and the emission of radiation. The classical theory of ge-
ometrically thin and optically thick accretion disks was developed
by Shakura and Sunyaev (1973) and Novikov and Thorne (1973).
They proposed a model assuming Keplerian rotation, where magneto-
rotational instability within the disk generates viscosity, transferring
angular momentum outward. This process allows matter to spiral
closer to the SMBH gradually. A significant fraction of gravitational
energy is converted into electromagnetic radiation during this journey,
with efficiency influenced by the SMBH's spin.

General relativity predicts an Innermost Stable Circular Orbit (ISCO)
around a black hole. Beyond this limit, free circular orbital motion
is unsustainable, and matter falls directly into the black hole's event
horizon without emitting its remaining energy. Therefore, a larger
ISCO implies a lower efficiency, as less gravitational energy is extracted
before the black hole consumes the gas. For a non-rotating black
hole (also called Schwarzschild black hole), the ISCO radius is $6\,r_g$

(r_g being the gravitational radius $r_g = GM/c^2$), corresponding to an efficiency of $\eta = 0.057$. Conversely, for a Kerr black hole rotating at its maximum spin, the ISCO approaches r_g, increasing efficiency and reaching $\eta = 0.42$.

The emitted spectrum from a geometrically thin and optically thick accretion disk can be approximated by assuming the disk comprises rings with infinitesimally small radial thicknesses. Each ring emits as a blackbody, and the temperature depends on its distance from the SMBH:

$$T(r) = \left(\frac{GM\dot{m}}{4\pi\sigma r^3} \right)^{1/4} , \tag{1.3}$$

where σ is the Stefan-Boltzmann constant. The integrated spectrum results from summing the contributions from all individual rings. Figure 1.5 illustrates how these factors affect the emitted SED. A larger ISCO means fewer inner rings, reducing the number of photons from the higher-temperature blackbody. Thus, the SED depends on the black hole's rotation, mass, and accretion rate. In luminous quasars, the peak emission typically falls in the UV/optical restframe range, recognized as the *big blue bump*.
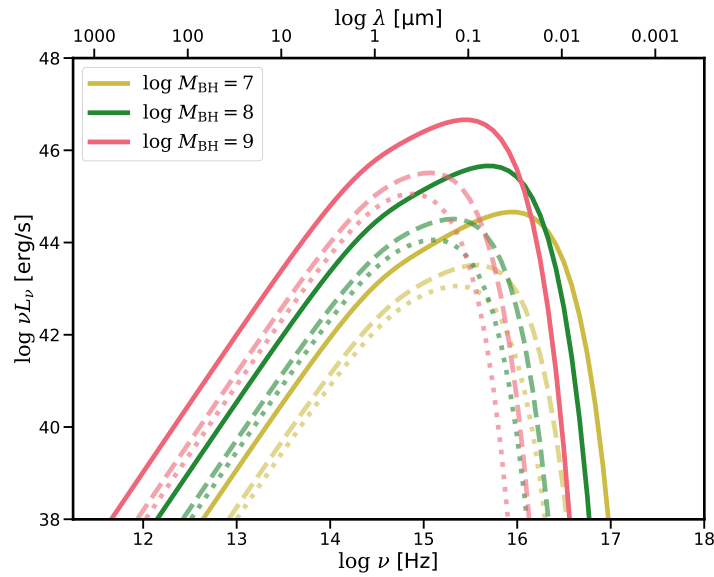
Figure 1.5: Each line represents the SED produced for a standard accretion disk. The solid line corresponds to $\lambda_{\mathrm{Edd}} = 1$, the dashed line to $\lambda_{\mathrm{Edd}} = 0.1$, and the dotted line to $\lambda_{\mathrm{Edd}} = 0.05$. Different colors indicate different black hole masses.

While this *central engine* solution is the standard, it is not universally applicable across all accretion regimes. In the very high accretion rate regime, the inward gravitational pull is so intense that the gas cannot radiate away all acquired energy as it spirals inward. Consequently, excess energy is advected into the black hole along with the matter. On the other side, in the very low accretion rate regime, the energy

released through viscous interactions is not efficiently radiated away, and plasma particles lose energy primarily through collisions. This causes the plasma to become non-relativistic, and the disk becomes optically thin. Further exploration of this regime will be discussed in the next section. For a more comprehensive discussion on this topic, refer to Abramowicz and Fragile (2013).

1.1.3.2 Advection dominated accretion flow

Substantial structural changes occur in the accretion process at low accretion rates compared to the unified model described in Section 1.1.2. The radiation pressure from the *central engine* weakens, causing the broad-line region and the torus to shrink or disappear (Elitzur and Ho, 2009). Simultaneously, the accretion flow becomes less dense, optically thin, and less effective at cooling. Consequently, the geometrically thin and optically thick disk becomes unstable and is supplanted by an advection-dominated accretion flow (ADAF) beyond a certain radius. Fig. 1.6 illustrates this truncated accretion disk, the transition radius, and the ADAF.
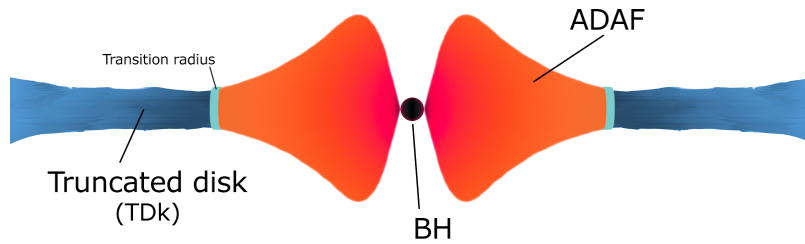
Figure 1.6: Schematic diagram of a possible hybrid scenario for a low accreting black hole. The diagram shows the truncated accretion disk (TDk), the transition radius, and the advection-dominated accretion flow (ADAF).

ADAFs exhibit a lower radiative efficiency compared to Shakura-Sunyaev geometrically thin disks, resulting in a significantly diminished luminosity. Fig. 1.7 depicts the transition of radiative efficiency from a thin disk to an ADAF and its dependence on the accretion rate. The low radiative efficiency stems from highly inefficient particle interactions due to the low plasma density, leading to a significant difference in electron and proton temperatures, where a Maxwell–Boltzmann statistical distribution is not attainable.

The rapid advection in ADAFs results in a rotation profile deviating from Keplerian motion. It also dissipates the orbital energy that cannot be radiated locally before being carried inward. ADAF solutions tend to be hot ($T \sim 10^{12}$ K), and quasi-spherical. Moreover, the low plasma density in an ADAF implies optical thinness, resulting in a SED that significantly differs from that of a blackbody. Specifically, the SED is
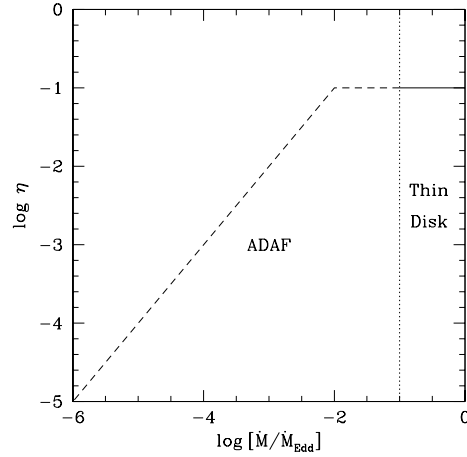
Figure 1.7: Radiative efficiency (η) for ADAF and thin disks as a function of the accretion rate. While η for standard thin disks is 0.1, it varies with the Eddington ratio (λ_{Edd}) for ADAFs. Credits: Narayan and McClintock (2008)

produced by a combination of synchrotron radiation, Bremsstrahlung radiation, and inverse Compton scattering. Fig. 1.8 compares the SEDs of different ADAF solutions at different accretion rates with a standard accretion disk of the same mass.
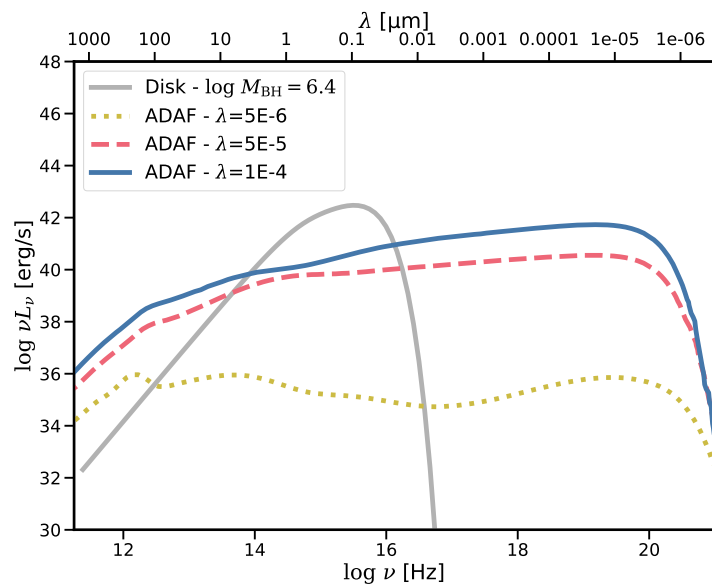
Figure 1.8: SEDs of ADAFs and a thin disk. Each line represents the SED produced for an ADAF of $10^{6.4}$ M$_\odot$ at different Eddington ratios (λ_{Edd}). The gray solid line represents a standard accretion disk with $\lambda_{\mathrm{Edd}} = 0.05$ for the same black hole mass for comparison. ADAF models from Beckert and Duschl (2002)

ADAFs are prevalent in Low-Luminosity AGN (LLAGN) (see Yuan and Narayan (2014) and references therein). Notably, two of the most extensively studied accreting black holes, Sgr A* at the center of our galaxy and M87* at the heart of the radio galaxy Messier 87, are examples of ADAFs. For a more comprehensive discussion of ADAFs, refer to the review article by Narayan and McClintock (2008).

1.2 THE EVOLVING AGN: BEYOND UNIFICATION

The AGN Unified Model AGN proposes that the observed differences in AGN types (Seyfert 1, Seyfert 2, Quasars) are primarily due to the orientation of the accretion disk relative to the observer's line of sight. According to this model, Seyfert 1 galaxies have their accretion disks oriented face-on, allowing us to see the broad emission lines from the BLR, while Seyfert 2 galaxies have their accretion disks oriented edge-on, obscuring the BLR. Quasars are thought to be similar to Seyfert 1 galaxies but with much higher luminosities. Even so, it also proposes that AGN are just stable peculiar objects whose emission is constant on time and just variable because of the effects of stochastic accretion.

However, this Unified Model scenario becomes more complex at low luminosity levels, where accretion physics differs (as explained in Section 1.1.3.2), and the typical structure may change. Although LLAGN Type 1 exists, represented by Seyfert galaxies and LINERs, the majority of the LLAGN population is Type II. These observations suggests that the standard unified model may not hold at very low luminosities (Ho et al., 2001).

On the other hand, because the physical processes within an AGN are primarily dictated by gas dynamics where the SMBH's gravity dominates, they should be relatively insensitive to the cosmological epoch. However, a redshift dependence exists: while finding a very luminous AGN in the local Universe is rare, it becomes more common looking backward in cosmic time. As illustrated in Figure 1.9, Hopkins et al. (2007b) obtained Luminosity Functions (LF) across different bands, revealing that lower luminosity AGN peak at lower redshifts, while the peak for high luminosity AGN shifts to $z \sim 2$–3, commonly referred to as cosmic noon.

Today, we know that AGN are not merely a particular type of celestial objects; their existence is intimately tied to the evolution of their host galaxies. Even SMBHs are not always active, and the active phase is just a moment in time, with certain cosmic moments that are more frequent in finding accretion activity. This AGN phase will depend on the intricate interplay between the black hole, its surrounding material, and the galaxy's overall evolution. While the fundamental physics governing SMBH gravity remains consistent
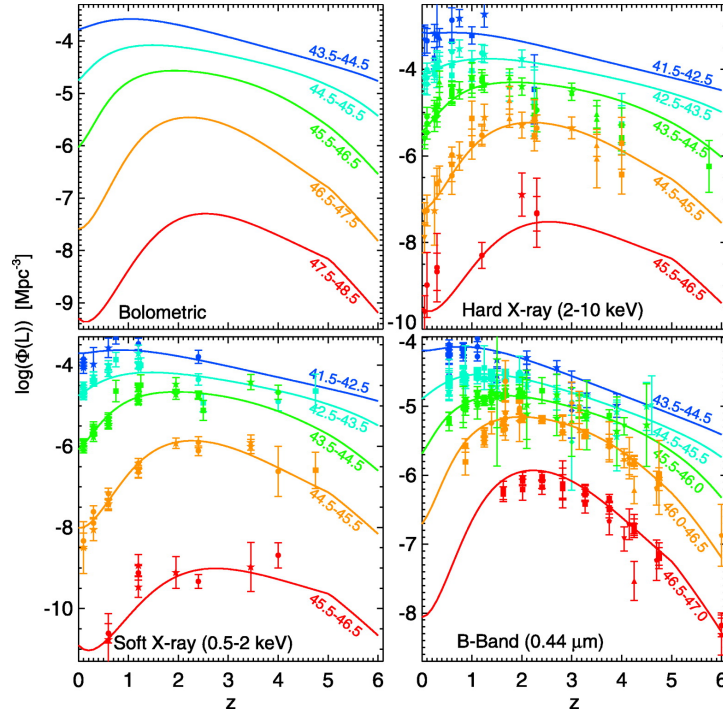
Figure 1.9: Luminosity functions for quasars illustrating the dependence of bolometric luminosity and the luminosity in three differebt bands (X-ray Hard, Soft, and B-band) on redshift. Credit: Hopkins et al. (2007b).

across all redshifts, the quantity of gas available to accrete and the mechanisms delivering this gas to the core of the galaxy vary. A new interpretation of how SMBH evolves challenges the previously dominant paradigm of AGN as objects solely defined by their viewing angle; instead, for example, merger and star formation can be related to AGN activity (e.g., Hopkins et al., 2007a).

The environment surrounding an AGN plays a crucial role in shaping what we ultimately observe. As Ramos Almeida and Ricci (2017) highlight, the opening angle of the obscuring material, responsible for the differences between Seyfert 1 and Seyfert 2 galaxies, depends heavily on the accretion rate of the black hole. Higher accretion rates generate stronger radiative pressure, clearing a wider path for the emitted radiation and revealing the broad emission lines. This adds a link between Luminosity and AGN types, and not only the inclination. Ananna et al. (2022) interprets the fraction of obscured AGN in terms of circumnuclear geometry and Eddington ratios. Specifically, at low Eddington ratios ($\log \lambda_{\mathrm{Edd}} < -2$), obscured AGN outnumber unobscured ones by a factor of ~ 4, reflecting the higher covering factor of the circumnuclear material. At high Eddington ratios ($\log \lambda_{\mathrm{Edd}} > -1$), the trend is reversed, with only $< 30\%$ of AGN showing high obscuration, which we suggest is mainly due to the small fraction of time spent in a highly obscured state.

A closer look at quasar populations further supports this evolutionary model. Obscured quasars (also called *red quasars*) are likely to be the result of a brief but violent phase in the evolution of galaxies when their black holes eject large amounts of energy into the surrounding dust and gas. This energy emission carries away any gas and dust in the vicinity, leaving a *blue quasar* behind (Klindt et al., 2019). The interstellar medium (ISM) from the host galaxy can also be an important source of obscuration at high redshift (Gilli et al., 2022). Besides, compact and dusty galaxies with strong star formation rate (SFR) can effectively hide an active and luminous SMBH that is buried in the host galaxy dust, showing that the obscuration can be produced outside the toroid Andonie et al. (2024).

Furthermore, Type I and Type II AGN can represent distinct populations (Elitzur, 2012) with Type II potentially residing in host galaxies exhibiting different properties than Type I, including lower black hole masses (Onori et al., 2017). In this evolutionary scenario, Type II AGN are characterized by galaxies with black holes accreting at high Eddington ratios but obscured within a dusty environment. The radiative pressure and other feedback processes act to push away the obscuring material, creating a window in which the AGN is observed as a Type I (Hopkins et al., 2005). It is evident that the evolutionary model of AGN transcends a simple geometric picture, encompassing the complex interplay between the black hole, its surrounding material, and the galaxy's evolution. Consequently, discussing AGN in the context of galaxy evolution is crucial. For a more detailed discussion, refer to Merloni and Heinz (2013).

1.2.1 Co-evolution of SMBHs and Host Galaxies

Since the groundbreaking discovery of the first quasar by Schmidt (1963), the intriguing connection between SMBHs and their host galaxies has been a subject of exploration (Lynden-Bell, 1969; Soltan, 1982; Salucci et al., 2000). Over the years, a wealth of evidence has accumulated (refer to Fig. 1.10), highlighting compelling parallels in the evolutionary trajectories of SMBHs and galaxies. Here is a summary of the key evidence:

1. Tight correlations between the mass of the central black hole (M_{BH}) and bulge properties, such as velocity dispersion (σ) and mass (M_{bulge}), imply a fundamental link between SMBH growth and galaxy formation. These correlations persist, albeit with a larger scatter, concerning global galaxy properties like stellar mass ($M_\star$) (Ferrarese and Merritt, 2000; Kormendy and Ho, 2013).

2. The cosmic evolution patterns of galaxy SFR density peaked at $z \sim 2$–3 and has been declining since then (Madau and Dickinson,
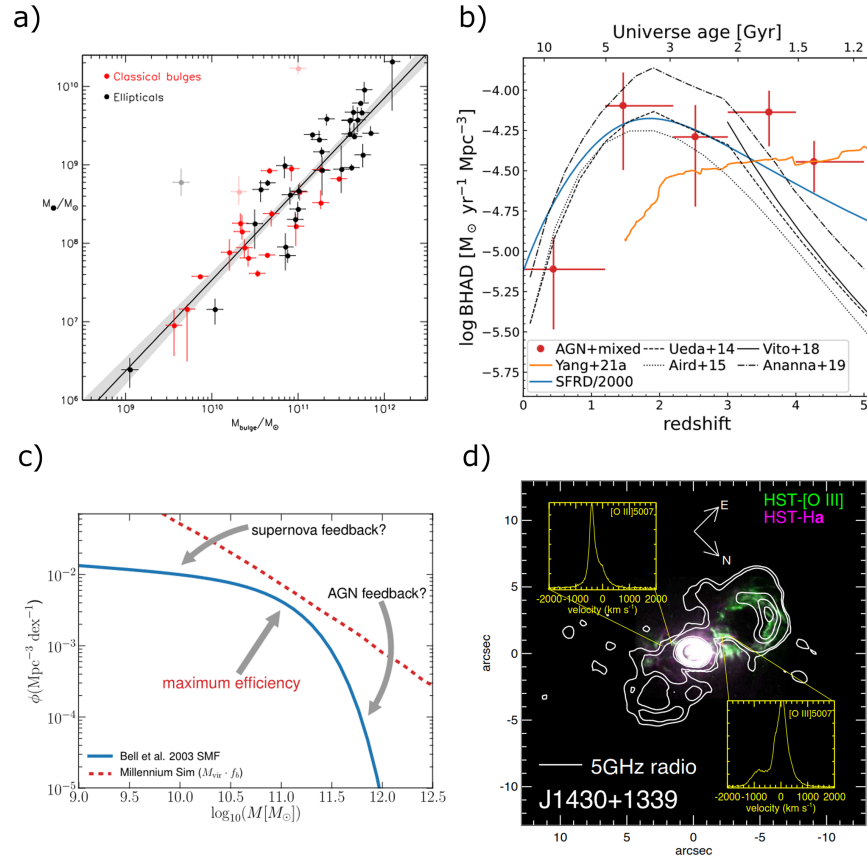
Figure 1.10: Compelling evidence for the co-evolution scenario: a) Black
Hole Mass correlates with bulge mass from its host galaxy (Ko-
rmendy and Ho, 2013); b) Different measurements of the Black
Hole Accretion Density (BHAD) exhibit a similar pattern to the
Star Formation Rate Density (SFRD) (orange line from Madau
and Dickinson, 2014) as a function of redshift. Credit: Yang
et al. (2023); c) The dashed line shows the baryon Mass function
expected from the theory without considering supernova and
AGN Feedback. The blue solid line shows the actual observa-
tions. Credit: Mutch et al. (2013); d) AGN Feedback caught in
the act on the Teacup galaxy. The radio emission from a jet (or
quasar winds), shown in contours, corresponds with ionized
outflows observed from OIII, shown in green (Harrison, 2014).

2014). Similarly, the black hole accretion rate density (estimated
from the UV-optical quasar luminosity function) exhibits intrigu-
ing similarities (Boyle and Terlevich, 1998), also showing a peak
at $z \sim 2$–3 and a decrease at present times. Similar trends are also
observed in AGN selections done with IR and X-ray (Delvecchio
et al., 2014; Aird et al., 2015; Carraro et al., 2020).

3. The imperative to quench star formation in high-mass galaxies
   becomes evident. Despite the absence of a theoretical limit on
   galaxy growth, the observed limit of 10^{12} $M_\odot$ for the most mas-

sive galaxies is attributed to AGN feedback, adversely affecting the star formation of their host galaxies (Croton, 2006; Mutch et al., 2013; Schaye et al., 2015).

4. Direct observations, including X-ray-emitting gas in ellipticals, quasar outflows, and ionized gas outflows in radio galaxies, consistently provide evidence supporting the active role of the so-called AGN Feedback in regulating star formation processes (for a review, see Harrison, 2017).

The co-evolution scenario includes AGN as an active player in galaxy evolution due to its ability to release a substantial amount of energy, approximately 10 % of the rest-mass energy that the SMBH accrete. This released energy can have a profound impact on the surrounding gas, regulating star formation and influencing the overall evolution of the host galaxy. Even with only a small fraction of this energy coupling to the gas, it has the potential to disrupt the equilibrium of the galactic environment.

1.2.2 AGN Feedback

The accretion process around SMBHs, initially occurring at small scales, extends its impact across much larger scales. The inflow of material and the effects of accretion span seven orders of magnitude, from the initial gas capture to the black hole's event horizon. AGN feedback operates at even larger scales, introducing an additional five orders of magnitude, ranging from AU-size scales at the black hole horizon to entire galaxy clusters measuring several hundred kiloparsecs (Merloni and Heinz, 2013). The accretion disk and powerful jets of an AGN release substantial energy in the form of radiation, outflows, and relativistic particles, profoundly influencing the evolutionary trajectory of host galaxies (e.g., Alexander and Hickox, 2012; Fabian, 2012). The efficient coupling of this energy with the galactic medium can lead to the heating, excitation, or removal of gas from the ISM (Silk and Rees, 1998). The modification of ISM properties induced by these processes has the potential to alter the star formation rate within the galaxy. Consequently, AGN activity emerges as a dynamic force that can either enhance or entirely suppress star formation, illustrating the intricate interplay between SMBHs and galaxy growth (e.g., Gaspari and Sądowski, 2017).

Concrete evidence supporting AGN feedback "*caught in the act*" at all these scales fortifies its role in shaping galaxy evolution. Powerful radio galaxies in clusters, such as Cygnus A (Perley et al., 1984) and M87 (Owen et al., 2000), showcase the impact of jets depositing magnetized relativistic plasma over substantial distances. High-resolution X-ray imaging of radio galaxies like Perseus A provides direct evidence of large cavities excavated in the hot, X-ray-emitting thermal

gas of galaxy clusters (Boehringer et al., 1993; Fabian et al., 2011), and its connection with spurs radio emission (Gendron-Marsolais et al., 2020) confirms past AGN activity at the cluster scale. On this macro scale, AGN activity may prevent the cooling of hot halos, resulting in a global suppression of star formation (Gaspari and Sądowski, 2017). Numerous galaxy formation models incorporate the necessity of this type of energy input from AGN to replicate the observed population of quiescent galaxies (e.g., Bower et al., 2006; Dubois et al., 2016).

Powerful winds driven by quasar accretion-disk radiative activity can push away material, generating powerful molecular outflows on galactic scales (Tombesi et al., 2015). Bischetti et al. (2017) show that luminous AGN are highly efficient at pushing large amounts of ionized gas outwards and generating powerful ionized outflows. Moreover, Matzeu et al. (2023) provides further evidence through the detection and characterization of ultra-fast outflows, supporting the existence of highly ionized matter from the inner scales of an AGN propagating at relativistic speeds and contributing to the self-regulated AGN feeding-feedback cycle.

On the other hand, Girdhar et al. (2024) show that moderate-power jets ($P_{\mathrm{jet}} \sim 10^{43}$ erg s^{-1}) can have a direct impact on molecular gas on small scales through direct jet-cloud interactions. Instead, jet cocoons can push gas aside at larger scales. Together, both processes could contribute to the long-term regulation of star formation. Studies of particular obscured AGN, such as XID2028 (Brusa et al., 2018; Cresci et al., 2023), uncover detailed interactions between the host galaxy ISM and multi-phase outflows, emphasizing the role of radio jets in AGN feedback at galaxy scales. There, an expanding bubble is detected, from which the fast and extended wind outflow emerges. The complex interaction between AGN activity and ISM properties makes it so that, in some instances, it suppresses star formation, while in others, it favors new star formation processes, offering a nuanced narrative of galactic evolution (see Harrison, 2017, for a comprehensive review).

These diverse observations are just some examples of the strong evidence for AGN feedback found in the literature. Together, all the work done by scientists in our field collectively strengthens the understanding of AGN feedback operating across a broad range of scales and environments. The inclusion of AGN in the co-evolution scenario stems from its energetic capabilities, with the released energy acting as a regulatory force on star formation and contributing to the intricate interplay between the SMBH and its host galaxy. The substantial observational evidence supporting AGN feedback reinforces its standing as one of the predominant theories explaining the co-evolution of supermassive black holes and galaxies.

To gain a deeper understanding of these observations, AGN feedback is commonly categorized into two modes: radiative and kinetic.

The scheme in Fig. 1.11 illustrates the main differences between these modes.

Radiative Feedback   Kinetic Feedback

Outflows driven by AGN radiation   Reheated atmosphere by AGN jets
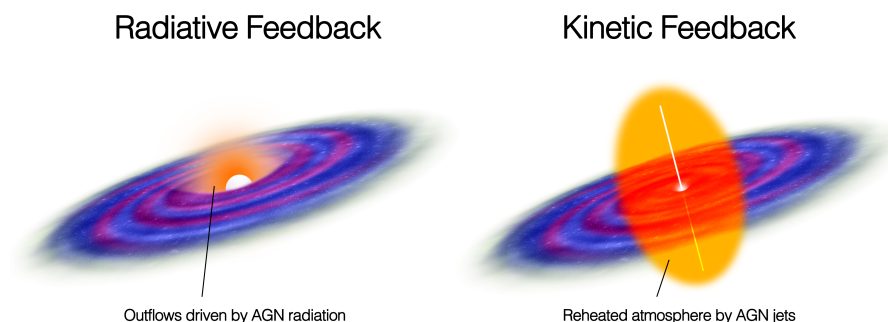
Figure 1.11: A simple scheme showing the main difference between radiative and kinetic feedback. While the former propels powerful outflows through radiative pressure, expelling gas from the galaxy's nucleus, the latter creates a cocoon by the radio jets that interacts with the ISM, generating turbulent motions, shock waves, and heating the environment.

Radiative feedback arises from AGN's intense luminosity, ionizing and heating the surrounding gas and dust. This thermal energy can prevent the collapse of dust clouds, effectively quenching star formation. This mode is also called quasar or wind mode and is associated with high accretion rates ($\lambda_{\mathrm{Edd}} > 0.01$). Furthermore, high-energy radiation propels powerful outflows through radiative pressure and ultra-fast outflow winds, expelling gas from the galaxy's nucleus. These winds traverse from the inner regions of the accretion disk to kiloparsec scales (King, 2005). This can remove the gas reservoir that is necessary for accretion and forming stars. This perspective is substantiated by observations, where outflows of kiloparsec scale are detected (Fiore et al., 2017), and hydrodynamical simulations (Wagner et al., 2013; Costa et al., 2015). In cosmological simulations, radiative mode feedback successfully curtails star formation at the high-mass end, aligning with stellar mass values observed in our Universe (Di Matteo et al., 2005). This mechanism assumes particular significance in the early universe when massive galaxies underwent rapid formation.

Kinetic feedback involves the expulsion of highly energetic jets, often accompanied by strong radio emission. These jets, propelled by magnetic fields and rotating SMBHs, penetrate deep into the galaxy's ISM, instigating interactions of their relativistic particles with the surrounding gas. This interaction results in the creation of cavities, shock waves, and turbulent motions, disrupting star formation, generating turbulence, and heating or compressing the gas. This mechanism, known as radio mode feedback, is believed to be more pivotal in the later stages of galaxy evolution and is associated with low accretion

rates. Its effects can extend to cluster scales, and it can also extinguish star formation at the high-mass end (e. g. Heckman and Best, 2014a).

While both modes can suppress star formation (i.e., negative feedback), especially through the cumulative effect of several AGN episodes, positive AGN feedback is not inconceivable. The movement of gas within a galaxy can generate compression that can stimulate star formation (Cresci et al., 2015). Moreover, within the same galaxy, both inhibiting and augmenting effects of AGN feedback can coexist (Bessiere and Ramos Almeida, 2022). It becomes evident that these feedback mechanisms are intricately tied to the specific characteristics of individual galaxies.

In local massive galaxies ($M_\star > 10^{11}\,M_\odot$) with old stellar populations, AGN kinetic feedback tends to dominate. In contrast, radiative feedback is more common in ongoing star formation and younger stellar populations at all redshifts. This suggests the idea that there are different phases in the AGN life, and the mode of feedback depends on the accretion rate. In any case, it is not clear whether the already quenched galaxies where we find kinetic feedback have star formation suppressed by this feedback or past episodes of radiative feedback. The life of an AGN has a short scale; this cycle is called a duty cycle with a typical length of 100 Myr, and it is expected that the radiative phase with a high accretion rate is just a short phase (5-10 Myr) (Novak et al., 2011).

Furthermore, the overall impact of each AGN feedback mode on the Universe remains shrouded in uncertainty. Exemplars like the Teacup Galaxy, showcasing a combination of a radio-quiet quasar and a radio jet causing disturbances, illustrate that both modes can be present simultaneously, highlighting the intricate and multifaceted nature of AGN feedback (Harrison et al., 2015; Audibert et al., 2023; Venturi et al., 2023). Further, radiative feedback is not confined to high-luminosity sources; while pronounced during the most luminous phases of AGN life, the radiative energy produced by inefficient accretion is potent enough to suppress star formation even at the lowest luminosity end (Almeida et al., 2023).

Despite compelling evidence for the active role of AGN feedback in galaxy evolution, some questions remain open. Is the quenching of local massive galaxies produced by kinetic feedback or previous periods of radiative feedback? Are the mass outflow rates the key that implies the material is removed from the galaxy, or is the heat produced by the shocks and turbulence enough to suppress star formation? Is AGN luminosity a good way to study accretion, or do the short timescales complicate catching the accretion and feedback moment in the act? Additionally, while AGN feedback can explain the observed M_{BH}–$M_\star$ scaling relation in the local Universe, the onset of its impact and the universality of this relation across cosmic time remains unclear. This can lead to potential biases in observational studies at moderate to

high redshift, where M_{BH} and λ_{Edd} are often inferred through this relation.

1.3 AIM OF THIS THESIS

This thesis is conducted within the collaborative framework of the Big Data Applications for Black Hole Evolution Studies (BiD4BEST)[5]. This project has received funding from the European Union's Horizon 2020 research and innovation program under the Marie Skłodowska-Curie grant agreement No 860744. The network is dedicated to unraveling the intricacies of black hole formation within the context of galaxy evolution. This collaboration brings together early-stage researchers, scientists, industrial experts, and science dissemination professionals in anticipation of new observational data from upcoming space missions. Furthermore, the Ph.D. program includes a 3-month internship in one of the network's industrial partners, where novel methods for studying big data and its potential applications to the industry were explored. The report of this secondment is detailed in Appendix A.

Focusing on the adult phase of AGN, this thesis delves into the interaction between galaxy properties and AGN activity. Our primary objective is to decipher the factors influencing accretion onto black holes and explore the impact of SMBH accretion on the co-evolution model across varying redshifts, particularly emphasizing the lowest luminosity regimes.

Moving forward, the thesis is meticulously organized into three distinct sections. The initial part contains two chapters that comprehensively discuss the methodology employed to derive the physical properties of AGN and their host galaxies. Subsequently, the second part unfolds through three interconnected chapters presenting the results obtained through our work. The thesis culminates in the final section, which includes a concluding chapter synthesizing the findings and discussing future research directions that will stem from the insights gained during this Ph.D. journey.

Methodology

GALAXIES AND AGN PROPERTIES FROM SPECTRAL FITTING   In Chapter 2, we delve into the utilization of spectra to ascertain the physical properties of objects, with a particular focus on galaxies hosting active nuclei and how the dynamic interplay between stars, ISM, and SMBH activity forms a spectrum. The analysis of these spectra can be a powerful tool that enables a comparative analysis between observed spectra and theoretical or empirical models. This method facilitates

---

the determination of temperature, pressure, chemical abundance, and motion through emission lines. Furthermore, the chapter explores the determination of SMBH mass from spectra.

SPECTRAL ENERGY DISTRIBUTION FITTING   In Chapter 3, we navigate through the application of SED analysis in astrophysics. This methodology is pivotal in determining the physical properties of astronomical objects, spanning galaxies and AGN. SED fitting involves the construction of models replicating observed emission spectra across a broad range of wavelengths, from radio waves to X-rays, and its comparison with real-world observations. We will discuss the Bayesian approach to this methodology, a popular SED fitting tool (Code Investigating GALaxy Emission; CIGALE[6]) and the models commonly used to produce the templates of different host galaxies and AGN.

Results

PROBING ACCRETION PROPERTIES UP TO $z \sim 2.5$ WITH MINIJPAS
Chapter 4 leverages the preliminary data from the Javalambre Physics of the Accelerating Universe Astrophysical Survey (J-PAS[7]) to obtain AGN physical properties up to redshift 2.5. Employing a multiwavelength approach, we utilize X-ray surveys to accurately characterize AGN populations. Our investigation encompasses the analysis of physical properties, with a special focus on their accretion ratios and their proxies, and an exploration of various co-evolution scenarios. While the study focuses on the preview data (miniJPAS; Bonoli et al., 2021), its potential extension to a larger dataset and wider spatial coverage for the future data release of J-PAS promises to provide a foundation for future investigations. The incorporation of statistical tools will facilitate a nuanced understanding of selection biases influencing accretion rate distributions.

A NEW SED FITTING MODULE TAILORED FOR THE LLAGN POPULATION
Addressing biases in the λ_{EDD} observed in the first part regarding luminosity, Chapter 5 introduces a novel module for CIGALE. This module was designed to study the low-luminosity population within AGN. We elaborate on the development of this tool, its physical motivation, and its application to a sample of 52 local LLAGN. The derived X-ray bolometric correction and exploration of UV-X-ray relations for LLAGN are presented, showing differences from the behavior of QSOs. The study also reveals that LLAGN may impact the specific star formation rate in their host galaxy's core. Future implementations will utilize incoming data from J-PAS and eROSITA to create the first census of bolometric luminosity for LLAGN.

---

6 https://cigale.lam.fr/
7 https://j-pas.org/

M58 AS A CASE STUDY FOR LLAGN FEEDBACK   In Chapter 6, we conduct an in-depth case study focusing on one of the galaxies from Chapter 5, the massive galaxy M58. The objective is to unravel the intricate interactions between a LLAGN and its host galaxy. Leveraging a combination of Spitzer spectral maps, Gemini NIRI imaging, ALMA CO 2-1, and HST multiband imagery, we dissect the complex relationships involving a radio jet, molecular gas, and the inner disk of the galaxy to understand the effects of LLAGN Feedback in detail.

Conclusions and Future Directions

CONCLUDING REMARKS   The final chapter (Chapter 7) serves as a synthesis of our findings, delving into the implications of our work on the co-evolution model and its broader significance in advancing our understanding of SMBHs and their host galaxies. Additionally, it offers a glimpse into future work, outlining the planned application of the acquired knowledge and methodologies during this Ph.D. in future projects. With the imminent arrival of new data, these endeavors can contribute further to understanding how AGN Feedback impacts host galaxies and validate the co-evolution scenario.

Part II

METHODOLOGY

2 | GALAXIES AND AGN PROPERTIES FROM SPECTRAL FITTING

The analysis of spectra is a fundamental tool in astrophysics, as they provide a wealth of information on the physical conditions and composition of astronomical objects and their environment. We can infer the temperature, pressure, chemical abundance, and even the motion of astronomical sources by discomposing and analyzing their light across different wavelengths. Thus, spectra fitting is a crucial technique in astrophysics that enables us to interpret and extract this information from observational data. It involves comparing an observed spectrum to a theoretical or empirical model and adjusting the model parameters to minimize the difference between the two. This process allows us to determine the object's physical properties from the observed spectral features.

The spectrum emitted from a galaxy is the result of the sum and interplay between the light emitted by its components: stars, gas, and dust. If a galaxy has an active nucleus, the continuum and the emission lines produced during the accretion process will be added to the galaxy spectra, depending on whether the light can travel without obstacles from the central engine to the observer or if it is absorbed in the way.

In this Thesis, we will use the spectra fitting methodology to fit emission lines from gas associated with AGN present in UV/optical restframe spectra (Chapter 4) and gas and dust associated with the interstellar medium in optical/IR (Chapter 6). From these spectra, we will obtain information about the physical properties of each source.

2.1 ISM AND ITS SPECTRAL FEATURES

The *interstellar medium*, referred to as ISM, constitutes the principal component of a galaxy after the stellar component. Consequently, its analysis is indispensable for comprehending galaxy evolution. A broad classification distinguishes it into gaseous and solid components. A more intricate scrutiny further divides the gaseous component into three phases: atomic, molecular, and ionized. It is crucial to note that this classification does not imply static conditions for the ISM; instead, processes such as recombination and ionization continually alter its phase. The description given here for the ISM, its phases, and its properties is largely taken from Draine (2011).

The *ionized phase* is composed of atoms that have undergone ionization and lose some or all of their electrons. This ionization can result from shocks, primarily caused by supernovae or photo-ionization from strong ultraviolet radiation fields. Emission nebulae and HII regions, recognized as large-scale structures, are formed. The temperature in this phase exceeds 10^4 K and is typically observed through recombination lines of Hydrogen (Hα, Hβ, etc.) and forbidden lines of O, N, Si, Ne in optical-IR spectra and in radio continuum.

The *atomic phase* comprises neutral atoms, with neutral Hydrogen (HI) being its primary component. This phase is pivotal, constituting 60 % of the Hydrogen content in the Milky Way in all its forms. Neutral gas is primarily observed through the HI 21cm line and absorption lines against stellar backgrounds in the UV-optical spectra. It can be further subcategorized into cold and warm phases. The cold phase, with temperatures of $T \sim 100$ K and densities $n_{\mathrm{HI}} \sim 30\,\mathrm{cm}^{-3}$, occupies only 1 % of the ISM volume. In contrast, the warm phase has higher temperatures, around $T \sim 5000$ K, but much lower densities $n_{\mathrm{HI}} \sim 0.6\,\mathrm{cm}^{-3}$.

The *molecular phase* comprises molecules forming clumpy structures known as molecular clouds, with typical temperatures of 10-50 K and sizes of a few parsecs. Stellar formation occurs in these regions due to their higher densities, $n_{\mathrm{H_2}} \sim 100 - 10^3$ cm^{-3}, compared to the rest of the cold ISM. They are also found in photodissociation regions (PDRs) and, under certain conditions, in shock fronts. Molecules and dust can be observed in emission and absorption in the IR-submillimeter spectra.

In their optical spectra, galaxies exhibit distinct ISM properties of the ionized phase. A quiescent galaxy without star formation processes produces a spectrum dominated by the continuum from old, cool, red stars, lacking emission lines. In contrast, a star-forming galaxy has a continuum that is bluer from its high proportion of hot, blue stars, which produce a lot of UV radiation.[1] This UV radiation ionizes the ISM, which produces permitted emission lines from the Balmer series, like Hα and Hβ, and low-ionization forbidden lines like [OI] λ6300Å, [NII] λ6583Å and [SII] λ6716,6731Å. Fig. 2.1 shows a comparison between the spectrum of galaxies to exemplify these differences. An active galaxy will also show emission lines from the Balmer series and higher ionization states of elements, as we will see in Section 2.2.

Conversely, the ISM's molecular phase is depicted in the infrared-submillimeter spectrum. The continuum in these spectra is dominated by old stars and the thermal emission of dust, with additional emission

---

1 The intrinsic differences in a galaxy's stellar continuum provide valuable information for fitting its stellar population, a process carried out by codes such as Bagpipes (Carnall et al., 2018). While this thesis doesn't delve into this aspect, a more detailed description of the stellar continuum is provided in Chapter 3, where the modeling of the host galaxy SED is thoroughly explained.
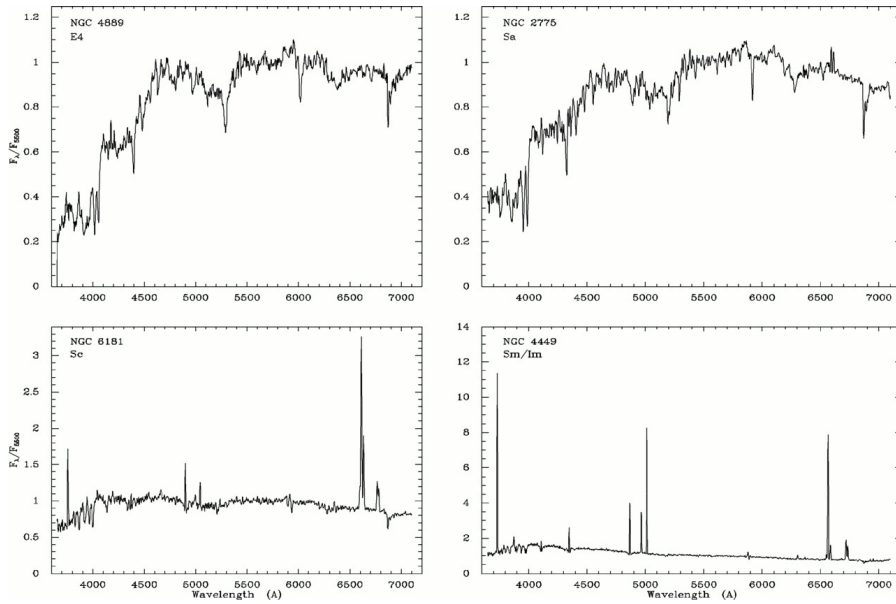
Figure 2.1: Integrated optical spectra of elliptical, spiral, and irregular galaxies. The spectra shown at the top are dominated by the continuum of old stars (quiescent), while the bottom spectra have strong emission lines typical of star formation. The fluxes have been normalized to unity at 5500 Å. Image credits: Kennicutt (1992)

lines depending on the ISM properties for different galaxies (Fig. 2.2). While the hydrogen molecule (H_2) is the key component of this phase, other molecules like carbon monoxide (CO), emitting in the submillimeter, act as indicators for molecular gas. A common technique to estimate the molecular gas mass is from the observed CO 1-0 line and applying a conversion factor (for details, see Carilli and Walter, 2013).

Detecting H_2 is challenging due to its symmetrical nature, lacking a permanent electric dipole moment. This restricts electronic dipole transitions, making them ineffective for energy removal. However, the rotational and vibrational states of H_2 molecules can emit lines in specific scenarios. A common method of exciting hydrogen molecules is exposure to far-ultraviolet (FUV) photons with energy levels of 6–13.6 eV. Consequently, H_2 emission is often detected in PDRs surrounding H II regions.

Another characteristic feature of the molecular phase spectrum is the emission from dust particles. If the dust has reached thermal equilibrium (200–600 K), it is termed *warm dust* and will re-emit in the mid-infrared (MIR) with a peak between 7 and 26 μm (Pier and Krolik, 1992; Ramos Almeida et al., 2009; Asmus et al., 2014). For cold dust, with temperatures between 10-100 K, the emission is also observed in the far-infrared (FIR) and submillimeter.

A particular dust molecule we will study in this work is Polycyclic Aromatic Hydrocarbons (PAH). PAH are flat molecules composed
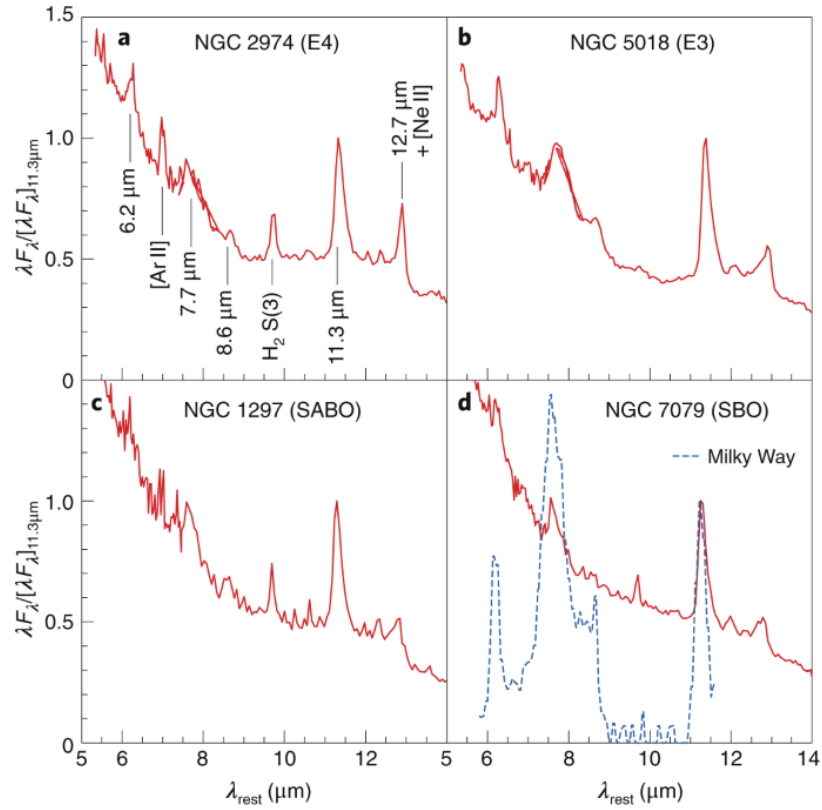
Figure 2.2: Integrated mid-infrared spectra of elliptical and spiral galaxies. While the PAH structures at 7.7 and 11.3 are present in these four examples, [ArII] and H_2 are not so common. Image credits: Li (2020)

mainly of benzene structures, consisting of a ring of carbons and hydrogens at their ends. These benzene groupings can contain up to 80 carbon atoms, resulting in sizes between 4-10 Å. PAH exhibit intense emission at 3.3, 6.2, 7.7, 8.6, 11.3, 12.7, and 17 μm, due to their vibrational transitions; they are excited only if they are small enough to absorb an optical or UV photon, which heats the molecule to temperatures $T > 250$ K. Notably, the emission is modeled as a Drude profile. The emission structures with which PAHs manifest in a given spectrum vary according to their ionization state: the emission at 11.3 μm is more intense in neutral PAH, while the vibrational mode at 7 μm is more important in ionized PAH (Draine and Li, 2007).

2.2 AGN AND THEIR SPECTRAL FEATURES

The spectral features of AGN distinguish them from non-active galaxies, primarily due to the presence of higher ionization states of elements. While narrow emission lines from the NLR may resemble those found in Star-Forming galaxies, AGN exhibit a broader range of ionization states. Emission lines such as [OII] λ3726,3729Å,

[OIII] λ4959,5007Å, and [NII] λ6548,6583Å, often accompanied by low ionization lines like [OI] λ6300Å, [SII] λ6716,6731Å, are more prominent than in HII galaxies. Additionally, moderately strong permitted lines of the Balmer series, HeIλ5876Å, HeIIλ4686Å in the optical regime, and Lyman series, CIVλ1549Å, MgIIλ2798Å in the UV regime, contribute to the distinctive AGN spectrum (for a more detailed description of typical AGN emission lines, see Netzer, 1990).

As discussed in Chapter 1.1, the nature of the observed lines depends on the AGN classification. In Type II AGN, only lines from the NLR are expected, while in Type I sources, the BLR is also observable. The BLR, illuminated by the intense radiation from the central accretion disk, exhibits high-velocity dispersion due to gravitational forces, leading to Doppler broadening in the permitted lines. This broadening is specific to the permitted lines, highlighting the high density of these regions. Type I AGN additionally display FeII complex emission believed to originate from the BLR.

On the other hand, some AGN do not exhibit high-ionization states and are classified as Low-Ionization AGN or LINERs. LINERs, often associated with lower luminosity AGN, display spectra dominated by low-ionization lines such as [NII] λ6548,6583Å and [OI] λ6300Å, with weaker higher ionization lines like [OIII] λ5007Å. While LINERs can be either Type I or Type II, the majority are Type II, displaying a lower tendency to exhibit broadening (Ho et al., 2001). Visual distinctions between Seyferts Type 1 and Type 2 and LINERs are illustrated in Fig. 2.3.

The optical spectra of AGN provide valuable insights into the physical conditions of the line-emitting gas, revealing details such as ionization level, electron temperature, density, and chemical composition. Nebular diagnostic methods, similar to those employed for HII regions, are utilized to extract this information. An exemplary technique is the use of diagnostic diagrams, pioneered by Baldwin et al. (1981), which helps differentiate between inactive and active galaxies. These diagrams, known as BPT diagrams, rely on observed line flux ratios, such as [OIII] λ5007Å/Hβ vs. [NII] λ6583Å/Hα and [OIII] λ5007Å/Hβ vs. [SII] λ6716,6731Å/Hα. These diagrams play a crucial role in distinguishing ionization levels corresponding to Seyferts, LINERs, or pure star-forming regions and are widely utilized in the literature (e.g., Kewley et al., 2006). However, it is essential to consider adjustments for high-redshift sources since the original BPT diagrams were developed based on local observations. High-redshift sources may exhibit different properties, as dominated by young stars or post-asymptotic giant branch stellar populations. Therefore, modifications and corrections are necessary to account for these variations in interpreting the diagnostic diagrams for high-redshift AGN (Hirschmann et al., 2023).

The electron density (N_e) within the narrow-line emission gas can be determined through standard nebular diagnostic methods that
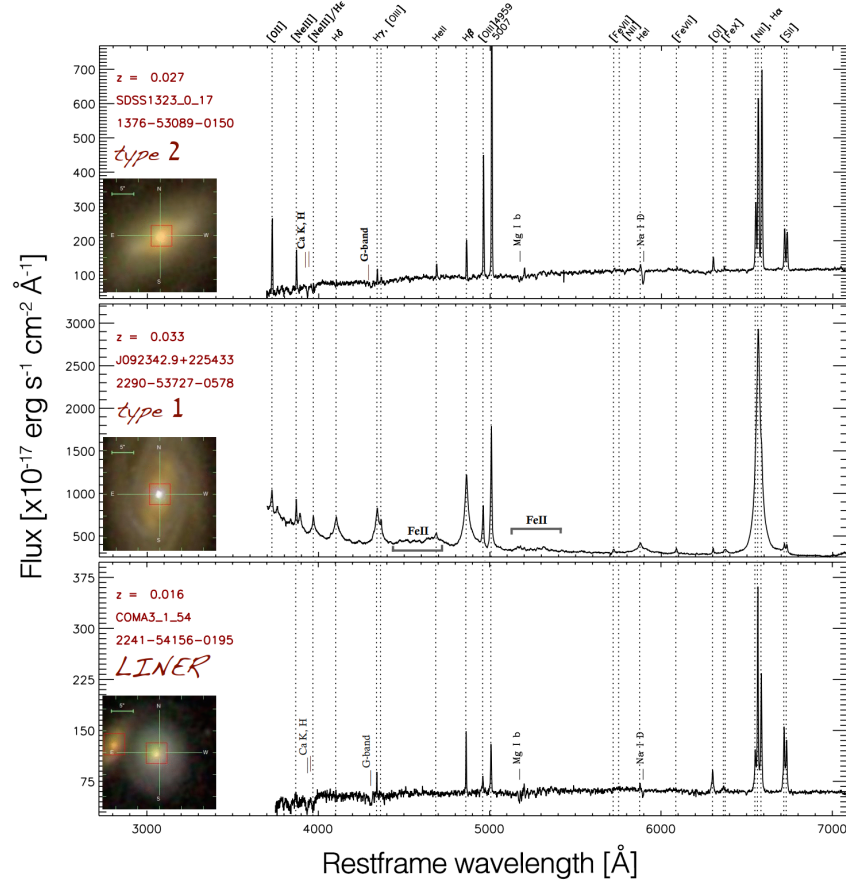
Figure 2.3: Optical spectra of AGN, showcasing a Type II AGN, a Type I AGN, and a LINER from top to bottom. While Type II AGN only show narrow lines, Type I AGN exhibit broad permitted lines and FeII emission. LINERs, on the other hand, show low-ionization lines. Image credits: Perna (2016).

consider collisional de-excitation effects. Typically, N_e estimates are derived from the flux ratio of the [SII] doublet, while electron temperature T_e can be obtained by combining information from the [OIII] lines. Surveys, such as the Sloan Digital Sky Survey (SDSS), have provided larger samples, yielding measurements in the NLR with values between $N_e \sim 10^2$–$10^3 \, \mathrm{cm}^{-3}$ and an average $T_e \sim 1.5 \times 10^4 \, \mathrm{K}$ (Zhang et al., 2013). Nevertheless, the NLR appears to be a multi-phase ionized gas where structures with different densities are in motion (Vaona et al., 2012). The N_e and T_e of the BLR gas cannot be directly derived from diagnostic line ratios. However, it is expected to be associated with denser regions ($N_e \sim 10^9 \, \mathrm{cm}^{-3}$) compared to the NLR, and the observed FeII can set upper limits to its temperature ($T_e < 3.5 \times 10^4 \, \mathrm{K}$, Osterbrock and Ferland, 2006).

The mass and size of emitting gas regions are determined by measuring the luminosity of key emission lines like Hβ and [OIII] $\lambda 5007$Å (Osterbrock and Ferland, 2006). Based on typical plasma properties

(N_e and T_e) and Hβ luminosities, the estimated mass of the ionized gas in their NLRs is around $10^7 \, \mathrm{M_\odot}$. These NLRs, assumed to have a spherical geometry, extend over a kiloparsec scale, as confirmed by various observational techniques, including long-slit spectroscopy, high-resolution imaging, and integral field unit studies (Hainline et al., 2014; McElroy et al., 2015). Notably, at this distance, the NLR gas cannot be gravitationally bound to the central black hole, suggesting that it belongs to the host galaxy's ISM and is photo-ionized by the AGN's radiation field.

Alternatively, assuming the virialized nature of the BLR, the virial equation:

$$M_{\mathrm{BH}} = \frac{rV^2}{G} \tag{2.1}$$

can be employed to estimate the BLR radius (r) and average rotational velocity (V) based on M_{BH}. For a black hole with a mass of $10^8 \, \mathrm{M_\odot}$ and an average velocity of $2500 \, \mathrm{km \, s^{-1}}$, the BLR size is calculated to be $0.07 \, \mathrm{pc}$. The substantial rotational component within the BLR favors a disk-like structure, though findings suggest both disk and symmetrical configurations (Pancoast et al., 2014). Equation 2.1 is derived under the assumption of virialized orbits in the BLR and can be utilized along with measures of BLR radius and velocities to provide a direct method for estimating black hole masses beyond the local Universe.

These assumptions about the BLR have led to the development of a popular technique for measuring black hole mass called Reverberation Mapping (RM). RM has been employed for the past two decades to provide accurate estimates of black hole masses (Kaspi et al., 2000; Bentz et al., 2009). To determine the BLR radius, a time delay is needed between changes in the continuum emission and the corresponding variations in the broad-line flux (Blandford and McKee, 1982). Reverberation results have also shown a correlation between the luminosity and the size of the broad-emission gas environment, indicating that more luminous objects have a larger BLR (Kaspi et al., 2005; Bentz et al., 2013).

While RM is a precise technique for estimating M_{BH}, it is time-consuming and requires high-quality spectra for reliable results. To simplify and expedite the process, RM-derived black hole masses have been used to calibrate simpler single-epoch methods (Fig. 2.4) that rely solely on the AGN luminosity and the width of broad emission lines (e.g., Vestergaard and Peterson, 2006; Shen and Liu, 2012). These single-epoch methods are more cost-effective as they require only a single spectrum per source. They have been successfully utilized to trace the growth of massive black holes over cosmic time (e.g., Merloni et al., 2010; Schulze et al., 2015) and determine black hole masses of Type II AGN through infrared lines in the local Universe (Ricci et al., 2017c,d).
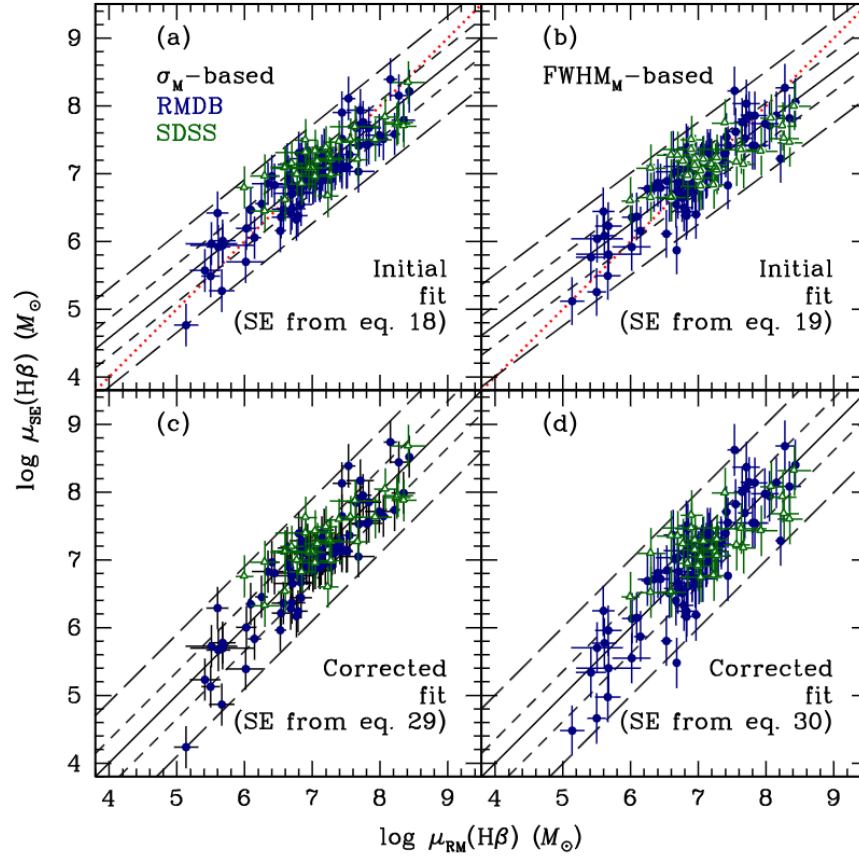
Figure 2.4: Black hole masses retrieved using Hβ emission line and the reverberation mapping and single-epoch spectra. Image credits: Dalla Bontà et al. (2020)

Accurately determining the velocity dispersion of BLR gas is crucial for estimating M_{BH}, as it is directly proportional to the BH's mass, as dictated by the virial theorem. However, the intricate geometry and dynamics of the BLR pose significant challenges to obtaining precise measurements. The BLR gas is turbulent, and a combination of thermal and non-thermal processes contributes to the broadening of its emission lines. Additionally, the BLR is not a spherical structure but rather an elongated disk or ring encircling the BH. Moreover, the BLR does not solely emit broad emission lines; FeII emission plays a crucial role in cooling the BLR, accounting for approximately 25 % of the total energy output in some AGN (Wills et al., 1985). Therefore, to accurately measure the velocity dispersion of BLR gas, it is essential to fit both the AGN's continuum and the iron emission properly. An example of this complex fit is shown in Fig. 2.5.

Once the fit properly removes possible host contamination and AGN continuum emission, the velocity dispersion of BLR gas can be measured. From there, the SMBH mass ($M_{BH,vir}$) is estimated using the equation below. Here, L represents the AGN luminosity at a
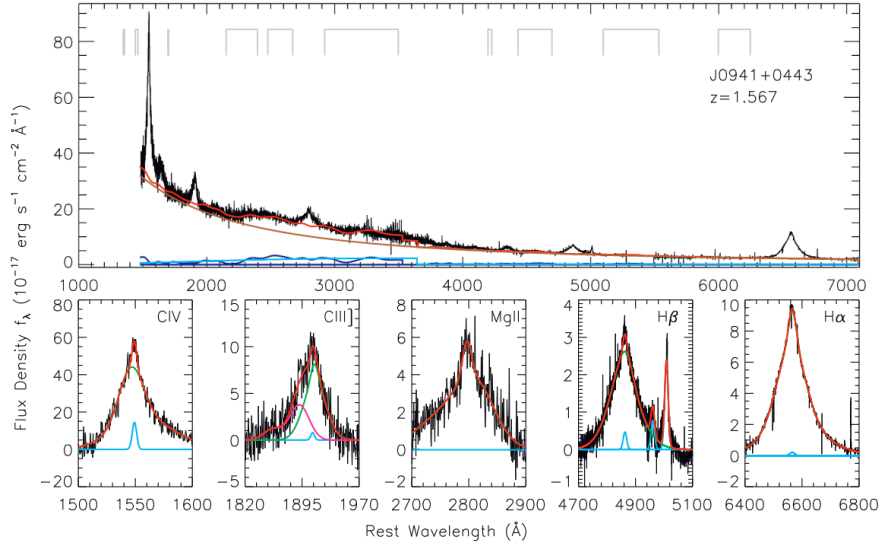
Figure 2.5: *Top panel:* A comprehensive fit of the pseudo-continuum for a typical QSO spectrum. The brown line represents the power-law continuum, the blue line depicts the FeII template fit, the cyan line portrays the Balmer continuum model, and the red line showcases the combined pseudo-continuum model to be subtracted. *Bottom panels:* Emission line fits used for estimating the black hole mass from CIV to Hα. The cyan lines represent the model narrow-line emission, the green lines represent the model broad-line emission, and the red lines represent the combined model line profiles. For CIII], the contamination from AlIII and SiIII] emission are shown in magenta. Image credits: Shen and Liu (2012)

specific wavelength or the luminosity corresponding to a particular spectral line, which varies based on the coefficients applied[2]:

$$\log\left(\frac{M_{\mathrm{BH,vir}}}{M_\odot}\right) = a + b\log\left(\frac{L}{10^{44}\mathrm{ergs}^{-1}}\right) + c\log\left(\frac{\mathrm{FWHM}}{\mathrm{kms}^{-1}}\right). \quad (2.2)$$

To perform the UV-optical spectra fitting, in this thesis, we will use PyQSOFit (Guo et al., 2018)[3]. PyQSOFit is a flexible tool for decomposing quasar spectra. It is a Python version with several enhancements of the original QSOFIT code (Shen et al., 2019) used for the RM project for SDSS sources. It allows the user to obtain information on quasar continuum and emission lines. It can decompose the host galaxy and quasar component with the PCA method, if needed, to then fit the continuum with several components (Power-Law, Polynomial, FeII, Balmer Continuum). Finally, it fits line complexes one by one, including Balmer series MgII, CIII], CIV, and Lyα complex. The use of this tool will be shown in Chapter 4.

---

2 Coefficients can be sourced from Assef et al. (2011) for Balmer lines (Hα and Hβ), Vestergaard and Osmer (2009) for MgII, and Vestergaard and Peterson (2006) for CIV.
3 https://github.com/legolason/PyQSOFit/tree/master

3 | SPECTRAL ENERGY DISTRIBUTION FITTING

Spectral Energy Distribution (SED) fitting stands as a powerful tool for deciphering the physical properties of astronomical objects. This technique involves constructing models that replicate the observed emission spectrum, spanning a wide range of wavelengths, from radio waves to X-rays. By comparing and minimizing the difference between these models to real-world observations, astronomers gain valuable insights into the nature of these objects, including their stellar composition, dust content, and SMBH activity.

The foundation of SED modeling lies in the understanding that galaxies with different properties emit differently. SED modeling also leverages the fact that the different components within a galaxy, such as stars, gas, dust, and an active SMBH, emit radiation at distinct wavelengths. These radiations are sometimes interconnected; for example, the dust reemits photons absorbed with high energy. By modeling the contributions from these components, one can infer the underlying physical characteristics of the object. For instance, while spectral fitting of emission lines can help understand the presence of specific elements or molecules, the overall shape of the SED can reveal the stellar population properties (such as age and metallicity) or the presence of an obscured AGN.

SED modeling has found widespread applications across various fields of astronomy, from studying the formation and evolution of galaxies to investigating the nature of AGN. It serves as a crucial tool for understanding the diverse phenomena that occur in the cosmos and continues to play a vital role in advancing our knowledge of the universe. In this chapter, we will delve into the details of the model used to build a host galaxy + AGN emission and the fitting process. We will also provide an overview of how we derive the physical parameters of our sources.

3.1 OVERVIEW OF THE CIGALE CODE

Various codes are available for performing SED fitting, each with specific advantages and disadvantages. Despite differences among them, the community has observed consistent results across different codes. A comparison conducted by Pacifici et al. (2023) reveals similar distributions of general physical parameters across various SED fitting codes, as illustrated in Figure 3.1.
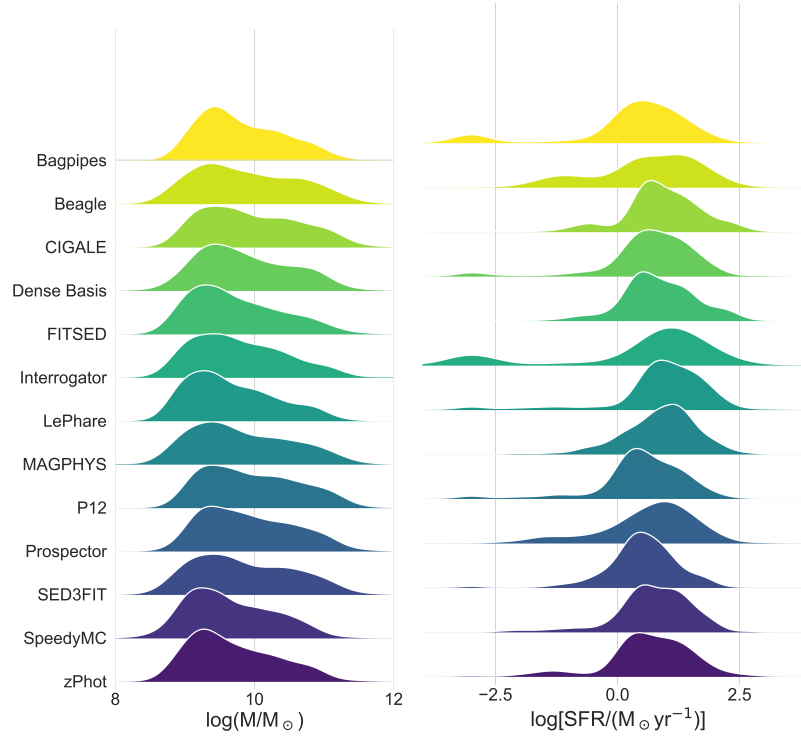
Figure 3.1: Distributions of stellar mass and SFR best-estimate results for a sample of $z \sim 1$ galaxies. Each row represents results from different SED fitting codes. Credit: Pacifici et al. (2023).

In this PhD Thesis, our focus centers on utilizing and enhancing the CIGALE code. Code Investigating GALaxy Emission (CIGALE) (Boquien et al., 2019) is a Python-based tool developed for interpreting galaxy SEDs. The latest version of CIGALE incorporates X-ray and radio models (Yang et al., 2020; Yang et al., 2022), and the code is available at `https://cigale.lam.fr`.

CIGALE is a powerful multiwavelength SED fitting code designed for extragalactic studies. Its capabilities range from statistically determining robust physical parameters across the X-ray to IR spectrum to accounting for dust attenuation and corresponding infrared re-emission through energy balance. The methodology involves comparing a galaxy's observed SED to a library of SED models, utilizing various physical models and templates. Subsequently, the code employs a Bayesian-like statistical analysis to identify the best-fit model and associated physical parameters.

However, despite its success, the existing CIGALE model encounters limitations when applied to low luminosity AGN. The intricacies of accretion physics in LLAGN remain a subject of debate, introducing uncertainties regarding the applicability of standard relations in these regimes. Chapter 5 explores some upgrades to the current CIGALE code to make it applicable for LLAGN.

3.1.1 The Bayesian Approach

The primary goal of the SED fitting process is to determine the physical parameters of the studied object. This is achieved by comparing observed SEDs with a grid of modeled SEDs covering a wide range of physical conditions. Many modern SED fitting codes adopt a Bayesian approach, considering both the goodness of fit and the reliability of the models in light of *prior* knowledge (Kass and Raftery, 1995).

This prior information cleverly influences the likelihood, giving more weight to values that better represent the expected fit. For instance, if a model fits a stellar population older than the Universe for that redshift, such a model should be down-weighted. X-ray information for AGN can also serve as a prior, as the X-ray emission for QSOs is expected to follow a certain relation with the UV emission. Applied to our case, Bayes' theorem expresses the probability of a model being a good representation of the data given the prior knowledge of the conditions related to that model. It is formulated as:

$$\mathcal{L}(\Theta|D) = \frac{\mathcal{L}(D|\Theta) \times \mathcal{L}(\Theta)}{\mathcal{L}(D)} \tag{3.1}$$

Here, $\mathcal{L}(\Theta|D)$ is the likelihood that the model Θ is true given data D (also called *posterior distribution*), $\mathcal{L}(\Theta)$ is the *prior information* on the model, and $\mathcal{L}(D|\Theta)$ is the likelihood that data D is explained by model Θ. $\mathcal{L}(D)$ represents the likelihood of all the models given the data (also called *"Bayesian evidence"* or marginal probability).

The likelihood function, indicating the confidence in a Θ model given real data D, is often expressed using the *chi-squared* metric for SED fitting:

$$\chi^2 = \sum_{i=1}^{N} \frac{\left(f_\Theta(\lambda_i) - f(\lambda_i)\right)^2}{\sigma_i^2} \tag{3.2}$$

where f is the observed flux, λ_i is the wavelength, σ_i is the uncertainty, and f_Θ is the model flux. The chi-squared is transformed into a likelihood via $\mathcal{L} = \exp(-\chi^2/2)$ assuming Gaussian error distributions. If normalized such that it integrates into unity, this is called the probability density function (PDF). By this definition, at a low χ^2, there is a high probability that the model is a good representation of the data, given the optimized model parameters.

In a Bayesian approach, priors shape the model space, reflecting our knowledge of the physical parameters. Understanding the posterior distribution of a physical parameter, such as the AGN's bolometric luminosity, provides insights into the reliability of the SED fitting. A well-constrained posterior has a distinct maximum with minimal dispersion, indicating a reliable estimate of the parameter with an error proportional to the scatter, contingent on the code used. On

the contrary, a poorly constrained posterior will display significant dispersion around one or more unclear maxima. This suggests that, for the range of values considered for this parameter, the overall shape of the emission remains unaffected. Such dispersion implies that all these values have a similar probability of being present in this source, rendering the value estimation unreliable.

In particular, in CIGALE, the estimation of physical properties is implemented through likelihood-weighted parameters on the fixed grid of models. From the complete set S_0 of models, the algorithm selects the subset S_1 of models closest to the rounded redshift[1] of the analyzed object. By default, redshifts are rounded to two decimal places, though this precision can be adjusted by the user. Subsequently, the multiplicative factors are computed to scale the S_1 models to the observations. The next step involves calculating the χ^2 (Eq. (3.2)) between all the S_1 models and the observations. Following this, the likelihood ($\mathcal{L} = \exp(-\chi^2/2)$) is computed for the S_1 models. This likelihood serves as a key metric in the estimation process.

The physical properties, along with their associated uncertainties, are then estimated. This is achieved by determining the likelihood-weighted mean and standard deviation of the S_1 models. The results, including the estimated physical properties and their uncertainties, along with the fluxes and properties of the best-fitting model, are saved. Additionally, the Bayesian analysis provides the option to save additional information, such as the best-fit spectrum with individual components (stellar populations, nebular emission, dust emission, etc.), the χ^2 distribution, and other relevant details. This Bayesian approach facilitates a comprehensive estimation of physical properties while considering the uncertainties associated with both the models and observations.

3.1.2 Creating the grid models

While the method described earlier is employed to constrain the physical properties, it becomes ineffective if the grid is biased or not representative of the source being fitted. This underscores the crucial importance of creating a well-constructed grid for comparison with observations. Given that our sources are active galaxies, it is imperative to generate extensive models that encompass both the host galaxy and its active nucleus. Here, the key aspects of modeling the host galaxy and active nucleus are presented, along with the models and parameters employed as input in CIGALE for grid creation. The specifics of the used grid will be thoroughly outlined for each study

---

[1] If redshift is considered a free parameter, the complete set will encompass a redshift grid, and it will be treated as another parameter within the likelihood-weighted estimation process.

in Tables 4.3 and 5.2. For a more in-depth understanding of CIGALE input, refer to the CIGALE manual[2].

3.1.2.1 Modeling the host galaxy

Understanding the emission from a host galaxy involves considering stars as the primary source of emission. These stars emit photons, which are subsequently influenced by the presence of gas and dust, undergoing processes of absorption and reemission. At the core of modeling stellar emission from a host galaxy lies the concept of a Simple Stellar Population (SSP). An SSP represents a cohort of stars born simultaneously, occupying the same volume of space, and originating from a gas cloud characterized by a homogeneous chemical composition. Constructing an SSP requires three crucial inputs: isochrones representing stellar evolution, libraries of stellar spectra, and an Initial Mass Function (IMF).

To compute the intrinsic stellar spectrum, CIGALE relies on a library of SSPs. Two popular libraries are used: `bc03` (Bruzual and Charlot, 2003) and `m2005` (Maraston, 2005). These libraries cover a broad range of metallicities. To account for differential reddening between young and old stellar populations, CIGALE also computes and stores separate spectra for old and young stars, enabling independent attenuation in a downstream module.

However, galaxies are not composed solely of stars from a single generation. Similar to the population within a country, galaxies consist of various generations, each influencing the subsequent one. Stellar evolution alters the galactic environment and its properties, subsequently affecting the characteristics of the new generation of stars. Therefore, to model a Complex Stellar Population (CSP), it becomes essential to incorporate its star formation history (SFH).

CIGALE provides three modules for defining analytic SFHs covering different general cases: SFH defined by single or double exponentials (`sfh2exp`), delayed SFH with an optional exponential burst (`sfhdelayed`), and periodic SFH (`sfhperiodic`).

The `sfhdelayed`, given by $\mathrm{SFR}(t) \propto t\tau^{-2}\exp(-t/\tau)$, where t is time, and τ is the time at which the SFR peaks, has become increasingly popular. This functional form provides a nearly linear increase in the SFR from the onset of star formation, avoiding abrupt changes seen in `sfh2exp`. The SFR smoothly decreases after peaking at $t = \tau$. The module also allows for an exponential burst, adding flexibility to capture the latest episode of star formation (Małek et al., 2018a).

Galaxies are also composed of dust. The presence of dust introduces an attenuation curve, absorbing the UV-optical stellar photons and reemitting them in the infrared spectrum, governed by a dust emission law. Figure 3.2 illustrates the intricate interplay of these elements and

---

2 https://cigale.lam.fr/documentation/

the methodology employed in constructing a host galaxy SED. For an in-depth exploration of how the selection of these parameters influences the SED, refer to Conroy (2013).
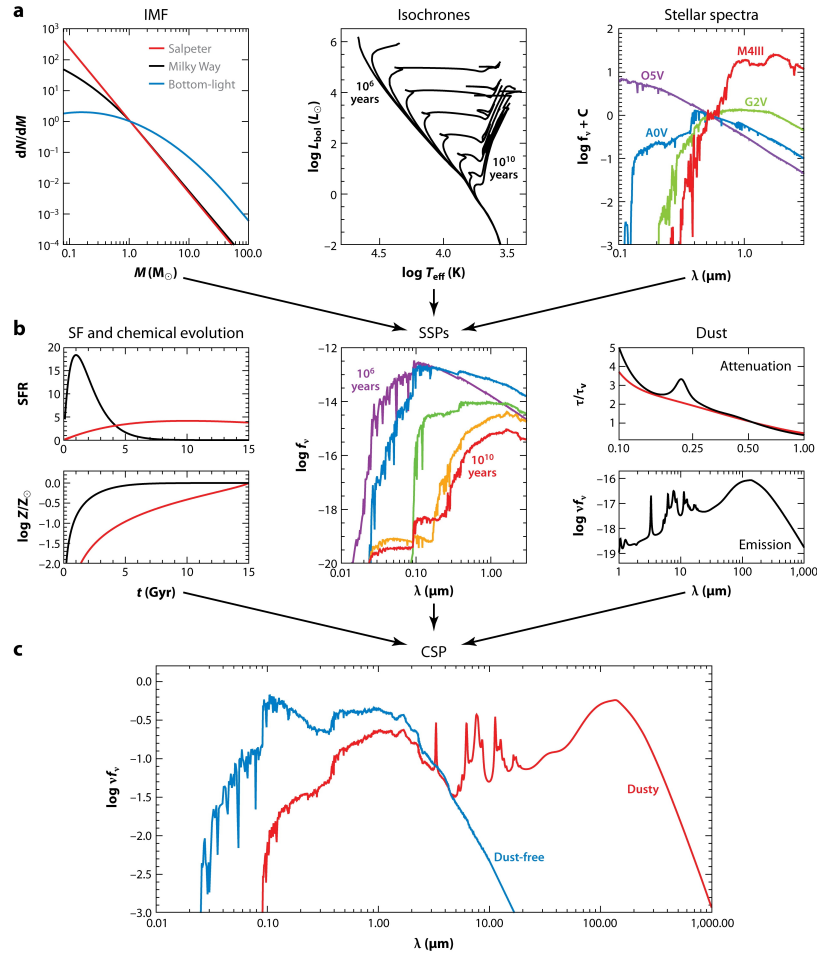
Figure 3.2: Illustration of the host galaxy modeling process: a) Simple Stellar Populations (SSPs) are created using an Initial Mass Function (IMF), isochrones for varying ages and metallicities, and stellar spectra for different types of stars. b) Utilizing the SSPs and information on star formation history, chemical evolution, and dust attenuation/emission enables the modeling of c) both dust-free and dusty host galaxy emissions. Image credits: Conroy (2013)

CIGALE employs attenuation laws to model the impact of dust on observed radiation. Attenuation laws vary with redshift and galaxy, demanding a broad range of coverage in terms of shape and normalization. CIGALE offers two approaches to model attenuation curves: the Charlot and Fall (2000) model and flexible laws inspired by the starburst curve (Calzetti et al., 2000).

The `dustatt_modified_CF00` module implements the Charlot and Fall (2000) model. It recognizes that attenuation curves differ for young stars embedded in their birth cloud and those that have entered

the ISM. The `dustatt_modified_starburst` module takes an empirical approach, using the Calzetti et al. (2000) starburst attenuation curve. This curve can be parametrized for flexibility, including adjustments to the slope and the introduction of a UV bump modeled as a Lorentzian-like Drude profile.

The attenuation that the dust produces in short-wavelength radiation is connected to the re-emission in the mid and far-IR. CIGALE considers four sets of models for dust emission: `dale2014` (Dale et al., 2014), `dl2007` and its update `dl2014` (Draine and Li, 2007; Draine et al., 2014), `casey2012` (Casey, 2012) and `themis` (Jones et al., 2017).

The `casey2012` model offers a straightforward fit based on far-IR emission of local ultraluminous infrared galaxies, combining a single-dust-temperature greybody to represent the reprocessed starburst emission in the entire galaxy with a mid-IR power law approximating hot-dust emission from AGN heating or clumpy, hot starbursting regions. This model excludes PAH emission and, because it already includes possible AGN heating, cannot be combined with AGN modules. The `dale2014` model uses empirical templates based on nearby star-forming galaxies. The dust mass is parametrized by a power-law index (α), tightly linked to the 60–100 μm color. While simple and easy to interpret, it shows limited variation in PAH emission relative to total infrared.

The `dl2007` model presented by Draine and Li (2007) uses a mixture of amorphous silicate, graphite, and PAH. The templates separate dust emission into diffuse and star-forming components, offering flexibility in accounting for various physical conditions. The `dl2014` module updates this model, expanding the parameter space and refining various aspects, such as the treatment of graphite and dust mass normalization (Draine et al., 2014). The DustPedia team has developed a module based on the THEMIS dust model, offering additional flexibility (Jones et al., 2017). While flexible, these models have a larger parameter space, making them computationally more expensive than the `dale2014` templates.

In addition to the dust emission mentioned above, another crucial component to model is gas. Nebular emission comprises continuum emission (mainly from free-free and free-bound emission) and recombination line emission.

Several photoionization codes, such as CLOUDY (Ferland et al., 1998), predict nebular emission based on the physical state of the gas. This emission can be added to the SED, with a high impact on performance, especially when line emission is considered. Line emission is vital when fitting data with narrow-band filters or spectra. Nevertheless, the contribution of nebular emission to broadband fluxes can range from 20-60% for low metallicity and young ages (Zackrisson et al., 2008). Nebular emission becomes more significant at high redshifts due to the redshifting of the spectrum, impacting galaxies

with high star formation rates and low metallicity, which is common at these redshifts (Atek et al., 2011)

Galaxies exhibit nebular emission, and CIGALE models this through a multi-step process. First, it selects a template based on the ionization parameter (U) and metallicity (Z). These templates, derived from Inoue (2011) and generated using CLOUDY 13.01 (Ferland et al., 1998, 2013), predict the intensities of 124 lines from HII regions. The templates are parametrized according to U, and Z, with a constant electron density set to $100\,\mathrm{cm}^{-3}$. Noteworthy improvements include refined sampling in $\log U$, extension down to $\log U = -4$, and adjustments in abundances based on the Orion nebula.

Computation of the nebular emission involves several steps. After selecting a template, the emission line spectrum is generated, each line having a Gaussian shape with a user-defined width to account for gas motion. The normalized nebular emission line spectrum is then rescaled based on the ionizing photon luminosity. However, not all Lyman-continuum photons ionize the surrounding gas due to processes such as escape or absorption by dust. The escape fraction, although generally low in the nearby universe, may be significant at high redshifts (Inoue et al., 2006; Hayes et al., 2011).

Finally, considering all these models that mimic the emission and absorption interplays, we can construct the grid of galaxy SEDs. Fig. 3.3 shows example SED fits for diverse galaxies morphologies.

3.1.3 Modeling the AGN

As discussed in Chapter 1.1, the diverse structures of an AGN contribute to its emission across a broad range of wavelengths, from X-ray to radio. The intricate interplay of these structures produces a large variety of SEDs, where changes in AGN luminosity and obscuration are key factors influencing the observed SED, as illustrated in Figure 3.4.

The central engine of the AGN, the accretion disk, generates emission following the standard accretion disk model discussed earlier. While a physically motivated SED would use a solution for this disk, such as the one proposed by Shakura and Sunyaev (1973), the inclusion of free parameters in the SED fitting, like the black hole mass, can introduce significant uncertainties. As a result, a common approach in SED fitting codes is to use seed photons from a parametrized disk following a broken power-law spectrum, as the one suggested by Schartmann et al. (2005). These seed photons are then absorbed and reemitted by other components of the AGN. Specifically, for the disk from Schartmann et al. (2005) the parametrization follows:
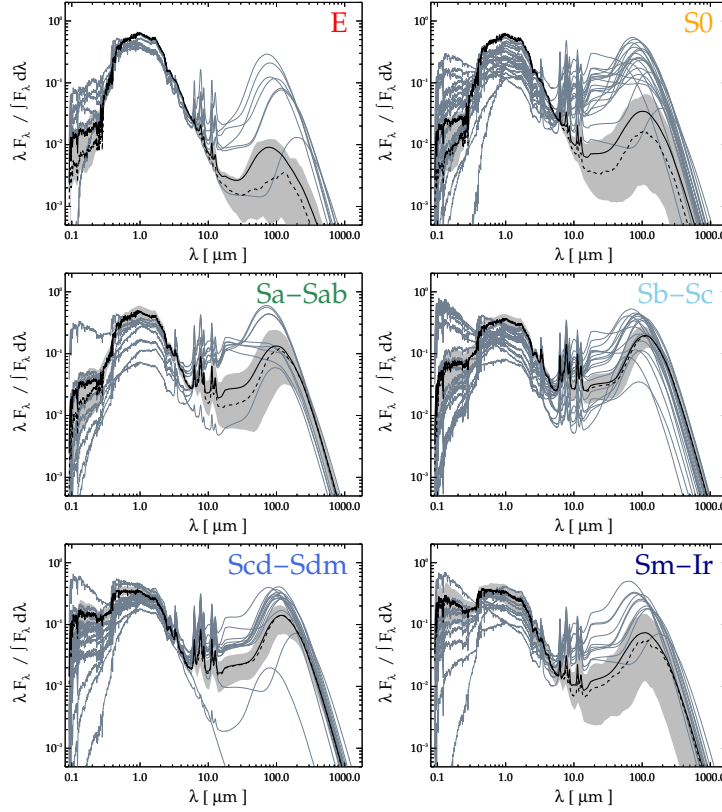
Figure 3.3: SEDs for different galaxies from DustPedia, ranging from Elliptical (E) and Lenticulars (S0) to diverse types of spirals (Sa–d), arriving at dwarf galaxies (Sm) and Irregulars (Ir). Solid black lines represent the average SEDs for each morphology, while dashed black lines are the median SEDs. Grey lines represent the 10% of galaxies showing the most deviant SEDs. Image credits: Bianchi et al. (2018)

$$
\lambda L_\lambda \propto
\begin{cases}
\lambda^2 & 0.008 \leqslant \lambda \leqslant 0.05\ [\mu\text{m}] \\
\lambda^{0.8} & 0.05 < \lambda \leqslant 0.125\ [\mu\text{m}] \\
\lambda^{-0.5+\delta_{\text{AGN}}} & 0.125 < \lambda \leqslant 10\ [\mu\text{m}] \\
\lambda^{-3} & 10 < \lambda \leqslant 1000\ [\mu\text{m}]
\end{cases}
\tag{3.3}
$$

where δ_{AGN} is used to introduce a deviation in the slope within the 0.125 to 10 μm band. For a QSO sample, Yang et al. (2020) obtained a $\delta_{\text{AGN}} = -0.36$ as a representative mean value of the AGN population.

The dusty torus, a structure of dense dust surrounding the central black hole, plays a crucial role in shaping the AGN's SED. One key parameter of the torus is the opening angle, or equivalently, the covering factor. Recent studies show that there is a relation between the Eddington ratio and the covering factor, where at a higher Eddington ratio, the covering factor is lower, interpreted as radiation pressure from the AGN blowing away the dust (e.g., Ricci et al., 2017b). But
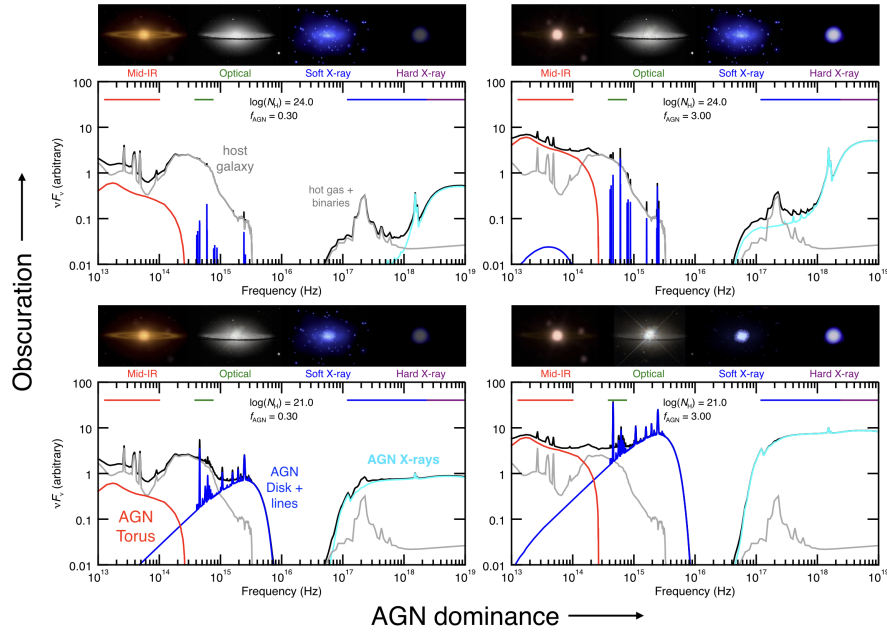
Figure 3.4: Illustration of an AGN SED model. The nuclear obscuration increases from bottom to top, and the relative luminosity of the AGN compared to that of the host galaxy increases from left to right. The bottom panels show the overall model spectral energy distribution (SED) (dark blue: accretion disk and optical/UV emission lines; red: AGN torus; light blue: AGN X-rays; gray: host-galaxy component; black: combination of AGN and host galaxy), indicating the emission from the host galaxy and the AGN. The top panels indicate the broad features predicted to be observed in imaging data in the mid-IR, optical, and X-ray bands. Image credits: Hickox and Alexander (2018)

even for AGN of similar mass and luminosity, a broad range of torus properties is observed (e.g., Burtscher et al., 2013).

The toroid can be modeled as a smooth or clumpy structure. While SED fitting models using smooth tori from Fritz et al. (2006) have successfully fit mid-IR emission in the past, recent high-resolution mid-IR imaging supports the idea of a clumpy structure. Models for smooth tori often predict weaker mid-IR emission for edge-on systems due to the torus having a large optical depth in the mid-IR, causing anisotropic emission (e.g., Fritz et al., 2006). In contrast, a clumpy torus is expected to show mid-IR emission less dependent on orientation, consistent with the observed relationship between X-ray and mid-IR luminosities (e.g., Gandhi et al., 2009; Asmus et al., 2015; García-Bernete et al., 2016).

The previously employed CIGALE AGN model, responsible for the UV-to-IR SED, was proposed by Fritz et al. (2006). This model assumed a smooth structure for the dusty torus. However, more recent theoretical and observational works suggest that the torus is primarily composed of dusty clumps (e.g., Nikutta et al., 2009; Ichikawa et al.,

2012a; Stalevski et al., 2012; Tanimoto et al., 2019). In response to this, the SKIRTOR model, a clumpy two-phase torus model based on the 3D radiative-transfer code SKIRT (Baes et al., 2011; Camps and Baes, 2015), has been introduced into the new version of CIGALE (Yang et al., 2020). This model produces a two-phase torus model with high-density clumps and a low-density medium filling the space between them. The difference in the SED between a pure smooth torus, a pure clumpy torus, and the two-phase model is shown in Fig. 3.5.
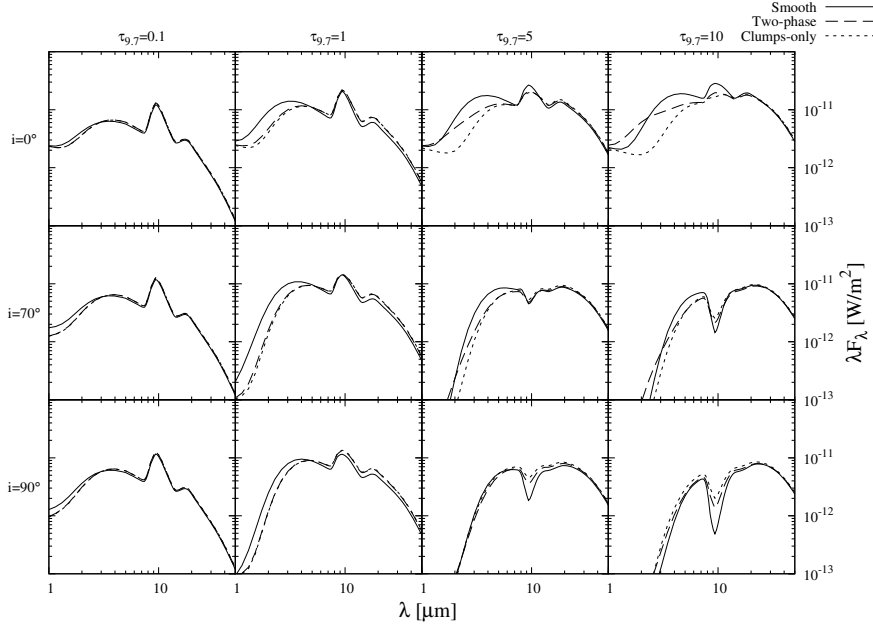
Figure 3.5: SEDs of different torus modeling. The solid line represents a smooth torus, the dotted line a clumpy torus, and the dashed line the two-phase model. Various columns depict different optical depths at 9.7μm, while different rows illustrate different inclinations. Image credits: Stalevski et al. (2011).

SKIRTOR considers anisotropy in the power source, AGN disc emission, in contrast to Fritz's model, which assumes isotropic disc emission. SKIRTOR also finds that having the dust distributed in a two-phase medium might offer a natural solution to the lack of emission in near-infrared, compared to observed data, which affects clumpy models currently available in the literature (Stalevski et al., 2012). CIGALE offers users the choice between SKIRTOR and Fritz's model, with SKIRTOR recommended for its closer adherence to observational data. In this thesis, SKIRTOR will be the model of choice.

The toroid, however, is not the only dust around the AGN. High-resolution observations using mid-IR interferometry have revealed substantial dust emission along the polar direction on parsec scales (e.g., Hönig et al., 2012; Tristram et al., 2014; López-Gonzaga et al., 2016). These polar structures, extending to larger scales (e.g., Asmus

et al., 2016), may be associated with an AGN-driven outflow (e.g., Schartmann et al., 2014). CIGALE included, together with the SKIR-TOR model, the polar dust component to include obscuration of type 1 AGN. This model assumes various empirical extinction curves, with the Small Magellanic Cloud (SMC) extinction curve recommended due to its preference in AGN observations (e.g., Hopkins et al., 2004; Salvato et al., 2009; Bongiorno et al., 2012). The extinction amplitude, parameterized as $E(B-V)$, is a user-defined free parameter. Since CIGALE maintains energy conservation, it implements dust emission to account for the radiative energy absorbed by the dust, assuming isotropic emission and a 'grey body' model (Casey, 2012).

CIGALE takes into account the viewing angle to model AGN emission accurately. Type 1 AGN, viewed from polar directions, exhibits strong UV-optical emission from the central engine with moderate dust obscuration from the polar dust. Type 2 AGN, observed from equatorial directions, have their disc emission significantly obscured by the torus. Users can either constrain the viewing angle based on known AGN classifications or allow CIGALE to explore multiple angles freely. CIGALE successfully identifies both properly confirmed Type I and Type II AGN. As demonstrated by Mountrichas et al. (2021) using an X-ray selected AGN sample, CIGALE correctly classifies all spectroscopic type 2 sources, either by estimating an inclination angle consistent with edge-on viewing or by detecting increased polar dust attenuation. Approximately 85% of spectroscopic type 1 AGN are also correctly identified by CIGALE's SED fitting analysis.

Besides UV and IR reemission, AGN also emit X-rays. The hot corona surrounding the black hole generates a power-law spectrum with a photon index (Γ) ranging between 1.8 and 2.0. This X-ray emission is linked to the UV emission from the accretion disk through the α_{ox}–$L_{2500\text{Å}}$ relation (Steffen et al., 2006; Lusso et al., 2010). Consequently, this relation proves invaluable for constraining UV luminosity using X-ray observations, particularly in the case of obscured AGN where direct UV measurements are challenging. The α_{ox}–$L_{2500\text{Å}}$ relation establishes a correlation between the intrinsic AGN luminosity at 2500Å and α_{ox}, defined as the SED slope between UV at 2500Å and X-ray at 2 keV:

$$\alpha_{\mathrm{ox}} = -0.3838 \log \left(\frac{L_{2500\text{Å}}}{L_{2\text{keV}}} \right) \tag{3.4}$$

Recent enhancements to CIGALE, incorporating an X-ray module, have significantly broadened its capabilities (Yang et al., 2020; Yang et al., 2022). The X-ray module enables CIGALE to model X-ray emission from both AGN and galaxies. For AGN, the X-ray spectrum is assumed to be a power law with an adjustable exponential cut-off. To ensure a comprehensive fit across X-ray and other wavelengths, CIGALE integrates the α_{ox}–$L_{2500\text{Å}}$ relation for AGN.

This relation operates under the assumption that the X-ray emission at 2 keV is linked to the intrinsic emission of the accretion disk at 2500Å. Using the X-ray as a prior, CIGALE penalizes AGN solutions deviating from this relation (with the user able to set the maximum allowed deviation $|\alpha_{ox}|_{max}$). To use this module, the input X-ray flux is required to be corrected for intrinsic absorption. CIGALE calculates models with varying α_{ox} values within a user-defined range and selects models consistent with X-ray observations.

In addition to AGN emission, galaxies can contribute to the X-ray spectrum, primarily due to low-mass X-ray binaries (LMXBs), high-mass X-ray binaries (HMXBs), and hot gas. The CIGALE model incorporates the recipe from Mezcua et al. (2018) to model X-ray emission from these components, with luminosities for LMXBs and HMXBs described as functions of stellar age and metallicity, while the hot-gas luminosity is expressed in terms of SFR.

Taking all these factors into consideration, CIGALE generates a grid of AGN models that are combined with the grid of host galaxies. An example of AGN fits for Type I and Type II is illustrated in Fig. 3.6, where the UV-optical absorption is evident for the Type II AGN.

In this chapter, the general capabilities of CIGALE are outlined. However, the specifics regarding the parameter settings for SED fitting will be addressed individually in future chapters. This approach is necessary as the input parameters for the SED fitting are highly dependent on the characteristics of the AGN and host galaxy populations being studied. Each case will therefore be customized to reflect the main aspects of the populations under examination, ensuring that the model settings are optimally configured for each scenario.
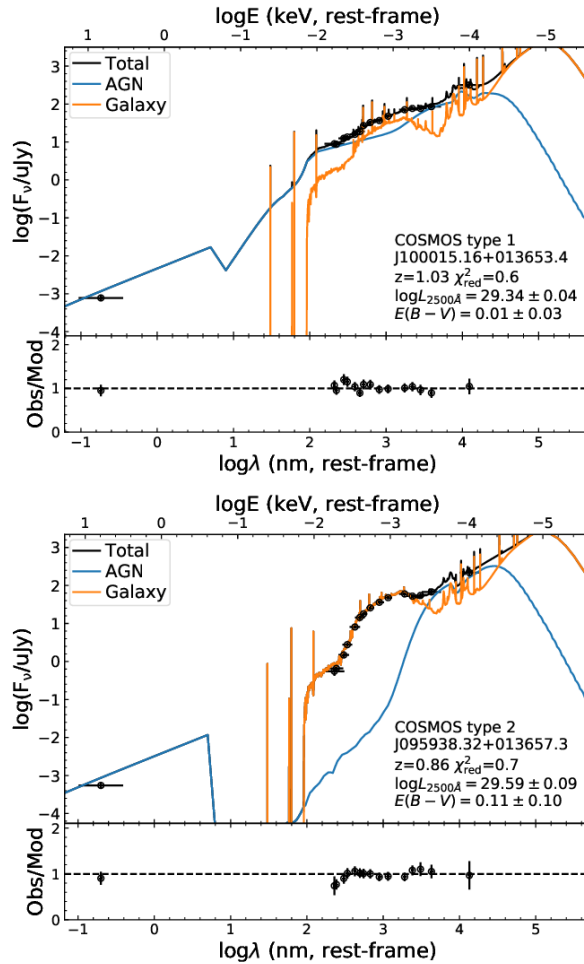
Figure 3.6: Example of CIGALE fit for an AGN Type I (top) and Type II (bottom). In the Type II case, the galaxy explains the emission in the optical bands, but the X-ray prior is crucial to fitting the IR reemission of the AGN. Image credits: Yang et al. (2020).

Part III

RESULTS

4 | PROBING ACCRETION PROPERTIES UP TO Z = 2.5 WITH MINIJPAS

The coevolution of SMBHs and their host galaxies is a fundamental aspect of cosmic evolution. As highlighted in Section 1.2.1, several studies have provided compelling evidence for a tight scaling relation between the SMBH mass and the stellar mass of their host galaxies in the local Universe, implying a connection between the growth of SMBHs and the formation and evolution of their host galaxies. Nevertheless, the specific details of this coevolution and the underlying mechanisms remain elusive.

In this Chapter, we investigate the relationship between black hole accretion rate (BHAR) and host galaxy properties by examining a sample of active galaxies at redshifts up to $z = 2.5$. SED fitting and spectral fitting are employed to derive the physical properties of these active galaxies, including their SMBH mass (M_{BH}) and stellar mass ($M_\star$), BHAR, SFR, and SFH. The analysis uncovers a significant difference between the λ_{Edd} and its popular proxy ($L_{\mathrm{X}}/M_\star$), suggesting that the instantaneous X-ray Luminosity may not reliably indicate the Eddington ratio.

We perform forward modeling for three evolution scenarios for each source to recover their integral properties at $z = 0$. By considering the SFR and BHAR, we demonstrate a notable reduction in the scatter between masses. Furthermore, by incorporating the SFH and a simple energy budget for the AGN accretion, we retrieve a relation similar to the calibrations known for the local Universe. Our findings suggest that the link between the SFR and BHAR, and their decoupling based on an energy limit, is crucial for understanding the coevolution of SMBHs and their host galaxies.

The work presented in this Chapter has been published in López et al. (2023) "The miniJPAS survey: AGN and host galaxy coevolution of X-ray-selected sources." Astronomy and Astrophysics, 672, A137.

4.1 INTRODUCTION

As discussed in Section 1.2.1, the connection between SMBHs and their host galaxies (Lynden-Bell, 1969) was proposed several years after the first discovery of a quasar in Schmidt (1963). Since then, this coevolutionary scenario has garnered supporting evidence. Especially, M_{BH} correlates with various properties of the host galaxy, such as the velocity dispersion of the bulge component, $M_\star$, and stellar luminosity

($L_\star$; see Ferrarese et al., 2006; Shankar, 2009; Kormendy and Ho, 2013; Graham, 2016, for reviews).

In Section 1.2.1, we mentioned that the SFR and the BHAR density share similarities, both peaking at $z \sim$ 2–3 and declining since then (Hopkins et al., 2006; Shankar et al., 2009; Madau and Dickinson, 2014). This tight correlation between the SFR and the BHAR across cosmic time suggests that the BH growth is closely linked to the SFH of its host galaxy (e.g., Merloni and Heinz, 2008; Shankar et al., 2013; Delvecchio et al., 2014; Aird et al., 2015; Aversa et al., 2015; Yang et al., 2018; Carraro et al., 2020).

The BHAR is a crucial parameter that describes the BH growth rate (Lapi et al., 2014). A way to normalize the BHAR for different BH masses is the Eddington ratio ($\lambda_{\mathrm{Edd}} = L_{\mathrm{AGN}}/L_{\mathrm{Edd}}$), which measures the luminosity produced by the AGN relative to the luminosity produced at the Eddington limit (L_{Edd}). The λ_{Edd} is an essential parameter in BH-galaxy coevolution models, as it determines the BH feedback efficiency and the degree of self-regulation of the BH growth (e.g., Granato et al., 2004; Di Matteo et al., 2005; Lapi et al., 2006). It is also essential to study the accretion rate and its correlation with properties of the host galaxy, such as the SFR, as this can provide insights into the feedback mechanisms that regulate the growth of both the black hole and the host galaxy (e.g., Heckman and Best, 2014b; Delvecchio et al., 2015; Hopkins et al., 2016; Suh et al., 2019; Carraro et al., 2020; Torbaniuk et al., 2021).

Despite the importance of the BHAR, it is not easy to measure it directly due to the faintness of some accreting BHs. The accretion can have different "*modes*" where the efficiency to produce the observed radiation changes (e.g., see Heckman and Best, 2014b, for a review). Photons from the accretion can also be absorbed by gas and dust that obscure observational indicators (for a recent review, see Hickox and Alexander, 2018). It is also difficult to directly measure λ_{Edd} because of its dependence on L_{AGN} and M_{BH}. Since hard X-ray photons are less affected by the obscuration, a popular approach is to use L_{X} as a proxy for L_{AGN}; also $M_\star$ can be a proxy for M_{BH}, and hence, for L_{Edd} (see Brusa et al., 2009; Georgakakis et al., 2017, for examples of these proxies). Combined, these proxies are easier to measure than λ_{Edd}, but they can also be subject to various uncertainties and selection biases (Xue et al., 2010; Reines and Volonteri, 2015).

An alternative method to estimate the L_{AGN} is through SED fitting. In Chapter 3, we explain how to disentangle the emission from the AGN and the stellar, nebular, and dust continuum of the galaxy hosting the AGN. This method has been employed to estimate the Eddington rates of AGN at various redshifts (e.g., Bongiorno et al., 2012; Merloni et al., 2014; Schulze et al., 2015; Duras et al., 2020). Due to its ability to unravel different types of emission, SED fitting is also utilized to study the relation between the host galaxy SFR and the

AGN (e.g., Masoura et al., 2018; Andonie et al., 2022). The accuracy of SED fitting improves when multiwavelength data are available, allowing observation of the AGN emission across different bands. Additionally, the use of narrow-band filters is particularly well-suited for AGN studies as it better constrains the stellar population of the host galaxy and, consequently, the AGN component.

A further degree of uncertainty in the AGN/galaxy co-evolution paradigm is whether the M_{BH}–$M_\star$ relation remains consistent across cosmic time. While the relation is well-known for the local Universe for active and inactive SMBHs (see Shankar et al., 2019, 2020; Bennert et al., 2021, for examples of recent studies), it is unclear if it holds further in time. Some authors show evidence of evolution in the relation (e.g., Decarli et al., 2010; Merloni et al., 2010). In Shen et al. (2015), the authors do not find a significant change in the relation until $z \sim 1$, but they find hints of a flat relation at higher redshifts. Studies such as Li et al. (2021) and Suh et al. (2020) show no significant evidence of an evolution in the relationship until $z \sim 0.8$ and 2.5, respectively. The lack of consensus also persists in large-scale cosmological simulations, where there is no agreement on the expected scaling relations at $z > 4$ (Habouzit et al., 2022). These simulations do not agree on the normalization, slopes, or even the scatter of these relations, even at $z = 0$ (Habouzit et al., 2021). Jahnke and Macciò (2011) suggest that the relationship does not imply a physically coupled growth and Graham and Sahu (2022) point that mergers shape the high end of this relationship. Nevertheless, biases cannot be ignored in these studies; for example, finding overmassive galaxies for a given BH mass at different redshifts can be dominated by observational biases (Matsuoka et al., 2014; Ding et al., 2020), and flux-limited samples are generally biased toward higher values of M_{BH} (e.g., Lauer et al., 2007; Schulze and Wisotzki, 2011). While the debate continues, it is clear that using $M_\star$ as a proxy to estimate M_{BH} must be taken cautiously.

The work is organized as follows. Section 4.2 presents the sample and all the data used for the study. The data analysis is presented in Sections 4.3 and 4.4, focusing respectively on the SED method used to derive AGN and host galaxy properties and the optical spectral fitting procedure used to derive the BH masses for our targets. Section 4.5 describes the best fit physical properties of the AGN and host galaxies, particularly the BH accretion rate. In Section 4.6, we model the evolution of the M_{BH}–$M_\star$ relation from the observed z out to $z = 0$, and finally, in Section 4.7, we summarize our conclusions. The cosmological parameters adopted for this work were $H_0 = 67.7 \, \mathrm{km \, s^{-1} \, Mpc^{-1}}$ and $\Omega_m = 0.307$, as derived by Planck Collaboration et al. (2016). The AB system will be used when quoting magnitudes unless otherwise stated. Solar masses and SFRs are scaled according to a universal Chabrier (2003) initial mass function.

4.2 SAMPLE

This section describes the data sets used in our analysis. In Section 4.2.1, we recount the miniJPAS survey, which lies along the Extended Groth Strip (EGS) field (Davis et al., 2007) and provides the optical data to characterize the AGN and their host galaxies. Section 4.2.2 shows the X-ray data available in the EGS field and the AGN selection in the X-rays. In Section 4.2.3, we describe the methodology followed to obtain the intrinsic X-ray fluxes. Finally, in Section 4.2.4 we explain the available data in other bands and the optical spectra for our source selection.

4.2.1 Narrow–band data from the miniJPAS survey

The Javalambre Physics of the Accelerating Universe Astrophysical Survey[1] (J-PAS, Benitez et al., 2014) is a recently developed survey slated to cover a substantial 8500 square degrees of the celestial sphere, representing about 20% of the entire sky. Facilitating this ambitious survey is the dedicated 2.55-meter telescope (JST/T250) at the Observatorio Astrofísico de Javalambre (OAJ), equipped with a cutting-edge camera featuring 54 narrow-band filters ($FWHM \simeq 145$ Å) covering the wavelength range of 3780 to 9100 Å, with two additional broader filters in the blue and red wings extending the range to 3100–10 000 Å. The intricate configuration of these filters is illustrated in Fig. 4.1. This setup is strategically designed to achieve three primary scientific objectives: accurate measurement of photometric redshifts for galaxies up to $z \sim 1$, studying stellar populations in nearby galaxies, and resolving broad spectral features of objects such as AGN and supernovae.
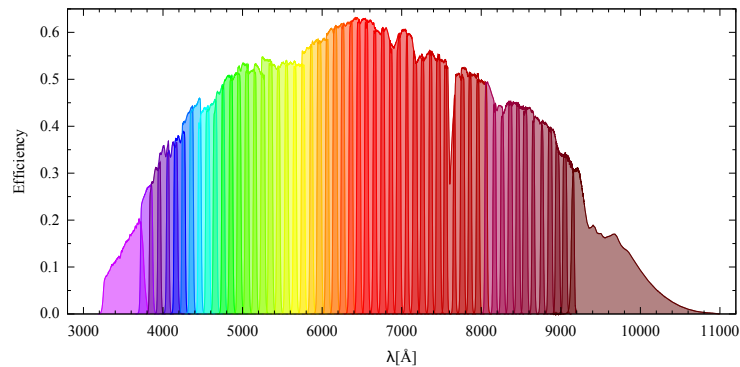
Figure 4.1: Transmission curves of the 56 J-PAS filters considering effects of the CCD quantum efficiency, the JST/T250 telescope transmission and sky absorption. Credits: Bonoli et al. (2021)

Through meticulous measurements of redshifts to billions of galaxies, J-PAS aims to provide crucial data that can help to unravel the

---

[1] j-pas.org

nature of dark energy and its implications for the universe's cosmology. Beyond its cosmological goals, J-PAS is capable to offer valuable insights into a diverse range of astrophysical topics, including the formation of the first stars and galaxies, the evolution of SMBHs, and the nature of AGN.

The main camera of the telescope, known as JCam, is a 1.2 Gigapixel camera spanning an area of approximately 4.2 deg^2 with its 14 CCDs. This extensive field of view allows for the complete inclusion of the Andromeda galaxy[2]. Currently, JCam is actively capturing and processing images for its initial data release. In the interim, while awaiting the assembly and testing of JPCam, the JST/T250 had been equipped with the JPAS-Pathfinder camera. This single CCD camera, located at the center of the focal plane, has a field of view of approximately 0.3 deg^2. It has been instrumental in conducting the first scientific operations of the JST/T250 and delivering, for the first time, the type of data expected from the full J-PAS survey.

This proof-of-concept survey, named miniJPAS (Bonoli et al., 2021), was carried out between 2018 and 2019 on the renowned EGS field, covering an area of approximately 1 deg^2. The J-PAS filter system effectively provides a low-resolution pseudo-spectrum (referred to as the J-spectrum) for every detected source and is particularly well-suited for studying AGN (Abramo et al., 2012), a focus of this work.

In the approximately 1 deg^2 of the sky covered, the miniJPAS catalog contains over 64 000 sources detected in the r band. This catalog achieves a 99% completeness up to $r = 23.6$ for point-like sources and up to $r = 22.7$ for extended sources (Bonoli et al., 2021). Point-like sources are defined as those with CLASSSTAR > 0.9 in the morphological classification from SExtractor (Bertin and Arnouts, 1996). As this work relies on photometric data up to $r < 23.6$, morphological information about the sources is not provided in this study.

miniJPAS offers different catalogs: *single* and *dual* modes. In single mode, the detection of sources is independent for each filter. This mode can be advantageous for obtaining information on faint sources with emission lines with a high signal-to-noise ratio (S/N). Because we are interested in obtaining a well-described shape of the optical SED, we used the dual mode. In this catalog, the detection is performed in a reference band (r band), and the photometry of all other filters is forced to the reference aperture (fixed shape and centroid). From the dual catalog of miniJPAS, we also picked two different photometries: `AUTO` and `PSFCOR`. The difference between them is that `AUTO` gives the magnitude within a Kron aperture, while `PSFCOR` is obtained in a smaller aperture and takes into consideration the differences in the point spread functions (PSFs) between the different filters (for details on the photometries definition, see Hernán-Caballero et al., 2021). In Section 4.3, we discuss and explain the choice of working with `AUTO`.

---

2 For details, see https://www.j-pas.org/news/show/197

We corrected all miniJPAS magnitudes for galactic extinction using the color excess $E(B-V)$ calculated from Bayestar17 (Green et al., 2018) for each filter (for details, see López-Sanjuan et al., 2019).

4.2.2 X–ray selection

We selected X-ray detection as our primary method for identifying AGN across a wide range of redshifts and luminosities, particularly due to its proficiency in uncovering AGN that may be obscured or overwhelmed by the host galaxy's flux in other spectral bands (see Brandt and Alexander, 2015, for a review). As we mentioned in Section 1.1, X-ray observations are crucial not only for their ability to penetrate high levels of obscuration but also for their effectiveness in identifying AGN across a wide range of Eddington ratios, which are often undetectable in optical and UV surveys. These unique capabilities of X-ray detection are key for constructing a comprehensive AGN sample that includes both obscured and unobscured types, as well as those with different accretion efficiencies.

The EGS field has benefited from extensive X-ray observations by Chandra (Laird et al., 2009; Nandra et al., 2015), yielding deep insights into the high-energy phenomena associated with AGN, and supplemented by broader surveys from XMM-Newton (Liu et al., 2020). The resulting catalogs from these observations are invaluable, providing measurements of X-ray fluxes in both the soft (0.5–2 keV) and hard (2–10 keV) bands, thus ensuring a robust selection of AGN candidates for further study.

We compiled these data into a unique catalog, prioritizing the deepest observations for sources with multiple detections. For the two Chandra catalogs, we employed a cross-matching radius of two arcseconds, which is consistent with Chandra's high angular resolution and typical astrometric accuracy. This radius ensures a balance between maximizing true source identification and minimizing the inclusion of unrelated background objects. In contrast, due to XMM-Newton's lower spatial resolution, we adopted a larger maximum separation of five arcseconds for cross-matching sources between Chandra and XMM-Newton. This adjustment accounts for XMM-Newton's broader point spread function and higher likelihood of positional uncertainties.

We also removed the spurious sources detected in Laird et al. (2009) following Nandra et al. (2015). Additionally, we excluded spectroscopically confirmed stars. Finally, our work resulted in a catalog of 4928 unique X-ray sources detected across ~ 6 deg^2 of the EGS field—1617 from Chandra observations and 3311 from XMM-Newton. Figure 4.2 illustrates a sky map of the compiled X-ray catalog alongside the miniJPAS footprint. The original catalogs also provided reliable counterparts, obtained using likelihood ratio analysis and deep optical/IR photometric data (for details, see Laird et al., 2009; Nandra et al.,

2015; Liu et al., 2020) and only ∼ 2% of the sources do not have any optical/IR counterpart.
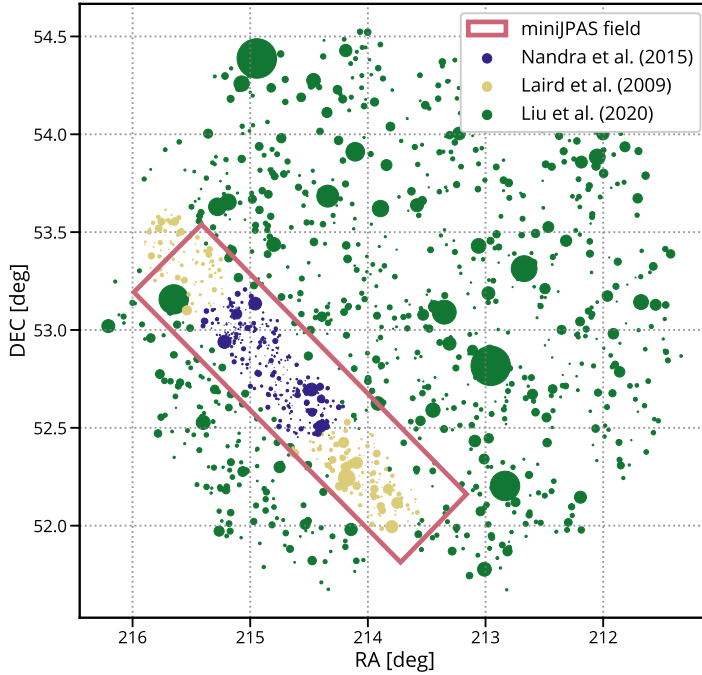
Figure 4.2: Sky map of the X-ray sources on and around the miniJPAS footprint (red box). Each dot represents an X-ray source in our compiled X-ray catalog, color-coded to show its original catalog. The size of the dots is proportional to their total X-ray flux measured in 0.5–10 keV.

One-third (1661) of our unique X-ray sources are located within the 1 deg^2 of the miniJPAS footprint and have a reliable optical/IR counterpart. We cross-matched these counterparts with the miniJ-PAS dual-mode catalog, up to $r < 23.6$ mag, resulting in 741 matches. When available, we added a confident spectroscopic redshift value from DEEP2 DR4 (Newman et al., 2013) and SDSS DR16 (Ahumada et al., 2020) using the optical/IR counterpart position and searching within a radius of one arcsec. This specific radius was chosen based on a detailed statistical analysis illustrated in Fig. 4.3, where we compared actual detections against a mock catalog of uniformly random sources. Our analysis revealed that the majority of legitimate cross-matches occur within one arcsecond. Beyond this threshold, the incidence of matches with the mock catalog—representative of spurious detections—increases significantly, suggesting a higher probability of erroneous matches. Therefore, the one arcsecond radius optimizes the likelihood of correct associations while minimizing the inclusion of spurious ones.

From this crossmatch, we found robust spectroscopic redshift values for 430 of the optical/IR counterparts (i. e. ZQUALITY ≥ 3 for DEEP2 and
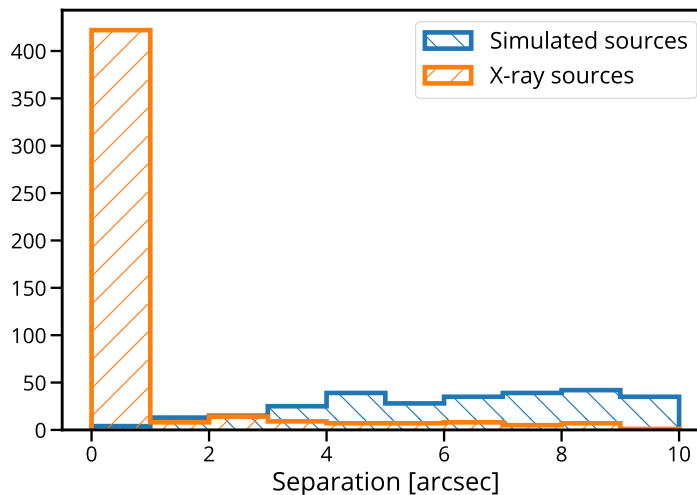
Figure 4.3: Histogram of the quantity of crossmatches as a function of separation distance. The blue bars represent our X-ray selected sources, while the orange bars depict matches from a mock catalog of uniformly random sources. Beyond one arcsecond, the number of matches with the mock catalog increases significantly, indicating a higher probability of spurious detections.

`zWarning = 0` for SDSS)[3]. We also excluded sources with any type of flag in all the miniJPAS narrow filters. These flags can be from the extraction process (close neighbor, saturated pixel, too close to a boundary, tiles overlap, between others) or because the images were affected by different technical problems in the CCD or telescope (see Bonoli et al., 2021, for details on flags). Finally, we are left with 370 sources with X-ray fluxes, optical photometry, and a reliable spectroscopic redshift value. In Table 4.1, we show the numbers of sources in detail for each cut. The selection done is generous to include all types of sources. In Section 4.3.1.3, we explain how insights from the SED fitting process are used to exclude a posteriori sources whose light is dominated by the host galaxy or the AGN, making the determination of their physical parameters unreliable.

4.2.3 X-ray flux correction

The X-ray photons suffer a photoelectric absorption that can be modeled depending on the hydrogen column density (N_{H}). This

---

3 Keeping only sources with a reliable spectroscopic redshift can introduce potential biases towards unobscured sources, high-luminosity AGN, or peculiar targets selected for spectroscopic follow-up, leading to a heterogeneous and potentially incomplete sample. A possible alternative is to consider redshifts calculated using photometric redshifts (for a review, see Salvato et al., 2019). Nevertheless, at the time of this publication, miniJPAS had not incorporated a reliable photo-z that includes AGN emission, so we decided to work with spectroscopic redshift values. Biases arising from this decision are discussed in Section 4.4.

	ALL	WITH $z_{\rm spec}$	$z < 2.5$
X-ray selection ($\sim 6\,{\rm deg}^2$)	4928	1394	1282
& inside miniJPAS area ($\sim 1\,{\rm deg}^2$)	1661	532	507
& miniJPAS detection	741	430	406
& miniJPAS not flagged	641	370	*347*
& reliable SED fit	-	-	**308**

Table 4.1: Total X-ray sources in the EGS field and our sample selection. The final sample is highlighted in *italic*, and the sources that surpass the SED fitting criteria are in **bold** (details of this criteria are discussed in Section 4.3.1.3).

absorption can be intrinsic to the source, occurring before the photons escape the host galaxy, or local, due to the ISM in the Milky Way.

Since the X-ray AGN photons originate from a nonthermal process, they can be modeled with power-law spectra, and we can predict the loss of photons for a given power-law index, redshift, and intrinsic $N_{\rm H}$. Because the response curve of each X-ray telescope is different and can change during its useful life, this relation also depends on the instrument and date of observation.

To estimate $N_{\rm H}$, we used the Hardness Ratio, ${\rm HR} = \frac{\rm H-S}{\rm H+S}$, where H and S are counts in the soft and hard bands, respectively. The hard band is measured in the 2–10 keV range, while S is in the 0.5–2 keV range. We use the software PIMMS[4] to predict how HR changes with redshift at a fixed $N_{\rm H}$ and photon index[5] (Γ) for Chandra and XMM-Newton main cameras and the representative observation date for each log. As an example, we show these predictions for Chandra sources with lines in Fig. 4.4. A similar approach to obtain $N_{\rm H}$ from HR was employed in Marchesi et al. (2016a).

We computed the bayesian HR using the program Bayesian Estimation of Hardness Ratios (BEHR; Park et al., 2006) for all the sources (shown as dots in Fig. 4.4). Finally, we selected the nearest curve for each source, estimating the closest value of intrinsic $N_{\rm H}$ for them.

The flux correction for the Milky Way absorption was already performed in the original catalogs. Then we just apply the correction for the intrinsic absorption to obtain the intrinsic values of X-ray flux on the soft and the hard bands. We use PIMMS, adopting the estimated intrinsic $N_{\rm H}$. In Fig. 4.5, we show the flux corrected for intrinsic absorption following the procedure outlined above as a function of the detected flux for the soft and the hard bands. As expected, absorption affects the hard band less than the soft band.

---

4 https://heasarc.gsfc.nasa.gov/docs/software/tools/pimms.html

5 Since the original catalogs do not have information to obtain fluxes from the photon counts, we used the original photon index, $\Gamma = 1.4$ for Chandra catalogs and $\Gamma = 1.7$ for XMM/Newton catalog.
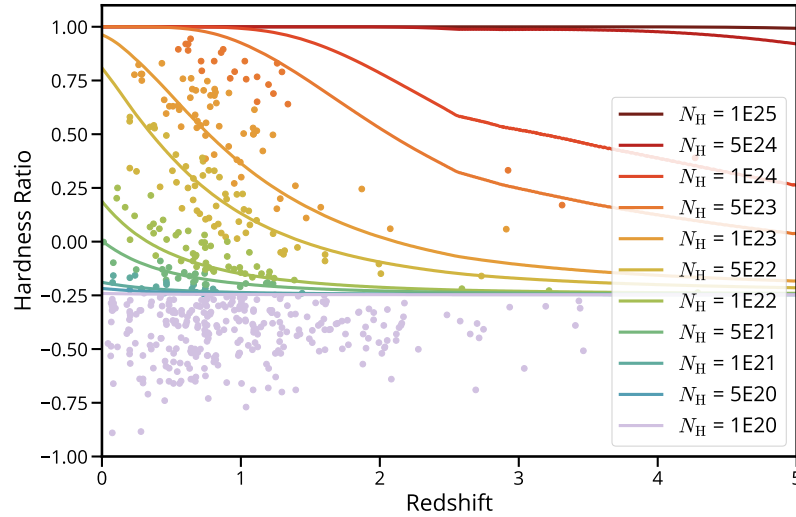
Figure 4.4: Hardness ratio as a function of redshift for Chandra sources in our sample (dots). The solid lines show the value of the corresponding column density, N_{H}, for a fixed $\Gamma = 1.4$. The color of each source corresponds to the assigned N_{H} (values in cm^{-2}).

In Fig. 4.6, we show the redshift distribution for all the X-ray sources with spectroscopic redshift measurements in the EGS field (1394 sources). The distribution drops significantly after $z = 1.5$, showing a small number of sources beyond $z = 3$. We decided to limit our sample to $z = 2.5$ for sources with miniJPAS detection to avoid diluting our sample at higher redshifts where only a few sources are present (see Table 4.1). This cut defines our final sample: 347 X-ray sources with spectroscopic redshifts and miniJPAS photometry (flagged). This subset is shown in red in Fig. 4.6.

In Fig. 4.6, we also display the histograms for the estimated intrinsic N_{H} and the X-ray absorption-corrected luminosity distribution for all the sources in the EGS field and for our final sample. The redshift and N_{H} distributions are self-similar between the full X-ray sample and our final sample. However, the L_{X} distribution for the final sample exhibits lower luminosities compared to the full EGS field, potentially revealing selection biases. These biases could be attributed to the spectroscopic redshift selection or to the characteristics of the miniJPAS survey, which might favor sources with intrinsically lower L_{X}. The main properties of the sources in our sample can be found in Table 4.2.

4.2.4 UV/IR data and optical spectra

In order to build a complete SED and to fit diverse host galaxy and AGN models, it is necessary to have multiwavelength data. Because of this, we included in our analysis all the available photometric data from UV and IR full-sky coverage surveys when they were available.
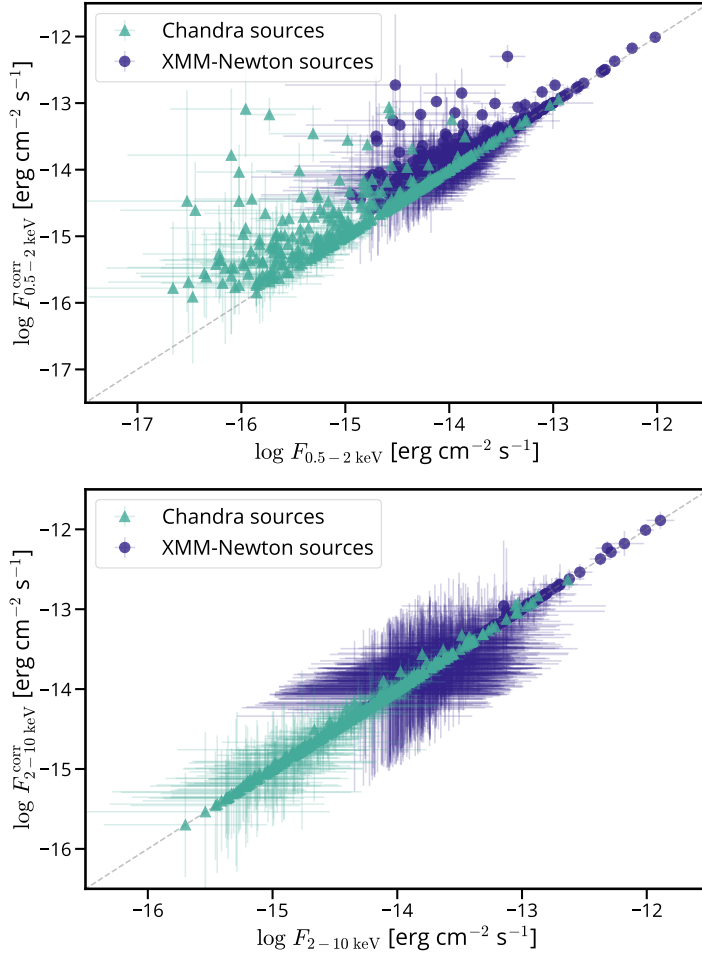
Figure 4.5: Intrinsic X-ray fluxes as inferred after the N_H correction vs. measured fluxes in the soft (0.5-2 keV, upper panel) and hard (2-10 keV, lower panel) bands.

The chosen filters cover UV to mid-IR with up to 68 bands, as shown in Fig. 4.7. This selection was made to cover the rest-frame UV to near-IR fluxes up to $z = 2.5$ for all sources. This will allow a good estimate of the SED, especially on the host galaxy emission.

For UV data, we crossmatched our catalog with GALEX GR6/7 (Bianchi et al., 2014) within a radius of five arcseconds. This radius was chosen to account for the PSF and astrometric accuracy of the instrument. We added fluxes in the near-UV (1350–1750 Å) for 257 sources and in the far-UV (1750–2800 Å) for 207 sources in our final sample. The magnitude limit in both filters is approximately 25.1 mag AB. This allowed us to obtain a reliable estimation of UV photons for the majority of our sample (around 80%), with only 18% of our nearby sources ($z < 0.5$) lacking rest-frame UV data. We corrected the UV fluxes for galactic extinction using the coefficients provided by Yuan et al. (2013).
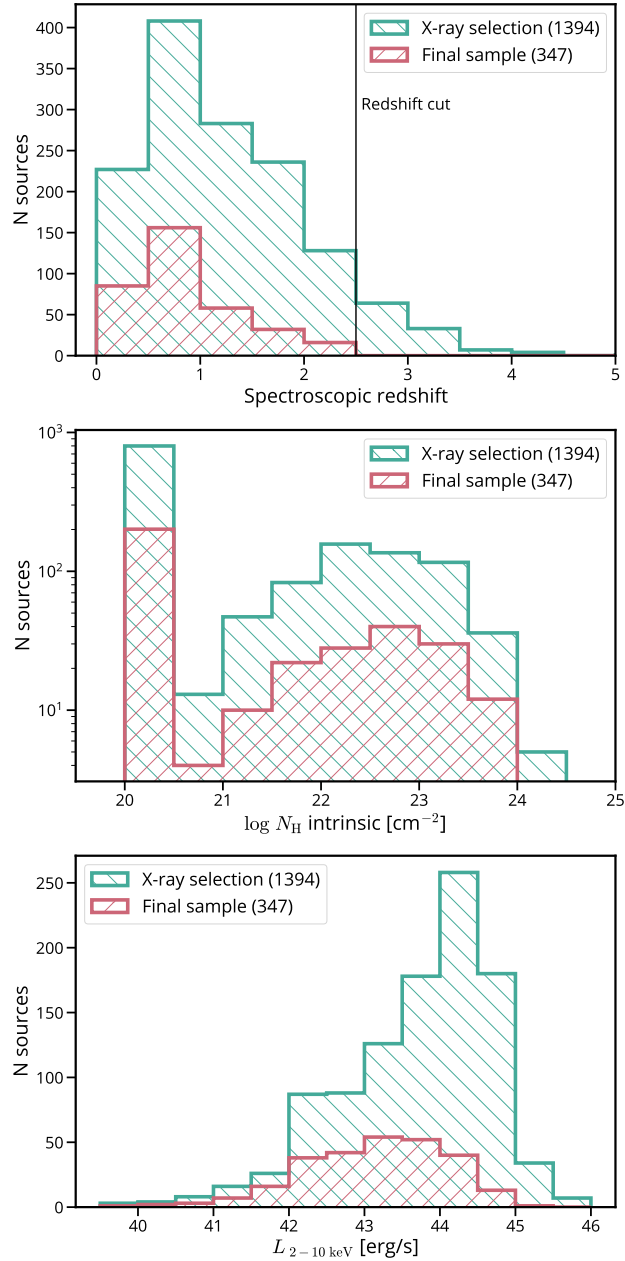
Figure 4.6: Distributions of spectroscopic redshifts (upper panel), intrinsic column density N_H (middle panel), and hard X-ray luminosity (lower panel) for all sources in the EGS sample (green) and our final sample with miniJPAS detection and good photometry used in this work (red).

For the near-IR range, we utilized the J, H, and Ks bands from Moles et al. (2008). The ALHAMBRA near-IR survey covered various fields of interest across the sky, including an overlap between the ALHAMBRA-6 field and our own. The magnitude limits in the AB system are approximately $J \approx 22.91$ mag, $H \approx 22.39$ mag and $Ks \approx 21.85$ mag. We found photometry in these bands for 120 sources in our

ID	ID MINIJPAS	RA	DEC	z	r	$\log L_X$	$\log N_H$
(1)	(2)	(3)	(4)	(5)	(6)	(7)	(8)
aegis_019	2241-15772	214.610	52.472	0.681	23.14	42.86	20.0
aegis_021	2241-19043	214.424	52.473	1.148	21.88	44.28	22.0
aegis_022	2241-15294	214.626	52.478	1.993	22.06	43.56	22.7
aegis_026	2241-14038	214.679	52.489	1.083	22.03	43.35	20.0
aegis_029	2241-15867	214.568	52.495	1.605	20.22	44.11	20.0
aegis_032	2241-17939	214.439	52.498	0.873	22.88	43.19	23.7
aegis_035	2241-12772	214.755	52.506	0.238	19.48	43.53	21.0
aegis_036	2241-19320	214.353	52.507	0.482	20.14	42.48	20.0
...	...	...	...	...	...	...	...

Table 4.2: Sources analized in this work. (1) and (2) are the ID used in this work and the miniJPAS catalog ID, (3) and (4) the coordinates in degrees, (5) redshift, (6) r-band magnitude, (7) X-ray luminosity in erg s^{-1}, (8) hydrogen column density in cm^{-2}.
The complete table can be accessed online at Vizier.
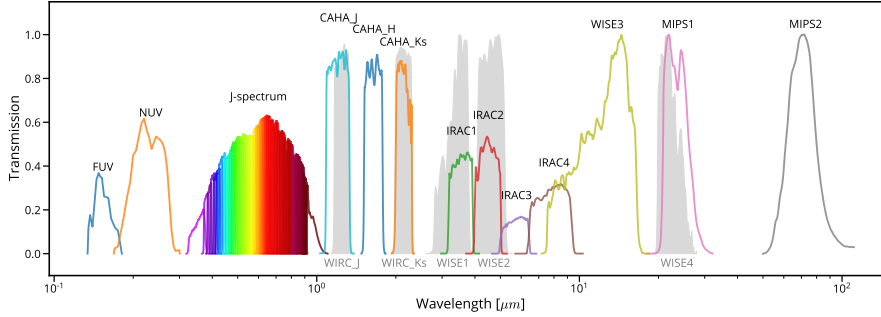
Figure 4.7: In color, the main filter coverage between UV and mid-IR. For our SED fitting, we have a total of 68 filters. The five filters shown in grayscale on the background are the second option in case the main does not have an observation on the target.

sample. For those without ALHAMBRA detections, we referred to the Palomar WIRC original AEGIS catalogs (Davis et al., 2007) and added J and Ks photometry for 67 and 178 sources, respectively. Overall, at least 298 sources (approximately 87%) have flux measurements in the NIR bands.

For mid-IR data, we used Spitzer IRAC and MIPS photometry from Barro et al. (2011). The four IRAC filters provided coverage between 3 and 10 microns. We found photometry for 273 sources in IRAC 1 and 2, 271 sources in IRAC 3, and 272 sources in IRAC 4. The flux limits are 23.9 mag AB for IRAC 1 and 2, and 22.3 mag AB for IRAC 3 and 4. For MIPS, we included 24 and 70 μm photometry for 251 and 135 sources, respectively, with flux limits of 19.5 and 15 AB mag at 24 and 70 μm, respectively. For sources lacking Spitzer observations, we used CatWISE2020 (Marocco et al., 2021) to obtain fluxes in the W1 (3.4 μm) and W2 (4.6 μm) bands, with flux limits of AB 20.4 and AB

19.8, respectively. To acquire fluxes for W3 (12 μm) and W4 (22 μm), we used the AllWISE catalog (Cutri et al., 2013), which has flux limits of 17.2 for W3 and 14.7 for W4.

We did a color correction following the recommendation by All-WISE website[6]. We used the published color correction from Wright et al. (2010), and the observed color W2-W3 to estimate the power-law index for each source and applied that color correction when the magnitudes were converted into fluxes. Upper limits at 5σ were added for undetected sources. In the case of W3, we also consider this filter for 262 sources ($\sim 75\%$ of the total sample) since this filter is in the gap between IRAC and MIPS (see Fig. 4.7). In total, we have at least 346 sources with some photometry between 3-10 μm, and 322 with photometry at 22-24 μm.

We also searched for available public spectra for our optical counterparts of each source within one arcsec. We used the spectra in the SDSS DR16 public archive[7] and from the DEEP2 survey (Newman et al., 2013). In the case of SDSS, we found that 101 sources have at least one spectrum. For sources with more than one SDSS spectrum, these were stacked to improve the S/N, obtaining a median spectrum for each source. For DEEP2 data, we used the 1-d spectra, obtained throughout a variant of Horne optimal extraction (see Newman et al., 2013, for details), for 111 sources. Since the DEEP2 spectra are not flux calibrated, we corrected them, considering the CCD sensitivity[8] as a function of wavelength. With that correction, we can better recover the correct shape of the spectra. This region of the sky was also targeted with MMT[9] (Coil et al., 2009; Yan et al., 2011). The authors shared with us their reduced spectra for 111 sources in our sample. Both SDSS and MMT spectra were flux calibrated. Considering all these spectra, we found at least one spectrum for 269 out of 347 miniJPAS sources. Details on the final spectra and their analysis can be found in Section 4.4.

4.3 PHYSICAL PARAMETERS ESTIMATION

4.3.1 SED fitting

We perform the SED fitting using CIGALE[10] (Burgarella et al., 2005; Noll et al., 2009; Boquien et al., 2019) with the X-ray module added by Yang et al. (2020) that makes it possible to include an AGN component in the X-rays. Recent works established CIGALE's efficiency in recovering specific physical parameters of the host galaxy and AGN.

---

6 wise2.ipac.caltech.edu/docs/release/allsky/expsup/sec4_4h.html

7 www.sdss.org/dr16/spectro/

8 https://www2.keck.hawaii.edu/inst/deimos/deimos_ccd_qe.html

9 https://www.mmto.org/

10 version: 2022.1

Mountrichas et al. (2021) used a set of mocks AGN and demonstrated that CIGALE could disentangle the AGN/host emission, finding an agreement between the true values of SFR and $M_\star$ and those recovered from the fitting. They also used an X-ray-selected sample with X-ray to far-IR photometry. They showed that CIGALE is powerful enough to correctly classify between type I and type II AGN, considering inclination and polar dust. Some parameters' accuracy can be improved by adding more bands; for instance, SFR is more robust when far-IR photometry is included. In our case, we did not include Herschel's data in the fitting because the available data in the field was not deep enough. Even without far-IR photometry, CIGALE can obtain reliable SFR for X-ray-selected sources with spectroscopic redshift using the rest of the photometric data (Masoura et al., 2018).

For this work, we construct the SED of each source using the redshift and photometric fluxes from all the available bands described in Section 4.2 and Fig. 4.7 (2–10 keV, 0.5–2 keV, FUV, NUV, the 56 miniJPAS optical filters, J, H, Ks, IRAC1-4, WISE3, MIPS1, MIPS2). For sources without detection in IRAC bands, we used the WISE bands (W1, W2, W4). In particular, for X-rays, CIGALE requests intrinsic fluxes. We set the 5σ upper limits for nondetected bands following the completeness studies from their original catalog. This wavelength coverage allows us to build a good rest-frame SED for the AGN and host galaxy, even at redshift 2.5.

As discussed in Chapter 3, CIGALE uses independent modules that model a unique physical feature or process. For each parameter of these modules, CIGALE builds a prior from a given grid of parameters. To choose the modules and the grid of parameters, we followed Mountrichas et al. (2021) because of the similarity of our sources. In Sections 4.3.1.1 and 4.3.1.2, we describe each module used for the host galaxy and AGN and the values adopted for the parameters. A full description of modules and parameters used as input is given in Table 4.3. CIGALE also estimates two values for each output parameter: one from the best-fit model (called *best* value) and another one that weighs all grid models (called *bayesian* value). These weights are based on the Bayesian likelihood $\exp(\chi^2/2)$ associated with each model.

4.3.1.1 *Host galaxy emission*

For the stellar component, we use a τ-delayed SFH. This parametrization is very versatile because it allows a smooth SFR with a similar shape as the average SFR density across cosmic time (Madau and Dickinson, 2014) and depends on the time at which the SFR peaks (τ) for each source. The functional form is $\mathrm{SFR}(t) \propto t\,\tau^{-2}\exp(-t/\tau)$, and after the maximum at $t = \tau$, the SFR smoothly declines. We also include the possibility of a recent burst following Małek et al. (2018b). The stellar templates are from Bruzual and Charlot (2003) and an initial mass function from Chabrier (2003), with a fixed solar metallicity

to avoid degenerations. The stellar emission is attenuated following the Calzetti et al. (2000) law, and the dust emission is modeled with the template from Dale et al. (2014). Since our photometric data includes narrow filters, emission lines typical of star-forming regions can be detected (Martínez-Solaeche et al., 2022). Because of that, we added a model for nebular gas that uses nebular templates from Inoue (2011), choosing a width of 300 km s^{-1} for narrow emission lines. CIGALE also includes the possibility of LMXB and HMXB fitting the X-ray emission.

4.3.1.2 AGN emission

For the active nuclei, we use the Skirtor model included in CIGALE (Yang et al., 2020). We followed Mountrichas et al. (2021) to model the different obscurations for Type I and Type II AGN, setting two possible inclinations (30 and 70 degrees) and a grid of values for the polar dust. We also set two possibilities for the torus optical depth at 9.7 μm (3.0 and 7.0).

The AGN fraction, frac$_{AGN}$, can be used to compare the emission of the host galaxy versus that of the AGN. This parameter represents the fractional contribution of the AGN's torus and polar dust emission to the integrated infrared luminosity. We utilized a grid covering possible values ranging from 0.01 to 0.99 in increments of 0.1 (0.01, 0.1, 0.2, ..., 0.9, 0.99), allowing for the possibility of obtaining a SED entirely dominated by either the host galaxy or the AGN.

The X-ray module helps to constrain the UV emission from the accretion disk using the α_{ox}–L_{2500} relation, and for it, we set an ample grid for possible values of α_{ox} (−1.9, −1.75, ..., −1.15, −1.0; Xu, 2011; Lusso and Risaliti, 2016). Considering that our X-ray fluxes are corrected for intrinsic absorption, we set a photon index typical for AGN of $\Gamma = 1.8$.

4.3.1.3 Fitting

We ran CIGALE for our final sample (347 sources) using the modules and parameters described in Table 4.3. The number of models computed per source by CIGALE is 5,544,000. We ran it for two different types of miniJPAS photometry: `AUTO AUTO` and `PSFCOR` .

Both photometries have their pros and cons. The `PSFCOR` considers issues like point-spread function variation on the focal plane for different dates, biases on filters, and aperture correction, among others. However, its small aperture gives a value below the galaxy's expected total flux. `AUTO` provides a closer value to the total flux, but it can be noisier due to a bigger aperture. To compare the SED fitting results of both photometric fluxes, we scale the J-spectra obtained from `PSFCOR` using the r_{mag}^{AUTO} as the reference value.

PARAMETER	MODEL/VALUES
Star formation history: delayed model and recent burst	
Age of the main population	500, 1000, 3000, 5000, 7000 Myr
e-folding time	500, 1000, 3000, 5000, 7000 Myr
Age of the burst	20, 200 Myr
e-folding time of the burst	50 Myr
Burst stellar mass fraction	0.0, 0.1
Simple Stellar population: Bruzual & Charlot (2003)	
Initial Mass Function	Chabrier (2003)
Metallicity	0.02 (Solar)
Galactic dust extinction	
Dust attenuation recipe	modified Calzetti et al. (2000)
$E(B-V)_{young}$	0.0, 0.1, 0.25, 0.5, 0.75, 0.9
UV^{λ}_{bump}	217.5 nm
Galactic dust emission: Dale et al. (2014)	
α slope in $dM_{dust} \propto U^{-\alpha}dU$	1.0, 1.5, 2.0, 2.5, 3
Nebular	
$\log U$	-2.0
Width lines	300 km/s
AGN module: SKIRTOR	
Torus optical depth at 9.7 microns $\tau_{9.7}$	3, 7
Viewing angle	30° (type 1), 70° (type 2)
Disk spectrum	Schartmann (2005)
Power-law index modifying the accretion disk	-0.36
AGN fraction	0.01, 0.1, 0.2, 0.3, ..., 0.9, 0.99
Extinction law of polar dust	SMC
$E(B-V)$ of polar dust	0.0, 0.01, 0.05, 0.1, 0.5, 1.0
Temperature of polar dust	100 K
Emissivity of polar dust	1.6
X-ray module	
AGN photon index Γ	1.8
α_{ox}	-1.9, -1.75, -1.6, -1.45, -1.3, -1.15, -1.0
Max deviation from $\alpha_{ox} - L_{2500Å}$	0.4
LMXB photon index	1.56
HMXB photon index	2.0
Total number of models per redshift	5,544,000

Table 4.3: Parameters and values for the modules used with CIGALE.
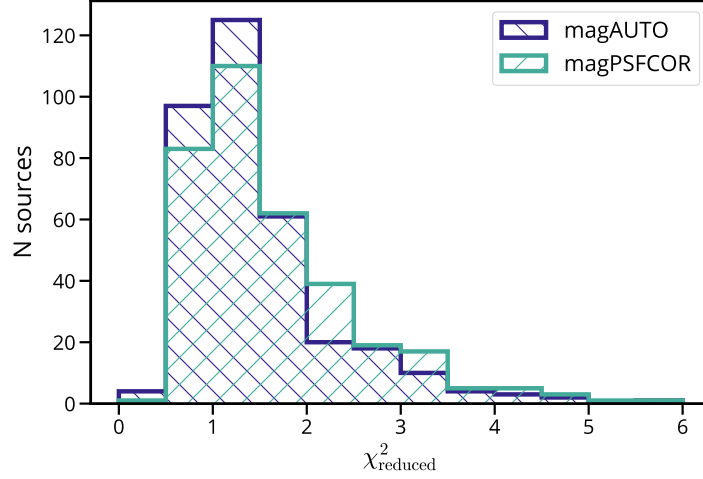
Figure 4.8: Histograms of reduced χ^2 for the SED fitting performed using two different sets of magnitudes extracted from miniJPAS catalogs, AUTO and PSFCOR.

In Fig. 4.8, we show the distribution of *reduced* χ^2 for the SED fitting with both types of photometries. Both distributions are similar, showing good fits, with a high number of sources near one and a decreasing tail beyond three, being AUTO the one with more sources near one. In Fig. 4.9, we show the comparison between physical parameters obtained from the SED fitting for both photometries. We used these parameters because they give basic information about the host galaxy ($M_\star$, SFR) and the AGN (L_{AGN}). In each panel, the physical properties are in agreement for both photometries with the small mention that the relative errors of the PSFCOR is slightly higher than for AUTO. The median of the relative errors for AUTO are $\tilde{\mathrm{RE}}_{\mathrm{M}_\star} = 0.16$, $\tilde{\mathrm{RE}}_{\mathrm{SFR}} = 0.24$ and $\tilde{\mathrm{RE}}_{\mathrm{L}_{\mathrm{AGN}}} = 0.26$ while for PSFCOR are 0.16, 0.33 and 0.27 respectively.

Since, in our analysis, it is necessary to obtain an estimation of the properties of the host galaxy and the AGN, we excluded the sources dominated by only one component (i.e., pure-AGN or pure-galaxy). Mountrichas et al. (2021) and Buat et al. (2021) show that, for a given parameter, if there is a large difference between the *best* value and the *bayesian* value, the estimation of such parameter is not reliable. Following this idea, we can exclude the sources where the difference between parameters is bigger than one order of magnitude for $M_\star$, SFR, and L_{AGN}. In other words, we can only keep sources with $0.1 \leq \frac{M_{\star,\mathrm{best}}}{M_{\star,\mathrm{bayes}}} \leq 10$, $0.1 \leq \frac{L_{\mathrm{AGN,best}}}{L_{\mathrm{AGN,bayes}}} \leq 10$ and $0.1 \leq \frac{SFR_{\mathrm{best}}}{SFR_{\mathrm{bayes}}} \leq 10$. In Fig. 4.10, we show the reliability of our fits using these criteria. The parameters obtained with the different miniJPAS photometries show similar distributions, centered in one with small dispersion. The choice of 1 dex as limit was made to exclude all outliers.

Fig. 4.9 already shown that there is no significant difference between the two photometries, besides that AUTO has marginally smaller relative
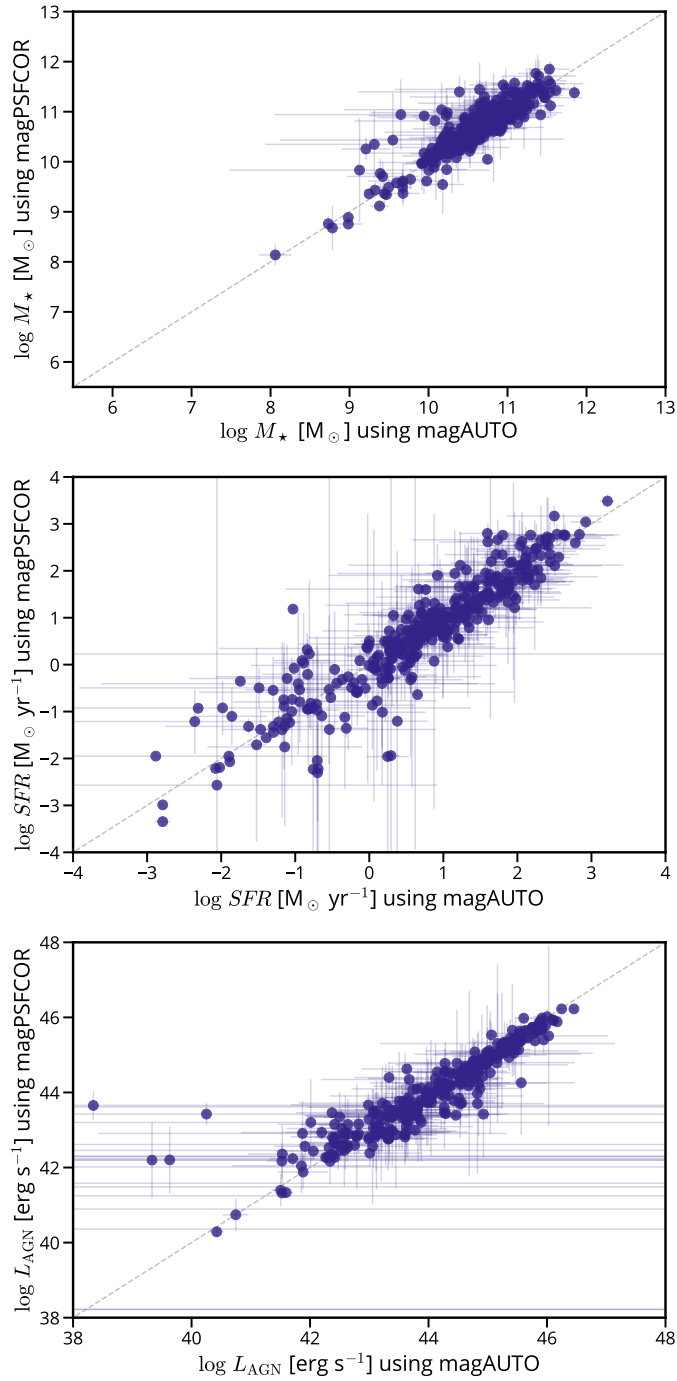
Figure 4.9: Physical properties estimated obtained from the SED fitting, using different miniJPAS magnitudes as input. In all panels, the 1:1 relation is the dashed line.

errors. Because that, from now on, we only present the results obtained using AUTO. We also remove the sources where the AGN luminosity is close to zero. Following these criteria, we remove 39 sources ($\sim 11\%$ of the sample). We are left with 308 sources with reliable measurements
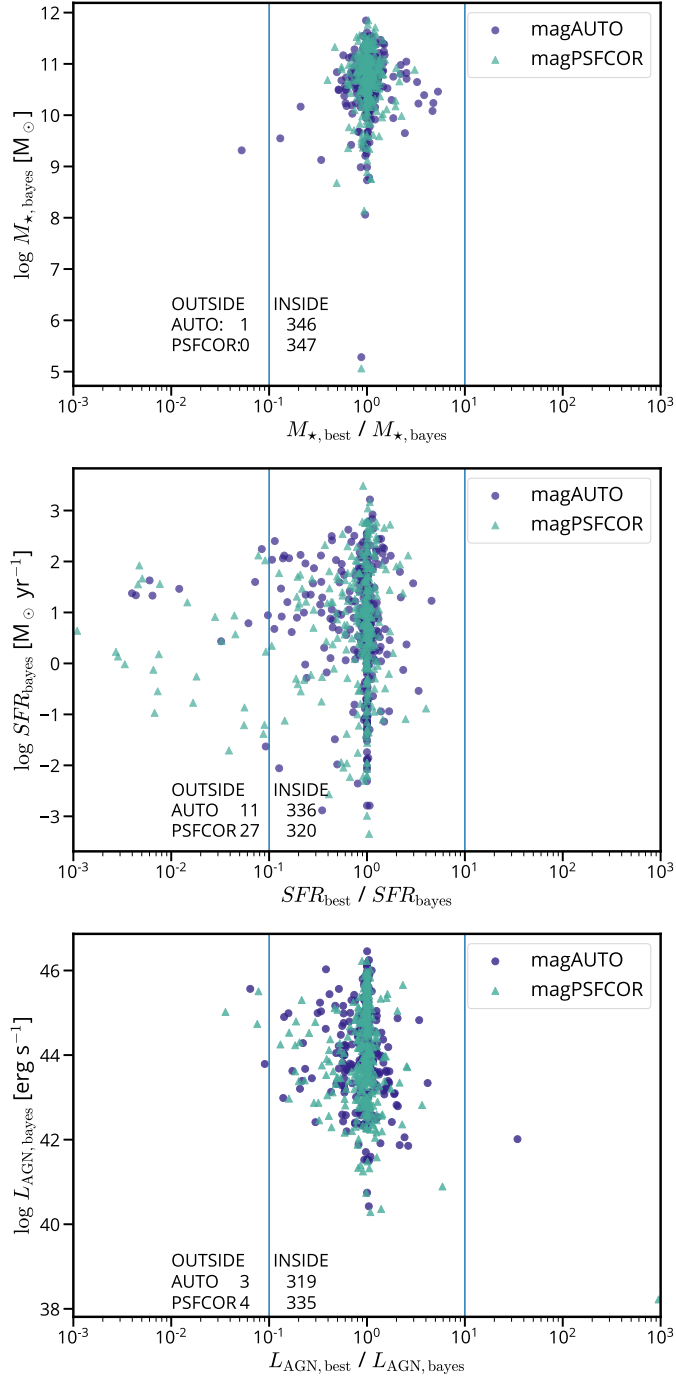
Figure 4.10: Criteria used to exclude the sources with unreliable physical parameters. The Bayesian values for $M_\star$ (upper panel), SFR (middle panel), and $L_{\rm AGN}$ (lower panel) are plotted against the ratio of best values over bayesian. The distribution is centered at 1. The solid vertical lines mark the limits of 0.1 and 10 adopted in this work. The different colors show the parameters and ratios obtained, assuming different magnitudes as input. The number of sources between and outside the limits is reported in the lower part of the plots.
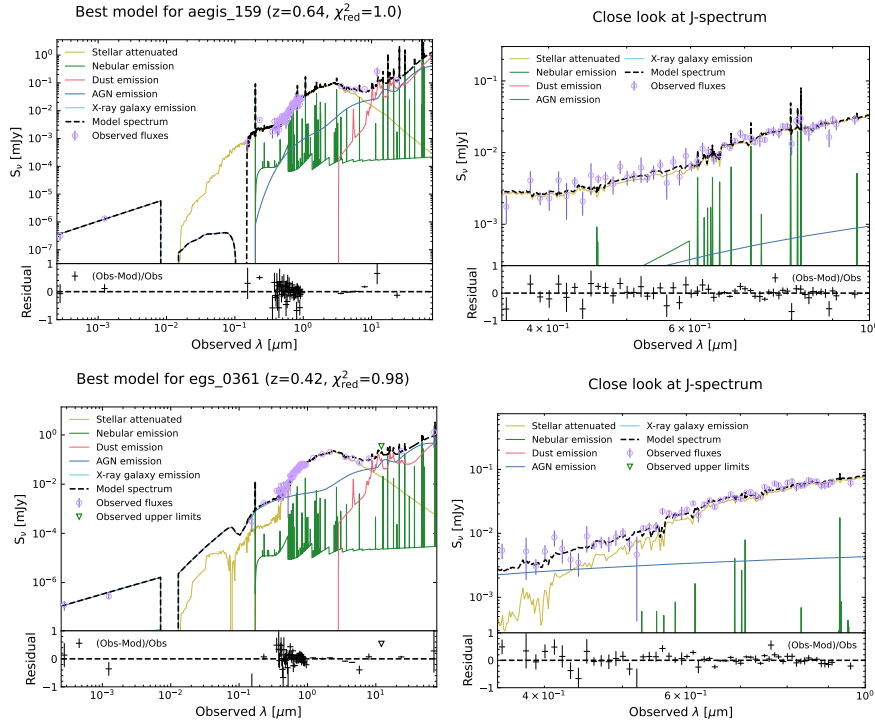
Figure 4.11: Examples of SED fits using CIGALE and their residuals. Pink circles show the photometry for each band used. Green triangles are upper limits. The black dashed line is the composite model, and the color lines are the individual components of the composite model. *Left:* Full range of wavelengths, from X-ray to IR. *Right:* Close up on optical miniJPAS J-spectrum.

of the AGN and the host galaxy components. Examples of SED fitting and its close-up to the miniJPAS J-spectra are shown in Fig. 4.11.

4.3.2 Spectra fitting

As we highlight in Chapter 2, the emission lines in a AGN spectrum can provide information about their obscuration and the SMBH properties. Broad lines are observable for Type I, while narrow lines are present in both types. Typically, we can assume that the SMBH's gravitational field dominates the gas cloud motion in the BLR. Thus, the width of these lines is related to the virialized mass of the SMBH. A spectral fitting is necessary to obtain a good measure of the width, considering all other features typical of AGN. In this section, we discuss the fitting process on Section 4.3.3, and the estimation of M_{BH} on Section 4.3.4.

4.3.3 Fitting

As described in Section 4.2.4, at least one spectrum is available for 269 sources of our initial sample. We did a cut of a mean $S/N > 3$ on these spectra. After we fit them, we obtained an acceptable FWHM of broad region lines of 113 AGN for our final sample. When more than one spectrum was available for the same source, we selected the one with the highest S/N.

We used PyQSOFit (Guo et al., 2018) to fit the continuum, iron emission, and emission lines of the AGN. We fit the spectra with a combination of continuum and line emission. We used a polynomial for the stellar continuum and a power law for the AGN continuum, and we also included iron emission. In the case of narrow lines, we allow one Gaussian with the same width for all the narrow features. Broad lines can be very complex because of the presence of asymmetries; in these cases, the width estimated by only one Gaussian gives systematically larger widths (Shen et al., 2008). Due to this overestimation, we allow between one and three Gaussians depending on the line, following Rakshit et al. (2020). The multicomponent Gaussian used to fit the narrow and broad emission lines are listed in Table 4.4.

LINE	WAVELENGTH [Å]	TYPE	NRO GAUSSIANS
Hα	6564.61	Broad	3
Hα	6564.61	Narrow	1
[NII]	6549.85	Narrow	1
[NII]	6585.28	Narrow	1
[SII]	6718.29	Narrow	1
[SII]	6732.67	Narrow	1
Hβ	4862.68	Broad	3
Hβ	4862.68	Narrow	1
[OIII]	4960.30	Narrow	1
[OIII]	5008.24	Narrow	1
[OII]	3728.48	Narrow	1
[SII]	6732.67	Narrow	1
MgII	2798.75	Broad	2
MgII	2798.75	Narrow	1
CIII]	1908.73	Broad	1
CIV	1549.06	Broad	3
CIV	1549.06	Narrow	1
Lyα	1215.67	Broad	1
Lyα	1215.67	Narrow	1

Table 4.4: Emission lines used in the spectral fit. Central wavelengths are at rest-frame.

In particular, we measured the FWHM of the broad component of Hα, Hβ, MgII, and CIV and the luminosity at 1350, 3000, and 5100 Å. For the DEEP2 spectra that are not flux calibrated, we scaled them to the luminosity (1350, 3000, and 5100 Å) of the closest narrow-band filter from miniJPAS photometry. Examples of spectral fits are shown in Figs. 4.12 and 4.13.

We set limits for the width of the emission lines fitted. To distinguish between broad and narrow lines, we used a value of 1000 km s^{-1}. The upper limit for the broad lines was 10 000 km s^{-1}. These limits come from the width bimodal distribution shown for X-ray-selected AGN lines (Menzel et al., 2016).

4.3.4 BH mass estimation

Although σ seems to correlate better with the masses calculated from the reverberation method, we use FWHM instead. The main criterion for this choice is that σ is too sensitive to noise on the wings of the emission lines (Shen and Liu, 2012). To estimate the error in the FWHM, PyQSOFit uses a Monte-Carlo approach to fit random mock spectra and obtain the uncertainties considering the flux errors and systematic errors for multiple decomposing components.

Several works calibrate the virial relation from a single-epoch spectrum (see Shen and Liu, 2012, for a compilation). Different lines have slightly different calibrations. For our M_{BH} estimation, we used the coefficients from Assef et al. (2011) for the Balmer lines (Hα and Hβ); Vestergaard and Osmer (2009) for MgII; and Vestergaard and Peterson (2006) for CIV. We used the Eq. (2.2) to estimate the black hole masses, with an overview of the coefficients in Table 4.5.

FWHM	LUMINOSITY AT	A	B	C
Hα	5100 Å	0.774	0.520	2.06
Hβ	5100 Å	0.895	0.520	2.00
MgII	3000 Å	0.860	0.500	2.00
CIV	1350 Å	0.660	0.530	2.00

Table 4.5: Coefficients used for different emission lines. Extracted from Shen and Liu (2012).

To obtain M_{BH} uncertainties, we propagate the FWHM and luminosity uncertainties in the Eq. (2.2), including the dispersion of the original fit where the coefficients a, b, and c were calculated. Similar to the spectra selection, to estimate M_{BH} when more than one line was present, we selected the one with higher S/N (if the corresponding fit was acceptable). We obtained black hole masses for 113 sources in our sample with reliable SED fitting. Sixty of these masses were obtained using SDSS data, 43 from MMT and 10 from DEEP2.
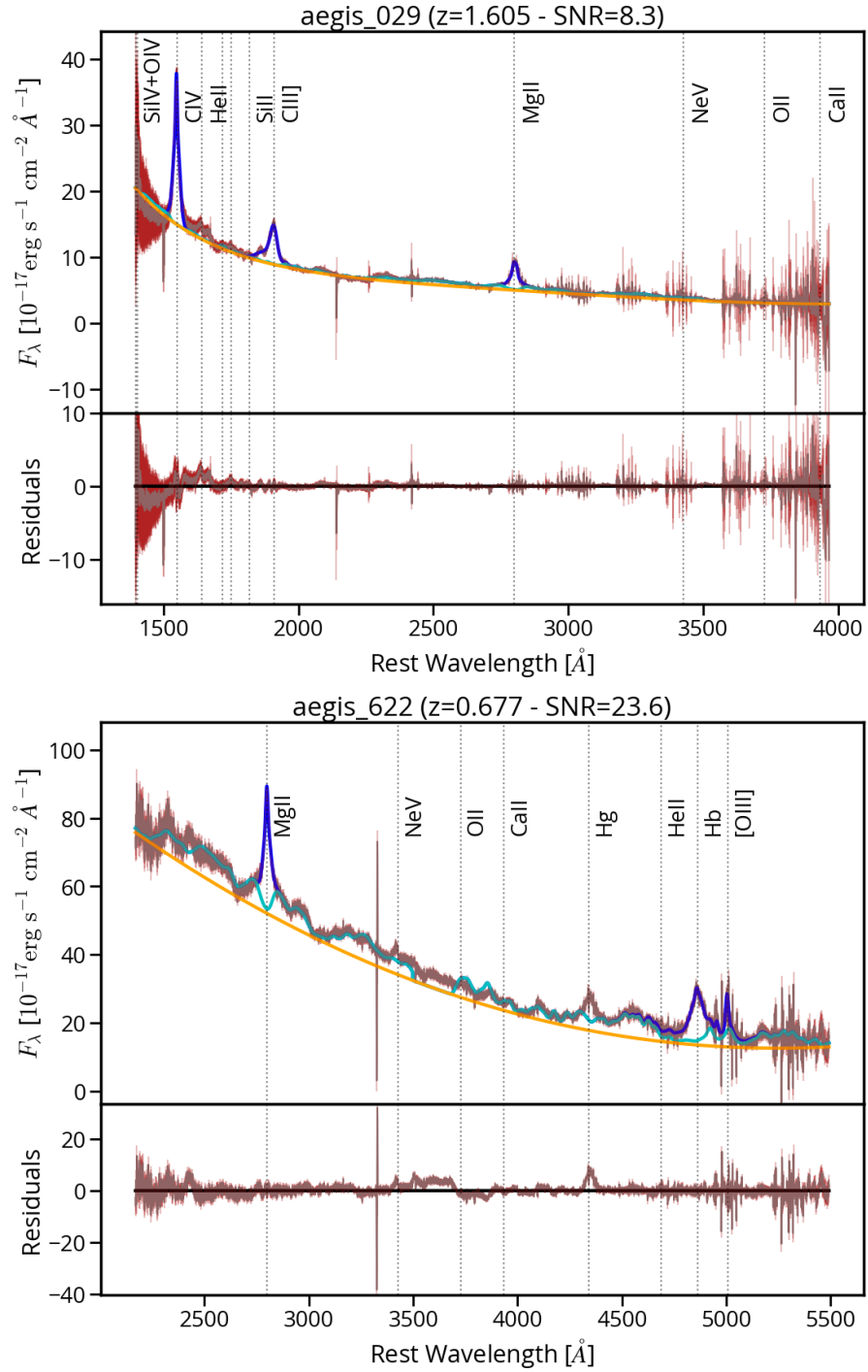
Figure 4.12: Examples of spectral fits using PyQSOFit, and their residuals. On gray, the spectra observed at rest-frame wavelength. The continuum was fit as a polynomial, shown in orange. On cyan, the Fe emission. On blue, the emission lines fitted in the process to obtain FWHM of the BLR.

As a sanity check, we compared our black hole masses with those obtained by Rakshit et al. (2020) for the 88 sources in common, as illus-
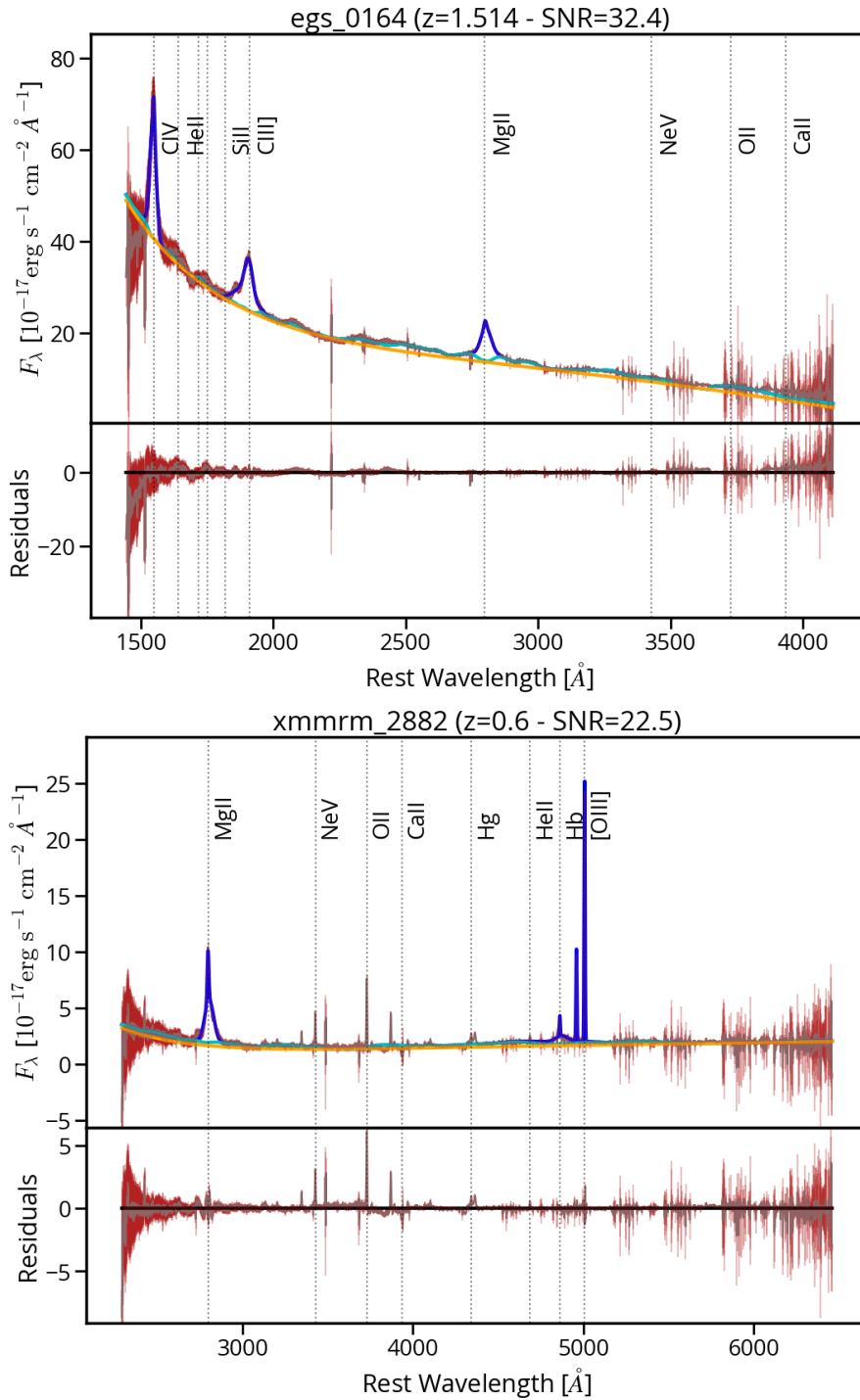
Figure 4.13: Same as Fig. 4.12

trated in Fig. 4.14. No systematic shift is evident between our masses and theirs. Discrepancies for certain sources could be attributed to differences in the fitted spectra; while they utilize the best SDSS spectra, we use SDSS stacked spectra or, if the signal-to-noise ratio was higher, spectra from a different epoch were obtained with MMT. Since our work incorporates stacking and includes spectra from other telescopes,

we were able to derive black hole masses for more sources in our sample.
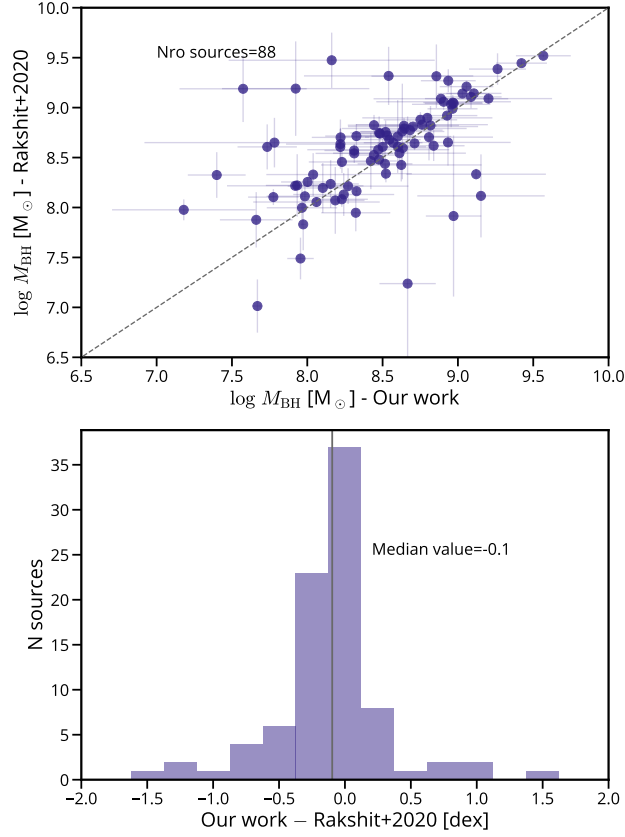
Figure 4.14: Upper panel: Comparison between our estimation of the black hole masses and the ones estimated by Rakshit et al. (2020) for the 88 sources in common. Bottom panel: Histogram of the logarithmic difference of the BH masses.

An alternative method for obtaining spectra-independent black hole masses involves directly measuring the broad lines from the J-spectra. Chaves-Montero et al. (2022) explored this approach with promising results compared to Rakshit et al. (2020). While this technique holds potential for extensive applications in future J-PAS work, its current limitations are sources brighter than $r < 21$ and $M_{BH} > 10^8$ M$_\odot$.

4.4 DISTRIBUTION OF PHYSICAL PARAMETERS

Until now, we have recovered reliable values of properties for 308 AGN and their host galaxies from SED fitting. We also estimate M_{BH} for a subsample of 113 sources. In this section, we show the distributions of these properties and the derivation of additional parameters that depend on them.
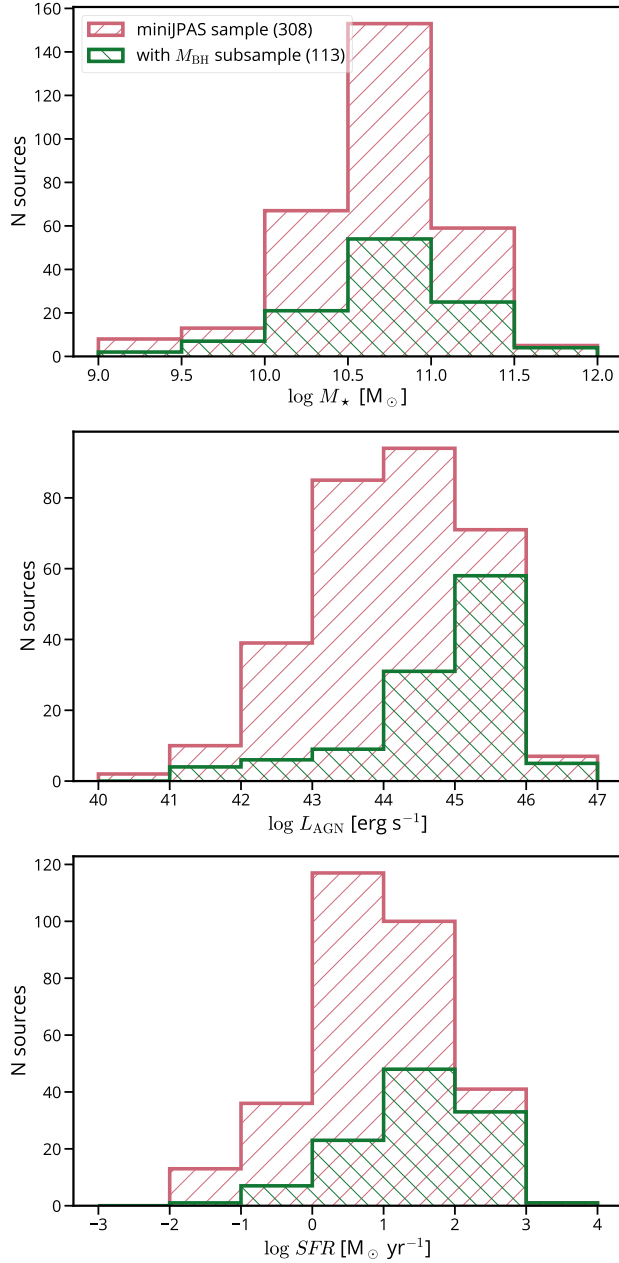
Figure 4.15: Histograms of the physical parameters estimated with the SED fitting ($M_\star$, L_{AGN} and SFR). In red is the full sample while in green is the subsample with an estimation of M_{BH} using the corresponding spectra.

The values derived for individual sources can be found in Table 4.6. In Fig. 4.15, we show the distributions of $M_\star$, SFR, and L_{AGN} for the entire sample of 308 miniJPAS sources for which these parameters have been derived (red) and the subsample of 113 sources for which we also have a reliable measurement of M_{BH} (green). While the distribution in $M_\star$ is very similar for the two samples, the subsample with measured BH masses is biased toward higher L_{AGN} and SFR.

ID	$\log M_\star$	SFR	$\log M_{BH}$	$\log L_{AGN}$	BHAR	$\log \lambda_{Edd}$
(1)	(2)	(3)	(4)	(5)	(6)	(7)
aegis_019	10.06 ± 0.26	6.73 ± 3.98	-	43.60 ± 0.55	-	-
aegis_021	11.37 ± 0.19	134.60 ± 174.72	-	46.25 ± 0.08	-	-
aegis_022	11.10 ± 0.22	124.05 ± 50.57	-	45.22 ± 0.05	-	-
aegis_029	10.39 ± 1.28	37.11 ± 29.93	8.48 ± 0.18	45.80 ± 0.05	1.11	-0.80
aegis_032	10.93 ± 0.22	5.36 ± 0.72	-	45.26 ± 0.18	-	-
aegis_035	10.31 ± 0.12	1.21 ± 0.27	7.77 ± 0.38	43.10 ± 0.41	0.05	-2.78
aegis_036	10.75 ± 0.25	7.63 ± 4.55	8.48 ± 0.01	44.55 ± 0.23	0.66	-2.04
aegis_037	10.26 ± 0.26	72.46 ± 7.58	7.78 ± 0.17	45.07 ± 0.06	0.21	-0.82
...	...	...	...	...	...	...

Table 4.6: Physical properties of the galaxies in the entire sample of 308 galaxies. (1) id used in this work, (2) stellar mass in $M_\odot$, (3) star formation rate in $M_\odot\,yr^{-1}$, (4) black hole mass in $M_\odot$, (5) AGN accretion luminosity in $erg\,s^{-1}$, (6)black hole accretion rate in $M_\odot\,yr^{-1}$, (7) Eddington ratio. The complete table can be accessed online at Vizier.

To quantify the difference, we performed a Kolmogorov-Smirnov test to check the null hypothesis that the subsample was drawn from the same probability distribution of the larger sample. We obtained a *p-value* smaller than 1% for L_{AGN} and SFR. While we cannot discard the null hypothesis for the $M_\star$ (*p-value* ~ 0.88), we can say our subsample shows a bias toward high values of L_{AGN} and SFR. The origin of this bias could be ascribed to the fact that it is easier to obtain well-defined spectra for more luminous sources, which in turn are powered, on average, by more massive black holes, possibly hosted in more gas-rich galaxies.

4.5 DISCREPANCIES BETWEEN EDDIGTON RATIOS AND PROXIES

We derived estimates of the Eddington ratios, which is a fundamental parameter for constraining BH cosmological evolution (Section 4.1), for the subsample of 113 sources with BH mass estimates based on BLR widths. The distribution of λ_{Edd} for this subsample is shown in the upper panel of Figure 4.16. This distribution shows a clear peak at around $\lambda_{\mathrm{Edd}} \sim 0.1$, with a steep fall off at larger Eddington values, and a slightly less abrupt one at lower Eddington ratios.

The Eddington ratio distribution of our sample is significantly different from those in other works (Vestergaard and Osmer, 2009; Lusso et al., 2012; Nobuta et al., 2012). In particular, we compared our results with Lusso et al. (2012) because both samples were X-ray selected, and physical properties were estimated using similar methods (SED and broad-line fitting). The Eddington ratio distributions differ by 0.5 dex (median) and 0.7 dex (mean). This discrepancy is likely due to a combination of selection effects and differences in the estimation of L_{AGN} in each study. Both samples are comparable in L_{X}, but the optical spectra analyzed in Lusso et al. (2012) are deeper than ours, reaching fainter magnitudes. Additionally, their estimation of L_{AGN} includes the bolometric AGN emission from 1 μm to 200 keV, whereas in our case, L_{AGN} corresponds solely to the integrated accretion disk luminosity (`agn.accretion.power` in CIGALE).

The integrated accretion disk luminosity is calculated as the intrinsic AGN disk luminosity averaged over all directions, excluding the torus and polar dust reemission. This accretion power provides a more suitable estimate for the Eddington ratio. However, it may show some disagreement with previous results, as the AGN bolometric luminosity is commonly used in the literature to derive Eddington ratios. In our sample, we observed a difference of 0.3 dex when comparing our L_{AGN} with the higher values of bolometric AGN luminosity (`agn.luminosity`) calculated from CIGALE, which includes all the AGN reemission.

For completeness, following other works in the literature (e.g., Aird et al., 2018), we also compute distributions using alternative measurements of the Eddington ratios, namely λ_{sBHAR}, defined as:

$$\lambda_{\mathrm{sBHAR}} = \frac{k_{\mathrm{bol}}\, L_{\mathrm{X}}}{1.3 \times 10^{38}\ \mathrm{erg\ s}^{-1} \times 0.002 \frac{M_\star}{\mathrm{M}_\odot}}.$$

For comparison, we adopt k_{bol} as 25. We note that in this case we can include all sources from our AGN sample as λ_{sBHAR} does not rely on BH mass measurements. This rate is defined as $\lambda_{\mathrm{sBHAR}} \approx \lambda_{\mathrm{Edd}}$ using the strong hypothesis that the mass of the SMBH scales directly with the total stellar mass of the host galaxy, with $M_{\mathrm{BH}} \sim 0.002\,M_\star$ (Marconi and Hunt, 2003; Aird et al., 2018). However, an important caveat is that this relationship is actually between the bulge stellar mass and the BH mass. While for the most massive galaxies, $M_\star^{\mathrm{bulge}}$ is approximately equal to $M_\star$, at lower masses and/or higher redshifts, this may not hold true.

We illustrate the λ_{sBHAR} for the entire miniJPAS X-ray sample (depicted by the red histogram) and for the subsample with a measured BH mass (illustrated by the green histogram) in the bottom panel of Fig. 4.16. A noticeable difference emerges between λ_{Edd} and its proxy λ_{sBHAR}, with the latter being approximately 0.6 dex larger. A Kolmogorov-Smirnov test comparing these distributions yields a *p-value* below 1%, strongly suggesting significant differences between the distributions. This raises concerns about the actual suitability of λ_{sBHAR} in constraining BH accretion rate models. A recent study by Mountrichas and Buat (2023) also discovered scatter between λ_{Edd} and its proxy λ_{sBHAR} in other AGN samples, emphasizing the need for caution when using the former as a proxy.

Although these two rates are conceptually similar, a striking disparity is evident in our sample. The pronounced difference can be attributed to the substantial assumption required to derive a λ_{Edd} without a measured BH mass, particularly given the significant scatter observed in our sample for the M_{BH}–$M_\star$ relation. In Section 4.6, we discuss into the nature of the scaling relation within our selection and explore its potential evolution across cosmic times.

4.5.1 SMBH mass accretion rates

In Section 4.1, we mentioned the importance of obtaining BHAR distributions. This rate in physical units ($\dot{M}_{\mathrm{BH}}$) can be derived starting from the AGN accretion luminosity (L_{AGN}). This is possible by assuming a proportionality between $L_{\mathrm{AGN}} \propto \dot{M}_{\mathrm{BH}}/\dot{M}_{\mathrm{Edd}}$, for all Eddington ratios (λ_{Edd}). Given that we have an estimate of M_{BH}, we followed Merloni (2004) and adopted a broken power-law, connecting the low accretion rate (radiatively inefficient) regime with the high
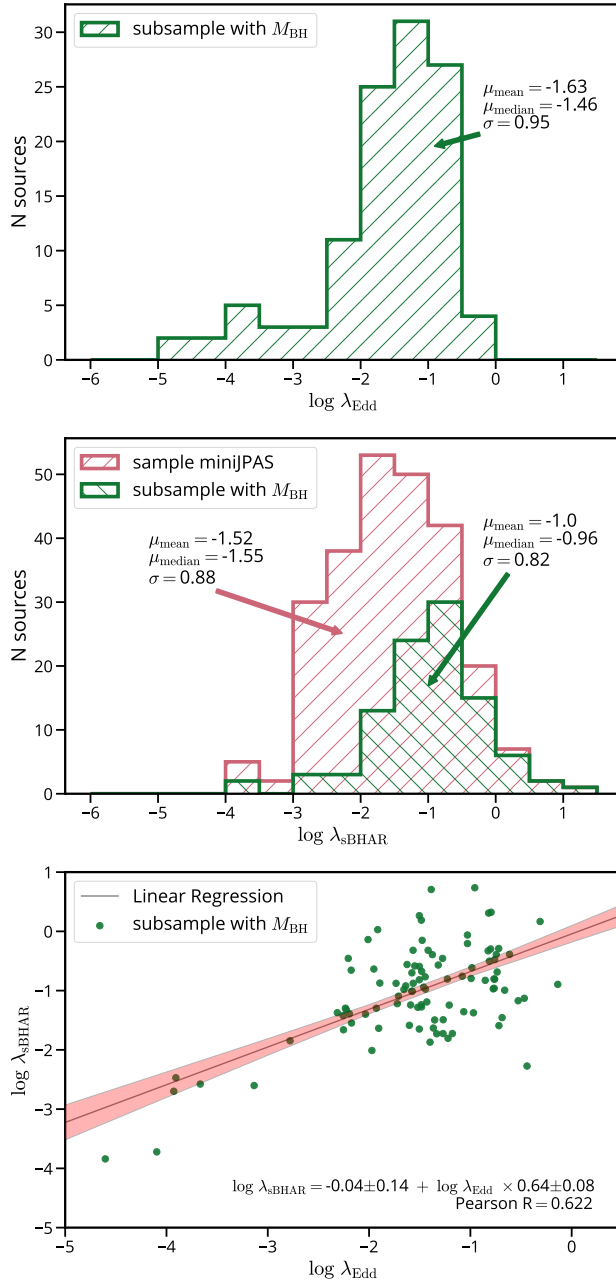
Figure 4.16: Upper panel: Histogram of Eddington accretion ratio (λ_{Edd}) for the sources with measured M_{BH}. Middle panel: Histogram of the specific accretion rate (λ_{sBHAR}, typically used as a proxy of λ_{Edd}), for both the sample with measured BH masses and the full miniJPAS sample. A difference in the shape of distributions can be seen for the subsample with measured BH masses by comparing the green histograms in the upper and middle panels. Lower panel: Plot of the relation between λ_{sBHAR}–λ_{Edd}. While they are defined to be equal, we found a poor correlation value and a systematic shift from the 1:1 relation in their linear regression (plotted as gray with 1-σ uncertainties in pink).

accretion rate one. The break is given at $\lambda_{crit} = 3 \times 10^{-2}$ (Merloni, 2008). Imposing continuity at λ_{crit}, yields the following equation:

$$\dot{M}_{BH} = \begin{cases} \dfrac{L_{AGN}}{\eta c^2} & \text{if } \lambda_{Edd} \geq \lambda_{crit} \\[3ex] \dfrac{\sqrt{\lambda_{crit} L_{AGN} L_{Edd}}}{\eta c^2} & \text{if } \lambda_{Edd} < \lambda_{crit}, \end{cases} \tag{4.1}$$

where η is the radiative efficiency, assumed as 0.1.
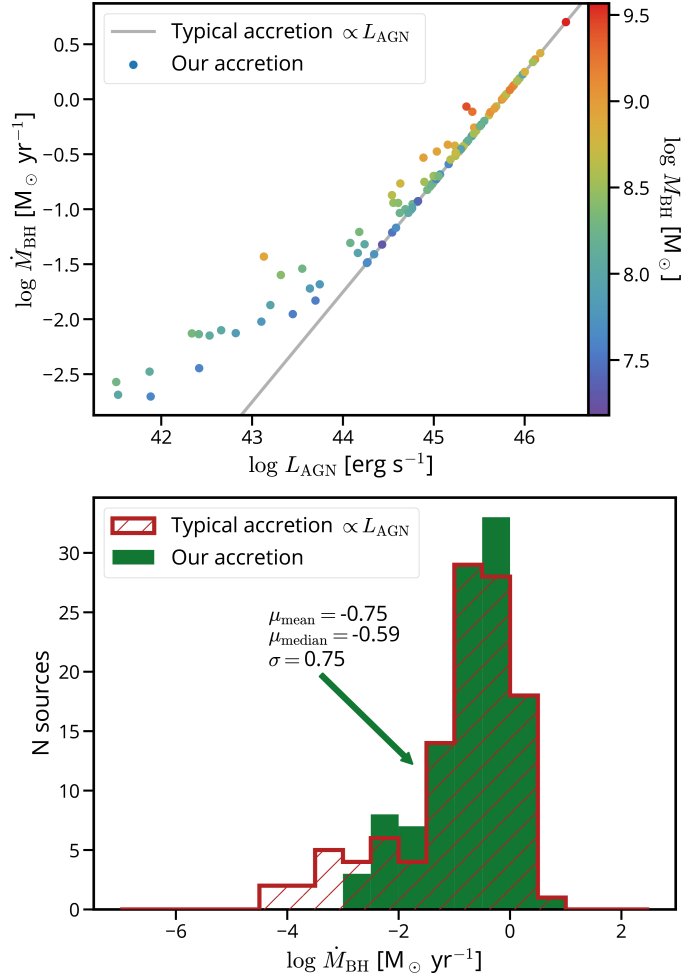
Figure 4.17: *Upper panel:* Accretion rate derived from Eq. (4.1) against L_{AGN} and color-coded with M_{BH}. The solid line is the typical accretion rate assuming a linear dependence with L_{AGN}, and it is equal to our accretion for sources with $\lambda > \lambda_{crit}$. *Lower panel:* Histogram of the accretion rates.

We applied Eq. (4.1) to derive the BHAR in physical units for our sources with measured M_{BH}. Figure 4.17 shows $\dot{M}_{BH}$ as a function of the AGN luminosity, color-coded by BH mass and the distribution of $\dot{M}_{BH}$. The shape of the distribution for higher values is, as expected,

similar to the distribution of λ_{Edd} (see Fig. 4.16). For lower values, it is less steep than λ_{Edd}, as a consequence of the change in the accretion regime. It is also less steep than a distribution derived from $\dot{M}_{\mathrm{BH}} \propto L_{\mathrm{AGN}}$, with a $\sigma = 0.75$ instead of $\sigma = 0.95$.

With Eq. (4.1), we recovered the change in the accretion mode, obtaining higher values of $\dot{M}_{\mathrm{BH}}$ than the typical accretion (as seen in both panels of Fig. 4.17). Our $\dot{M}_{\mathrm{BH}}$ also shows similar correlations with SFR as Delvecchio et al. (2015) and Masoura et al. (2018), even with the two regimes.

4.6 SCATTER ON THE SCALING RELATION

In the previous sections, we derived reliable stellar and BH masses for 113 miniJPAS sources with $z < 2.5$. These two quantities are compared, with the associated uncertainties, in the upper left panel of Figure 4.18. For reference, we also included the relation $M_{\mathrm{BH}} = 0.002\,M_\star$ used to define λ_{sBHAR} and based on Marconi and Hunt (2003). We also plot the local scaling relation derived by Shankar et al. (2020), based on the BH masses measured from the velocity dispersions from Savorgnan et al. (2016). Since the methods of measuring masses can have biases due to, for example, the spatial resolution of the instrument used, we also included an unbiased relation proposed by Shankar et al. (2016). Finally, we included the parametrization obtained by Georgakakis et al. (2021), where they presented an empirical model for BH populations in large cosmological volumes.

Our sample does not follow any of the local relations closely. Overall, a correlation between $M_\star$ and M_{BH} is not statistically significant, with a Pearson correlation coefficient of only ~ 0.3. This study is not the first to find overmassive BHs compared with the local M_{BH}–$M_\star$ scaling relation. For instance, Ding et al. (2020) studied a sample of AGN between $1 < z < 2$, and they found M_{BH} almost three times more massive than those predicted by typical local M_{BH}–$M_\star$ relations. Selection effects may also contribute to the observed discrepancies. For example, requiring spectroscopic redshifts and measurable M_{BH} could bias the overall BH mass distribution towards higher values. Additionally, flux-limited samples may favor actively accreting BHs, playing a role in these discrepancies.

Merloni et al. (2010) obtained stellar and black hole masses, and their SFR and BHAR for a sample similar in size (~ 100) of X-ray-selected AGN at $z \sim 1.2$. They showed that assuming constant rates for star formation and BH accretion, an evolution of the sources over 300 Myr reduces the scatter of the relation, moving the sources' positions in the M_{BH}–$M_\star$ plane closer to the local scaling relations. Thanks to our comprehensive multiwavelength analysis, we also have reliable estimates of the SFR and BHAR for all the sources in our sample,

allowing us to apply a similar method to study the possible influence of co-evolution on this scatter in the scaling relation.
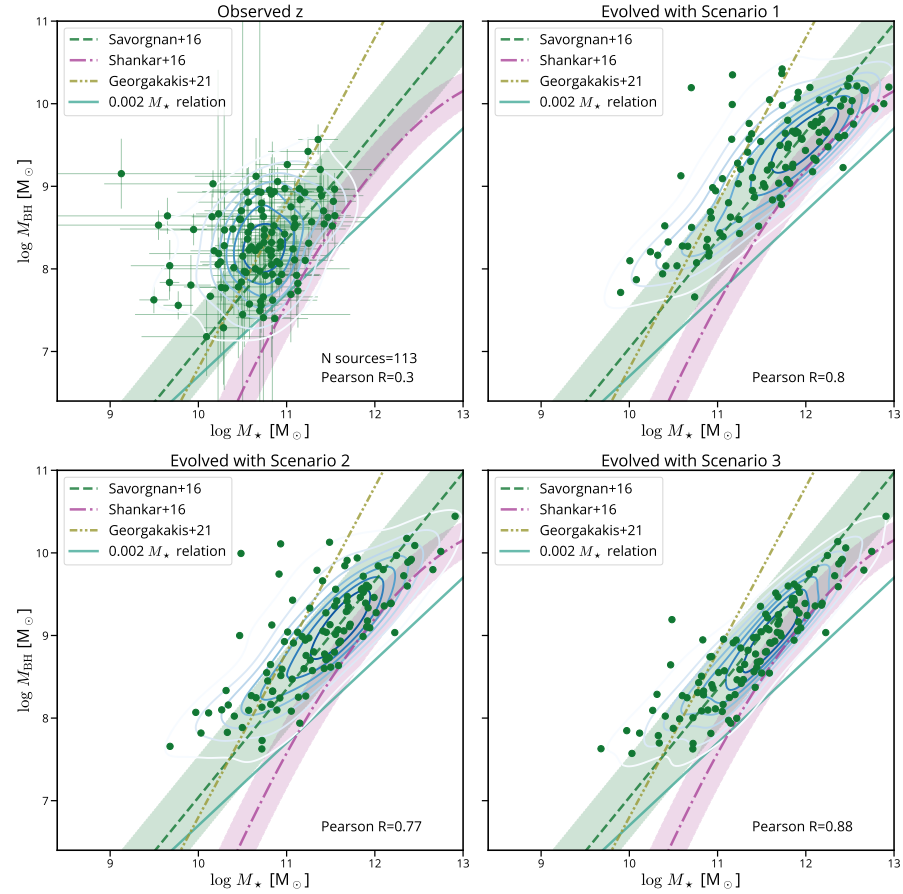
Figure 4.18: *Upper left panel:* The observed M_{BH}–$M_\star$ relation for all the **113** sources in our sample, at the observed redshift. Green solid dots are the value of masses for each source, with associated uncertainties, while contours are the distribution of these dots. In all panels, we show the expected local M_{BH}–$M_\star$ scaling relations: in turquoise the 0.002 $M_\star$ from Marconi and Hunt (2003); in green the relation from Savorgnan et al. (2016) with uncertanties at 1-σ; in purple the unbiased version from Shankar et al. (2016) with uncertainties; and in brown the parametrization by Georgakakis et al. (2021). The other three panels show the forward modeling of our sources to $z = 0$ using different methods. *Upper right panel:* the most basic model, with constant rates (Scenario 1). *Lower left panel* the model with a variable rate following the SFH (Scenario 2). *Lower right panel* the model with a variable rate following the SFH and the energy limit for the black hole accretion (Scenario 3). See Section 6 for details. We also show the number of sources and the Pearson correlation value on each bottom right corner.

A simple constant model for the rates can be a valid assumption for evolution within short times (like nearby sources). Still, a constant value of SFR across longer times is likely an oversimplification. In fact,

a galaxy will increase its stellar mass during its lifetime following an SFR that is not constant, and that depends on the gas reservoir and its cooling time. This reservoir change over time by the effect of, for example, supernova, AGN feedback, and/or mergers (Granato et al., 2004; Lapi et al., 2006; Monaco et al., 2007; Fontanot et al., 2020). A similar situation occurs for the SMBH mass. There are hints pointing out that the BH accretion rate shows a similar trend as the one observed in the star formation up to the peak epoch of galaxy-AGN coevolution ($z \sim 3$, e.g., Madau and Dickinson 2014; Aird et al. 2015). Nevertheless, this evidence is valid only for active black holes, where the accretion can be measured. To take into account the AGN duty cycle (Hickox et al., 2014), a more complex approach is necessary, based on continuity equation approximations (e.g., Small and Blandford, 1992; Shankar et al., 2013), as well as direct measurements of average BH accretion rates across large samples of active and inactive galaxies (e.g., Yang et al., 2018; Carraro et al., 2020).

We applied these basic ideas and performed forward modeling of our source properties to estimate the host galaxy stellar and BH masses that each source will have at $z = 0$, assuming an isolated evolution (merger-free). While mergers can be the main triggering mechanism of AGN activity for luminous sources (Treister et al., 2012; Goulding et al., 2018; Gao et al., 2020), observational studies and simulations suggest that mergers are not the dominant source of BH growth globally (Aversa et al., 2015; Steinborn et al., 2018; McAlpine et al., 2020), and even galaxies without major mergers since $z \sim 1$ follow the M_{BH}–$M_{\star}$ relation (Martin et al., 2018). In any case, while our isolated evolution does not include the possibility of mergers, the measured accretion rate can be the result of a previous interaction of the host galaxy with their surroundings.

We considered three different evolving scenarios to model the late evolution of BHs and their host galaxies down to $z = 0$: (1) constant growth, (2) variable growth, and (3) variable growth with an energy limit. Each model starts from the values of $M_{\star}$ and M_{BH} measured at the observed z and from the estimated instantaneous rates (SFR and BHAR). Then, using a time step of 100 Myr, the model predicts the increment for both masses for each bin in time.

In the *first scenario* (Scenario 1), we assume constant rates across time, equal to the measured SFR and BHAR at the redshift of the sources, extending up to $z = 0$. This approach mirrors the method used in Merloni et al. (2010). It is important to note that this is the simplest assumption and may lead to somewhat overestimated masses.

The *second scenario* (Scenario 2) incorporates an evolution for both rates. For the SFR, we follow the SFH derived from the SED fitting. Instead of using analytical law for the BH growth (like Bondi accretion) and modeling the BH feedback, we choose a more straightforward approach. Silverman et al. (2008), Madau and Dickinson (2014), and

Aird et al. (2015) show that SFR density is related to the BHAR until $z = 3$ for active galaxies, obtaining the BHAR from the X-ray luminosity function for AGN. Newer studies, like Yang et al. (2018) and Carraro et al. (2020), show that this average relation is also valid for samples in different stages of their duty cycle (detected and not detected in X-ray). Since all this evidence suggests that the SFR's shape is similar to BHAR at least until $z = 3$ (Aird et al., 2015), we used the τ-delayed model of SFH of each source to obtain their BHAR at each time step. To scale the BH accretion history, we used the observed value of BHAR at observed z.

The *third scenario* (Scenario 3) is similar to the second one, but a simple energy budget limits the BHAR. The BH is temporarily switched off if the total energy released by the AGN is larger than the gravitational binding of the host galaxy. This approach emulates a duty cycle and gives each source the possibility of periods of non-nuclear activity while the SF continues. While the shape of the relation is similar in studies for galaxies with diverse duty cycles (Yang et al., 2018) and for only active galaxies (Aird et al., 2015), the peak of the average BHAR at $z = 2$ for AGN is three times bigger than the BHAD at $z = 0$. Our sources are X-ray detected, so the accretion activity is high at the observed z. Thus, using these BHARs to model the accretion across history (as in scenario 2) can produce overmassive BHs; considering a duty cycle is fundamental for the evolution of each source (not averaged). In other words, each source has an energy budget and an active BH for the zero time step (equal to the observed z). For the following time steps, if the energy limit allows it, the BH will be active, accrete, and follow the BHAR modeled (as scenario 2); if not, the BH will not have activity while the host galaxy will continue to form stars. This scenario better represents the normalization limits for the empirical BHAR-SFR relation for an X-ray-selected sample.

Examples of scenario evolution are presented in Figs. 4.19 and 4.20. While the stellar mass growth follows a simpler pattern, based on a constant SFR or following the SFH, the black hole mass growth can be more intricate. In Scenario 3, the BH mass build-up typically occurs at high redshift, and the accretion may pause at certain points in cosmic evolution until the galaxy forms stars, thereby increasing its gravitational binding and allowing the AGN to reignite.

For Scenario 3, we calculated the energy released by the AGN at each time, as $\dot{E}_{\mathrm{BH}}(t) = \eta \epsilon c^2 \dot{M}_{\mathrm{BH}}(t)$, where η is the radiative efficiency and ϵ is the coupling efficiency and represents the energy fraction that couples with the surrounding medium. We used $\epsilon = 0.1$ adopted as maximum value in Weinberger et al. (2017). This value is also representative of other feedback models (Harrison et al., 2018). For the gravitational binding energy, $E_{\mathrm{gb}}(t) = \frac{GM_{total}^2(t)}{r(t)}$, where r is a radius representative of the galaxy. We took it from the relation between $M_\star$-size from Ichikawa et al. (2012b). This relation is independent of
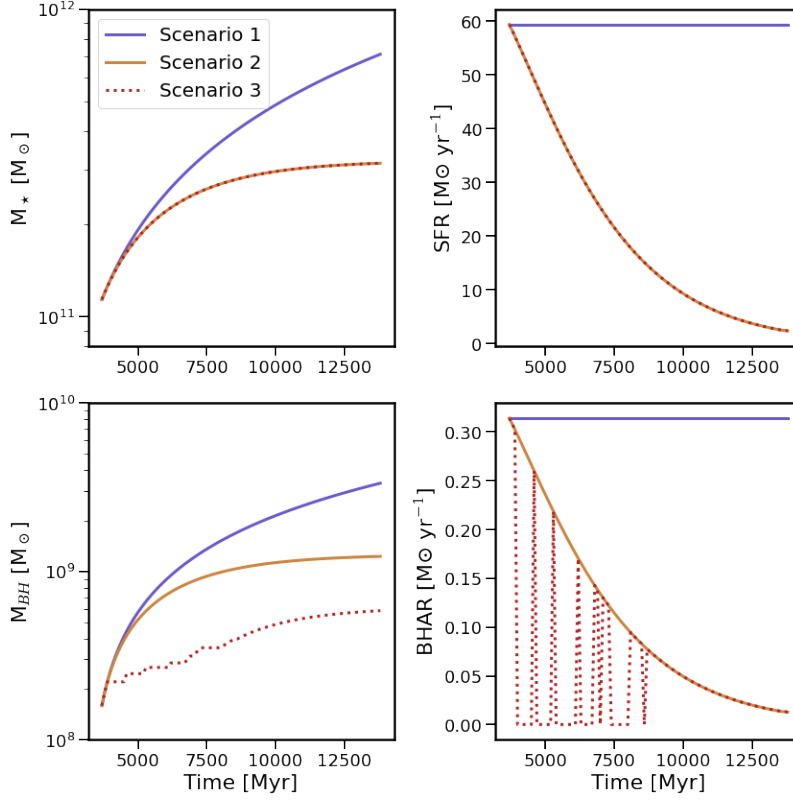
Figure 4.19: Different coevolution scenarios for selected sources. The first column displays the $M_\star$ (top) and M_{BH} (bottom) evolution with cosmic time for the different assumptions: a constant SFR (Scenario 1), the SFH derived from the SED fitting (Scenario 2), and imposing an energy budget for the BH (Scenario 3). The second column illustrates the SFH (top) and the black hole accretion history (bottom), with the solid blue line representing Scenario 1, the solid orange line representing Scenario 2, and the dashed red line representing Scenario 3. For some sources in Scenario 3, accretion pauses at certain moments in cosmic evolution until the galaxy forms stars, increasing its gravitational binding and allowing the black hole activity.

redshift and type of galaxy, and the radius is calculated for each bin in time. We used $r = r_{90}$ since it contained 90% of the light, and we are using all the source's light to estimate the $M_\star$. Because this, $M_{total}(t)$ takes into account the most massive components inside the r_{90}: $M_\star(t)$ and $M_{\mathrm{halo}}(t)$ up to that radius. Considering the initial $M_\star$, SFR and SFH, we calculated $M_\star(t)$ at each bin. For $M_{\mathrm{halo}}(t)|_r$, we used the $M_\star$–M_{halo} relation from Girelli et al. (2020). This M_{halo} is the total mass of the halo, so we used a Jaffe profile[11] and the total mass to recover the fundamental parameters of the halo mass distribution and integrate $M_{\mathrm{halo}}(t)|_r$. After all the energies are calculated, we checked

---

11 Other profiles with the same dependence were also tested, like the isothermal sphere, without significant changes. More variables are needed for more complex profiles, like the Einasto profile.
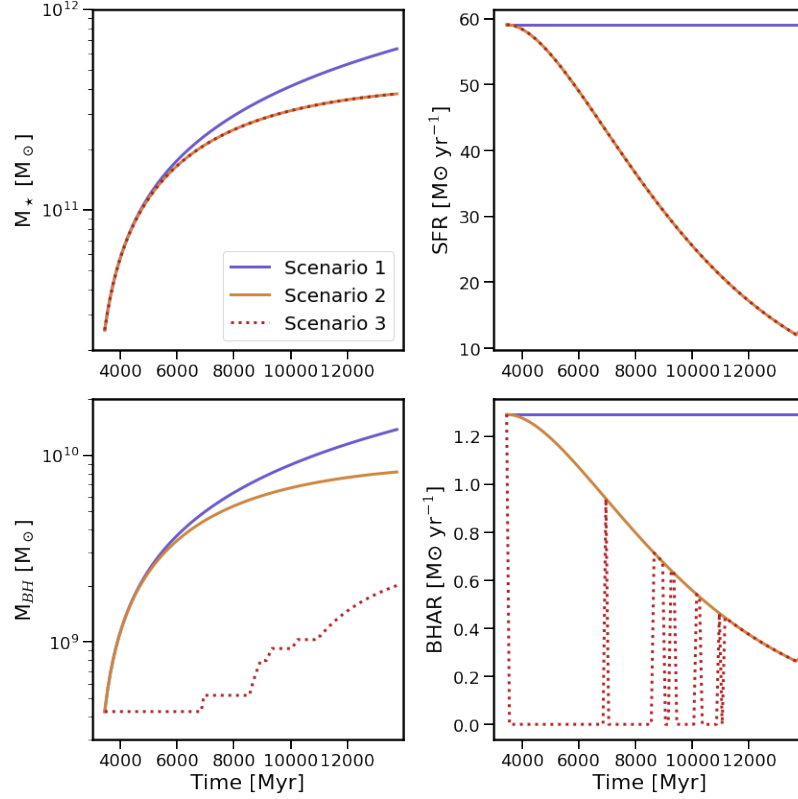
Figure 4.20: Same as Fig. 4.19.

for each bin in time if $E_{\mathrm{BH}}(t) \leq E_{\mathrm{gb}}(t)$. If the energy is below the limit, the BH can accrete, following an accretion history with the same shape as the SFH (mimicking a BHAR-SFR relation). If not, the accretion stops and remains zero for that time bin. BH accretion can start again if the stellar mass increases due to high SFR, thereby increasing the gravitational binding energy.

The results of the forward modeling in the three scenarios described above are shown in Fig. 4.18 (upper right, lower left, and lower right, respectively). We performed a linear fit of the M_{BH}–$M_{\star}$ relation evolved at $z = 0$, and in all three cases, the Pearson correlation coefficient factor increased substantially compared with the first panel.

With the simplest model (Scenario 1), the sources seem to follow a relation of 0.01 between masses, with a correlation factor of ~ 0.8. While this can be promising, the constant rates bring an estimate of $M_{\star}$ and M_{BH} considerably higher than those observed in the local Universe. While in the local Universe the highest values are $M_{\mathrm{BH}} \sim 10^{10}\mathrm{M}_{\odot}$ (Bennert et al., 2021) and $M_{\star} \sim 10^{12}\mathrm{M}_{\odot}$ (Karachentsev et al., 2013), we predict masses ~ 10 times higher.

Both BH and stellar masses distributions on the model following the Scenario 2 have slightly lower values than in Scenario 1. While $M_{\star}$ has values comparable to those observed in the local universe, M_{BH} keeps being too high.

The model with an energy limit for the BH accretion (Scenario 3) has the highest correlation coefficient factor (0.88) and masses closer to the local ones. Furthermore, our sample is closer to the dynamically measured relation (Savorgnan et al., 2016) and unbiased relation (Shankar et al., 2020) than the relation obtained from forwarding model (Georgakakis et al., 2021), with almost all its scatter inside the 1-sigma uncertainty of the dynamically measured relation. With this scenario, we show that imposing an energy limit on the BH decouples the link between rates for specific periods of their evolution being critical to reproduce the M_{BH}–$M_\star$ relationships. This limit is effortless to compute and still capable of lowering the BH masses at redshift zero, signaling that our simple assumptions are reasonable.

Neither of the three scenarios was very sensitive to small changes in how $\dot{M}_{BH}$ was derived. We ran them for the typical derivation $\dot{M}_{BH} \propto L_{AGN}$ without significant changes in the correlation values. We also applied the scenarios to 100 sets of different rates as a sanity check. We started from the same initial measured masses, but we evolved these sources with SFR, SFH, and L_{AGN} randomly sampled from a normal distribution centered in the mean value of our sample and with the same scatter. We found that for random samples, the evolution shows average correlation values significantly lower than our sample (~ 0.5). Therefore, for our forward modeling is essential to set actual input rates for each source and will not produce the same results for random samples.

The forward models explained in this Section are naive and straightforward by design since they are based on a short set of observational inputs. The principal limitation is not having information about the gas reservoir of the galaxy; thus, accretion and star formation do not have a limit depending on how much gas is available. In this sense, our models are just a higher limit of how much the galaxy and its SMBH can grow. Nevertheless, we compared our results with a more complex evolution model implemented in the Magneticum simulations[12]. Magneticum is a set of fully hydrodynamical cosmological simulations that can trace structures through cosmic time, with different resolutions and box volumes (details on Hirschmann et al., 2014; Teklu et al., 2015). In particular, we crossmatched our sources at observed redshift with the Magneticum/Box2, finding a similar stretch on the M_{BH}–$M_\star$ relation at lower redshift on the evolved sources at $z = 0$.

4.7 CONCLUSIONS

We studied the host galaxy and central BH properties of a sample of X-ray-selected AGN using narrow-band data from the miniJPAS

---

[12] http://www.magneticum.org

survey together with available multiwavelength data from UV to mid-infrared. We obtained robust parameters from SED fitting for 308 sources. We also measured BH masses from single-epoch spectra for a subsample of 113 sources. For this subsample, we provided reliable estimates of BH accretion rates and Eddington ratios. We also studied three different possible evolutionary scenarios for the subsample with BH mass estimates.

We summarize below the main results of our work:

1. The distribution of the Eddington ratio for our sample overgrows to lower values, peaking at $\lambda_{\mathrm{Edd}} \sim 0.1$, and decreasing toward $\lambda_{\mathrm{Edd}} \sim 0.0001$ (see the upper panel of Fig. 4.16). Since our sample is biased toward high-luminosity AGN, the distribution at $\lambda_{\mathrm{Edd}} < 0.01$ needs to be studied with complete samples down to a luminosity of 10^{42} erg s^{-1} in the future.

2. We found that the distribution of Eddington ratios is on average about 0.6 dex smaller than its commonly used proxy λ_{sBHAR} (see Fig. 4.16 for a comparison). This difference must be studied in detail and highlights the importance of using high-quality photometric and spectroscopic data to derive physical parameters of accreting black holes.

3. We derive accretion rates in physical units that depend on the expected radiative efficiency (see Eq. (4.1) and Fig. 4.17), using the estimated accretion luminosities and BH masses, obtaining less scatter than the accretion rates derived with a linear relation with L_{AGN}.

4. We do not find a correlation between the measured BH mass (M_{BH}) and the galaxy stellar mass ($M_{\star}$) for the sources in our sample (upper left panel in Fig. 4.18).

5. The fact that in our sample we measure overmassive BHs for their stellar masses compared to the local relations can be either ascribed to biases on L_{AGN} or to evolutionary effects. To test this second hypothesis, we applied forward modeling for our sources to the present time, considering three different scenarios for the growth history of both BH and host stellar masses. For all scenarios the M_{BH}–$M_{\star}$ relation streches toward $z = 0$.

6. We found that the scenario that uses the SFH measured from the SED fitting, the SFR-BHAR relation, and an energy limit on the BH accretion as main hypotheses would evolve the sources to a M_{BH}–$M_{\star}$ relation closer to the local one (see Section 4.6 and lower right panel of Fig. 4.18).

7. We cannot reproduce the diminution of scatter on the evolved M_{BH}–$M_{\star}$ from observed M_{BH} and $M_{\star}$ and selecting random

BHAR and SFR. Thus, the critical point is to start from the actual differential terms. Our evolution scenarios predict that sources below (above) the M_{BH}–$M_\star$ relation will experience faster (slower) BH growth compared to galaxy build-up.

8. The evolved M_{BH}–$M_\star$ relation is consistent with the main relations observed for the local Universe. Our model evolves the galaxy in an isolated way following an empirical relation and without invoking the presence of mergers. All of these may witness a physical connection between integral and differential properties of the host galaxy and their central BHs and are essential to reproduce observations in the local Universe.

9. The finding of "overmassive" and "undermassive" central BHs, compared with the M_{BH}–$M_\star$, do not imply that M_{BH}–$M_\star$ evolved with time. More evidence is needed to confirm the scatter being reduced across cosmic times to understand better the coevolution scenario.

This work also demonstrates the importance of having narrow-band, medium-deep photometry in the optical to characterize host galaxy properties of AGN at moderate to high redshift. With its full capability, J-PAS will increase orders of magnitudes the size of samples to shed more light in the framework of galaxy evolution studies.

Finally, we note that the biases of the present work depend mainly on the target selection bias for the cross-matched spectra and the relatively low number of sources in our sample, as a result of only a tiny fraction of the sky being covered by miniJPAS observations. In the future, combining extensive area X-ray surveys (like eROSITA, Predehl et al., 2021) with the more extensive coverage of the sky by J-PAS will allow us to repeat the study with a much larger sample and implement other statistical techniques to understand better the importance of the host parameters in the accretion ratios. Recovering the black hole masses from the J-spectra is also possible for the brighter, more massive sources, and an excellent photo-z estimation for AGN will allow us to study the coevolution scenario without needing a spectrum.

5 | A NEW SED FITTING MODULE TAILORED FOR THE LLAGN POPULATION

The temptation of unraveling the complete AGN population with SED fitting is undeniable. However, SED fitting is bound by its assumptions and a pre-defined grid, as thoroughly discussed in Chapter 3. There, we demonstrate that the prevalent approach involves employing a sum of power laws to model the accretion disk, resulting in AGN representations consistent with the paradigm of a standard accretion disk.

As already mentioned for the work presented in Chapter 4, biases are primarily ascribed to flux limit and area coverage. The upcoming JPAS data release is expected to address some of these limitations with a larger sample. However, neither larger works with SDSS (Rakshit et al., 2020) nor surveys with deep coverage of the local Universe like BASS (Koss et al., 2022b) can entirely overcome the limitations and biases imposed on Eddington ratios. Fig. 5.1 vividly illustrates the biases on Eddington ratios that are present for extensive surveys: the low log $\lambda_{\rm Edd}$ population (log $\lambda_{\rm Edd} < -2.5$) is hardly sampled in typical AGN surveys at moderate to high-z.

Understanding the AGN population below log $\lambda_{\rm Edd} < 3$ is challenging, partially because the luminosities can be contaminated by host galaxy emission in that regime. However, SED fitting is the ideal tool to deal with this type of contamination since it allows for the simultaneous fitting of both components. The main challenge arises from assumptions. Below log $\lambda_{\rm Edd} < -3$, the central engine is assumed to be radiatively inefficient, where the standard accretion disk may not be the only possible solution to accretion.

This chapter is based on recent work (López I.E. et al. "A tailored CIGALE module for Low-Luminosity AGN," submitted to Astronomy & Astrophysics), where we introduce a dedicated module for the CIGALE code, tailored explicitly for precise SED fitting of LLAGN. This module was thoroughly tested on a sample of 52 X-ray-detected local LLAGN, demonstrating its effectiveness in estimating AGN parameters, even in the presence of galaxy contamination. We will also discuss X-ray bolometric correction and spectral index correlations that our results predict for the low-luminosity regime. The enhanced code will provide the community with a robust toolkit to explore the lower-luminosity regime. This will enable the unveiling of hidden supermassive black holes at low accretion, capturing an AGN census and enhancing our understanding of the role of LLAGN in galaxy evolution.
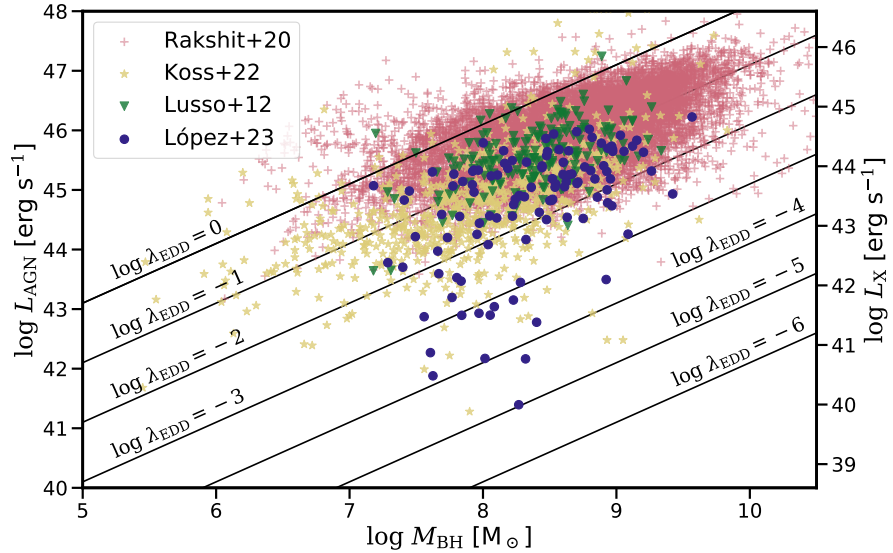
Figure 5.1: Bolometric AGN luminosity and its distribution with black hole mass. Solid lines represent various theoretical Eddington ratios. The SDSS data from Rakshit et al. (2020) is in pink. Yellow stars represent the data from the BASS survey (Koss et al., 2022b), and green triangles depict the Type I QSO from Lusso et al. (2012). In blue, the sources from López et al. (2023) and described in Chapter 4. On the right, an X-ray luminosity axis is provided for effortless comparison, assuming a bolometric correction factor of $k = 25$ (Aird et al., 2018).

5.1 INTRODUCTION

LLAGN can be defined as galaxies with X-ray luminosities less than 10^{42} erg s^{-1} and additional evidence of nuclear activity, such as AGN-like spectra (Ptak, 2001). This category often includes Low-Ionization Nuclear Emission-line Regions (LINERs, Ho, 1999). Seyferts, with generally higher luminosities, are typically categorized directly as AGN. However, exceptions exist, as seen in the case of low-luminosity Seyferts like NGC 1566 (Agüero et al., 2004). Behind these blurred boundaries, the community keeps debating whether LLAGN are downscaled versions of their brighter counterparts (e.g., Maoz, 2007) or whether they are dominated by different accretion physics (e.g., Ishibashi et al., 2014).

In the local Universe, LLAGN are more common than QSOs. The steep luminosity function of AGN suggests that LLAGN could be more prevalent at all redshifts than previously assumed, as indicated by various studies (e.g., Schawinski et al., 2009; Aird et al., 2012). Despite their prevalence, their nature is not fully understood due to lower luminosity compared to brighter AGN (Padovani et al., 2017; Hickox and Alexander, 2018). While AGN are known to significantly influence galaxy evolution through AGN feedback mechanisms, the potential role of LLAGN in galaxy evolution has not been fully elucidated.

LLAGN can hide compact jets and release kinetic energy through them (e.g., Fernández-Ontiveros et al., 2023). Unlike the massive jets observed in radio-loud AGN, the lower-power jets from LLAGN may remain confined within the host galaxy, substantially affecting the interstellar medium (ISM) and altering star formation processes (Mukherjee et al., 2018). LINERs can be radio-quiet or radio-loud, with low-accreting black holes that launch sub-relativistic and relativistic jets, respectively (Baldi et al., 2021b). Beyond kinetic feedback, winds from sustained radiatively inefficient accretion can also suppress star formation (Almeida et al., 2023). For instance, in the Sombrero galaxy, winds—driven either by radiatively inefficient accretion or by jets—induce outflows exceeding 1000 km/s (Goold et al., 2023). Chapter 6 will present in detail such a case, the LLAGN M58, where a radio jet confined to the host galaxy has a heavy impact on its ISM and affects star formation (Ogle et al., 2024).

Although these examples provide insights into the impacts on individual sources, as a collective, LLAGN might play a pivotal role in galaxy evolution, a role that is yet to be fully characterized. The high accretion phase of an AGN lasts only 5-10% of its duty cycle, with most of its cycle being in a low-accreting phase (Novak et al., 2011). Furthermore, local LLAGN may be the relics of previously high-accreting AGN. A comprehensive understanding of LLAGN properties and their evolution is vital for a thorough perspective on AGN and galaxy evolution.

While the luminosity definition of LLAGN allows for the possibility of high-accreting low-mass black holes, the local population of LLAGN generally exhibits low accretion rates ($\log \lambda_{\mathrm{Edd}} < -3$, Ho, 2009). The accretion process in LLAGN is to occur through a radiatively inefficient mode, where gas cannot efficiently radiate its thermal energy due to either low density or strong magnetic fields. This leads to lower radiative efficiency and a harder X-ray spectrum (product of the optically thin free-free emission), distinguishing them from higher-luminosity AGN. Additionally, LLAGN lack a big-blue bump associated with the blackbody radiation of the internal orbits of a thin accretion disk; instead, they show a red-bump (see Fig. 5.2, Ho, 2008).

As we discuss in Chapter 1, the exact mechanism driving accretion in LLAGN is still debated, with proposed models including hot, advection-dominated accretion flows (ADAF), adiabatic inflow-outflow solutions (ADIOS), and convection-dominated accretion flows (CDAF; for a review, see Yuan and Narayan, 2014). Additionally, standard accretion disks (geometrically thick, optically thin disks) truncated at an inner radius and hybrid models combining truncated disks with hot flows are considered plausible mechanisms (Taam et al., 2012; Bu and Yang, 2019). Clarifying the nature of the accretion flow in LLAGN is essential for understanding their evolution, fueling
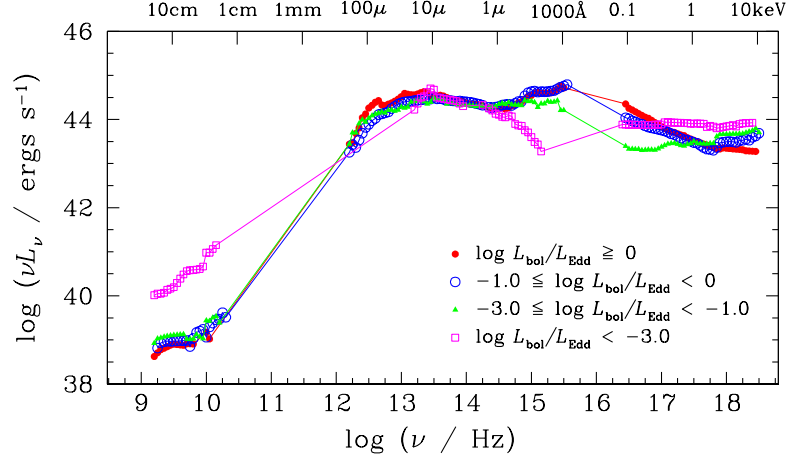
Figure 5.2: SEDs for radio-quiet AGN binned by Eddington ratio. The magenta line represents the LLAGN, which lacks the UV photons but shows a red bump in the IR. The SEDs are normalized at 1 micron. Credit: Ho (2008).

mechanisms, and the growth of supermassive black holes in the local universe.

The identification and characterization of LLAGN present challenges due to their lower brightness and potential contamination from star formation and X-ray binaries (e.g., Annuar et al., 2020). SED fitting, utilizing multiwavelength data, emerges as a powerful tool for addressing these challenges. We highlight in Chapter 3 that SED fitting can be used to disentangle different physical mechanisms at play from the AGN and its host galaxy, providing insights into accretion disk and dusty torus properties, as well as host galaxy characteristics such as SFR and $M_\star$. Crucially, SED fitting stands out as the optimal method for obtaining the AGN bolometric luminosities.

As we mention in Chapter 3, various SED-fitting popular codes are available and have recently been shown to yield similar distributions of general physical parameters (Pacifici et al., 2023). In particular, CIGALE leverages the wealth of information in multiwavelength data by incorporating related processes as priors in Bayesian fits (Boquien et al., 2019). The inclusion of the X-ray component in the AGN model, referred to as X-CIGALE, has expanded the capabilities of CIGALE Yang et al. (2020). X-CIGALE incorporates a power law emission to model the intrinsic hot corona emission based on the empirical relation for QSOs between X-ray at 2 keV and UV at 2500 Å (α_{ox}, Just et al., 2007; Lusso et al., 2010). However, in contrast to the L_{2500}–α_{ox} relation well-established for high-luminosity QSOs (e.g., Lusso et al., 2010),
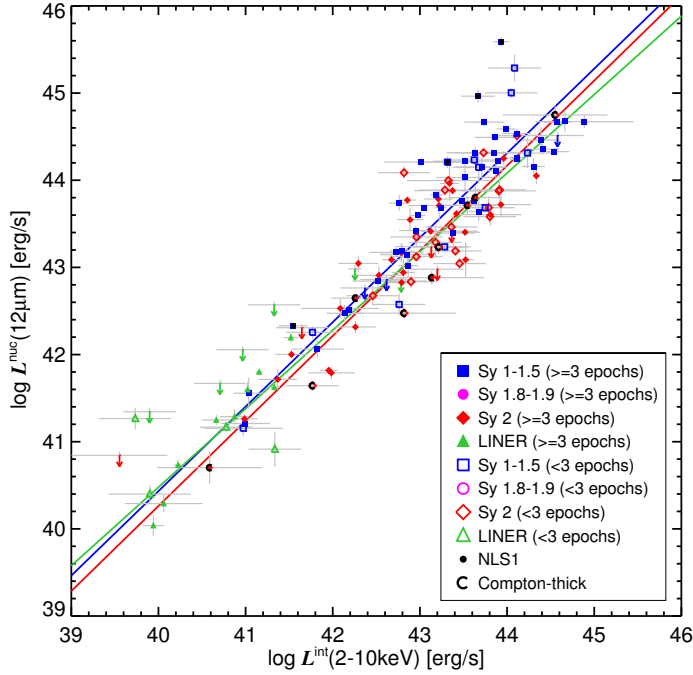
Figure 5.3: Relationship between the nuclear 12 microns and intrinsic 2–10 keV luminosities for different types of AGN. The blue, red, and green lines represent the best-fit relationships for type 1, type 2, and LINER, respectively. Credit: Asmus et al. (2015)

the relation for LLAGN remains elusive, perhaps due to intrinsic differences in the accretion process.

A promising avenue for investigating LLAGN is the L_X–$L_{12\mu m}$ relation, establishing a connection between intrinsic X-ray luminosity (2-10 keV) and the nuclear 12 micron luminosity, as shown by Gandhi et al. (2009). These emissions share a common bond since mid-infrared (MIR) emission is also reprocessed UV emission. The nuclear dust absorbs the emission generated by accretion and reemits it thermally in the IR. This relation has been systematically explored across various luminosity regimes and seems valid for Seyferts and LINERs in the luminosity regime $L_X = 10^{40}$–10^{45} erg s^{-1} (Asmus et al., 2015; Fernández-Ontiveros et al., 2023). Additionally, it has already been incorporated into SED fitting methodologies, providing an alternative approach to link X-ray emission with optical-IR emission (Duras et al., 2020).

This Chapter introduces a novel X-ray module into the widely utilized SED fitting code CIGALE. This module integrates two principal components: the L_X–$L_{12\mu m}$ relationship, employed as a prior, and a central accretion engine modeled as an ADAF, complemented by an optional truncated accretion disk. We apply this new module to an X-ray-detected sample comprising 52 local LLAGN, for which we obtain the X-ray intrinsic fluxes and the UV-to-FIR photometry. After validat-

ing our methodology with secondary AGN samples and comparing our findings for the LLAGN with those from previous studies, we analyze the X-ray bolometric correction, extending down to the lower limit of $L_{\text{Bol}} = 10^{39}$ erg s^{-1}. Furthermore, we address the issue of galaxy contamination, investigate α_{ox} parameter for LLAGN, noting deviations from QSO extrapolations, and assess the influence of LLAGN on star formation, comparing it with a sample of high-luminosity AGN.

This new CIGALE module provides a potent toolkit for probing the lower-luminosity regime, facilitating the study of supermassive black holes in states of low accretion, and is poised to augment future AGN censuses, thereby enriching our understanding of the role these LLAGN play in the evolution of galaxies.

5.2 THE CODE

5.2.1 Motivation

CIGALE is recognized as a powerful multiwavelength SED template fitting tool tailored for extragalactic research (refer to Chapter 3). It can accurately derive physical parameters spanning the X-ray to radio spectrum, meticulously accounting for dust attenuation in the UV-optical and its corresponding infrared re-emission via energy balance. This process involves fitting observed SEDs with a user-generated model library incorporating diverse physical templates. The likelihood distribution is computed using each fit, and a Bayesian-like analysis allows for extracting key physical parameters.

Notable enhancements to CIGALE were done by Yang et al. (2020) and Yang et al. (2022), particularly the integration of an X-ray module and the SKIRTOR AGN model (Stalevski et al., 2012, 2016a). The X-ray module employs the α_{ox}–L_{2500} relation from Just et al. (2007) as a foundational prior, bridging UV photons from the accretion disk with X-rays from the corona. This well-established relation for QSOs correlates the intrinsic AGN luminosity at 2500 with α_{ox}, the SED slope between 2500 UV and two keV X-ray bands, as modeled in a standard scenario where UV-optical photons are inverse-Compton scattered to X-ray energies (Haardt and Maraschi, 1991).

The SKIRTOR model encapsulates emissions from three AGN main components: the accretion disk, polar dust, and a clumpy torus. Notably, for the emission of the accretion disk—also referred to as the central engine or seed photons—CIGALE adopts a range of parametric disk models. This allows introducing a delta parameter (δ_{AGN}) to modulate the power-law slope within the 0.125 to 10-micron range. The details of the standard disk model with the parametrization of Schartmann et al. (2005) were discussed in Chapter 3.

CIGALE also includes an alternative accretion disk model based on the original SKIRTOR disk, improved to better reproduce with observational data (Feltre et al., 2012), maintaining a similar form to the model described above.

Despite its efficacy across a broad wavelength range and its substantial contributions to galaxy astrophysics, CIGALE's application to LLAGN reveals notable limitations. For instance, while Maoz (2007) observed similarities between LLAGN and QSOs, suggesting potential model applicability, divergences in accretion flow-dominated UV photon populations in LLAGN challenge the universal application of the α_{ox}–L_{2500} relation. The complex accretion physics of LLAGN continues to fuel debate, highlighting the need for tailored approaches rather than relying on universally applied relations.

Ho (2008) show fundamental discrepancies in LLAGN SEDs relative to QSOs, notably below $\log \lambda_{Edd} < -3$, characterized by a dominant red bump over the expected big blue bump. This discrepancy complicates the direct application of QSO models to LLAGN. Additional studies, such as Xu (2011), have explored the α_{ox}–L_{2500} relation for samples of Seyferts and LINERs, revealing certain similarities with established QSO calibrations. However, their determination of L_{2500} is through proxies derived from Hβ and B-band ($\sim$4420 Å) extrapolation. Even in models assuming LLAGN as scaled versions of QSOs, pure ADAF models deviate slightly from the L_{2500}–α_{ox} relation observed in QSOs (Maoz, 2007). Furthermore, Esparza-Arredondo et al. (2020) demonstrated that certain faint AGN deviate from the expected relation. Nemmen et al. (2014), through a physically motivated SED fitting, predicted an α_{ox} for LLAGN far from extrapolations of its high-luminosity counterparts, emphasizing the influence of radiatively inefficient accretion processes.

To overcome the challenges posed by the unique accretion physics of LLAGN, we propose a novel X-ray module (IRX) designed specifically for these sources. Recognizing the current uncertainties in their accretion physics and the need for a more customized approach, we propose two main changes: the seed photons from the central engine and the prior link of the X-ray emission to the rest of the SED.

Nonetheless, the current adaptation of this module introduces a critical caveat. Given that an ADAF has a considerable synchrotron emission it can also be observed in the radio and submillimeter (sub-mm) wavelengths, so careful consideration is required for another important component of the AGN framework: radio jets. Typically, radio jets are accounted for exclusively within radio frequencies for high-luminosity AGN. The radio module extends to the far-IR in CIGALE, modeling the synchrotron emission as a power law. This specificity enables the distinct determination of the spectrum slope, differentiating it from other sources, such as star-forming regions, modeled with another power law with a different slope.

However, the emission from radio jets spans the entire electromagnetic spectrum, not just the radio domain. This omnipresence can complicate SED fittings that omit their modeling, leading to potential contamination of SEDs intended to map the photon production by SMBH accretion processes. As highlighted by Nemmen et al. (2014), while the typical ADAF exhibits a SED characterized by distinct bumps, the average jet emission in LLAGN manifests as a softer, more constant output across the spectrum from 100 microns to X-ray wavelengths. This spectral behavior makes it impossible to fit without a constraint from the radio bands. Because of that, in this work, jet emission will be neglected in the X-ray to IR analysis. In future studies, we will incorporate the ADAF emission into the radio module of CIGALE, facilitating the differentiation between potential jet models and ADAFs. This development will allow for precisely fitting and identifying sub-mm and radio emissions in LLAGN, thereby excluding potential synchrotron interference in the broader spectrum. Such advancements will enable us to avoid possible synchrotron emission in the rest of the spectra and thus model the total emission from an AGN more accurately and better understand the role of jets in LLAGN activity.

5.2.2 The new module

We have introduced two main modifications to enhance the utility of CIGALE's AGN model for LLAGN.

Firstly, the modeling of seed photons emanating from the central engine has been refined by incorporating a combination of a truncated thin disk and an ADAF. The ADAF and its differences with a standard accretion disk were previously discussed in Chapter 1. In general, traditional accretion disks, characterized as geometrically thin and optically thick, generate an SED that is the sum of blackbody emission. In contrast, ADAFs are hot, optically thin solutions, quasi-spherical in shape, and their SED is produced by synchrotron radiation, Bremsstrahlung radiation, and inverse Compton scattering. A truncated disk emulates the blackbody spectrum like a standard disk but without the innermost and hotter orbits responsible for UV photon production. The details of the implementation are described in Section 5.2.2.1.

Secondly, we revisit the connection between the X-ray module and the UV-to-IR SKIRTOR model. The traditional α_{ox}–L_{2500} relation is replaced with an empirical L_X–$L_{12\mu m}$ relation (Asmus et al., 2015). This relation connects the intrinsic X-ray luminosity (2-10 keV) and the nuclear 12 micron luminosity. The details of this implementation are outlined in Section 5.2.2.2.

5.2.2.1 A new central engine

For the ADAF component, we parameterize the mean SED based on the ADAF template from Nemmen et al. (2014). This module employs a physically motivated code, considering a hot, geometrically thick, optically thin two-temperature accretion flow with primary radiative processes being synchrotron emission, bremsstrahlung, and inverse Compton scattering. Our parameterization is limited to the UV-to-IR bands, as different CIGALE modules address radio and X-ray. The parameterization is as follows:

$$
\lambda L_\lambda^{\mathrm{ADAF}} \propto
\begin{cases}
\lambda^{1.5} & 0.008 \leqslant \lambda \leqslant 0.075 \ [\mu\mathrm{m}] \\
\lambda^{1.15} & 0.075 < \lambda \leqslant 0.300 \ [\mu\mathrm{m}] \\
\lambda^{1.45} & 0.300 < \lambda \leqslant 1.1 \ [\mu\mathrm{m}] \\
\lambda^{0.95} & 1.1 < \lambda \leqslant 2.7 \ [\mu\mathrm{m}] \\
\lambda^{0.45} & 2.7 < \lambda \leqslant 20 \ [\mu\mathrm{m}] \\
\lambda^{-0.5} & 20 < \lambda \leqslant 100 \ [\mu\mathrm{m}] \\
\lambda^{-3} & 100 < \lambda \leqslant 1000 \ [\mu\mathrm{m}]
\end{cases}
. \tag{5.1}
$$

In Nemmen et al. (2014), the option of a truncated accretion disk just outside the ADAF is also considered. These truncated disks are crucial for modeling an IR-bump not present in the non-thermal continuum (for an example, see Sombrero galaxy in Fernández-Ontiveros et al., 2023). However, these two components are not independent, as they share bonding conditions with the ADAF. Furthermore, an external disk will reprocess the X-ray radiation produced by the ADAF. Fortunately, Nemmen et al. (2014) demonstrates that this effect is negligible, resulting in a SED identical to the standard disk. Building upon this, we separate both SED components and model the disk as follows:

$$
\lambda L_\lambda^{\mathrm{TDk}} \propto
\begin{cases}
\lambda^{6} & 0.08 \leqslant \lambda \leqslant 1.5 \ [\mu\mathrm{m}] \\
\lambda^{0.8} & 1.5 < \lambda \leqslant 3 \ [\mu\mathrm{m}] \\
\lambda^{-0.5} & 3 < \lambda \leqslant 10 \ [\mu\mathrm{m}] \\
\lambda^{-3} & 10 < \lambda \leqslant 1000 \ [\mu\mathrm{m}]
\end{cases}
. \tag{5.2}
$$

We have modified the δ_{AGN} parameter within CIGALE to introduce a scaling factor between a truncated disk and the ADAF continuum. With $\delta_{\mathrm{AGN}} = 0$, the central engine is represented solely as an ADAF. Conversely, increasing values of δ_{AGN} indicate progressively stronger emissions from the truncated accretion disk relative to the ADAF. Figure 5.4 showcases the SED comparison between the standard QSO accretion disk model from Schartmann et al. (2005), the mean ADAF SED delineated by Nemmen et al. (2014), and our new UV-to-IR parametrization implemented in CIGALE. This comparison highlights the impact of varying δ_{AGN} on the relative strength of the truncated
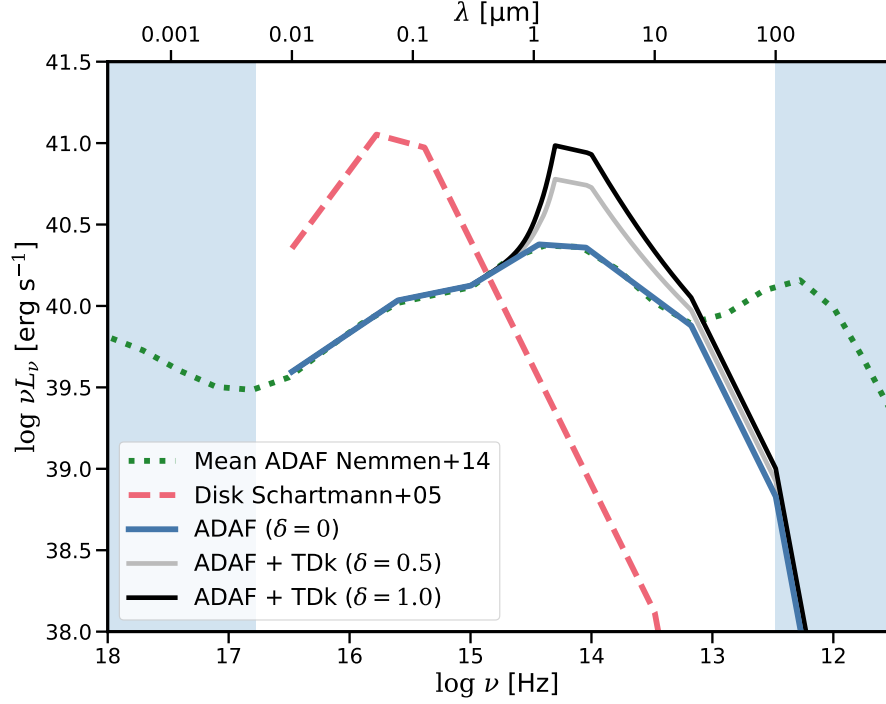
Figure 5.4: SED for different accretion modes. The dotted green line represents the mean ADAF from Nemmen et al. (2014). The solid blue line illustrates the pure ADAF as parametrized in our work. At the same time, black and grey indicate the effects of altering the δ_{AGN} parameter, which introduces a truncated accretion disk. For comparative purposes, the dashed red line depicts the parametrization by Schartmann et al. (2005), commonly used in CIGALE for QSOs with standard accretion disks. The blue-shaded regions denote the wavelength ranges where the other modules of CIGALE operate, specifically X-ray on the left and Radio on the right.

accretion disk within the total SED, illustrating the adjustable nature of our model in accommodating different LLAGN configurations. The total SED is given by:

$$\lambda L_\lambda^{Total} \propto \lambda L_\lambda^{ADAF} + \delta_{AGN} \times \lambda L_\lambda^{TDk} \tag{5.3}$$

This simplification allows the SEDs of both components to be managed independently, accommodating scenarios with and without a red bump.

5.2.2.2 A new way to connect X-ray to the SKIRTOR model

The decision to move away from the α_{ox}–L_{2500} relation is motivated by the lack of reliable calibrations for this relation in the low-luminosity regime. Given that this relation links photons from the accretion disk with reprocessed emissions in the X-ray spectrum,

changes in the UV photon population could significantly alter its calibration.

In contrast, the L_X–$L_{12\mu m}$ relation is based on a direct linkage between two different reprocessed photon types: X-ray and MIR. This relation has proven valid for a wide variety of AGN types, including Seyferts I, II, and LINERs, across five orders of magnitude up to $L_X \sim 10^{45}$ erg s^{-1}. Notably, this relation has been successfully utilized by Duras et al. (2020) for SED fitting, providing estimates of bolometric luminosity and corrections across various bands widely accepted in the field.

The L_X–$L_{12\mu m}$ relation is founded on the principle that UV-optical photons, originating from accretion physics, are reprocessed into X-rays by the corona and into IR by nuclear and polar dust. Interestingly, this relation appears unaffected by obscuration, exhibiting less than 0.1 dex differences between unobscured and highly obscured objects (Asmus et al., 2015). This stability is attributed to emissions from the polar outflow regions in the MIR and potentially higher covering factors in more obscured objects, which mitigate differences due to anisotropic viewing angles. This characteristic makes the relation particularly suitable for LLAGN, which, at low Eddington ratios, are believed to have high covering factors (~ 80–85% Ramos Almeida and Ricci, 2017). Mason et al. (2012) demonstrated the applicability of this relation to LLAGN using Spitzer data. Further validation is provided by Fernández-Ontiveros et al. (2023), who found that at sub-parsec resolution, all their LLAGN samples conformed to the L_X–$L_{12\mu m}$ relation as delineated by Asmus et al. (2015), confirming its broad applicability to LLAGN.

We implement this relation into the new X-ray module for CIGALE through the parameter α_{IRX}, defined as:

$$\alpha_{\mathrm{IRX}} = \log \frac{L^{\mathrm{int}}_{2-10 \text{ keV}}}{L^{\mathrm{nuc}}_{12\mu m}} \qquad (5.4)$$

We have set α_{IRX} with a default value of 0.3, allowing for a minimum value of 0.0 and a maximum of 0.6, with intermediate values possible. This choice is supported by the findings of Asmus et al. (2015), where the dispersion is measured at 0.33. The calculation of $L^{\mathrm{nuc}}_{12\mu m}$ in CIGALE considers the sum of the three AGN components (accretion disk, polar dust, and toroid), while $L^{\mathrm{int}}_{2-10 \text{ keV}}$ is derived from the power-law fit for the AGN component due to the intrinsic nature of X-ray data. We assume the relationship holds at low luminosities because even at low accretion rates, both processes will be similarly affected due to the scarcity of UV photons. As usual, potential host contamination from X-ray binaries and host galaxy dust emissions will be accounted for in the grid models for SED fitting.

These refinements aim to provide a more precise and customized modeling strategy for LLAGN within the CIGALE framework. The

code is accessible through the official CIGALE repository[1]. Although initially devised for CIGALE, the underlying concept is versatile and can be adapted for other computational frameworks. By addressing the existing model's limitations and uncertainties, we expect to enhance parameter accuracy and achieve a more authentic depiction of the physical phenomena occurring in LLAGN.

5.3 DATA AND FITTING

This section describes the two samples used to evaluate the new CIGALE module presented in this work. The primary sample discussed in Section 5.3.1 comprises 52 local galaxies classified as Seyferts and LINERs. This sample will assess the LLAGN properties and validate the module's performance in the low luminosity regime. A subset of the primary sample, with independent bolometric luminosities, will be used to test the module's specific validity in this regime. As a secondary sample (Section 5.3.2), we use the COSMOS and SDSS QSO samples employed in previous CIGALE studies. These sources will be used to confirm the validity of our analysis's higher luminosity regime of the L_X–$L_{12\mu m}$ relation, a key underlying assumption. Finally, Section 5.3.3 discusses the fitting methodology and goodness of the fit.

5.3.1 LLAGN Sample

We compiled a sample of 52 local galaxies, each featuring a central X-ray detection with luminosities falling below 10^{44} erg s^{-1}. Characterized by low accretion rates, as indicated by their Eddington ratios ($\log \lambda_{\mathrm{Edd}} < -3$), these galaxies are predominantly classified as radiatively inefficient accretion flow (RIAF) candidates. This classification suggests that the central engine might operate under a radiatively inefficient accretion mode (Ho, 2009). The calculation of Eddington ratios was primarily based on bolometric corrections from X-ray luminosities, adopting a $k_X = 15.8$ as per Ho (2009), or through SED fitting for each source, as detailed in studies by Eracleous et al. (2010) and Nemmen et al. (2014).

Most of these galaxies are located within 40 Mpc and exhibit a size of less than five arcmin in radius. They span a wide range of morphologies, with their Hubble types ranging from -5 to 5. The SMBH masses, as retrieved from the literature, predominantly fall within the range of $7 < \log M_{\mathrm{BH}} < 9$, though the sample includes several galaxies hosting less massive SMBHs. A comprehensive list of

---

1 The current version of this code is available on this branch: https://gitlab.lam.fr/cigale/cigale/-/tree/alpha_irx?ref_type=heads

the galaxies and their characteristics can be found in Table 5.1, with
the distributions of these properties depicted in Fig. 5.5.

ID	RA	DEC	Z	DIST	$\log L_{\mathrm{X}}$	REF
NGC1052	40.269	-8.2558	0.00496	19.19	41.20	2
NGC2273	102.536	60.8457	0.00613	29.76	40.89	1
NGC2685	133.894	58.7343	0.00295	13.26	39.00	2
NGC2655	133.909	78.2234	0.00467	23.82	41.20	2
NGC2768	137.906	60.0373	0.00451	22.07	39.73	1
NGC2787	139.826	69.2033	0.00232	7.41	39.20	1
NGC2841	140.511	50.9766	0.00211	14.51	38.94	1
NGC3031	148.888	69.0652	-0.00013	3.59	39.15	1
NGC3079	150.491	55.6799	0.00368	19.01	40.05	1
NGC3147	154.223	73.4007	0.00934	42.72	41.92	1
NGC3185	154.410	21.6883	0.00410	24.98	39.40	2
NGC3190	154.526	21.8326	0.00437	23.98	40.07	1
NGC3193	154.603	21.8940	0.00460	33.01	38.76	1
NGC3414	162.817	27.9750	0.00490	25.92	40.48	1
NGC3516	166.697	72.5685	0.00883	38.01	42.49	1
NGC3718	173.145	53.0679	0.00331	16.98	41.22	1
NGC3898	177.313	56.0843	0.00385	21.97	38.93	1
NGC3945	178.306	60.6755	0.00427	21.57	39.80	1
NGC3953	178.454	52.3266	0.00350	18.93	38.04	1
NGC3982	179.117	55.1252	0.00371	21.55	40.78	5
NGC4013	179.630	43.9468	0.00277	19.71	38.80	1
...	...	...	...	...	...	...

Table 5.1: Key properties of galaxies in the LLAGN sample. Distances are given in Mpc and X-ray luminosities in erg s^{-1}. The table includes references for the X-ray luminosities: 1 for Williams et al. (2022), 2 for González-Martín et al. (2009), 3 for Osorio-Clavijo et al. (2023), 4 for Yun et al. (2022), 5 for Kammoun et al. (2020), 6 for Cappi et al. (2006), and 7 for Masini et al. (2022).

In particular, ten galaxies were classified as Seyfert galaxies with low Eddington ratios: NGC2273, NGC3185, NGC3516, NGC3982, NGC4051, NGC4151, NGC4258, NGC4565, NGC4725, NGC5273. While the accretion regime is already inefficient, a standard accretion disk is not probable; sixty percent of them have independent evidence of showing radiatively inefficient accretion. Some galaxies show hints of having an ADAFs scenarios like NGC3516 (Cao and Wang, 2014), NGC4258 (Doi et al., 2005; Szanecki et al., 2023), NGC4565 (Doi et al., 2005; Liu and Wu, 2013) or NGC 5273 (Giroletti and Panessa, 2009). NGC4051 are discussed to be a pure accretion flow scenario (Peterson et al., 2000; Meyer-Hofmeister and Meyer, 2011), or a truncated accretion disk with a comptonized region (Zhang and Wu,
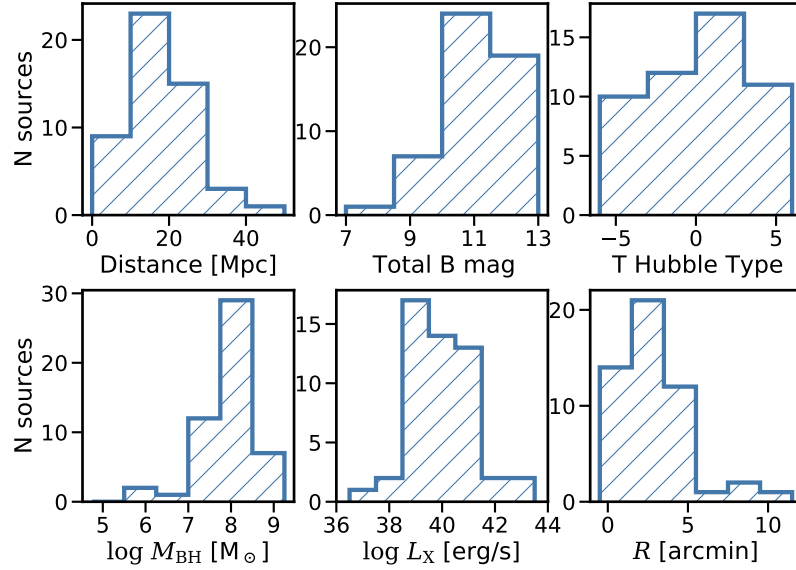
Figure 5.5: Distributions illustrating the fundamental properties of the host galaxies and their associated supermassive black holes in the LLAGN sample considered in this work.

2006). NGC4151 is discussed to be a pure accretion flow scenario (Niedźwiecki et al., 2015), a truncated accretion disk (Szanecki et al., 2021) or a hybrid-scenario (Alexander et al., 1999; Mahmoud and Done, 2020).

The rest of the samples are classified as LINERs, from which all show evidence of hosting an AGN, mainly through the ionization power of its central X-ray emission (e.g., NGC2655, Reynaldi et al., 2020) or through radio nuclear emission with compact jets (e.g., Baldi et al., 2018, 2021a). For sixty percent of them, there are independent hints of an ADAF scenario or non standard accretion disk scenario: NGC1052 (Yuan et al., 2009; Falocco et al., 2020), NGC2787 (Doi et al., 2005; Pellegrini, 2005; Liu and Wu, 2013), NGC2841 (Pellegrini, 2005), NGC3031 (Doi et al., 2005; Nemmen et al., 2014), NGC3079 (Chang et al., 2002), NGC3147 (Doi et al., 2005; Liu and Wu, 2013), NGC3414 (Wójtowicz et al., 2023), NGC3718 (Doi et al., 2005), NGC4111 (Hauschild Roier et al., 2022), NGC4125 (Pellegrini, 2005), NGC4138 (Liu and Wu, 2013), NGC4203 (Doi et al., 2005; Yuan et al., 2009; Liu and Wu, 2013), NGC4261 (Pellegrini, 2005; Yuan et al., 2009; Nemmen et al., 2014), NGC4374 (Doi et al., 2005; Pellegrini, 2005), NGC4438 (Pellegrini, 2005), NGC4457 (Nemmen et al., 2014), NGC4486 (Doi et al., 2005; Pellegrini, 2005; Nemmen et al., 2014), NGC4494 (Nemmen et al., 2014), NGC4552 (Doi et al., 2005; Pellegrini, 2005; Nemmen et al., 2014), NGC4579 (Doi et al., 2005; Yuan et al., 2009; Nemmen et al., 2014), NGC4594 (Pellegrini, 2005; Liu and Wu, 2013; Nemmen et al., 2014), NGC4698 (Tran et al., 2011), and NGC4736 (Liu and Wu, 2013; Nemmen et al., 2014).

The primary X-ray catalogs utilized for sample compilation include Williams et al. (2022), Osorio-Clavijo et al. (2023), and González-Martín et al. (2009). These catalogs offer spectral fits to data from the Chandra and XMM-Newton telescopes, focusing on various models tailored to spectral features. Our emphasis is on the intrinsic emission from the corona or ADAF, characterized by power-law spectra. The extracted gamma (Γ) and normalization values for the power-law component were used to compute X-ray fluxes in both the soft (0.5-2 keV) and hard (2-10 keV) X-ray bands.

For specific sources, we utilized data from catalogs that incorporate reflection components, complex thermal elements, or torus models to understand their obscuration better. We used better constraints on the intrinsic power-law spectra of telescopes such as Swift-BAT or NuSTAR less affected by obscuration. For detailed information on individual sources, we refer to Yun et al. (2022) for NGC 5033, Kammoun et al. (2020) for NGC 3982, and Masini et al. (2022) for NGC 4258. Additionally, for NGC 4051, NGC 4151, and NGC 4725, the spectral fittings are taken from Cappi et al. (2006).

For each galaxy, we conducted photometry spanning UV to FIR bands using calibrated images from the DustPedia database[2]. We performed forced photometry in a 9-arcsecond radius aperture centered on each galaxy (refer to Fig. 5.6 for an example). This aperture covered GALEX NUV and FUV filters, ugriz SDSS bands, JHKs bands from 2MASS, Spitzer IRAC1-4 and WISE 1-4, Spitzer MIPS 24-70 microns, 100, Herschel PACS 70-100-160 microns, and Herschel SPIRE 250 microns. The 9-arcsecond radius was deliberately chosen to align with the diameter required to encompass the FWHM of the PSF for each filter in our analysis. Upper limits at 3σ were set for non-detected sources.

Using the Photutils library version 1.9[3], we utilized a two-dimensional modeling approach to perform background calculations. To determine the background, we also implemented a sigma clipping technique and, where feasible, masked the galaxy using a mask derived from the largest isophote in the DustPedia database. Additionally, we applied aperture corrections and corrected for Milky Way extinction.

5.3.2 AGN Samples

We conducted validation tests using well-established datasets from high-luminosity AGN studies to verify the robustness of the hypothesis outlined in Section 5.2.2.2 regarding our newly developed IRX-CIGALE module. Specifically, we utilized the COSMOS and SDSS QSO samples referenced in previous CIGALE publications (Yang et al., 2020; Yang et al., 2022), enabling direct comparisons with established

---

2 http://dustpedia.astro.noa.gr/Data
3 https://photutils.readthedocs.io/
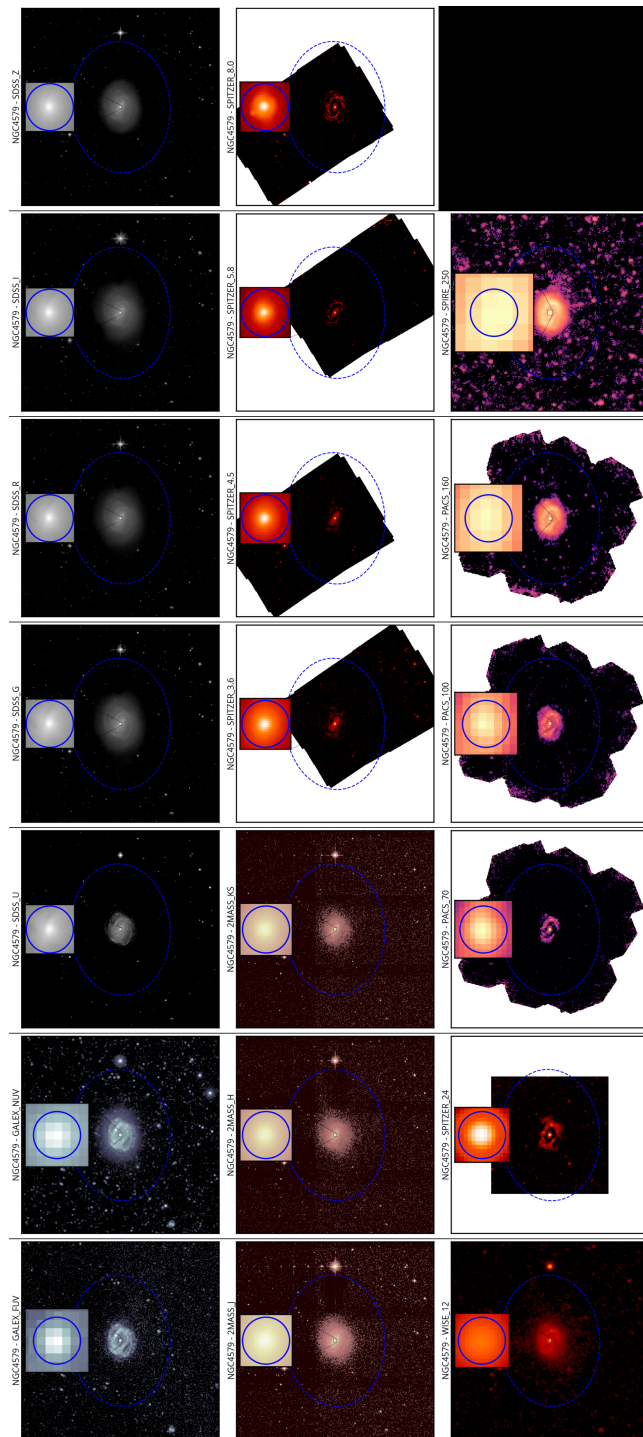
Figure 5.6: Example of forced aperture photometry with a 9-arcsecond radius, executed across all wavelengths from GALEX NUV to Herschel SPIRE 250 microns. The blue ellipse delineates the galaxy's boundary as identified by isophotes from DustPedia. An inset offers a detailed view of the 9-arcsecond aperture region utilized in this analysis, showcased as a blue circle.

X-ray modules. These studies determined the bolometric luminosity of AGN using the α_{ox} prior, which we adopted as a benchmark to assess the robustness of our new prior.

The SDSS sample consists of type 1 AGN that are optically selected from the DR14 quasar catalog (Pâris et al., 2018), including 1986 AGN detected in the 2–12 keV X-ray band with XMM-Newton at a significance level greater than 3σ. Galactic extinction corrections were applied to ensure the reliability of this dataset. The COSMOS sample, derived from the COSMOS-Legacy survey, comprises 590 X-ray-selected AGN with photometric data sourced from the COSMOS2015 catalog (Laigle et al., 2016) that spans 14 broad optical and infrared bands. Redshift measurements were taken from Marchesi et al. (2016b).

For both the SDSS and COSMOS samples, the SED fitting methodology followed the parameters established in Yang et al. (2020), keeping the classic accretion disk model from Schartmann et al. (2005) and incorporating the new module using the α_{ir} for comparative analysis (see Section 5.4.1).

5.3.3 LLAGN Fitting

The SED fitting process for the LLAGN sample was conducted using a combination of CIGALE modules, comprehensively modeling both AGN and host galaxy emissions. The host galaxy characterization was performed using a Chabrier (2003) IMF with two possible metallicity values, a delayed star formation history for the stellar population and accounting for dust extinction. Dust emissions were effectively modeled using the Themis module (Jones et al., 2017). For the AGN component, seed photons were modeled using our novel ADAF + TDk approach, detailed in Section 5.2.2. This method allows adjustable parameters to explore the relevance of the truncated disk with δ_{AGN} values set at 0 and 1.0, accommodating a wide range of AGN fractions. The toroid's opening angle was set at $70°$, achieving a covering factor of 80% to model better the type of obscuration typical in low-accreting sources (Ricci et al., 2017a). Viewing angles were adjusted to allow a direct view of the central engine ($i = 10°$) or complete cover ($i = 80°$), with intermediate angles tested but showing no significant impact on the results. The X-ray module was also employed to model emissions from the host galaxy, accounting for emissions from X-ray binaries and the AGN X-ray power law across a range of power indexes. A detailed list of the parameters used in the CIGALE input is presented in Table 5.2.

Galaxies with fits resulting in $\chi^2_{red} > 5$ were excluded from the analysis, leading to the exclusion of only three galaxies out of the initial 52: NGC4013, NGC4826, and NGC5866. NGC4013 and NGC5866 present challenges due to their dusty nature and pronounced side-

PARAMETER	MODEL/VALUES
Star formation history: delayed model and recent burst	
Age of the main population	3000, 5000, 7000, 10000 Myr
e-folding time	100, 500, 1000, 3000 Myr
Burst stellar mass fraction	0.0, 0.1
Simple Stellar population: Bruzual & Charlot (2003)	
Initial Mass Function	Chabrier (2003)
Metallicity	0.008 (LMC), 0.02 (Solar)
Galactic dust extinction	
Dust attenuation recipe	modified Calzetti et al. (2000)
E(B-V)$_{lines}$	0.1, 0.3, 0.5, 0.7
E(B-V)$_{factor}$	0.1, 0.44, 0.7
Power law	-0.4, 0.0
Galactic dust emission: Themis Jones et al. 2017	
q_{HAC}	0.02, 0.17, 0.24
U_{min}	0.1, 0.5, 2.5, 5.0, 10.0, 50.0
α slope	2.1, 2.5, 2.9
gamma	0.4
AGN module: SKIRTOR	
Torus optical depth at 9.7 microns $\tau_{9.7}$	3, 7, 11
Opening angle	70°
Viewing angle	10° (type 1), 80° (type 2)
Disk spectrum	**ADAF + Truncated disk**
Delta parameter for the truncated disk	**0, 1.0**
AGN fraction	0.001, 0.01, 0.05, 0.1, 0.2, 0.3
Extinction law of polar dust	SMC
$E(B-V)$ of polar dust	0.0, 0.3, 0.6
X-ray module: this paper	
AGN photon index Γ	1.6, 1.8, 2.0, 2.5, 3.0, 3.5
α_{irx}	0, 0.15, 0.3, 0.45, 0.6
Total number of models per redshift	671,846,400

Table 5.2: Parameters and values for the modules used with CIGALE for the LLAGN sample.
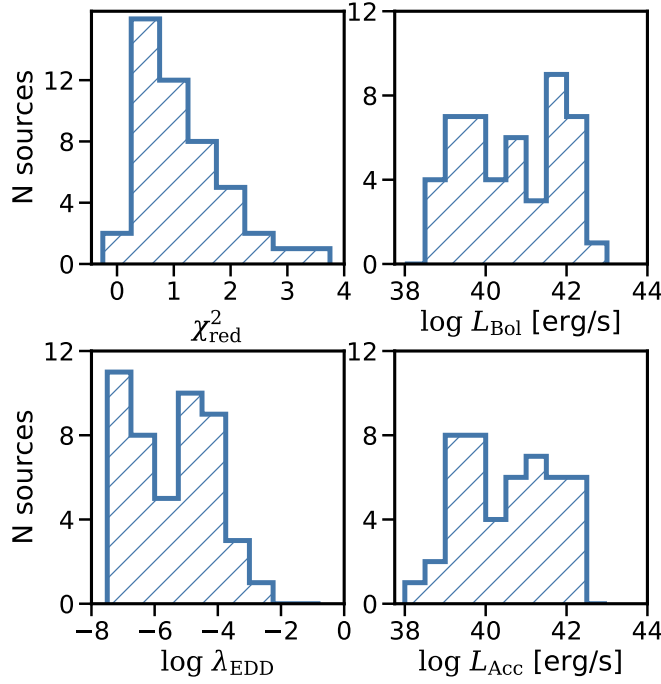
Figure 5.7: Distribution of reduced chi-square (χ^2_{red}) values and key AGN properties derived from the SED fitting of the LLAGN sample. Reduced chi-square values near 1 signify a good fit quality. This figure also shows the values for AGN properties, such as bolometric luminosity (L_{Bol}) and accretion luminosity (L_{Acc}), from which we calculated the Eddington ratio (λ_{EDD}) for each source.

view orientation, complicating AGN detection and subsequent SED fitting. Specifically, NGC4013 experiences additional complexity due to star contamination near its center. Although NGC4826 has no side-view orientation, it is characterized by a prominent absorbing dust lane.

The analysis of SED fitting results revealed a median reduced χ^2 value of 1.02 and a mean value of 1.24, affirming consistently satisfactory fit quality. Figure 5.7 displays the distribution of essential AGN properties, including luminosities and Eddington ratios. The accretion luminosity (L_{Acc}), representing the total radiation output of the central engine averaged across all directions, is contrasted with the bolometric luminosity (L_{Bol}), which encompasses all AGN emissions, including dust re-emission. The measured luminosities for all sources span a broad range from 10^{38} to 10^{43} erg s^{-1}. Utilizing L_{Acc} alongside M_{BH} data sourced from the literature enabled the derivation of Eddington ratios predominantly within the range of 10^{-8} to 0.001, aligning with expectations for this sample. Figure 5.8 offers visual confirmations of the SED fitting outcomes for a selection of galaxies, showcasing the model's proficiency in mirroring observed SED patterns. Additionally, a compilation of the primary physical parameters estimated from the CIGALE output is cataloged in Table 5.3.
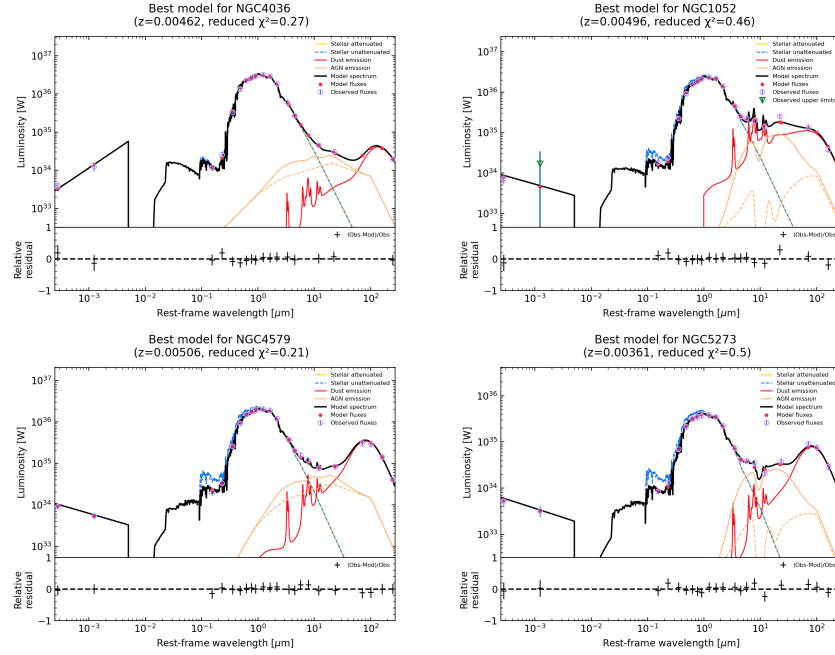
Figure 5.8: Example of the best fit achieved with our module for the LLAGN sample: NGC4036 and NGC4579 are presented on the left, showcasing a direct view of the central engine ($i = 10°$), with NGC4579 additionally exhibiting some dust extinction in the polar direction ($E(B - V)_{\text{polar}} = 0.3$). Conversely, on the right, NGC1052 and NGC5273 are depicted, illustrating an obscured view of the central engine ($i = 80°$), highlighting the impact of viewing angle on the observed SED characteristics.

5.4 RESULTS AND DISCUSSION

This section delineates the outcomes derived from applying our novel CIGALE module, which is tailored to fit the SEDs of LLAGN. Specifically, Section 5.4.1 validates our methodological approach, outlines the selection of our principal hypothesis, and contextualizes our findings within the existing literature. In Section 5.4.2, we explore the X-ray bolometric corrections within the low-luminosity regime. Section 5.4.3 studies the modeled α_{ox} indices extracted from our SED fits, investigating their alignment with established scaling relations observed in QSOs. Furthermore, Section 5.4.4 evaluates the specific star formation rates ($sSFR$) derived from our analysis, facilitating a comparison with a sample of high-luminosity QSOs.

5.4.1 Validation

The incorporation of the L_X-L_{IR} relation is substantiated by the findings presented in Section 5.2.1. This relation establishes a robust connection between the AGN's X-ray and mid-infrared emissions, spanning at least five orders of magnitude in luminosity. It applies

to a broad range of AGN types and is minimally affected by obscuration. Diverse AGN samples covering different luminosity ranges were employed to validate its inclusion in our module.

For the high-luminosity regime ($L_{\mathrm{Bol}} > 10^{42}$ erg s^{-1}), bolometric luminosities used for reference were derived for the SDSS and COSMOS samples using the conventional CIGALE approach (α_{ox}). In the low-luminosity regime, bolometric luminosities from Eracleous et al. (2010) were adopted for the 14 sources in common, and a bolometric correction of $k_{\mathrm{X}} = 15.8$ (Ho, 2009) was assumed for the remaining sources.

Figure 5.9 compares these bolometric luminosities with those obtained in this work. The AGN samples exhibit linear fits closely following the 1:1 relationship within the error margins. However, for the SDSS QSOs, a deviation from the 1:1 relationship is observed beyond a luminosity of 10^{45} erg s^{-1}. This deviation could be attributed to the increasing influence of photons from the big blue bump at higher luminosities. For the LLAGN sample, a similar luminosity trend is observed, but the reference values fall above the 1:1 relationship. Our luminosities plotted originate from AGN modeling, while the reference values are derived from observations with an angular resolution of 1 arcsec (Eracleous et al., 2010). This large aperture could introduce significant host galaxy contamination, explaining the observed offset. Additionally, the other reference values were determined using a bolometric correction larger than the one obtained in our study, a point we will discuss further in the next section.

In Fig. 5.10, we compare the mean SEDs for the high-luminosity Type I and Type II AGN from the COSMOS sample with our LLAGN model. All SEDs include the central engine plus the toroid and polar dust emission. For the AGN sample, the conventional CIGALE approach is used; instead, the LLAGN model incorporates the ADAF+TdK as the central engine.

The SEDs reveal distinguishing characteristics between Type I and Type II AGN. Type II AGN exhibits weaker UV-optical emission due to the torus constraining the central engine. Beyond 1 micron and into the infrared bands, both SEDs become more similar, with a subtle divergence observed in the 9.7-micron silicate complex. This feature manifests as either absorption or emission depending on the optical depth at 9.7 microns, accompanied by a small bump emission at 50 microns for Type II AGN.

While QSOs encompass higher luminosities, both LLAGN models display comparatively lower luminosities. Initially, the mean SED of LLAGN shows characteristics of obscuration, as expected, since most LLAGN are Type II. This obscuration does not precisely match the shape of a Type II from COSMOS, exhibiting a less abrupt thermal emission at 1 micron. Transparent lines in Fig. 5.10 represent individual sources, revealing that some sources exhibit UV-optical slopes
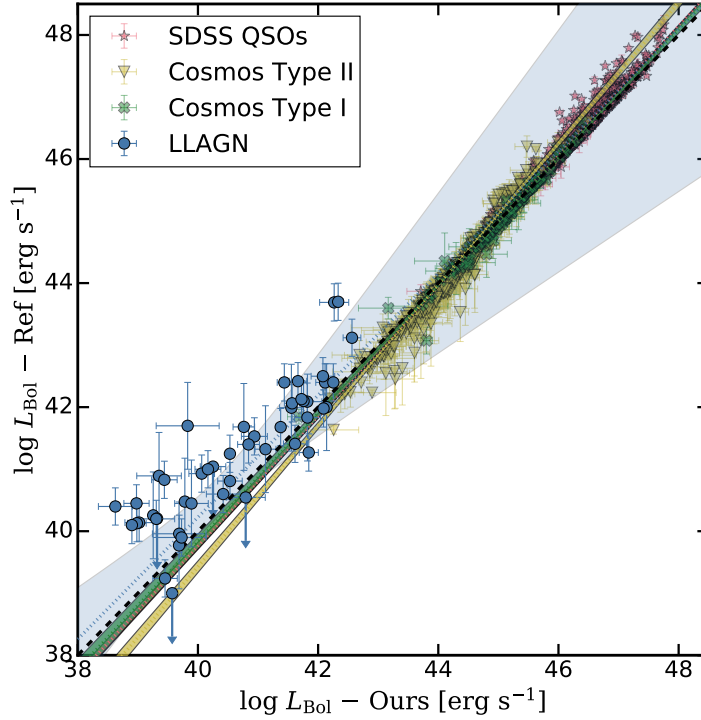
Figure 5.9: Comparison of bolometric luminosities between this work and reference values. The dashed black line represents the 1:1 relation. A linear fit is shown for each sample with a dotted line following the same colors and with a shadow area of the 3-sigma deviation.

closer to Type II, indicative of unabsorbed ADAF. These non-obscured LLAGN showcase the expected UV shape (Fig. 5.4). Introducing the ADAF model brings about a notable change in the infrared, where remission from polar dust and the toroid alters the power slope of the overall AGN emission.

5.4.2 Bolometric correction on the lower-luminosity regime

The X-ray bolometric correction (k_X) is essential for converting observed X-ray luminosity (L_X) of an AGN into its total bolometric luminosity. This correction addresses the fact that X-rays represent only a portion of the total radiation emitted by the AGN. However, X-rays play a significant role in conducting AGN surveys as AGN emissions dominate this energy band and can be easily identified. This becomes particularly vital in our LLAGN sample, where emissions from the host galaxy overshadow the UV-optical ranges, necessitating the consideration of the host galaxy's impact on bolometric luminosity.

SED fitting has proven to be an invaluable method for determining L_{Bol} of AGN. This technique comprehensively estimates total AGN luminosity as detailed in Section 5.3.3. By comparing L_{Bol} with L_X, we derive the bolometric correction factor k_X, such that $L_{Bol} = k_X \times L_X$.
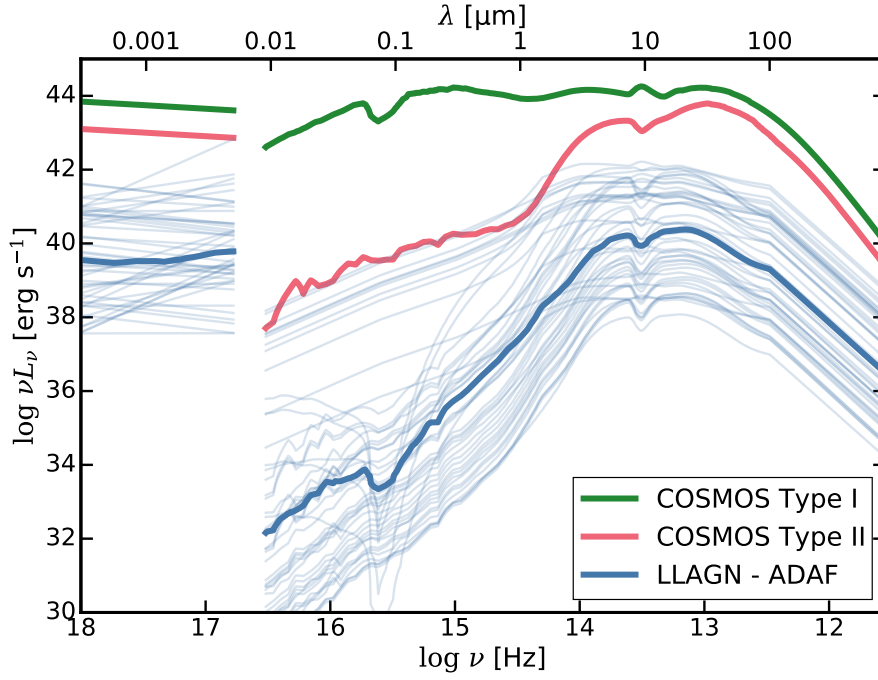
Figure 5.10: Comparison of the mean SEDs fitted for QSOs from COSMOS between Type I and Type II, alongside our mean LLAGN SED using the ADAF+TDk model. Transparent lines represent the individual SEDs of LLAGN that were fitted. X-ray emission is intrinsic and does not account for absorption.

The concept of X-ray bolometric correction has been the subject of detailed investigation in studies by Hopkins et al. (2007b), Lusso et al. (2012), and Duras et al. (2020). Notably, Duras et al. (2020) developed a function for k_X that leverages SED fitting incorporating an infrared-X relation within a similar framework to ours, parametrizing how k_X varies with luminosity:

$$k_X(L_{\mathrm{Bol}}) = a\left[1 + \left(\frac{\log\left(L_{\mathrm{Bol}}/[\mathrm{erg\,s}^{-1}]\right)}{b}\right)^c\right].\tag{5.5}$$

This formula demonstrates the dependence of k_X on bolometric luminosity, which becomes flatter below a specific luminosity threshold. Extrapolations from Duras et al. (2020) suggest a $k_X = 10.96$ for the lower luminosity regime, while Eracleous et al. (2010) and Ho (2009) propose $k_X = 50$ and $k_X = 15$, respectively.

In Fig. 5.11, we compare the relationship between L_{Bol} and L_X for our LLAGN sample with the sample from Nemmen et al. (2014) and the low-luminosity extrapolation from Duras et al. (2020). The Pearson correlation coefficient is approximately 0.9. A linear regression performed on our data yields:

$$L_{\mathrm{Bol}} = (9.65 \pm 1.004) \times L_X.\tag{5.6}$$
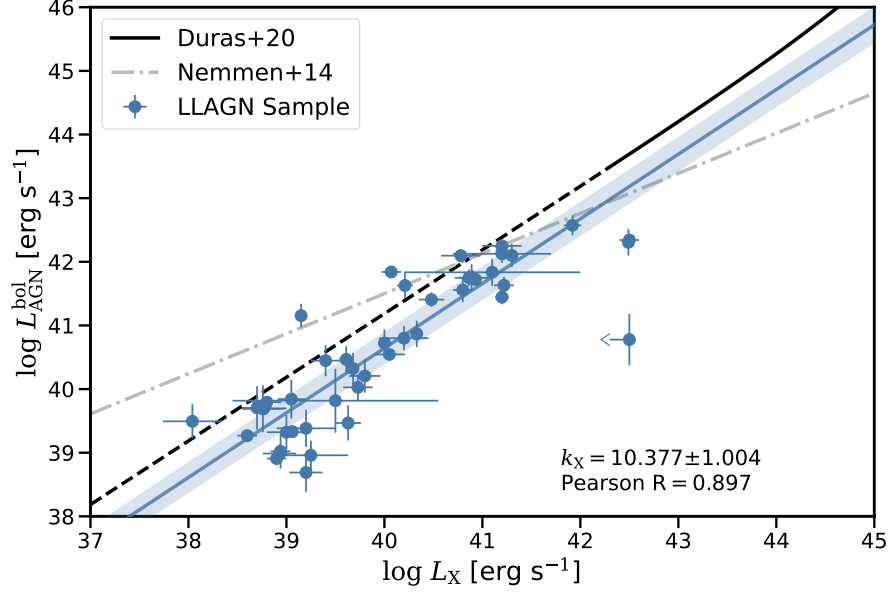
Figure 5.11: Upper panel: Blue dots depict the measured X-ray luminosities plotted against the bolometric luminosities for our LLAGN sample, with a blue line indicating the linear regression fitted to this data. In contrast, the data and bolometric correction from Nemmen et al. (2014) are shown as grey stars and a dotted line, respectively. The solid black line represents the bolometric correction from Duras et al. (2020), transitioning to a dotted line where it extrapolates beyond the data. Lower panel: X-ray bolometric correction (k_X) plotted against bolometric luminosity. The solid black line denotes the bolometric correction from Duras et al. (2020), accompanied by black pentagons representing its binned data. Our binned data for the LLAGN sample are illustrated with blue diamonds. The dotted yellow line represents the fit to Eq. (5.5) using a combination of our binned data and that from Duras et al. (2020). Red crosses mark the binned data from the pure AGN X-ray luminosities modeled by CIGALE. Shaded regions indicate the 1-sigma uncertainties.

This fit indicates a k_X value lower than those typically reported in the literature, yet it aligns closely, within error margins, with the extrapolation by Duras et al. (2020). Differences from previous studies can be attributed to several factors in our methodology: our specific modeling of the accretion process, a larger sample size that reduces the impact of statistical fluctuations, and the inclusion of host galaxy X-ray emissions in our modeling.

Our fit of k_X, as illustrated in the lower panel of Fig. 5.11, combines our observational binned data from the lower-luminosity regime with the high-luminosity binned data from Duras et al. (2020). This comprehensive approach allows us to provide an expression for k_X that spans nearly ten orders of magnitude in luminosity. The fitting achieves a χ^2 of 0.73, with parameters $a = 7.85 \pm 0.95$, $b = 45.04 \pm 0.27$, and

$c = 55.87 \pm 6.64$. The binned data, comprising observational L_X and L_{Bol} derived from SED fitting, reveal a lower k_X value in the first bin, indicative of the host galaxy's X-ray emission becoming comparable to that of the AGN and influencing the relationship. This underscores the significant role of host galaxy X-ray contributions, primarily from X-ray binaries, in shaping the bolometric correction calculation.

We also plot the k_X values obtained from modeling pure AGN X-ray emissions in CIGALE, yielding a mean $k_X \sim 7.5$. This value closely aligns with our fit, emphasizing the consistency of our approach in modeling the AGN and host galaxy X-ray emissions and their collective impact on the bolometric correction. CIGALE considers that the host galaxy X-ray emission is primarily produced by low-mass X-ray binaries (LMXBs), high-mass X-ray binaries (HMXBs), and hot gas (Yang et al., 2020). The CIGALE X-ray module utilizes the recipe from Mezcua et al. (2018) to model X-ray emission from these components, with luminosities for LMXBs and HMXBs described as functions of stellar age and metallicity. In contrast, the hot gas emission is quantified in terms of SFR. While shocks produced, for example, by a supernova and AGN feedback, can produce X-ray emission, CIGALE does not yet include shock models. Figure 5.12 showcases sources where the hard X-ray band significantly contributes to the host galaxy's X-ray emission, demonstrating CIGALE's capability to distinguish between LLAGN and host galaxy contributions, thereby refining the bolometric correction calculation.

The debate surrounding the accretion mechanisms in LLAGNmotivated the inclusion of an ADAF and the possibility of a truncated thin disk, as elaborated in Section 5.2.2. Although it is hypothesized that all sources in our sample undergo a non-standard form of accretion, only 60% have independent evidence supporting this premise. To assess the potential for a traditional accretion mechanism, we implemented a SED fitting approach that utilizes the L_X–$L_{12\mu m}$ correlation and a standard accretion disk. This approach incorporates the Schartmann et al. (2005) accretion disk model with adjustments in the optical slope ($\delta_{AGN} = -0.36, 0.36$). Analysis of the reduced chi-square values revealed comparable fitting quality between the ADAF and conventional disk accretion models, highlighting a limitation in employing SED fitting as a discriminant between these models. Moreover, the bolometric luminosities derived from both ADAF and disk models are within error margins of each other. It is noteworthy, however, that bolometric luminosities obtained via the disk model are marginally higher, exhibiting an average difference of 0.1 dex. This finding indicates a notable consistency in bolometric corrections across different accretion scenarios.

This comparison reveals that although the distribution of UV-to-IR photons may vary, the total integrated luminosity exhibits no significant dependency on the chosen accretion model. This independence
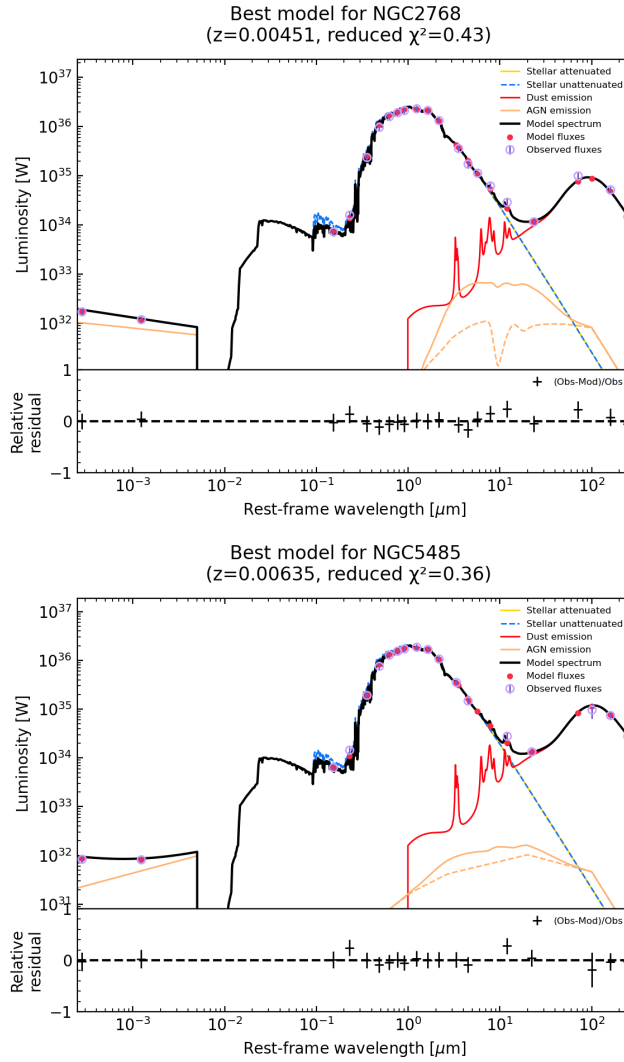
Figure 5.12: Examples of SED fitting for the LLAGN sample, where the host galaxy can emit in the X-ray hard band, modifying the contribution of an AGN to this band.

arises because the L_X–$L_{12\mu m}$ relationship, which serves as a foundational prior for AGN emission, effectively balances the SED profile. This equilibrium compensates for the lack of UV photons with an increased presence of IR emissions, resulting in a bolometric correction that remains unaffected by the accretion mode. This finding underscores the model-independence of bolometric corrections, emphasizing their reliability across different accretion regimes.

5.4.3 Galaxy contamination

Exploring the influence of different photometric apertures on the SED fitting for our LLAGN sample sheds light on how solid this module is for future applications. We specifically evaluated how different
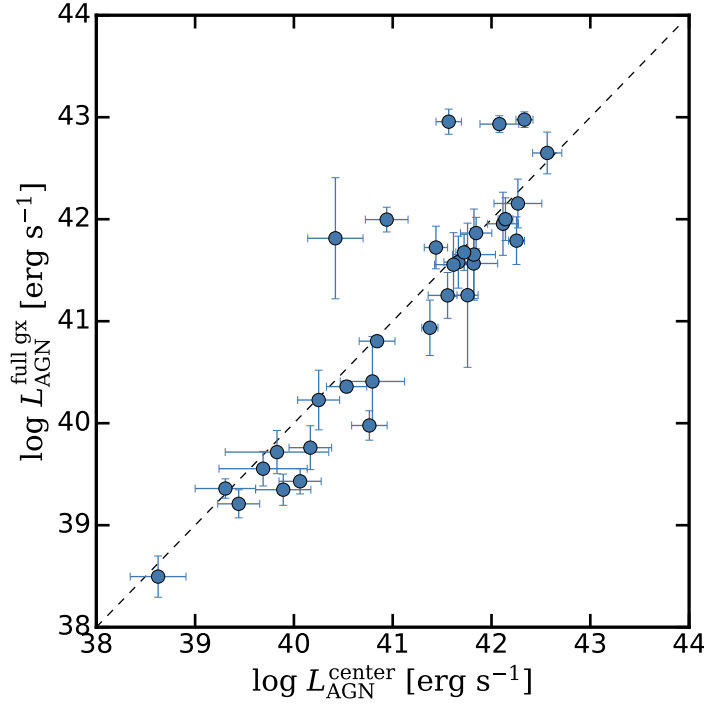
Figure 5.13: Comparison of bolometric luminosities obtained using a central aperture-based photometric approach and entire galaxy photometry for the LLAGN sample. The dotted line represents the 1:1 relationship. Excluding a few outliers, our sources generally exhibit lower luminosities for the entire galaxy fit but align with the 1:1 relation within uncertainties. This suggests that bolometric luminosity can be accurately estimated even in scenarios with significant host galaxy contamination.

the AGN properties obtained from our 9-arcsec central photometry are from those obtained from entire galaxy photometry provided by DustPedia.

Figure 5.13 compares bolometric luminosities calculated using these two distinct methods. The congruence observed between the results signifies that our module effectively discerns the LLAGN bolometric luminosities across a wide luminosity range. Moreover, the findings from the aperture-based method closely mirror those acquired through full galaxy photometry. However, the full galaxy photometry seems to have lower luminosities than the central aperture but follows the 1:1 relation within the uncertainties, suggesting minimal discrepancy within the bounds of error.

This consistency in bolometric luminosity estimation becomes particularly pertinent for sources at higher redshifts. At such distances, an instrument's PSF might encapsulate emissions from the central regions and the periphery of galaxies, potentially complicating the task of distinctly resolving galactic structures. Despite these challenges, the IRX module demonstrates a steadfast capability to accurately es-

timate bolometric luminosities, demonstrating its effectiveness even when full galaxy photometry is employed. These observations highlight the utility of this module when the photometry accounts for the galaxy's total emitted flux, extending its applicability to high-redshift observations.

5.4.4 α_{OX} in Low–Luminosity AGN

Our approach does not dictate a specific value for α_{ox} but instead facilitates the reconstruction of the modeled 2500 Å emission at its core to compare with the 2 keV emission. This methodology allows for examining the α_{ox} behavior within the modeled framework, offering predictions for the low-luminosity domain.

The fundamental premise of the α_{ox}–L_{UV} relationship is the interplay between 2 keV and 2500 Å emissions. Figure 5.14 delineates this association and juxtaposes it with the linear correlations observed in both high and low-luminosity regimes, as reported by studies such as Lusso et al. (2010), Just et al. (2007), and Xu (2011). Our analysis reveals a shift towards lower UV luminosities for comparable X-ray luminosity levels. The equation for the linear fit to our data is as follows:

$$\log L_\nu(2\ \mathrm{keV}) = (0.78 \pm 0.10) \times \log L_\nu(2500) + (4.02 \pm 2.31) \quad (5.7)$$
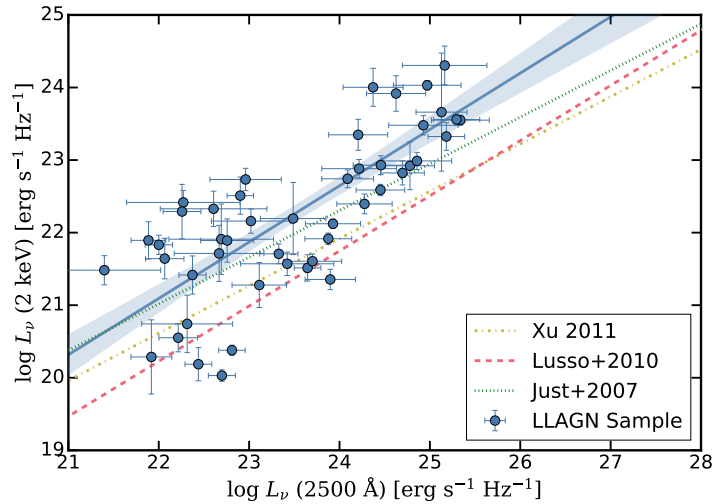
Figure 5.14: Comparison of the relationship between 2 keV and 2500 Ångström emissions with Lusso et al. (2010), Xu (2011), and Just et al. (2007) data. Our linear fit is a solid blue line, with shaded regions being the uncertainties at 1-σ.

Although a linear fit approximates the overall trend, the residuals indicate considerable scatter ($\sigma \sim 0.74$).

Figure 5.15 presents the α_{ox} relationship with UV and X-ray luminosities. In the QSO regime, a pronounced correlation exists between α_{ox} and UV luminosity, which is less apparent with X-ray luminosity. Lusso et al. (2010) found α_{ox} to loosely correlate with L_{2500}, exhibiting more scatter with L_{2keV}. Xu (2011) noted a similar pattern for L_{2500} within the LLAGN regime, albeit with greater dispersion, while no distinct correlation emerged for L_{2keV}. In the QSO regime, the predominance of UV photons, primarily from the big blue bump, over corona-generated X-rays domain the relation and determines the α_{ox}.

Our findings in the lower luminosity range, as illustrated in blue in Fig. 5.15, uncover a weak correlation of α_{ox} with UV luminosity, characterized by a slope of 0.08 ± 0.04, and a slight inverse correlation with X-ray luminosity, indicated by a slope -0.09 ± 0.03. The dispersion of residuals in both cases is $\sigma \sim 0.27$. The α_{ox} values in LLAGN primarily range between 0 and 1, covering four X-ray and UV luminosities magnitudes. Furthermore, our data straddle the extrapolated fit from Lusso et al. (2010) in the 2500 Å luminosity plane, suggesting that neither consistent nor variable behaviors can be conclusively dismissed, especially considering the margin of error.

While UV and X-rays exhibit correlation in the high-luminosity regime, the source of X-ray photons in low-luminosity AGN may not solely be a hot corona. ADAFs are known for their pronounced emission in hard X-rays. Hence, X-ray photons in this context could stem from various processes, including inverse-Compton scattering, but operating at disparate scales. This complexity could account for the observed significant dispersion in the L_{2keV}–L_{2500} relationship.

We further examine the α_{ox}–λ_{Edd} domain to gain deeper insights. The correlation found in QSOs sources by Lusso et al. (2010), where sources with higher accretion rates showcase elevated α_{ox} values, corroborates the notion that increased accretion intensifies the big blue bump, thereby boosting UV photon production. In contrast, an anticorrelation in LLAGN was observed by Xu (2011), suggesting a divergent behavior in this regime.

Our findings, depicted in Fig. 5.16, reveal that LLAGN tend to exhibit either a mild correlation or maintain constant α_{ox} values across different accretion rates. By binning our data, combining it with the data retrieved by Lusso et al. (2010), and applying a broken power-law fit, we capture behavior spanning nine orders of magnitude in λ_{Edd}. The equation fitted is:

$$-\alpha_{ox}\left(\lambda_{Edd}\right) = a \left[1 + \left(\frac{\log\left(\lambda_{Edd}\right)}{b} \right)^{c} \right]. \tag{5.8}$$

Since the accretion regime is supposed to switch at $\log \lambda_{EDD} = -3$, we anchor $b = 0.001$. The fit yields a χ^2 of 0.4, characterized by parameters $a = 0.39 \pm 0.03$ and $c = 0.18 \pm 0.03$. Figure 5.16 showcases the behavior of the relation.
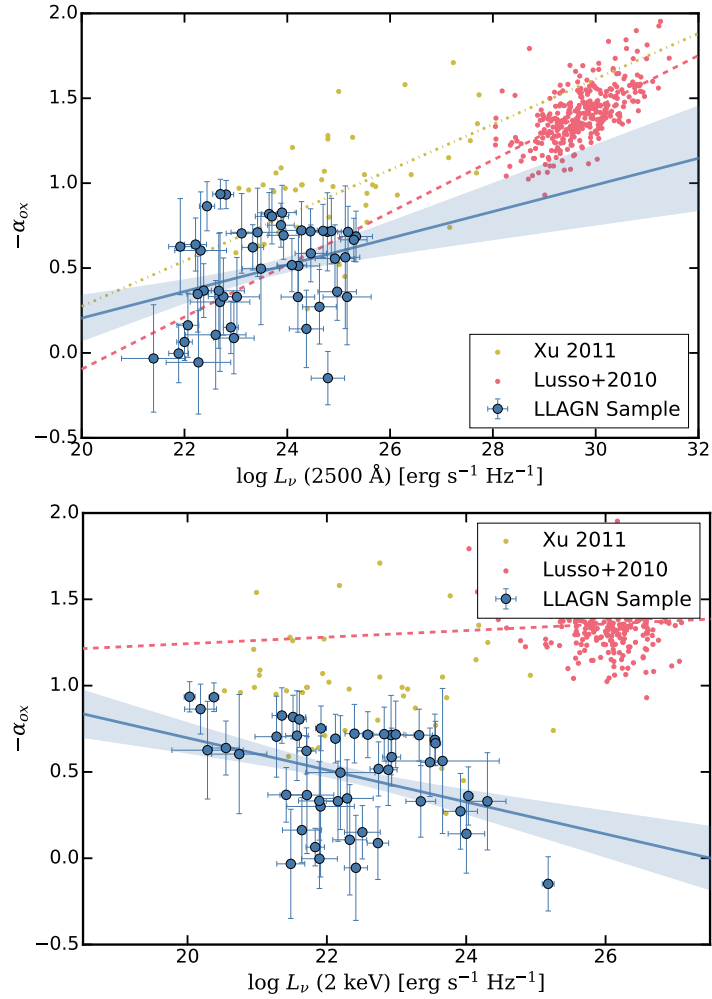
Figure 5.15: Comparison of spectral index $\alpha_{\rm ox}$ with 2500 Ångström luminosity (top) and two keV X-ray luminosity (bottom). The AGN sample by Lusso et al. (2010) is in red, the LLAGN sample by Xu (2011) is in yellow, and our values from the model LLAGN for each source are in blue.

This outcome is consistent with the UV/X-ray correlation depicted in Fig. 5.14, suggesting a stable ratio between these emissions and a uniform $\alpha_{\rm ox}$. Whereas in conventional QSOs, variations in accretion rates can modify the big blue bump across the UV-optical spectrum, in the low-luminosity regime, the accretion flows predominantly generate the optical/UV photons. This process involves the inverse Compton scattering of soft synchrotron photons by hot electrons within the ADAF, a phenomenon governed more by magnetic field dynamics than by mass influx into the flow.

Nonetheless, a deeper exploration is warranted to grasp the ramifications of this accretion paradigm fully. Measuring UV emissions in LLAGN is complicated by their inherently faint nature, and our analysis leverages ADAF-centric modeling. For instance, the study by
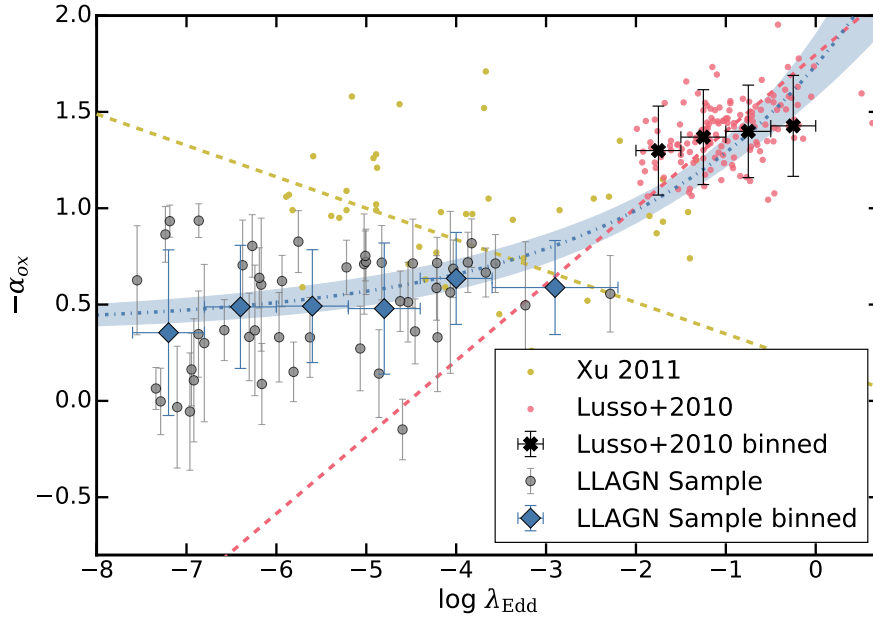
Figure 5.16: Comparison of the spectral index α_{ox} with the Eddington ratio (λ_{Edd}). The AGN sample from Lusso et al. (2010) is represented in red, the LLAGN sample from Xu (2011) is in yellow, and our modeled values for each LLAGN source are in grey. Our binned data are depicted as blue diamonds, while the black crosses represent the binned data from Lusso et al. (2010). The dashed blue line indicates the fit to all the binned data. Contrary to the anticorrelation proposed by Xu (2011), our fit follows a constant value for the low regime. Shaded regions indicate the 1-sigma uncertainties.

Xu (2011) relies on UV luminosity estimations derived from optical photon proxies, like continuum or emission lines. Future research employing high-resolution data across UV, optical, and infrared spectrums from instruments like the *Hubble Space Telescope* (HST) and the *James Webb Space Telescope* (JWST), will be crucial for more accurately delineating the SED in the central parsec of these galaxies.

5.4.5 LLAGN effects in SFR

As we highlight in Chapter 1, AGN feedback is known to affect the SFR of host galaxies, with even LLAGN capable of influencing their environments. Instances such as NGC4579 (**Ogle2024**) demonstrate how radio jets can impact the ISM, suppressing star formation within the galaxy's inner disk. Similarly, Almeida et al. (2023) have shown that the diminished radiative power characteristic of an ADAF can effectively hinder star formation by heating and ionizing surrounding gas. However, the precise dynamics between LLAGN activity and SFR remain partially understood.

Figure 5.17 showcases a comparative analysis of the specific star formation rate ($sSFR=SFR/M_\star$) versus the Eddington ratio for the selected sample of LLAGN. The *sSFR* is derived for different apertures from the complete galaxy aperture data sourced from Dustpedia (first panel) and those derived from our targeted central nine arcsec photometry (second panel). Given our sample's average distance, the latter encompasses an effective area roughly equivalent to a 1.5 kpc diameter.

To contextualize our findings within the broader AGN spectrum, we compare these results against the miniJPAS sample from Chapter 4 and the sample of high-luminosity AGN from the BASS survey (Koss et al., 2022a,b). The comparison with the latter sample is pertinent, as our LLAGN sample and the BASS survey's local X-ray detected AGN at similar evolutionary stages within their respective host galaxies. Utilizing high-luminosity AGN data from the BASS survey along with their corresponding host galaxy properties (Koss et al., 2021), it appears that a relation exists across different Eddington ratios, wherein the *sSFR* calculated for the entire galaxy increases by at least two orders of magnitude at higher Eddington ratios. This trend suggests the existence of underlying feedback or fueling dynamics that interlink star formation with SMBH accretion processes.

Nevertheless, for most of the LLAGN in our sample, the *sSFR* experiences a significant drop (approximately -1.4 dex from its mean value) when calculated from 9 arcsec photometry. This is illustrated in the second panel of Figure 5.17, where arrows indicate the change in integrated *sSFR* versus the central *sSFR* for each source, predominantly showing a decrease along the *sSFR* axis. This pattern suggests that LLAGN may predominantly suppress star formation in the central regions of their host galaxies.

These findings indicate that the influence of AGN on star formation extends beyond high-luminosity sources, with LLAGN also affecting their host galaxies' SFRs—primarily within central regions. This impact might also stem from prior AGN activity, leaving an altered LLAGN and ISM as a remnant of such events. Future investigations leveraging the Hα emission as a proxy for the historical activity of the fading AGN (Esparza-Arredondo et al., 2020) could offer further insights into the specifics of each scenario. Nonetheless, a rigorous comparison with inactive galaxies is necessary to address this trend comprehensively. This study only aims to introduce a novel approach to SED modeling for LLAGN and explore its potential applications, leaving a detailed examination of the mechanisms affecting and suppressing star formation for subsequent research.
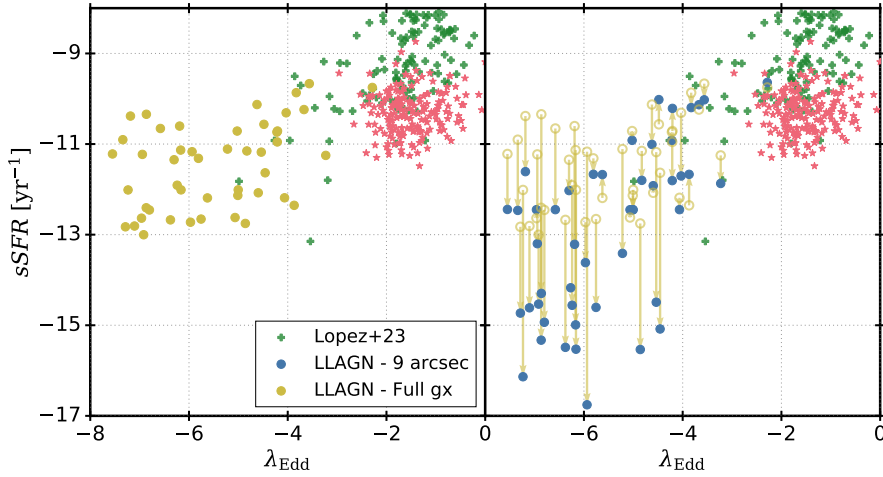
Figure 5.17: Comparison of specific star formation rate (sSFR) versus Eddington ratios across different luminosities and photometry methods. In the left panel, high-luminosity AGN from the BASS survey is represented by red stars, our sample from mini-JPAS by green crosses, while the LLAGN sample, derived from full-galaxy photometry, is shown as yellow dots. The right panel illustrates the adjustment of sSFR for the LLAGN sample when central photometry is applied. Yellow arrows indicate the shift from the initial sSFR values (yellow empty dots) to the recalculated values (blue dots), highlighting a possible localized impact of LLAGN on star formation rates within the galaxy's central regions.

5.5 SUMMARY AND CONCLUSIONS

This work introduces an innovative CIGALE code module tailored to analyze low-luminosity AGN. By implementing empirical relationships and physically-based accretion models, this module enhances our understanding of LLAGN through SED fitting, avoiding commonly used QSO extrapolation. Key findings from our comparison of local LLAGN properties to those of QSOs using this new module include the following:

1. The creation of a specialized CIGALE module for LLAGN SED fitting. This development leverages the empirical L_X–$L_{12\mu m}$ relationship to link AGN X-ray and infrared emissions. It introduces the option of modeling the central engine with both an ADAF and a truncated accretion disk.

2. A comprehensive dataset of 52 X-ray-detected local galaxies, primarily LINERs and Seyferts, was compiled to test and affirm the module's accuracy in lower luminosity ranges. Comparison of these with higher luminosity AGN from the COSMOS and SDSS samples facilitated a robust comparative analysis, validating the

module's effectiveness through its alignment with established reference values.

3. The new module demonstrated exceptional precision in estimating LLAGN bolometric luminosities, effectively mitigating galaxy contamination. This is particularly noteworthy in cases where the central aperture might not entirely capture galaxy emissions (refer to Section 5.4.3).

4. We expand the X-ray to bolometric correction formula to the lower luminosity regime, arriving to do it applicable across ten orders of L_{Bol}. While this formula shows lower values of k_{X} for LLAGN than other assumed values, it is consistent with extrapolations for high-luminosity AGN from similar methodology studies. Our method is compared with standard accretion models, underscoring the robustness and model independence in characterizing the AGN emission across all ranges of luminosities (refer to Fig. 5.11).

5. The analysis of the α_{ox} index revealed patterns that deviate from those seen in the high-luminosity regime. Unlike in QSOs, where α_{ox} demonstrates a correlation with λ_{Edd}, in LLAGN, α_{ox} tends to remain constant or exhibit only weak correlations. This difference may indicate a shift in accretion physics and photon production mechanisms within LLAGN environments (see Fig. 5.16).

6. The *sSFR* decreases by 1.4 dex in mean value from an aperture that includes the entire galaxy to one with a diameter of approximately 1.5 kpc. This suggests a potential feedback mechanism from present or past AGN activity localized at the center of these galaxies (refer to Fig. 5.17).

Our findings substantially advance the characterization and comprehension of LLAGN, a category of active galactic nuclei with significant analytical challenges. These insights pave the way for future explorations into LLAGN's distinctive attributes and impacts, emphasizing the critical role of a multi-wavelength perspective in AGN research.

ID	log $L_{\rm Acc}$ [erg s^{-1}]	$\lambda_{\rm Edd}$	log $L_{\rm Bol}$ [erg s^{-1}]	log $L_{\rm X}^{\rm mod}$ [erg s^{-1}]	log L_{2500} [erg s^{-1} Hz^{-1}]	log $L_{2\ {\rm keV}}$ [erg s^{-1} Hz^{-1}]	$\alpha_{\rm OX}$
NGC1052	42.16 ± 0.23	8.61E-05	42.11 ± 0.15	41.13 ± 0.09	25.12 ± 0.28	23.66 ± 0.81	-0.56 ± 0.42
NGC2273	41.82 ± 0.21	3.29E-05	41.81 ± 0.24	40.90 ± 0.14	24.77 ± 0.27	22.92 ± 0.32	-0.71 ± 0.23
NGC2685	39.35 ± 0.45	6.78E-07	39.30 ± 0.30	38.47 ± 0.16	22.31 ± 0.50	20.74 ± 0.39	-0.60 ± 0.34
NGC2655	42.02 ± 0.31	3.48E-05	42.25 ± 0.08	41.20 ± 0.04	24.97 ± 0.37	24.03 ± 0.06	-0.36 ± 0.16
NGC2768	40.14 ± 0.25	4.21E-07	40.06 ± 0.21	39.17 ± 0.13	23.11 ± 0.30	21.27 ± 0.30	-0.70 ± 0.23
NGC2787	38.43 ± 0.57	7.87E-08	38.62 ± 0.28	37.87 ± 0.20	21.39 ± 0.62	21.48 ± 0.20	0.03 ± 0.31
NGC2841	38.95 ± 0.16	2.82E-08	39.02 ± 0.23	38.13 ± 0.20	21.91 ± 0.22	20.28 ± 0.51	-0.62 ± 0.28
NGC3031	40.96 ± 0.25	6.02E-06	41.12 ± 0.17	40.40 ± 0.05	23.92 ± 0.30	22.12 ± 0.06	-0.69 ± 0.14
NGC3079	40.68 ± 0.02	1.48E-04	40.53 ± 0.02	39.52 ± 0.04	23.64 ± 0.14	21.51 ± 0.18	-0.81 ± 0.12
NGC3147	42.37 ± 0.27	9.28E-05	42.56 ± 0.14	41.82 ± 0.05	25.33 ± 0.31	23.55 ± 0.06	-0.68 ± 0.14
NGC3185	40.45 ± 0.47	9.46E-06	40.41 ± 0.27	39.61 ± 0.07	23.42 ± 0.51	21.57 ± 0.16	-0.71 ± 0.26
NGC3190	41.84 ± 0.27	2.53E-05	41.84 ± 0.15	41.18 ± 0.07	24.78 ± 0.32	25.17 ± 0.08	0.14 ± 0.15
NGC3193	39.64 ± 0.54	1.20E-07	39.68 ± 0.44	38.87 ± 0.28	22.60 ± 0.58	22.32 ± 0.24	-0.10 ± 0.31
NGC3414	41.30 ± 0.26	9.92E-06	41.37 ± 0.08	40.36 ± 0.05	24.27 ± 0.30	22.39 ± 0.13	-0.72 ± 0.16
NGC3516	42.20 ± 0.41	6.20E-05	42.26 ± 0.24	41.44 ± 0.11	25.16 ± 0.46	24.30 ± 0.26	-0.32 ± 0.28
NGC3718	41.32 ± 0.31	2.91E-05	41.66 ± 0.14	41.01 ± 0.06	24.21 ± 0.41	22.88 ± 0.12	-0.51 ± 0.20
NGC3898	39.10 ± 0.14	1.13E-07	38.98 ± 0.15	38.01 ± 0.14	22.06 ± 0.21	21.64 ± 0.27	-0.16 ± 0.18
NGC3945	39.99 ± 0.34	6.89E-07	40.16 ± 0.21	39.34 ± 0.10	22.96 ± 0.39	22.73 ± 0.15	-0.08 ± 0.21
NGC3953	39.25 ± 0.14	6.45E-07	39.45 ± 0.20	38.69 ± 0.14	22.21 ± 0.21	20.55 ± 0.19	-0.63 ± 0.15
NGC3982	42.21 ± 0.13	2.73E-04	42.09 ± 0.09	41.09 ± 0.05	25.18 ± 0.20	23.32 ± 0.19	-0.71 ± 0.15
NGC4036	41.40 ± 0.28	1.38E-05	41.61 ± 0.19	40.80 ± 0.11	24.37 ± 0.33	24.00 ± 0.26	-0.14 ± 0.22
...	...	...	...	...	...	...	...

Table 5.3: Properties obtained from the SED fitting of the LLAGN sample. Luminosities in erg s^{-1}, except for monochromatic luminosities that are in erg s^{-1} Hz^{-1}. For the full table, see López et al. (2024).

6 | M58 AS A CASE STUDY FOR LLAGN FEEDBACK

Understanding the intricacies of the LLAGN population is essential for comprehending its role in the galaxy evolution scenario. Despite a possible general understanding through a deep AGN census across a vast population, the mechanisms of how LLAGN affects its host galaxy remain elusive. Questions abound: Does LLAGN induce a galaxy to form fewer stars like their high-luminosity counterparts? Is this quenching actively occurring on LLAGN, or are its manifestations residual effects of prior AGN activity? Is the ISM impact primarily orchestrated through the radiative prowess of an ADAF or via kinetic radio jets manifested in low-accreting SMBHs?

This Chapter embarks on meticulously examining a single source to shed light on the intricate LLAGN feedback effects. Spectral maps from the Spitzer telescope unveil a conspicuous disk of intensely luminous, warm molecular gas situated in the core of Messier 58, a massive spiral galaxy hosting a radio-loud AGN. Intriguingly, the inner 2.6 kpc of the galaxy appears to be overrun by shocks from the radio jet cocoon. The molecular gas seems shocked in situ, corresponding to lanes of dusty molecular gas that spiral toward the galaxy's nucleus. Both ionized and molecular gas exhibit pronounced kinematic disturbances, marked by velocity dispersions reaching up to 300 km/s.

The dissipation of associated kinetic energy and turbulence, likely injected into the ISM through radio-jet-driven outflows, emerges as a potential driver for the observed molecular and ionized gas emissions within the inner disk. Remarkably, despite the jet and AGN activity, the PAH composition in the inner disk remains seemingly unaffected. PAH ratios align with excitation by the interstellar radiation field originating from aged stars in the bulge, with no discernible contribution from ongoing star formation.

The work presented in this Chapter has been published in Ogle, López et al. (2024), "Radio Jet Feedback on the Inner Disk of Virgo Spiral Galaxy Messier 58" and accepted for publication in the Astrophysical Journal. It offers insights into the profound implications of jet-shocked H_2. This phenomenon holds the potential to significantly curtail star formation, acting as a regulatory force on the stellar mass within the inner disk and the supermassive black hole in an otherwise typical spiral galaxy.

6.1 INTRODUCTION

Low-power radio jets are common in galaxies with AGN (Ho and Ulvestad, 2001; Chiaraluce et al., 2019). While not as dramatic as those in radio galaxies and quasars, these jets play a crucial role in influencing host galaxies and serve as a testing ground for theories related to AGN kinetic feedback. As discussed in Chapter 1, AGN feedback can affect star formation by heating or ejecting interstellar and intergalactic medium (ISM and IGM) (Springel et al., 2005; Croton et al., 2006). This feedback is vital not only in quasar-driven galaxy collisions but also in regulating gas and star formation in the bulges and inner disks of typical spiral galaxies. Low-power jets, for instance, can displace dust, create radio "bubbles," and propel ionized gas away from the galactic center (e.g., Harrison et al., 2015). In the later stages of cosmic evolution, radio jet feedback may help maintain the scaling relations discussed in Chapter 1 in the presence of ongoing gas accretion.

The MOHEG Phenomenon

In Chapter 2, we emphasize the detection of H_2 emission in PDRs around HII regions. In star-forming galaxies, the ratio of H_2 luminosity to total IR luminosity (L_{TIR}, defined as the spectral range between 3-1100 μm) is typically $L(H_2)/L_{TIR} < 0.001$ (Rigopoulou et al., 2002; Higdon et al., 2006; Roussel et al., 2007). However, there are galaxies, termed Molecular Hydrogen Emission Galaxies (MOHEGs), where H_2 emission is notably intense (Roussel et al., 2007), with the ratio reaching values up to two orders of magnitude higher:

$$\frac{L(H_2)}{L_{TIR}} \sim 0.001 - 0.1 \tag{6.1}$$

MOHEGs typically exhibit characteristics such as being luminous in IR (LIRGs), undergoing or having undergone collision processes, being central galaxies in clusters, or being radio galaxies (Ogle et al., 2007, 2010). A study by Ogle et al. (2010) found that one-third of nearby 3CR radio sources (z < 0.22) are MOHEGs. This systematic analysis established criteria based on hard X-ray luminosity, mid-infrared dust emission (24 μm), and PAHs emission to identify the triggering origin of H_2 emission.

For example, the luminosity ratio between H_2 and the PAHs structure at 7.7 μm, for galaxies with normal star formation is $\frac{L(H_2)}{L(\text{PAH 7.7})} \sim$ 0.014, while for MOHEG with radio-jets is $\frac{L(H_2)}{L(\text{PAH 7.7})} > 0.04$. This makes the H_2 emission an excellent tracer of AGN feedback on molecular gas in active galaxies over a wide range of power, including starbursts, LINERs, Seyferts, quasars, and radio galaxies (Higdon et al., 2006; Veilleux et al., 2009; Ogle et al., 2010; Lambrides et al., 2019).

AGN in the *Spitzer Infrared Nearby Galaxies Survey* (SINGS; Kennicutt et al., 2003) indeed show elevated H_2 emission compared to normal, star forming galaxies (Higdon et al., 2006).

NGC 4258, the first detailed study

The first galaxy studied in detail from the SINGS sample was NGC 4258 (Ogle et al., 2014). This case allowed the spatial resolution of the interaction between the jet and interstellar medium using molecular Hydrogen emission. NGC 4258, a nearby spiral galaxy hosting a LINER nucleus and low-power radio jet, exhibited strong H_2 emission along anomalous arms. These arms, where molecular gas is shock-heated by a radio jet along the disk plane, drive ionized outflows (van der Kruit et al., 1972; Ogle et al., 2014; Appleton et al., 2018). The heating of molecular gas to temperatures exceeding 200 K may directly inhibit star formation in the inner disk of this spiral galaxy.

M58, the second detailed study

M58 (NGC 4579) resides in the Virgo Cluster at z=0.00506. It is a massive, star-forming galaxy, with a mass in stars of $1.5 \times 10^{11} M_\odot$ and a dust-corrected star-formation rate of $0.9 M_\odot$ yr^{-1} (de los Reyes and Kennicutt, 2019a,b). Hosting a low-luminosity Seyfert 1.9 or LINER AGN, it has an X-ray luminosity of $L_X = 10^{34.1}$ W and a black hole mass of $M_{BH} \sim 10^{7.8}$ M$_\odot$ (Merloni et al., 2003). The AGN SED lacks a big blue bump component and aligns with an ADAF (Nemmen et al., 2014). VLA 4.9 GHz (D array) and 1.4 GHz (A-array) observations (Fig. 6.1) reveal a radio jet at arcsecond to arcminute scales (Ho and Ulvestad, 2001; Vollmer et al., 2013). This radio jet has a radio power of 1.0×10^{23} W Hz^{-1} measure at 1.4 GHz (Ho and Ulvestad, 2001; Vollmer et al., 2013). VLA C-array observations resolve the jet on the 100 pc scale, approximately aligned with the rotation axis of the galaxy's inner disk (Fig. 1b). Narrow-band ($H\alpha$) imaging shows a bright, kpc-scale disk of ionized gas, and Chandra detects X-ray emission from hot gas closely associated with it (Fig. 1b; Pogge, 1989; Eracleous et al., 2002).

We present Spitzer spectral mapping and Gemini NIRI imaging of M58's inner disk, focusing on the AGN and its radio jet's impact on molecular and ionized gas in the central few kpc. This analysis is supported by archival ALMA CO 2-1 observations, ground-based and *HST* multi-band imaging, and optical spectroscopy. Adopting the SN 1989M (type Ia) distance of 21 Mpc (Ruiz-Lapuente, 1996), we calculate sizes and luminosities, with the corresponding spatial scale being 101 pc/arcsec.
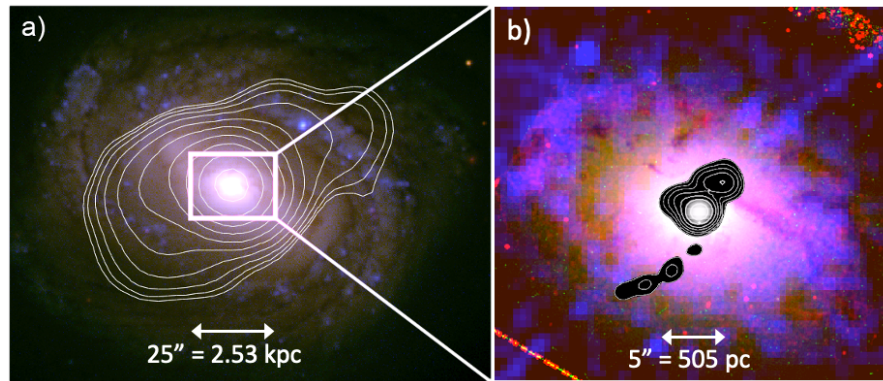
Figure 6.1: Archival multiwavelength observations of M58 with a close-up of the kpc-scale disk. *a)* SDSS *u*, *g*, *r* (blue, green, red) image with 4.9 GHz surface brightness contours of the radio jet from the VLA D array. *b) HST* Hα (red) and F547M continuum (green), *Chandra* 0.5-8 keV X-rays (blue), and radio contours from the VLA at 1.4 GHz (A array). The blue, diagonal streak is an artifact of the *Chandra* readout. Both images are roughly centered on the AGN (RA = 189.43134°, Dec = 11.81819°), with standard orientation.

6.2 OBSERVATIONS

6.2.1 Spitzer Spectral Maps

M58 was observed as part of a Spitzer IRS program to study the effects of AGN on their host galaxies (PI Smith, J.D. - Program 3471). M58 was mapped using slit-stepping with both the SL and LL low-resolution gratings. The SL cubes cover 5.2-14.3 μm, with a pixel scale of 1.''85/pixel and a resolving power of 60-127. The LL cubes cover 13.9-38.3 μm, with a pixel scale of 5.''07/pixel and a resolving power of 57-126. We utilize only the central $55.5'' \times 55.5''$ regions of the maps covered by both gratings. The simultaneous background, covering an off-galaxy location, was subtracted from the map. We constructed spectral cubes using `cubism` (Smith et al., 2007a).

We use a novel method[1] to model and measure MIR spectral feature strengths and derived quantities in the *Spitzer* IRS spectral cubes. First, we fit each spaxel using a combination of dust continuum, PAH feature, and emission line models, similar to those used by `pahfit` (Smith et al., 2007b), utilizing the python package `lmfit` for Levenberg-Marquardt least-squares fitting (Newville and al., 2023). Next, we use the best-fit spectral parameters for each spaxel to generate feature flux maps. Finally, we use line and feature ratios and equivalent widths to identify and extract spatial regions with distinct MIR spectra. We note that this is a less biased, empirical way of identifying, grouping, and extracting spaxels than the more common method of extracting spectra

---

1 https://github.com/ie-lopez/MPF/tree/main

in circular or elliptical apertures. We let the data tell us which regions to extract, and spatially disjoint regions with similar spectra can be combined for the highest possible spectral S/N. We do not consider the instrumental PSF when fitting the spectral cube. However, linking the fit parameters of associated spectral features (e.g., all PAH features or all H_2 lines) helps to mitigate spatial and spectral sampling issues at the initial spaxel-fitting stage, and combining multiple spaxels in the subsequent spectral extractions and model fitting largely averages over any sub-PSF variations.

6.2.2 Gemini NIRI Imaging

Data were obtained using the Near InfraRed Imager (NIRI) on the Gemini-North Telescope at Mauna Kea in Hawaii during semester 2021A (program GN2021A-Q-137, PI: I.E. Lopez) on nights with the best photometric quality (IQ20%). The observations were designed to map H_2 emission in high spatial resolution, resolving structures down to ~ 40 pc. We used the narrow-band filter G0216 to isolate the H_2 1-0 S(1) line centered at 2.12 μm and the *K*-continuum filter centered at 2.09 μm to obtain the continuum emission. The f/6 configuration was adopted, providing a field of view of 120□″, pixel size of 0.″117, and median seeing FWHM of 0.″35. We applied a dithering pattern to cover the gaps and remove the sky background, cosmic rays, and bad pixels. In each filter, we coadded sets of 8×30 sec exposures to avoid saturation of the galaxy's center. In total, each filter has an exposure on-source of 2160 seconds. Using darks and flat frames, we corrected for thermal emission, dark current, and hot pixels. We also applied a flux calibration using images from both narrow filters of the standard star FS132. We used Gemini Observatory's software DRAGONS (Data Reduction for Astronomy from Gemini Observatory North and South) for the data reduction (Labrie et al., 2019).

6.2.3 Optical Narrowband Imaging

We observed M58 in Hα + [NII] with the f/3.2, 0.7m Jeanne Rich Telescope (Rich et al., 2019) in order to image ionized gas across the galaxy to low surface brightness levels. The FLI09000 CCD camera has 2.″23 pixels and a 0.57 deg^2 ($45' \times 45'$) field of view. We took $\sim 300 \times 5$ minute exposures (25 hr) in a custom four nm-wide interference filter, centered at 660.5 nm; and $\sim 120 \times 5$ minute (10 hr) in a custom 20 nm-wide offband continuum filter centered at 644 nm. The on-band filter was designed to cover the Hα emission line over a redshift range of $z = 0.0050 - 0.0084$ and also includes the adjacent [NII] emission lines. The observations were strongly dithered to minimize background gradients and to allow building the flat with the science images. The reduction was done with standard subtrac-

tion of averaged bias and dark images. The flat was constructed by masking the science images with `SExtractor` (Bertin and Arnouts, 1996) and `NoiseChisel` (Akhlaghi and Ichikawa, 2015), which after normalization and combination, produces the flat. The astrometry was calculated using the `Astrometry.net` software package (Lang et al., 2010) and SCAMP (Bertin, 2006). The images were photometrically calibrated to SDSS and sky subtracted with a conservative procedure using Zernike polynomials, avoiding an over-subtraction of the images. Finally, all images were combined with a weighted mean. The emission line flux is calibrated against the flux measured inside an $r = 37''$ diameter by Theios et al., 2016: $F(\text{H}\alpha+[\text{NII}]) = 2.5 \times 10^{-15}$ W m^{-2}.

6.2.4 Optical Spectroscopy

We observed M58 with the Kast Double Spectrograph on the 3m Shane Telescope at Lick Observatory on May 26, 2022. We used the 600/4310 grating to cover a wavelength range of 3500-5600Å on the blue side and the 1200/5000 grating to cover 5760-6790Å on the red side. We used a 2$''$0-wide slit, giving a spectral resolution of $\sigma = 0.90$Å (40 km s^{-1}) at 6600Å. This long slit, with a length of 400$''$, was oriented at PA $= 57$ deg. The detector samples the spectrum at 1.02 Å/pixel on the blue side and 0.65 Å/pixel on the red side. We extracted spectra in 29 variable-sized spatial regions along the slit. Data reductions included bias subtraction, flat-fielding, cosmic ray rejection, off-source background subtraction, wavelength calibration using an internal lamp spectrum, flux calibration with a standard star, and correction for wavelength-dependent atmospheric extinction. Given the sky background variability on a timescale of 10 min, primarily from artificial light pollution that changes with elevation, it was necessary to utilize a region along the slit that had the weakest source signal to make an additional background correction.

6.2.5 Archival Data

In addition to the VLA data described at Chapter 6, we utilize the PHANGS-ALMA v4.0 CO 2-1 data cube and moment maps for M58 from the ALMA data set (ADS/JAO.ALMA#2017.1.00886.L: P.I. Schinnerer; Leroy et al., 2021a,b). The maps have 1$''$ angular resolution and $\sim$ 2.5 km s^{-1} velocity resolution. We utilize photometry from the PACS instrument (Poglitsch et al., 2010) on the ESA Herschel Space Observatory(Pilbratt et al., 2010) to measure the cold dust mass. Multi-band *HST* imaging in the F791W, narrowband F658N, and offband F547M filters provide a high-resolution view of Hα and dust absorption (Fig. 6.1). *GALEX* FUV imagery traces recent star formation. Chandra ACIS-S imaging spectroscopy (Obs. ID 807;
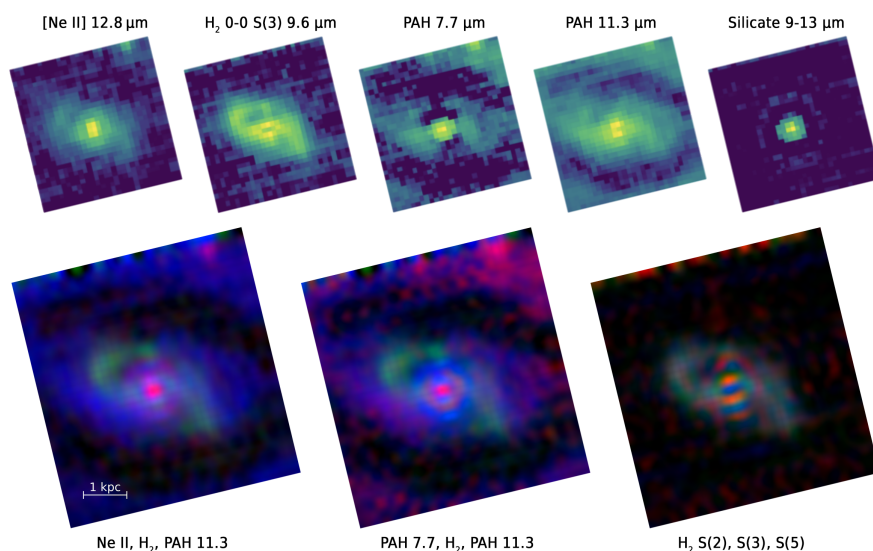
Figure 6.2: *Spitzer* spectral feature maps of M58, extracted from the IRS SL spectral data cube. Top: individual feature maps at native resolution, centered on the nucleus, and at the standard orientation. The silicate dust emission is localized to the unresolved AGN point source and follows the $\sim 10-13\ \mu$m PSF. Bottom: multicolor feature maps covering the same area but resampled to a finer grid using sinc interpolation. Bottom left: $r, g, b = $ [NeII] 12.8 μm, H_2 S(3) 9.6 μm, PAH 11.3 μm. Both the AGN and a star-forming region in the NW spiral arm show up as red, neutral PAH emission from diffuse ISM blue and shocked molecular gas green. Bottom center: $r = $ PAH 7.7 μm, $g = H_2$ S(3) 9.6 μm, $b = $ PAH 11.3 μm. Ionized PAH emission appears red, neutral PAH emission blue, and warm molecular gas green. Bottom right: $r, g, b = H_2$ S(2), S(3), S(5) pure rotational lines, following warm molecular gas over a range of temperatures. Note: The airy rings of the AGN PSF, increasing in diameter with wavelength, are not real structures in the galaxy.

Eracleous et al., 2002) highlights emission from hot ($\sim 10^7$ K) gas at the galaxy center (Fig. 6.1).

6.3 RESULTS

As Fig. 6.2 shows, the nucleus of M58 is bright in all MIR spectral components, including ionized gas, H_2, PAH features, and warm dust. Silicate emission at 9-13 μm from warm dust heated by the AGN is only detected in a central, unresolved point source, following the *Spitzer* PSF. The inner ($r = 2.6$ kpc) disk is traced by diffuse 11.3 μm PAH emission. The 7.7 μm PAH feature and the [NeII] 12.8 μm line are enhanced in star-forming regions found in the NW spiral arm of the galaxy that passes through the corner of the maps.

The most striking feature in the *Spitzer* spectral maps shown in Fig. 6.2 is the unusually luminous, extended H_2 pure rotational line emission in the inner disk. The Gemini NIRI image of the H_2 1-0 S(1) rovibrational line at 2.12 μm shown in Fig. 6.3 has a very similar spatial distribution to the lower energy H_2 pure-rotational lines and similar flux to the H_2 0-0 S(3) line (Table 6.1). The $\sim 10\times$ higher resolution Gemini image clearly shows that the warm H_2 follows the dust lanes resolved by *HST*.

There is a weaker association of H_2 with molecular gas traced by the ALMA CO 2-1 map (Fig. 6.3; Leroy et al., 2021b). There appear to be significant differences in the spatial distribution of warm H_2 rovibrational emission and CO 2-1. In particular, the H_2 emission is most intense closest to the nucleus and radio jet. In contrast, the CO 2-1 emission appears to peak along the spiral dust lanes just exterior to the nucleus, with additional clumps along the outer circumference of the inner disk. The H_2 emission shows similar clumping in the inner disk but lacks a detailed correspondence to the clumps in the CO 2-1 maps. The CO 2-1 lines most likely trace cooler, denser clumps than H_2 1-0 S(1), which are nonetheless also shock-heated, as revealed by their unusually high surface brightness compared to CO 2-1 in the outer spiral arms of the galaxy.

The [NeII] 12.8 μm emission from ionized gas in the inner disk follows a similar pattern to that seen in H_2, suggesting that it is closely associated with the warm molecular gas and energized by the same source (Fig. 6.2). Similarly, Hα + [NII] correlates with H_2 in the dust lanes seen in the *HST* image (Fig. 6.3). Additional diffuse ionized gas emission surrounds the nucleus and fills the inner disk.

6.4 DISCUSSION

As described in Chapter 6, we fit the individual spaxels in the *Spitzer* spectral cube with a combination of dust continuum, PAH, and emission line features. Then, we use the models to create feature flux maps for all model components showcased in Fig. 6.2. Next, we use the PAH 7.7/11.3 and H_2 S(3) / PAH 11.3 μm ratios measured from these maps to identify zones with distinct MIR spectra (Fig. 6.4: SF Zone, inner disk Zones 1, 2, and 3, and NUC). These ratios indicate the relative contributions of star formation, diffuse ISM, and shocks to the MIR spectra. Spaxels in the SF Zone were selected to have PAH 7.7/11.3 > 0.9, and those in inner disk Zones 1-3 PAH 7.7/11.3 $<= 0.9$. Zones 1-3 were further selected to have H_2 S(3) / PAH 11.3 in the ranges < 0.25, 0.25–0.7, and > 0.7, respectively. The nucleus was not identified by feature ratios. Instead, we sum the spectrum of the spatially unresolved nucleus (NUC) inside a 5×5 spaxel (934 pc $\times$ 934 pc) box centered on the AGN point source, covering the central

FEATURE	SF	ZONE 1	ZONE 2	ZONE 3	NUCLEUS
PAH 6.2	16.4 (1.1)	17.0 (1.9)	18.1 (3.0)	2.5 (0.9)	15.0 (3.3)
PAH 7.7	49.6 (3.2)	35.4 (5.4)	39.0 (8.8)	6.0 (1.0)	51.8 (4.7)
PAH 8.6	11.8 (0.7)	7.8 (1.2)	$\cdots$	$\cdots$	$\cdots$
PAH 11.3	24.8 (1.3)	47.9 (2.2)	61.7 (3.4)	8.8 (1.2)	47.2 (4.4)
PAH 12.0	6.4 (0.8)	12.4 (1.4)	17.5 (2.2)	2.7 (0.7)	6.0 (2.7)
PAH 12.6	13.7 (0.7)	22.9 (1.2)	29.2 (1.8)	$\cdots$	17.2 (2.0)
PAH 17	10.2 (2.0)	20.6 (5.7)	28.8 (7.3)	5.8 (1.3)	19.0 (4.4)
PAH 6.2/11.3	0.66 (0.05)	0.36 (0.04)	0.29 (0.05)	0.28 (0.11)	0.32 (0.08)
PAH 7.7/11.3	2.00 (0.17)	0.74 (0.12)	0.63 (0.15)	0.69 (0.14)	1.10 (0.14)
PAH 8.6/11.3	0.48 (0.04)	0.16 (0.03)	$\cdots$	$\cdots$	$\cdots$
PAH 12.0/11.3	0.26 (0.03)	0.26 (0.03)	0.28 (0.04)	0.31 (0.09)	0.13 (0.06)
PAH 12.6/11.3	0.55 (0.04)	0.48 (0.03)	0.47 (0.04)	$\cdots$	0.36 (0.05)
PAH 17/11.3	0.41 (0.08)	0.43 (0.12)	0.47 (0.12)	0.66 (0.17)	0.40 (0.10)
H_2 0-0 S(5) 6.91	0.92 (0.34)	2.21 (0.60)	12.62 (0.94)	3.46 (0.32)	10.09 (1.49)
H_2 0-0 S(4) 8.03	0.35 (0.29)	$\cdots$	5.17 (0.96)	1.41 (0.28)	3.38 (0.62)
H_2 0-0 S(3) 9.66	0.85 (0.16)	6.05 (0.33)	22.85 (0.57)	7.07 (0.19)	14.62 (0.73)
H_2 0-0 S(2) 12.28	0.53 (0.19)	2.19 (0.32)	8.29 (0.51)	2.64 (0.18)	4.37 (0.59)
H_2 0-0 S(1) 17.04	1.38 (0.33)	9.06 (0.54)	14.77 (0.70)	3.54 (0.18)	9.35 (1.80)
H_2 0-0 S(0) 28.22	0.33 (0.07)	0.81 (0.16)	0.70 (0.20)	0.14 (0.07)	0.66 (0.33)
H_2 S(1)/ H_2 S(0)	4.2 (0.3)	11.2 (0.2)	21.1 (0.3)	25.3 (0.5)	14.2 (0.5)
H_2 S(3)/ PAH 11.3	0.034 (0.007)	0.13 (0.01)	0.37 (0.02)	0.80 (0.11)	0.31 (0.03)
H_2 1-0 S(1)	$\cdots$	$\cdots$	33.1 (1.0)	6.70 (0.20)	19.4. (0.58)
$H\alpha+$ [NII]	9.26 (0.09)	22.45 (0.02)	76.34 (0.08)	20.82 (0.02)	97.07 (0.10)
Solid Angle [$\square''$]	281.	541.	318.	92.	86.
T_l	50	150 (20)	240 (20)	300 (20)	160 (60)
n	4.8 (0.2)	5.3 (0.2)	4.9 (0.2)	5.4 (0.3)	4.3 (0.3)
$M(H_2^{warm})$	3.4×10^7	5.4×10^6	2.2×10^6	3.7×10^5	3.0×10^6
M_{dust}	4.5×10^5	1.3×10^6	1.7×10^6	$\cdots$	2.8×10^5
$M(H_2^{warm})/ M_{dust}$	76	4.2	1.3	$\cdots$	11
F(CO 2–1)	48.	76.	286.	119.	194.
L'(CO 2–1)	1.3×10^7	2.0×10^7	7.7×10^7	3.2×10^7	5.2×10^7
M_{gas}(CO 2–1)	5.2×10^7	8.2×10^7	3.1×10^8	1.3×10^8	2.1×10^8
M_{gas} / M_{dust}	115.	63.	182.	$\cdots$	750.
$L(H_2$ S(0) – S(3))	1.6 (0.2)	9.6 (0.4)	24.6 (0.6)	7.1 (0.2)	15.3 (0.7)
$L(H\alpha+$ [NII])	4.89 (0.05)	11.85 (0.01)	40.29 (0.04)	10.99 (0.01)	51.23 (0.05)
L(CO 2-1)	0.02	0.031	0.116	0.048	0.078
L(2-10 keV) $\cdots$	$\cdots$	$\cdots$	$\cdots$	$\cdots$	200.

Table 6.1: M58 Line Fluxes and other properties derived. In general, fluxes are in 10^{-17} W m^{-2}, masses in $M_\odot$, temperatures in K and luminosities in 10^{32} W. In particular, F(CO 2-1) is measured in Jy km s^{-1} and L'(CO 2-1) in K km s^{-1} pc^2.
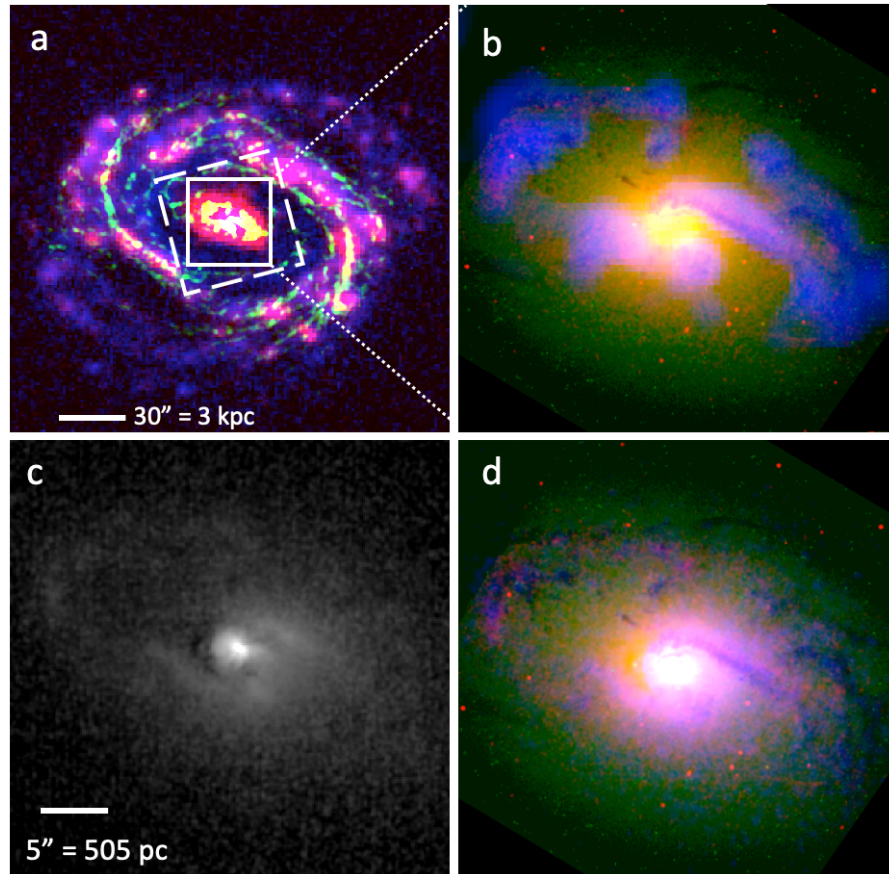
Figure 6.3: a) Hα+[NII], CO 2-1, and GALEX FUV (r, g, b) image of M58.
While the outer disk features star formation along the spiral arms,
the inner disk is weak in FUV emission but strong in Hα+[NII]
emission from jet-shocked ionized gas. The long-dashed bound-
ary indicates the region mapped by Spitzer IRS. b) *HST* Hα+[NII],
F547M continuum, and CO 2-1 (r, g, b). Ionized gas emission
peaks at the nucleus but also correlates with molecular gas in
the dust lanes. (c) Gemini NIRI image of H_2 1-0 S(1), tracing
shock-heated warm molecular gas. (d) *HST* Hα+[NII], *F457M*
continuum, and H_2 1-0 S(1) (r, g, b) image of M58 inner disk.
There is a rough correspondence between the two warm molecu-
lar gas tracers, but the H_2 emission is relatively stronger in the
nucleus and inner spiral. Clumpy H_2, CO, and ionized gas are
found along the outer edge of the inner disk. Lower surface
brightness ionized gas emission is found throughout the inner
disk. All images are centered on the AGN with the north up.
Zoomed-in panels b, c, and d are all at the same scale.

peak of the PSF. We model the summed spectra of each zone, allowing
all PAH feature fluxes to vary independently, and tabulate the feature
fluxes of the best-fit models for the zones in Table 6.1.

6.4.1 PAH Ratios Unaffected by Jet Feedback

The PAH 7.7/11.3 ratio is primarily an indicator of PAH ionization level, set by the UV radiation field. It is typically highest in PDRs associated with regions of active star formation (Draine and Li, 2007; Chastenet et al., 2023). Most of the SF zone spaxels fall in the NW spiral arm at the corner of the map Fig. 6.4, where our Hα image shows an abundance of discrete star-forming HII regions (Fig. 6.3). We estimate the star formation rate using the prescription SFR(PAH 7.7) = $2.4 \times 10^{-9} L$(PAH 7.7) (Roussel et al., 2001). The mean SFR surface density in the SF Zone is $\Sigma_{SFR} = 5.7 \times 10^{-3} M_\odot$ kpc^{-2}, roughly twice the mean for the whole galaxy (de los Reyes and Kennicutt, 2019a,b).
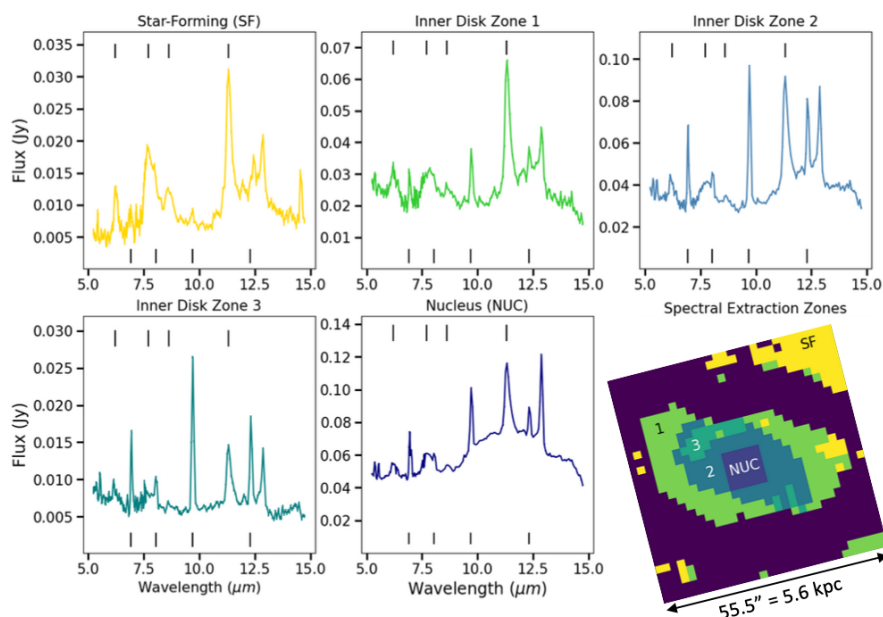
Figure 6.4: *Spitzer* IRS spectra of M58 regions selected by PAH 7.7/11.3 μm and H$_2$ S(3)/PAH 11.3 μm feature ratios. At standard orientation, a color-coded map of spaxels included in each spectral extraction zone is given at the bottom-right. PAH feature wavelengths (6.2, 7.7, 8.6, 11.3 μm) are indicated at the top of each panel, and H$_2$ 0-0 pure rotational lines at the bottom (S(5), S(4), S(3), S(2)). The PAH 7.7/11.3 ratio is high in the SF Zone and low in the other zones where star formation is absent. The H$_2$ S(3) / PAH 11.3 μm ratio, highest in Zone 3, reflects the fraction of shock-heated molecular gas.

In comparison, there is relatively little star formation in Zones 1-3 of the inner disk, which display low PAH 7.7/11.3 ratios. The PAH 6.2/11.3 and PAH 8.6/11.3 ratios, which track ionization, are also lower in the inner disk than in the SF Zone (Table 6.1). The bright ionized gas emission in this region has emission line ratios characteristic of shocks or LINER photoionization rather than star formation (discussed in Section 6.4.7). Furthermore, the FUV continuum surface brightness

of the inner disk is low, and there are no obvious clumps in the *HST* Hα + [NII] image attributable to star formation (Fig. 6.3). We estimate SFR(PAH 7.7) < $0.03 M_\odot$ yr^{-1} and a mean SFR surface density of < $3 \times 10^{-3} M_\odot$ kpc^{-2} in Zones 1-3, combined. On the other hand, an ultracompact nuclear ring of young stars with a radius of 150 pc is seen at NUV wavelengths by *HST* (Comerón et al., 2008). The elevated UV field in this ring may account for the slightly elevated PAH 7.7/11.3 ratio in the nucleus (1.1) compared to the inner disk (0.6-0.7).

LLAGN are often found in the bulges of massive galaxies where there is little star formation activity, and their radio luminosity correlates with bulge mass (Nagar et al., 2005). Star formation may be suppressed in such an environment by radio-jet feedback, morphological quenching (Martig et al., 2009), or the increased velocity dispersion of gas in the gravitational field of the bulge (Gensior et al., 2020). The PAH 7.7/11.3 ratios of 0.6-0.7 observed in Zones 1-3 are comparable to those found for dusty elliptical galaxies that lack star formation (Kaneda et al., 2008). The PAH emission from the inner disk of M58 (and elliptical galaxies) is most likely excited by the interstellar radiation field from old stars in the galaxy bulge, as demonstrated for dust continuum emission in the bulge of M31 (Groves et al., 2012).

It has been suggested that AGN X-rays or shocks may destroy small PAH molecules and thereby lower the PAH 7.7/11.3 ratio in galaxies with AGN activity (Smith et al., 2007a; Diamond-Stanic and Rieke, 2010; García-Bernete et al., 2022; Zhang et al., 2022). However, it is difficult to disentangle the effects of PAH size distribution and UV ionization level on the PAH 7.7/11.3 ratio (Draine et al., 2021). Notably, there is no significant variation in the PAH 7.7/11.3 or other PAH ratios across Zones 1-3, in spite of their differences in H_2 surface brightness and H_2 / PAH 11.3 ratio. This may indicate that the PAH composition is insensitive to the relatively weak shocks from the low-power radio jet that are heating the H_2.

There is a strong correlation between the PAH 17 μm and PAH 11.3 μm feature intensities in SINGS galaxies, as both arise from neutral PAHs (Smith et al., 2007a). Moreover, the PAH 17/11.3 ratio strongly depends on the size of PAHs ((Draine and Li, 2007)). Notably, the literature suggests that galaxies hosting a LLAGN might exhibit an enhancement in the PAH 17 μm emission compared to those without an AGN (Kaneda et al., 2008), hinting at the potential contribution of AGN feedback to the presence of large PAHs in interstellar space. However, we find normal levels of PAH 17 emission in all regions of M58 (Table 6.1), with PAH 17/11.3 = $0.4 - 0.7$, compared to 0.35-0.72 for the SINGS sample. The PAH 17/11.3 ratio is the same in the inner disk and SF zone. The relatively large uncertainty in the PAH 17 μm measurement for the nucleus precludes a definitive statement on whether or not it is enhanced.
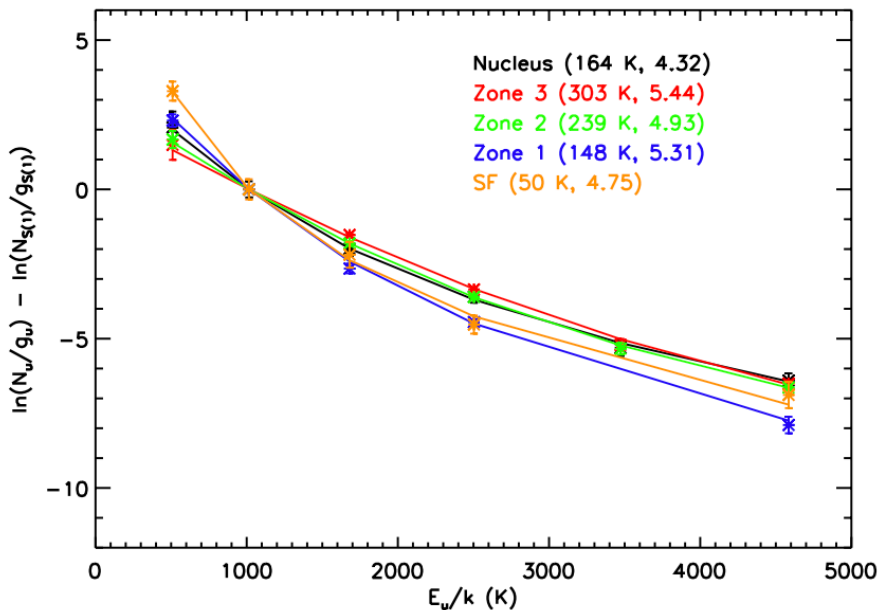
Figure 6.5: H_2 excitation diagrams for each zone, including pure-rotational line levels S(0) through S(5). Column densities (data points) are normalized to the H_2 0-0 S(1) upper level, for comparison purposes. The power-law model fits the temperature distribution of each zone indicated by the solid lines, with fit parameters (T_l, n) given in parentheses (see also Table 6.1). The SF region has the highest H_2 0-0 S(0) upper-level column density, consistent with a relatively cooler temperature distribution.

6.4.2 Shock–Heated Molecular Gas

We present H_2 fluxes in Table 6.1. We expect the H_2 0-0 S(3)/ PAH 11.3 ratio to roughly follow the ratio of warm (> 150 K) H_2 to total gas mass, assuming that the PAH 11.3 carrier abundance is constant, which may hold true in the absence of significant metallicity and ionization variations. The summed H_2 0–0 S(0)–S(3) line over PAH 7.7 has been used as a shock indicator in radio galaxies (Ogle et al., 2010), but has the disadvantages of (1) being affected by photoionization in PDRs, (2) the weakness of PAH 7.7 emission in a low UV field, and (3) requiring measurement of four H_2 lines. We recommend using H_2 0-0 S(3)/ PAH 11.3 instead, which is less sensitive to PAH ionization and only requires the measurement of two adjacent spectral features.

We find a H_2 S(3) / PAH 11.3 ratio of 0.034 ± 0.007 in the SF Zone, consistent with PDR emission. The ratio is much greater in the inner disk, ranging from 0.13 at its outer edge (Zone 1) to its greatest value of 0.80 in Zone 3. Its value in the nucleus is also high (0.31 ± 0.03). We suggest that shocks and turbulence driven by the radio jet cocoon or jet-driven outflows may be responsible for the very luminous, extended H_2 emission that we observe in the inner disk of M58.

We fit the H_2 excitation diagram for each spectral zone with a power-law temperature distribution $dN/dT \sim T^{-n}$ (Fig. 6.5; Table 6.1), following the method of Togi and Smith (2016). A continuous temperature distribution is expected for molecular gas with a range of densities, and a power-law distribution provides a good fit to the data. This is preferable to two-temperature models, which arbitrarily split the temperature distribution into two bins. The power-law model is parameterized by the power-law index n, the minimum detectable H_2 temperature T_l, and the total warm H_2 mass. It is clear from the excitation diagrams (Fig. 6.5) and H_2 0-0 S(1)/H_2 0-0 S(0) ratios (Table 6.1) that the SF region has relatively more H_2 at cooler temperature than do the inner disk and nucleus. Our best-fit temperature distribution models have $n = 4.32 - 5.44$, similar to values for the SINGS galaxy sample, which have a mean value of $n = 4.84 \pm 0.61$ (Togi and Smith, 2016). For constant T_l, smaller values of n indicate relatively more molecular gas at high temperatures. For constant n, larger values of T_l indicate relatively more warm gas contributing to the H_2 emission lines. We find that n is relatively constant in the inner disk but that T_l increases from 150 K in Zone 1 to 300 K in Zone 3, following the trend of increasing H_2 surface brightness and H_2 / PAH 11.3 ratio. Conversely, the nucleus has lower T_l than Zone 3 and Zone 2, consistent with its lower H_2 / PAH 11.3 ratio. As expected, the SF region has T_l of 50 K, below which the H_2 lines are not effectively emitted.

The total warm H_2 mass in the inner disk and nucleus is $1.1 \times 10^7 M_\odot$. In comparison, the total H_2 mass within $r = 2.1$ kpc, estimated from the CO 1-0 flux is ~ 50 times greater, at $5 \times 10^8 M_\odot$ (García-Burillo et al., 2009). Similarly, we estimate a cold molecular mass of $5.2 \times 10^8 M_\odot$ from the ALMA CO 2-1 flux in the same region, assuming the standard $\alpha_{CO} = 4 M_\odot$ / (K km s^{-1} pc^2) and $R_{21} = 0.6$. However, the CO mass estimates are sensitive to the distribution of molecular gas temperature. In the shocked inner disk of M58, both lines are enhanced at the elevated temperatures that we measure for warm H_2, leading to an overestimate of the molecular gas mass.

6.4.3 Dust Mass and PAH Abundance

To estimate the dust mass in each zone, we measured photometry from GALEX FUV and NUV, SDSS *ugriz*, our Gemini Ks image, *Spitzer* IRAC bands 1-4, PAH 7.7, 11.3 μm, MIPS 24 μm, and Herschel PACS 70, 100, and 160 μm bands (Fig. 6.6). We fit each SED with a grid of CIGALE models (Boquien et al., 2019; Nersesian et al., 2019; Yang et al., 2020), using a Chabrier IMF with solar metallicity and delayed star formation history for the stellar population, modified by dust extinction. We use the dust emission models of Draine et al. (2014), with dust grain densities reduced by a factor of 0.81 compared to Draine and Li (2007). We turned off the nebular emission, which
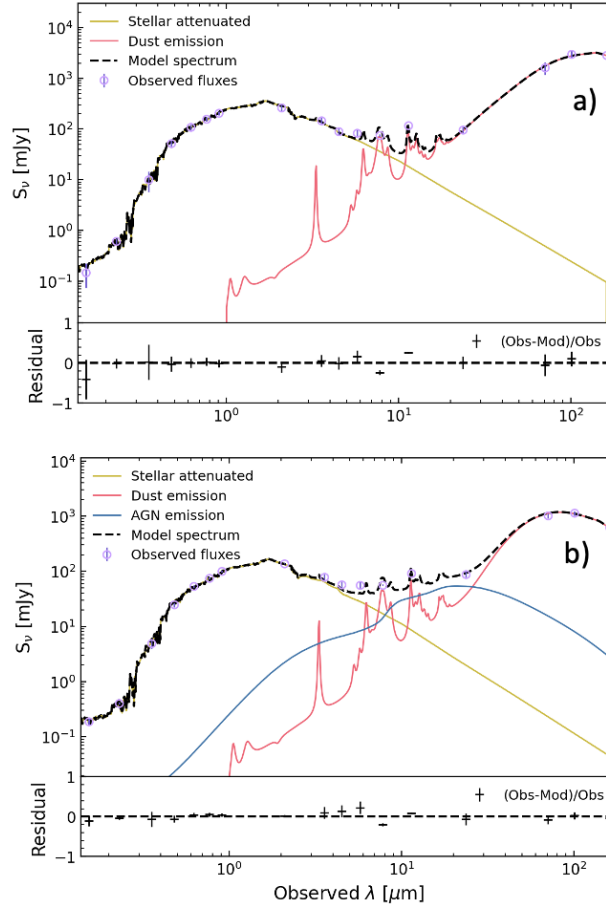
Figure 6.6: a) SED of M58 Inner Disk Zones 1-3, including a dust-attenuated stellar population and emission from dust and PAH molecules. b) SED fit of the nucleus, including hot dust emission from the AGN.

would otherwise require shock modeling. The best-fit dust model has a PAH mass fraction $q_{PAH} = 0.019 \pm 0.003$, apparently lower than that of the diffuse ISM in the solar neighborhood ($q_{PAH} = 0.045$). However, CIGALE doesn't self-consistently account for the SED incident on the PAH molecules. Draine et al. (2014) find that a similar value of $q_{PAH} = 0.02$ in the central 1kpc of M31 corrects to 0.04-0.05 after properly accounting for the SED of the bulge stars. Assuming a similar correction applies at the center of M58, the actual q_{PAH} appears to be consistent with the Galactic ISM and M31, with no indication of PAH depletion.

The dust masses derived from our SED fits of each zone are given in Table 6.1 (except Zone 3, which is too small to resolve at long wavelengths). We find a total dust mass of $M_{dust} = 3 \times 10^6 M_\odot$ from our fit of the combined SED of Zones 1-3, excluding the nucleus. Assuming a standard dust mass percentage of 1%, this corresponds to a total gas mass of $3 \times 10^8 M_\odot$. The molecular gas mass estimated
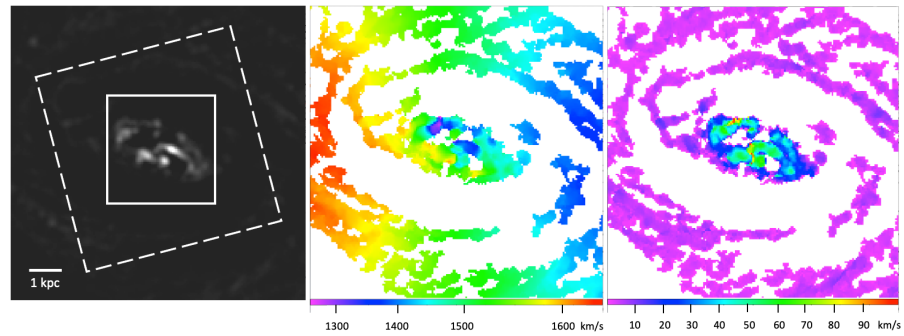
Figure 6.7: ALMA CO 2-1 emission line moments 0, 1, and 2 from PHANGS-ALMA (Leroy et al., 2021b). The dashed and solid squares correspond to the *Spitzer* IRS map in Fig. 6.2 and the Gemini H$_2$ 1-0 S(1) image in Fig. 6.3. The brightest CO 2-1 emission correlates with high-velocity dispersion in Zones 2 and 3 of the inner disk and in the nucleus.

before from CO (1-0) and (2-1) is a factor of 1.8 greater than this, confirming that shocks throughout the inner disk are boosting these CO emission lines. In the nucleus, the CO 2-1 line is boosted by a factor of ~ 8 relative to dust emission, indicating even more heating of molecular gas by the jet. Using the lower gas mass estimated from dust and assuming that most of the gas in the inner disk is molecular yields warm H$_2$ percentages of $1 - 4\%$ in Zones 1 and 2. On the other hand, Zone 1 and the SF zone have $M(\text{CO 2-1})/M_{\text{dust}}$ values that are consistent with the Galatic value of ~ 100, indicating that the CO emission is not boosted in the outer part of the inner disk. Evidence for jet shock-heated CO is found under similar conditions in NGC 4258, where the standard α_{CO} value yields a molecular gas mass estimate that is $\sim 10\times$ greater than that inferred from the dust mass estimated from SED-fitting (Ogle et al., 2014).

It is also instructive to compare the warm H$_2$ mass to the dust mass in each spectral zone (Table 6.1). First, we find $M(\text{warm H}_2)/M(\text{Dust})$ ~ 80, close to the Galactic value of ~ 100 in the SF region. Because of the low T$_l$ value in the SF region, there is a large contribution to the H$_2$ emission from cold gas and we recover almost all of the gas mass. On the other hand, the H$_2$ emission in the inner disk is dominated by gas with $T > 150 - 300$ K, and the H$_2$ line fluxes are insensitive to the presence of colder molecular gas. This is reflected in low values of $M(\text{H}_2)/M_{\text{dust}} = 1 - 4$. Colder molecular gas may be present, but its emission would be relatively faint and difficult to separate from the emission of the warmest gas.

6.4.4 Comparison of H$_2$ and AGN Energetics

The X-ray luminosity of the nucleus measured by XMM and Chandra, $L(\text{2-10 keV}) = 2.0 \times 10^{34}$ W (Bianchi et al., 2009), is not enough to

power the observed H_2 luminosity of the inner disk plus nucleus, $L(H_2$ S(0) - S(3)) = 5.7×10^{33} W. The CO 1-0 and CO 2-1 luminosities from the same region are only 3.0×10^{30} W and 2.7×10^{31} W, respectively, and contribute relatively little to cooling the molecular gas. Following Ogle et al. (2010), the maximum conversion efficiency of X-ray heating, referenced to the 2-10 keV band luminosity is about 0.01, whereas the observed ratio is much greater: $L(H_2)/L_X = L(H_2$ S(0) - S(3)) / L(2-10 keV) = 0.29. This is similar to 3C radio galaxies (Ogle et al., 2010), where the AGN X-ray luminosity is also not luminous enough to power the observed H_2 emission. The relatively low X-ray luminosity of the AGN may also explain why it has no apparent impact on the PAH size distribution. If the X-rays from the AGN are not luminous enough to heat the molecular gas across the kpc-scale inner disk significantly, perhaps they are also ineffective at destroying PAH molecules there. We do not rule out a more significant role for X-ray heating in the unresolved nucleus.

6.4.5 Molecular Gas and Dust in the Spatially Unresolved AGN

The spiral of dusty warm molecular gas found in the galaxy center may be the primary source of fuel powering the AGN. The *Spitzer* NUC zone, with $r = 4.6''(465$ pc), contains 33% of the H_2 flux in the inner disk, both for the H_2 0-0 S(1) and H_2 1-0 S(1) lines, and 27% of the warm H_2 mass ($3 \times 10^6 M_\odot$). Our SED fit of the diffuse ISM plus dusty torus in the NUC region yields a cold ISM dust mass of $3 \times 10^5 M_\odot$, corresponding to a gas mass of $3 \times 10^7 M_\odot$. The close correspondence between the spatial profiles of the pure-rotational and rovibrational lines means that we can reasonably scale the *Spitzer* NUC values to estimate the warm H_2 mass within the Gemini NIRI PSF. Most of the H_2 1-0 S(1) flux in the inner disk is resolved by Gemini NIRI (Fig. 6.3), with only 3% contained within $r = 0.35''(35$ pc) of the nucleus. Assuming a constant ratio for H_2 1-0 S(1) / H_2 0-0 S(1) yields an unresolved warm H_2 mass of $\sim 9 \times 10^4 M_\odot$ within this radius. Scaling the dust mass yields a ten times larger total gas mass of $\sim 9 \times 10^5 M_\odot$ within $r = 35$ pc.

As noted above, the nucleus displays point-like continuum emission at 9-13 μm from silicate dust heated by the AGN. Our model of the NUC SED (Fig. 6.6) employs the SKIRT two-phase dusty torus model (Stalevski, 2012; Stalevski et al., 2016b). The SED fit does not include the full *Spitzer* IRS spectrum and, therefore, does not yield the most accurate torus parameters. For reference, the best-fit torus model from our SED fit has an inclination of $i = 50°$, optical depth $\tau = 3$, and polar dust temperature of 230 K, consistent with the observed silicate emission. Regardless of the large uncertainties in the model, we do obtain a robust torus IR luminosity of $L_{\mathrm{torus}} = 3.7 \times 10^{34}$ W that is

consistent with the AGN bolometric luminosity of $L_{\text{bol}} = 1.0 \times 10^{35}$ W. (Merloni et al., 2003).

We leave a more detailed analysis of the dusty torus spectrum to future work (see Section 7.1). Together with the existing ALMA CO observations, our upcoming *JWST* MIRI MRS and NIRSpec IFU observations of the full complement of H_2 pure rotational lines will give the mass, temperature distribution, and kinematics of molecular gas available to fuel the AGN on 10-100 pc scales. They will also map the kinematics and determine mass outflow rates of any ionized or molecular gas outflows. This will enable us to determine if AGN jet feedback is effective at throttling AGN accretion.

6.4.6   Highly Turbulent CO Kinematics Driven by Jet Feedback

M58 shows evidence of disturbed molecular gas kinematics, as observed in CO 1-0 and 2-1, including components that do not follow the regular rotation curve of the galaxy (Fig. 6.7; García-Burillo et al., 2009; Leroy et al., 2021b; Stuber et al., 2021). In Fig. 6.8, we show the ALMA CO 2-1 line profiles extracted from the zones of the inner galaxy where we performed our analysis of the *Spitzer* spectral maps Fig. 6.8. Since these lines are integrated over a range of rotational and peculiar velocities, they are broader than the velocity dispersion seen in the spatially resolved map. Relatively narrow line components ($\sigma = 19 - 36$ km s^{-1}) are found in the SF Zone and Zone 1, following the regular rotation of the galaxy disk. Zones 2 and 3 of the inner disk and the nucleus show much broader line components ($\sigma = 60 - 120$ km s^{-1}). The integrated CO 2-1 line profile of the inner disk plus nucleus shows a single broad peak with $\sigma = 100$ km s^{-1} (FWHM $\sim$ 240 km s^{-1}). Of note is the broad blue wing in Zone 3, which can be seen as an anomalously blue-shifted emission against the regular rotation of the galaxy disk, which might indicate a molecular outflow component.

The inner disk has a markedly higher velocity dispersion than the surrounding galaxy disk (Fig. 6.7). The brightest CO 2-1 emission occurs where the velocity dispersion is $\sigma_{\text{CO}} = 40 - 60$ km s^{-1}, compared to a median of ~ 10 km s^{-1} outside of the inner disk. While we do not have direct H_2 kinematic information, we assume it has a similar velocity dispersion to the CO 2-1 emitting molecular gas. Under this assumption, we estimate the turbulent kinetic energy of the $3 \times 10^6 M_\odot$ of warm H_2 in Zones 2 and 3 to be $\sim 6 \times 10^{45}$ J, for $\sigma_{\text{CO}} \sim 50$ km s^{-1}. The corresponding turbulent energy dissipation time for $L(H_2 \text{ S(0) - S(3)}) = 3 \times 10^{33}$ W is only 7×10^4 yr. That means that H_2 is a very effective coolant, and the turbulent kinetic energy must be replenished with ongoing kinetic energy deposition by the jet and/or AGN-driven outflows in order to maintain the observed H_2 luminosity.
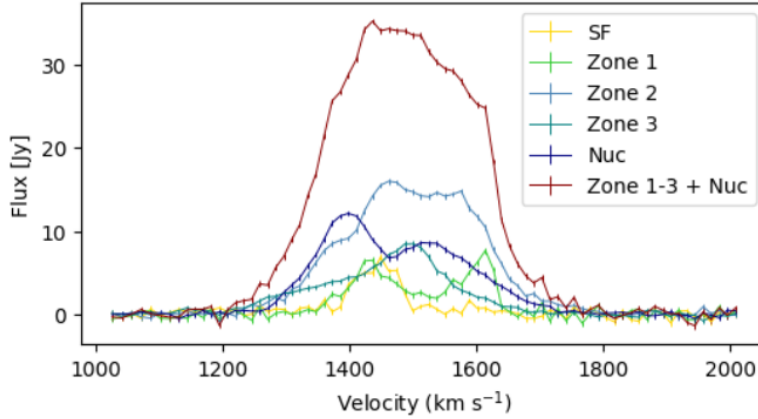
Figure 6.8: ALMA CO 2-1 emission line profiles for the SF Zone, inner disk Zones 1-3, Nucleus, and summed over Zones 1+2+3+Nucleus.

The high temperature and velocity dispersion of the warm H_2 are hostile to star formation. At the observed minimum temperature of $T_l \sim 250$ K and density equal to the H_2 o-o S(3) critical density of $n \sim 10^4$ cm^{-3}, the Jeans mass is $\sim 900 M_\odot$. Star formation is unlikely to proceed under these conditions. However, since the warm H_2 percentage is only 1-4%, it remains to be seen if star formation may proceed in the cooler, less turbulent cloud cores. The overall lack of star formation in the inner disk suggests that conditions are, in fact, not conducive to it. However, the presence of a circumnuclear ring of young stars demonstrates that conditions may have been more favorable for star formation at that location in the recent past.

6.4.7 Jet Shock–Ionized Gas with Disturbed Kinematics

We measured ionized gas line fluxes and kinematics from our long-slit optical spectroscopy, extracted along PA = 57 deg (Fig. 6.9). We used a Bagpipes (Carnall et al., 2018) 12 Gyr-old burst model, with exponential decay to model the average stellar population in the inner disk and bulge. A more detailed fit and discussion of the stellar population are outside the scope of this paper. We scaled and subtracted the template from our 2D spectra to remove the stellar continuum, which would otherwise have a large effect on our emission line measurements. We simultaneously fit Gaussian profiles to Hα and the [NII] doublet, tying together the line widths. The [NII] doublet flux ratio was fixed to 1:3 as required by atomic physics, but the [SII] doublet ratio was allowed to vary since it is sensitive to density. We use the [NII] 6583.45 Å line center and width to measure velocity and velocity dispersion, and correct the velocity dispersion for the instrumental resolution of $\sigma = 40$ km s^{-1}.

We find star-forming emission line ratios at the ends of the long slit, where it extends to cover the spiral arms of the galaxy (Fig. 6.10).
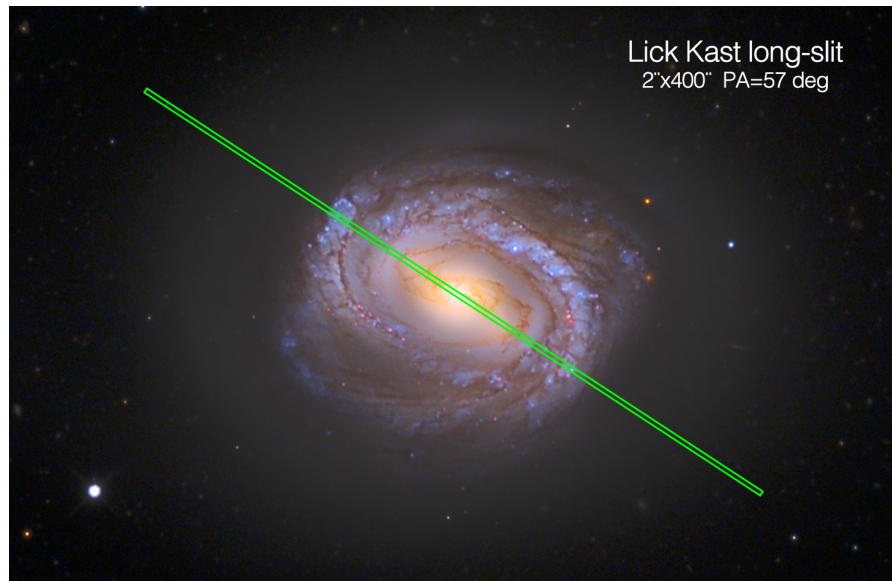
Figure 6.9: Position of the long-slit along the major axis of M58 from wich we derived the optical spectra show in Figs. 6.10 and 6.11.

These star-forming regions follow the overall rotation of the galaxy. For an assumed disk inclination of 36 deg, we find a deprojected rotation speed of ± 236 km s^{-1} at a distance of 52$''$ (5.2 kpc) from the galaxy center. The velocity dispersion is low (< 70 km s^{-1}), and the lines are marginally resolved or unresolved, given the instrumental spectral resolution.

The ionized gas kinematics in the inner disk are highly disturbed (Fig. 6.11), with velocity offsets of -130 to $+300$ km s^{-1}. The velocity dispersion in this region ranges from 90-310 km s^{-1}, reaching values considerably higher than the CO velocity dispersion ($\sigma_{\mathrm{CO}} < 120$ km s^{-1}). The [N$\textsc{ii}$] surface brightness profile declines with increasing radius outside of $r = 15''$ (1.5 kpc) and breaks at $r = 23.8''$ (2.4 kpc), perhaps delimiting the furthest extent of significant AGN and radio jet influence.

At all locations in the inner disk and nucleus of M58, we find [N$\textsc{ii}$]/H$\alpha = 1.5 - 2.1$, [O$\textsc{i}$]/H$\alpha = 0.16 - 0.38$ and [S$\textsc{ii}$]/H$\alpha = 0.7 - 1.6$, characteristic of shocked gas or LINER photoionization (Veilleux et al., 1995). Emission from any star-forming regions in the inner disk is overwhelmed by the extended, high-surface brightness emission from shocked gas or the AGN. We compare shock models from the MappingsV database (Sutherland and Dopita, 2017; Alarie and Morisset, 2019), for solar abundance and a characteristic magnetic field strength of 30 μG, to the observed optical line ratios (Fig. 6.12). Taken together, the line ratios are jointly consistent with the models for a narrow range of shock velocities ($V_{\mathrm{sh}} = 210 - 260$ km s^{-1}). However, a broader range of velocities is allowed ($V_{\mathrm{sh}} = 170 - 440$ km s^{-1}) if each line is emitted under different conditions. This range of shock ve-
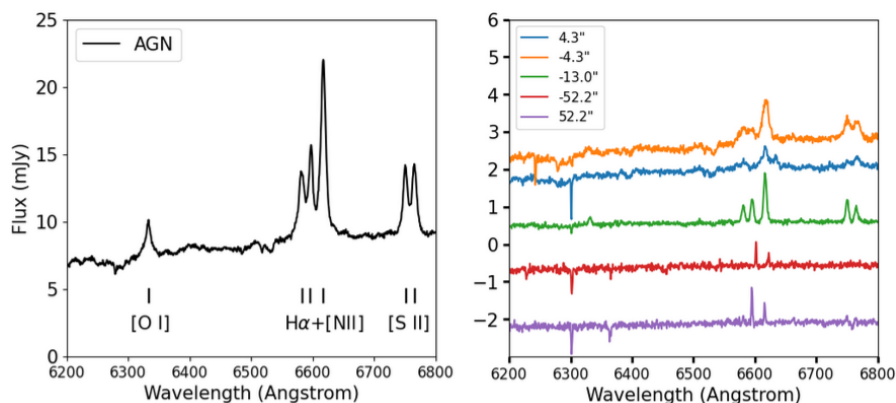
Figure 6.10: Lick Kast long-slit optical spectra along the major axis of M58. Left: The LINER AGN spectrum, extracted in an $2''2$ wide aperture, displays quite broad forbidden emission lines. Right: Spectra labeled by distance from the nucleus. The forbidden emission lines and Hα are very broad within $10''$ (1 kpc) of the AGN, but become narrower at larger distances. The inner disk shows LINER-like line ratios along its entire extent. The emission lines from star-forming regions in spiral arms at 5.3 kpc (offset in flux for clarity) are much narrower and show velocity offsets owing to galaxy rotation.

locities is broadly consistent with the observed velocities and velocity dispersion of the ionized gas.

We use our JRT image (Fig. 6.3) to measure the Hα+ [N II] doublet emission line fluxes in the zones identified in the *Spitzer* maps (Table 6.1). The H$_\alpha$+ [N II] line luminosity of the inner disk (Zones 1-3) is 6.3×10^{33} W. Utilizing the optical line ratios observed in our Lick spectrum, we estimate a total optical emission line luminosity of $\sim 9 \times 10^{33}$ W from the inner disk, ~ 1.7 times its H$_2$ pure-rotational line luminosity (L(H$_2$ S(0) - S(5)) = 5.4×10^{33} W). Modulo other unmeasured emission lines, this indicates that similar kinetic power is dissipated in the warm molecular and ionized gas phases of the inner disk.

6.4.8 Prevalence of Jet–Shocked Molecular Gas in Nearby Galaxies with Massive Bulges

The presence of strong H$_2$ emission in galaxies with AGN was clearly demonstrated by *Spitzer* (Roussel et al., 2007; Smith et al., 2007b; Diamond-Stanic and Rieke, 2010; Ogle et al., 2010). We plot H$_2$ 0-0 S(3) / PAH 11.3 against PAH 7.7/11.3 to compare H$_2$ emission from shocks versus star formation (Fig. 6.13). The SINGS galaxy nuclear spectral types are given by Dale et al., 2006; Smith et al., 2007b, based on the spectroscopy of Moustakas and Kennicutt, 2006. Almost all of the star-forming, non-AGN galaxies in the SINGS sample fall in
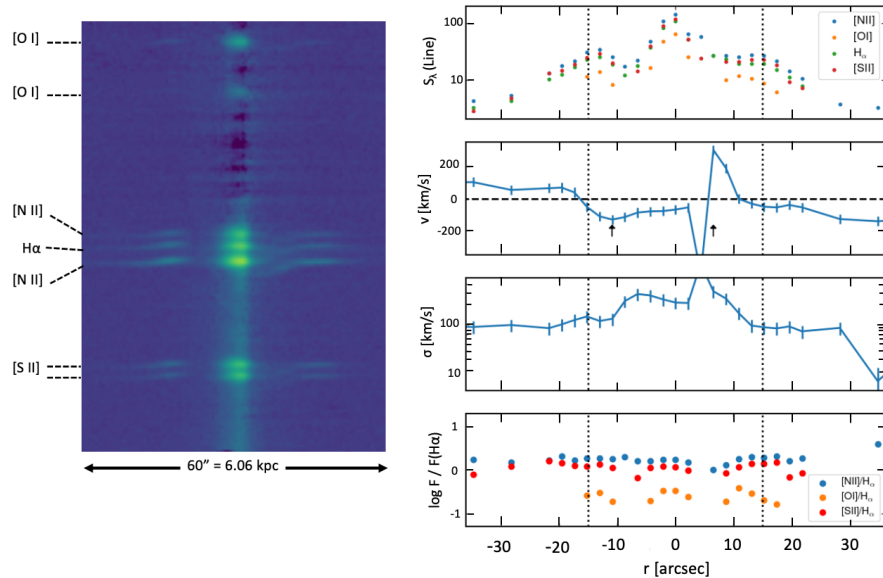
Figure 6.11: Ionized gas lines in the inner disk. Left: 2D spectrum of [OI] 6300, 6363, Hα + [NII], and the [SII] doublet. The continuum has been subtracted using a stellar population model. The dark horizontal bands are from atmospheric H_2O absorption. Right: Emission line surface brightness [1×10^{-17} W m^{-2}□$''^{-1}$], line-of-sight velocity, velocity dispersion, and line flux ratios with respect to Hα. Velocity is corrected for an offset of 146 km s^{-1} from the CO 2-1 systemic velocity of 1480 km s^{-1}. Velocity dispersion is corrected by subtracting the instrumental resolution of 40 km s^{-1} in quadrature. The ionized gas is kinematically disturbed, showing large redshifts and blueshifts relative to the galaxy rotation curve at the arrowed locations. Velocity and velocity dispersion go off scale at the location of the line splitting, where the single-velocity component fit is inadequate. Line ratios are consistent with shock heating and/or LINER photoionization.

the lower right corner of this diagram, indicating weak H_2 emission and PAH emission dominated by PDRs powered by hot, young stars. Seyfert galaxies, on the other hand, generally have H_2/ PAH 11.3 > 0.02, indicating shocked molecular gas. Most LINER AGN have less H_2 emission, though several (6/17) do have elevated H_2/ PAH 11.3, indicating shocked molecular gas. As discussed by Diamond-Stanic and Rieke, 2010, for Seyferts, there appears to be an anti-correlation between H_2 and PAH 7.7 relative to PAH 11.3, with the strongest H_2 emitters having the least PAH 7.7 in their nuclei. They suggest that this may reflect the destruction of small PAHs by shocks. Instead, we suggest that this may be a direct consequence of star-formation suppression in galaxy centers by AGN feedback.

M58 has extremely high H_2/ PAH 11.3 in its inner disk, on par with the 3C radio galaxies (Ogle et al., 2010). NGC 4258 (not in the
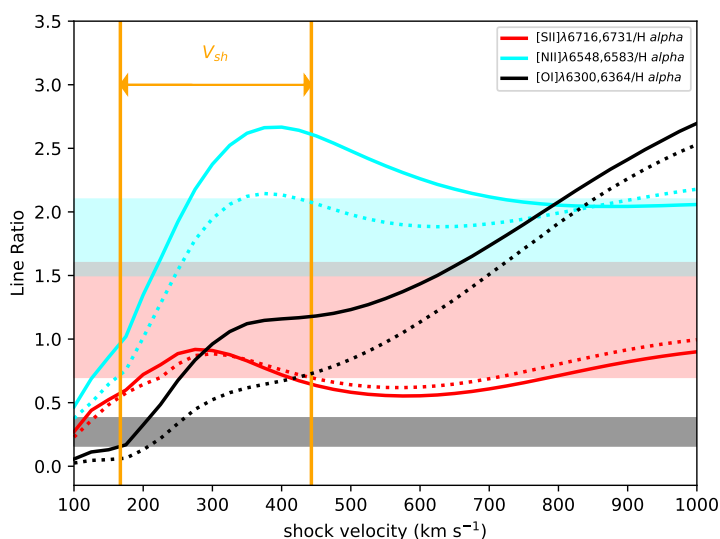
Figure 6.12: Shock models from the MappingsV database, for solar abundance, 30 μG magnetic field, and two ionized gas densities (solid, dotted: $n = 100$, 10 cm^{-3}). The shaded areas show the observed ranges for three optical line ratios, which individually match the models for shock velocities in the range $V_{\rm sh} = 170 - 440$ km s^{-1}.

SINGS sample) also shows extremely strong H_2/ PAH 11.3 emission associated with its radio jet (Ogle et al., 2014). In fact, eight of the SINGS galaxies with H_2/ PAH $11.3 > 0.05$ have radio-loud AGN. Half of these are E/S0 galaxies (NGC 1266, 1316 = Fornax A, 4125, 4552), and the other half are early-type spirals with large bulges (NGC 2841, 4450, M58, 4725). All but one have weak PAH 7.7 μm emission in their *Spitzer* spectra, indicating little star formation in the galaxy center. The one exception is the peculiar, post-starburst galaxy NGC 1266, which has ongoing nuclear star formation and is well known for its jet-driven molecular outflow (Alatalo et al., 2014). All of these galaxies have massive bulges and supermassive black holes capable of launching radio jets. The association of excess H_2 emission with radio-loud AGN supports the hypothesis that the warm molecular gas in these galaxies is heated by radio jet feedback. The lack of star formation in the centers of these galaxies is also consistent with the hypothesis that this feedback mechanism suppresses star formation.

6.4.9 Multiphase Jet–Disk Interaction

Our *Spitzer* IRS and Gemini observations of the inner disk of M58 reveal copious emissions in pure rotational and rovibrational lines of warm H_2. As we have shown, this emission is too luminous to be powered by X-rays from the AGN. Similar power is emitted in
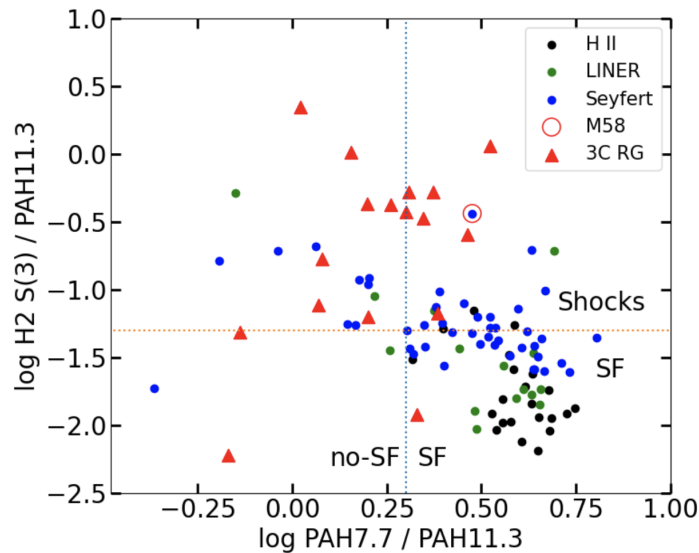
Figure 6.13: Shocks vs. star formation. Feature flux ratios for galaxy nuclei compiled from the SINGS sample (Roussel et al., 2007; Smith et al., 2007b), supplemented by 35 RSA Seyferts (Diamond-Stanic and Rieke, 2010), and 3C radio galaxies (Ogle et al., 2010). The H_2 0-0 S(3) / PAH 11.3 flux ratio is > 0.05 in galaxies with shocked molecular gas. The large value of this ratio in Seyferts and radio galaxies is indicative of AGN kinetic feedback. The PAH 7.7/ PAH 11.3 ratio is a good indicator of star formation, falling in the range of 2.0-6.0 for most spiral galaxies and < 2.0 for elliptical galaxies. M58 has H_2 0-0 S(3) / PAH 11.3, comparable to the most extreme 3C radio galaxies.

optical emission lines from ionized gas in the region, with line ratios indicative of shock-heating. Both molecular and ionized gas have large velocity dispersion, providing a reservoir of kinetic energy and turbulence that may be the proximate power source for the high surface brightness line emission. M58 is one of eight radio-loud AGN in the SINGS sample that display luminous H_2 emission and H_2/PAH 11.3> 0.05, supporting the idea that the radio jet may be the primary power source in the kpc-scale disk. Extended X-ray emission is also found in the inner disk of M58, perhaps tracing the edges of the hot radio jet cocoon, where it intersects dense gas associated with the spiral molecular gas lanes (Fig. 6.1).

We suggest that the rich phenomenology described above can be explained by the interaction of the M58 radio-jet cocoon with the ISM of the inner disk. Unlike the anomalous arms in NGC 4258 (Ogle et al., 2014), where the radio jet is initially directed in the plane of the disk, the morphology of the shocked molecular and ionized gas emission in M58 is consistent with a radio jet orientation perpendicular to the disk. The radio jet drives an energy bubble into the ISM, intersecting the inner disk in a roughly circular footprint. The spiral structure inside this footprint comes from dusty molecular gas organized in a spiral

lane that converges on the galaxy's nucleus. The waist of the radio jet cocoon, as delimited by the region of highest CO velocity dispersion and surface brightness, is currently restricted to a radius of 1.6 kpc. Lower surface brightness emission from H_2 and ionized gas out to 2.6 kpc (in Zone 1) may be energized by residual turbulence in gas that has been disturbed by prior radio outbursts that have expanded outward to this larger radius.

We estimate the M58 jet power to be $P_{jet} \sim 2 \times 10^{36}$ W from its 1.4 GHz radio power of $\nu S_\nu = 1.4 \times 10^{32}$ W, using the relation of Cavagnolo et al., 2010, which is based on the measurement of jet cavity powers for low-power radio jets. The power we measure in the H_2 S(0) - S(3) pure rotational and optical ionized gas lines amounts to $\sim 0.2\%$ and 0.5%, respectively, of this jet power estimate. The jet power is, therefore, more than sufficient to drive the observed line emission from the inner disk. Only a tiny percentage of the jet power is deposited into the inner disk, since the jet has escaped the confines of the disk, extending at least seven kpc into the galaxy halo.

The energy of the hot radio jet cocoon may be transferred directly to the molecular gas by shocks driven into the spiral lanes by the cocoon or by a higher-density wind of ionized gas that blows outward from the nucleus. Similar phenomenology is seen in planetary nebulae(e.g., O'Dell and Handron, 1996), where a hot, ionized wind ablates knots of molecular gas, forming cometary tails of molecular gas that emit strongly in H_2 (see Farber and Gronke, 2022, for hydrodynamical simulations of these clouds). The high systematic velocity offsets of ionized gas that we observe may be consistent with ionized outflow. Further, more detailed spectral mapping of ionized gas in the inner disk is needed to confirm this.

Our description of the radio-jet AGN feedback in M58 is both motivated and supported by hydrodynamical simulations of the propagation of radio jets through a clumpy, multi-phase ISM (Mukherjee et al., 2016, 2018; Meenakshi et al., 2022). The jet-disk simulations (Mukherjee et al., 2018) only employ powerful jets ($P_{jet} = 10^{38} - 10^{39}$ W), typical of radio galaxies, so a quantitative comparison of our results with these simulations is not possible. Instead, we compare our results to the simulations of lower-power jets ($P_{jet} = 10^{36} - 10^{38}$ W), comparable to the M58 jet, propagating in an initially spherical ISM geometry (Mukherjee et al., 2016). These simulations show that the radio jet creates a hot energy bubble in the ISM, surrounded by a forward shock. Dense clouds are shredded and accelerated in the hot energy bubble, creating a wind. Low-power jets like the M58 jet are trapped for a longer time than high-power jets, potentially hollowing out a large cavity in the ISM. However, low-power jets are less effective than high-power jets at accelerating clouds to high velocities, with outflows attaining velocities of < 300 km s^{-1}, comparable to the ionized gas velocities we observe in M58. The simulations do not

include a molecular gas component, so there is no direct prediction of the effects of the jet on the H_2 temperature and velocity dispersion.

6.5 SUMMARY AND CONCLUSIONS

We find high-surface-brightness H_2 and CO emission from warm molecular gas in the inner ($r = 2.6$ kpc) disk of the spiral galaxy M58. This corresponds to emission of similar brightness from ionized gas lines and thermal X-ray emission. The optical forbidden line ratios from ionized gas in the inner disk are consistent with shock heating by low-velocity shocks ($V_{sh} = 170 - 440$ km s^{-1}). We suggest that the molecular and ionized gas emissions are excited by shocks and turbulence driven by the radio jet cocoon and radio-jet-driven outflows into the multi-phase ISM. The observed high-velocity dispersion of the molecular and ionized gas serves as reservoirs of kinetic energy that must be constantly replenished to support the observed H_2 and ionized gas line luminosity.

The PAH mass fraction and feature ratios in the inner disk of M58 indicate normal PAH abundances for solar metallicity gas, with no significant contribution from star-forming regions. The PAH emission is likely excited by the diffuse radiation field from old stars in the bulge of M58. There is no indication of PAH destruction by jet-driven shocks or X-rays from the AGN.

Eight other massive, nearby galaxies observed by *Spitzer* show high H_2 0-0 S(3)/PAH 11.3 (> 0.05), similar to M58 and the 3C radio galaxies. All of these H_2-luminous galaxies have radio-loud AGN. This supports a picture where radio-jet feedback is very disruptive to gas in galaxy centers, driving shocks and turbulence that heat both the ionized and molecular ISM. The high molecular gas temperatures and turbulence in the inner disk of M58 are certainly not conducive to star formation and may be a signature of negative radio-jet feedback on star formation. On the other hand, most Seyfert galaxies show lower levels of enhanced H_2 emission, possibly excited by less powerful radio-quiet AGN outflows. The observed anticorrelation between H_2 and PAH 7.7 μm emission in Seyferts indicates that radio-quiet AGN may also suppress star formation.

Part IV

CONCLUSIONS AND FUTURE DIRECTIONS

7 │ CONCLUDING REMARKS

This thesis provides a comprehensive exploration of various facets of active galaxies, spanning from their peak of activity at cosmic noon until the local population of the lowest luminosities. The investigation encompasses host galaxy properties, the impact of supermassive black holes and their accretion activity on the interstellar medium, star formation, and the overall galaxy buildup. Our research has always employed a multi-wavelength approach, leveraging data spanning from X-ray to radio wavelengths over the entire Ph.D. program to gain a holistic understanding of these intriguing astrophysical entities.

Our research has made significant contributions to our understanding of AGN and their impact on galaxy evolution. We developed a method to exploit the narrow-band data from J-PAS to characterize AGN accretion properties while constraining the host galaxy properties at the same time. With that, we create a toy model that, based on a few assumptions, can model the evolution of these sources forward until the relation is noticed in the local universe. On this track from cosmic noon until now, we have started to consider the LLAGN population more central, usually left aside from X-ray surveys because of their intrinsic low-luminosity and/or their host galaxy contamination problem. We develop a module for a popular SED fitting code that considers non-standard accretion modes, and with that, we recover the hidden AGN in these sources. This can impact future work since an easy-to-use tool exists to incorporate them in larger samples now. This could lead to a new generation of census on LLAGN, with the upcoming data of new surveys. Finally, we put the magnifying glass on one of these LLAGN to understand the mechanism of how it affects the ISM. Understanding LLAGN feedback and constraining its effects can lead to heavy implications for our broader understanding of galaxy evolution and the mechanisms that regulate star formation and feedback processes in the universe.

We presented 3 main pieces of work, all interconnected and detailed below.

1. In Chapter 4, we explore the coevolution of SMBHs with their host galaxies by studying a sample of X-ray-selected AGN out to z∼2.5 from the ∼1 deg² covered in the miniJPAS survey. We derive robust physical parameters for the host galaxies and central SMBHs using SED fitting and single-epoch spectroscopy. We also roughly get an idea of the X-ray obscuration on these

sources using the hardness ratio. The SED fitting is done from photometric data from X-ray to infrared, using a large number of surveys and centering in the narrowband filter from miniJPAS. The spectra fitting is done by combining diverse telescopes and carefully fitting the broad lines of each of these sources.

Our analysis reveals possible differences between the Eddington ratios and its commonly used proxy $L_X/M_\star$. These differences can be explained since our sources do not follow the mass scaling relation that links $M_\star$ with M_{BH} and is used to calibrate the Eddington ratios proxy. Additionally, we investigate three different evolutionary scenarios for the SMBH and host stellar masses to forward-modeling these sources until z=0 and compare it with the local scaling relation. From this analysis, we deduce that there is a shared connection between SFR and accretion, although this association is not present at all the moments in the the entire cosmic evolutionary process. The best evolutionary scenario is when the SFR and accretion are coupled for the activity period but decouple completely when accretion expels so much energy that it can tear apart the galaxy.

2. Chapter 5 delves into the realm of low-luminosity AGN by developing a novel module for SED fitting tailored specifically for their analysis. This module incorporates empirical relations that relate the emission of the central engine at X-ray and IR wavelengths and physically motivated accretion models following accretion flows and truncated accretion disk, enabling us to characterize the AGN properties of LLAGN accurately. We validate our module for a large sample of well-studied AGN and for a sample of local galaxies that fulfill classification as LLAGN. This module can work even in full-galaxy contamination since we include the contribution from the expected binary population from the stellar emission.

From the SED fit of these galaxies, we derive an X-ray bolometric correction lower than other works in the literature. We also prove that this bolometric correction is reliable since it is accretion model-independent. We also show that the α_{ox} index showcases deviations from the high-luminosity regime. We also prove that the LLAGN impact on the sSFR is similar to the AGN sample from Chapter 4, but it mainly affects the center of the galaxy ($\sim$1.5 kpc)

3. Chapter 6 focuses on a particular case of how an LLAGN impacts the ISM of its host galaxy. Using *Spitzer* observations of the spiral galaxy M58, we found high-surface-brightness H_2 from warm molecular gas in the inner disk at a kpc scale, along with emission of similar brightness from ionized gas lines and thermal X-ray emission. Using high-resolution images from Gemini, we

resolve the H_2 emission in the center of the galaxy, showing the same structure as CO from ALMA and dust lanes from HST.

The temperature of the inner disk, calculated through H_2 excitation diagrams, is higher than the temperature observed in the spiral arms, where stars are forming. Through PAH ratios and SED fitting, we determine that the star formation is suppressed in the inner disk, while the PAH is not being destroyed as happen in more luminous AGN. The optical forbidden line ratios from ionized gas indicated shock heating by low-velocity shocks, suggesting that the molecular and ionized gas emissions are excited by shocks and turbulence driven by the radio jet cocoon and radio-jet-driven outflows. The high-velocity dispersion of the molecular and ionized gas served as reservoirs of kinetic energy that must be constantly replenished in order to support the observed H_2 and ionized gas line luminosity. In addition, we analyzed H_2 and PAH emission from a sample of eight other massive, nearby galaxies and found that they exhibit high H_2 0-0 S(3)/PAH 11.3 ratios, similar to M58 and typical radio-loud galaxies. All of these H_2-luminous galaxies have radio-loud AGN, suggesting that radio-jet feedback is a key driver of the observed H_2 emission and the disruption of the ISM.

7.1 FUTURE DIRECTIONS

In Chapter 4, we emphasized the significance of narrow-band and medium-deep optical photometry in characterizing host galaxy properties of AGN at moderate to high redshift. The comprehensive capabilities of J-PAS are poised to increase sample sizes exponentially, shedding more light on galaxy evolution studies. In the future, the synergy between extensive X-ray surveys, such as the first all-sky eROSITA survey (Merloni et al., 2024), and the broader sky coverage provided by J-PAS will enable the replication of our study with a significantly larger sample. This expanded dataset will facilitate the implementation of advanced statistical techniques to comprehend better the influence of host galaxy parameters on accretion ratios. Additionally, extracting black hole masses from J-spectra, particularly for brighter, more massive sources, becomes feasible. Furthermore, the excellent photo-z estimation for AGN obviates the need for a spectrum, thus enabling a comprehensive study of the coevolution scenario.

Moving forward, our research should concentrate not only on enlarging sample sizes but also on incorporating more detailed modeling of AGN and their feedback mechanisms. By delving into these diverse aspects of AGN, we aim to deepen our understanding of these enigmatic objects and their role in shaping the cosmos. In particular, the SED fitting module introduced in Chapter 5 opens up opportunities

to extend our analysis to lower luminosities, correlating with lower accretion ratios, and thus to a realm where other types of feedback dominate. Also, in this case, the combination of eROSITA and J-PAS can effectively constrain the luminosity function ($\Phi(L)$) at lower levels, offering insights into the local population. On the other hand, the Lemmings sample of the statistically complete Palomar sample of 280 local galaxies (Baldi et al., 2018, 2021a) can be used to comprehensively explore the low-luminosity AGN population in local galaxies with extreme details, leveraging a wide array of multi-wavelength data that includes radio observations from the eMerlin array.

To construct a comprehensive $\Phi(L)$ distribution across a wide luminosity range, we propose merging the complete Lemmings sample with other AGN studies covering higher luminosity regimes, such as BASS[1] (Koss et al., 2022a) or QSOs from SDSS (Lyke et al., 2020). Leveraging accurate measurements of bolometric luminosity for LLAGN, as presented in Chapter 5, enables the construction of $\Phi(L)$ from $\Phi(L_X)$ with appropriate bolometric corrections. Simultaneously, we possess $\Phi(\sigma)$ for these samples, allowing us to derive $\Phi(M_{BH})$ assuming a scaling relation. The relationship between these functions is mediated through the duty cycle ($U(M_{BH})$) and the probability of observing an SMBH accreting at a specific λ ($P(\lambda)$):

$$\Phi(L) = \int P(\lambda)U(M_{BH})\Phi(M_{BH})d\lambda \qquad (7.1)$$

Furthermore, exploring the parameter space involving scaling relation, Eddington distribution, and duty cycle is essential. To achieve this, an MCMC code is being developed to enable the exploration of different assumptions and obtain the most likely values for free parameters, thereby providing valuable constraints. Through these methodologies, our objectives include constraining the scaling relation, ensuring self-consistency of the data, and exploring the demographics of BHs in a complete sample of local galaxies. This comprehensive analysis promises valuable insights into BH seed formation, subsequent growth, and intricate connections with host galaxy properties.

In relation to the results and open questions presented in Chapter 6, I am PI of an approved JWST proposal (Cycle 2 GO, ID: 3671), that focuses on illuminating the intricate ISM-jet interaction processes in M58. The observations are scheduled for next spring (between 12th May and 30th June), giving us the possibility of continuing to work on new cutting-edge data in the near future. This 17-hour program will leverage a diverse suite of instruments to delve deep into M58's heart, probing its SMBH's impact on surrounding gas and stars.

Among these, the MIRI MRS will conduct a 2x2 pointing mosaic (Fig. 7.1d), mapping the shock-induced H_2 emission spanning the

---

5-27 μm wavelength range. Dust features, such as PAH features and silicate emission, will be observed in this range with unprecedented details. Further enriching this data set, the NIRSpec IFU will contribute another 2x2 mosaic with a 10 pc spatial resolution. This refined scrutiny will target the 1.7-5 μm wavelength range, observing the rovibrational H_2 lines, Paα, and the 3.3 μm PAH feature. Accompanying images will encompass key features across a significant portion of the galaxy to provide a broader context. NIRCam will cover aspects like the stellar continuum, H_2 1-0 S(1) emissions, hot dust continuum, and the 3.3 μm PAH feature across the galaxy's bulge and approximately 80% of its disk. MIRI Imaging will capture features like the 7.7 and 11.3 μm PAH emissions, H_2 0-0 S(3) emission, and the warm dust continuum, spanning the entire bulge and about 30% of the galaxy's disk.
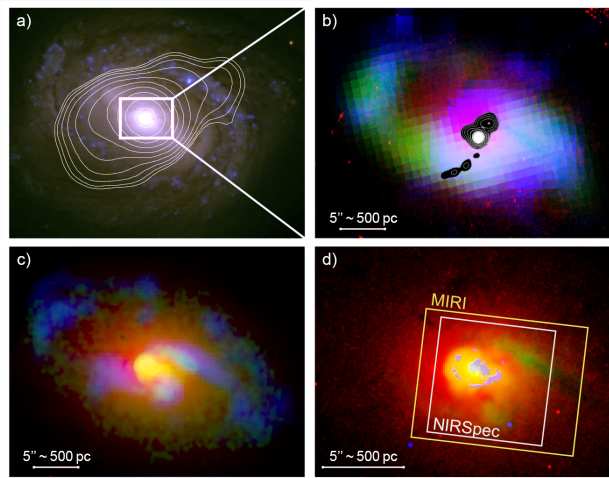
Figure 7.1: Multiwavelength emission of M58 with a close-up of the jet-shocked cocoon and the footprint of coverage for JWST IFUs. *a)* SDSS filters u, g, r (blue, green, red) and contours from VLA 5 GHz. *b)* HST Hα (red), Spitzer map H_2 S(3) (green), X-ray Chandra 0.5-8 keV (blue) and contours from VLA B-array 20cm. *c)* HST F791W continuum (red), Gemini H_2 1-0 S(1) (green) and ALMA CO 2-1 (blue). *d)* HST Hα (red), Gemini H_2 1-0 S(1) (green) and HST F250W (blue) tracing the SF ring.

The forthcoming analysis of this data aims to validate the scenario proposed in Chapter 6, providing fresh insights into H_2 heating mechanisms, spatially-resolved AGN impact on SF processes, and potential ionized outflows, linking their origins to AGN-driven winds or jet-induced shock interactions. Contextualizing the findings from the M58 case involves a comparative analysis with other galaxy samples, particularly those from the ReveaLLAGN project (ID: 2016, Goold et al., 2023) and PHANGs sample (ID: 2107, Lee et al., 2023). This comparative analysis will enable a broader understanding of the effects of recent AGN activity and the frequency of the M58 scenario. This, in

turn, will contribute to constraining the prevalence of this scenario in the LLAGN population and understanding its impact on the broader framework of galaxy evolution.

Part V

APPENDIX

A | INDUSTRY SECONDMENT

This appendix presents a comprehensive overview of my experiences during the industry secondment at Prewarp[1], a prominent data science consultancy. Executed over three full months from March to May 2022, this secondment was a collaborative effort with Giovanna Speranza (Instituto de Astrofisica de Canarias), a fellow PhD student from the BiD4BEST ITN program. Integral to my Ph.D. journey, this secondment empowered me to apply my academic analytical skills to tangible business challenges, bridging the gap between theory and practical application.

Prewarp, a private company specializing in utilizing artificial intelligence for robust analyses and strategic decision-making in merchandising, served as the backdrop for my secondment. Specifically, I contributed to the forecast module for clothes sales at Bally[2], enhancing prediction accuracy for the subsequent discount period. The skills honed during this period have direct applicability to my Ph.D. project, where I aim to leverage machine learning techniques to establish connections between the physical properties of galaxies.

The assignment at Prewarp not only enriched my academic pursuits but also equipped me with invaluable insights into data science and machine learning techniques. This newfound knowledge is poised to enhance my research endeavors significantly. Beyond the academic realm, the secondment provided me with practical experience in data science analysis, amplifying my post-PhD employability. Exposure to a non-academic work environment further honed my entrepreneurial, project management, teamwork, agile product development, and communication skills.

A.1 INTRODUCTION

Prewarp's expertise lies in addressing decision problems related to inventory and pricing within the fashion industry. It focuses on optimizing markdown decisions to boost profits while minimizing waste. The methodology extends to improving predictions of demand for upcoming seasons, facilitating informed production planning for sustainable product lifecycles.

At the core of Prewarp's approach is a two-step algorithm. The first step involves forecasting sales for upcoming weeks, while the

---

1 https://www.prewarp.co/

2 https://www.bally.it

second recommends price markdowns to maximize profits. This study primarily concentrates on enhancing the forecast module.

The forecast module's principal objective is to estimate the sales of a specific product (n) in a given week (w). Leveraging historical data from fashion companies, the module employs a baseline model based on simple linear regression. This model considers three features: the price fraction, the previous week's sales rate, and the week's sales rate for the target week.

$$\ln\left(\lambda_n^w + 1\right) = \beta_0 + \beta_1 \ln \frac{p_n^w}{p_n^T} + \beta_2 \ln\left(\lambda_n^{w-1} + 1\right) \tag{A.1}$$

Here:

- λ_n^w represents the sale rate for item n in week w.

- p_n^w denotes the markdown price for item n in week w.

- p_n^T stands for the original price for item n.

- β encompasses the coefficients of the linear regression.

This model serves as a benchmark for comparison with alternative models and feature sets.

A.2 FEATURES AGGREGATION

Even with sophisticated neural network models, the predictive capability heavily relies on the quality of the selected features. Drawing inspiration from the work of Caro and Gallien (2012), which primarily focused on Zara[3] data, we adapted the feature selection process to cater to the unique characteristics of Bally, a luxury brand. Key features, such as 'previous sales quantity' and 'price fraction,' were readily available from PreWarp. However, our study delved deeper, exploring additional features essential for a more nuanced forecast. These features included:

1. *Product Age:* This metric estimates how long a product has been in stock before being sold. Calculated by determining the duration between the product's introduction and the last monitored date when the product remained unsold, accounting for sale season dates if applicable.

2. *Broken Assortment Effect:* Representing the decline in demand when inventory falls below a certain level, we computed the minimum value between 1 and the ratio of stock quantity to a predefined threshold (f).

---

3 https://www.zara.com

3. *Normalization Factor:* This factor compares sales in a given week with the mean sales throughout the year, considering seasonality. Calculated using historical data, it provides a contextualized measure for predicting future sales trends.

A.2.1 The Linear Model

Equation A.1 establishes the foundation for the basic linear regression model, considering fundamental features. Expanding upon this, we incorporated the three additional features detailed in Appendix A.2. The updated linear regression model becomes:

$$\ln\left(\lambda_n^w + 1\right) = \beta_0 + \beta_1 \ln \frac{p_n^w}{p_n^T} + \beta_2 \ln\left(\lambda_n^{w-1} + 1\right)$$
$$+ \beta_3 \ln\left(\min\{1, \frac{I_r^w}{f}\}\right) + \beta_4 \ln\left(\text{prod\_age}\right)$$
$$+ \beta_5 \ln\left(\text{norm\_coef}\right)$$

Here, I_r^w represents the stock quantity for a specific item-color r in week w, and f is the threshold for the broken assortment effect. Application of this updated model to Bally's data across different sales regions resulted in improved forecasts compared to linear regression with only the basic features.

Evaluation metrics, such as Mean Absolute Percentage Error (MAPE) and Mean Absolute Scaled Error (MASE), play a pivotal role in assessing model performance. The full feature set demonstrated a notable improvement of approximately 10% in MAPE, while MASE values closely aligned with those derived from the basic features.

A.2.2 The Tree Model

Tree models, including decision trees, represent a class of supervised machine-learning algorithms widely used for regression problems.

A.2.2.1 Decision Tree

The decision tree model, providing mean values for predictors at each leaf, was implemented using the *sklearn.tree.DecisionTreeRegressor* class. The model was configured with a maximum depth of 10 nodes and a leaf condition of at least 5% of the total sample. However, this model exhibited limitations in predictive power, yielding discrete values.

A.2.2.2 Linear Tree

The linear tree model, featuring a linear regressor in each leaf, was implemented using a compatible *sklearn* class. While it outperformed

the decision tree, its predictive accuracy fell short of the linear model with the complete set of features. Further refinement through hyperparameter tuning and data clustering based on text features may enhance future performance.

Polynomial Tree

Efforts were made to enhance the linear tree model by generating polynomial features up to the second order using *sklearn.preprocessing.PolynomialFeatures*. However, this approach did not yield improvements over the linear tree model.

A.2.3 The Clustering Model

We explored the application of the KMeans clustering model combined with Principal Component Analysis (PCA). PCA, a valuable tool for feature reduction, was performed using *sklearn.decomposition.PCA* on the Bally data. Despite the common practice of combining PCA with k-means clustering, our analysis indicated that component reduction was unnecessary due to the relatively low number of features (as illustrated in Section A.2). Furthermore, PCA revealed the independence of all five features, allowing their continued use for predictions. While PCA informed us that four clusters were optimal for the Bally data, KMeans clustering was applied using *sklearn.cluster.KMeans*, and subsequent linear models were employed for each cluster.

A.2.4 Fixed–Sales Model

Recognizing the unique dynamics of luxury brand sales, distinct from fast-fashion retailers like Zara, we devised a fixed-sales model. Drawing inspiration from Caro and Gallien (2012), the model maintained a fixed last week's sales rate. Starting from Eq. (A.1), the fixed-sales model evolved as follows:

$$\ln(\widetilde{\lambda}_n^w + 1) = \ln(exp(\beta_0)) + \beta_1 \ln(f_n^w) + \beta_2 \ln(\lambda_n^{w-1} + 1)$$
$$\widetilde{\lambda}_n^w + 1 = exp(\beta_0)(f_n^w)^{\beta_1}.(\lambda_n^{w-1} + 1)^{\beta_2}$$

If we call $S_f := [\widetilde{\lambda}_n^w + 1]_f$ as the function when the price fraction is set to f, for two price fractions we have:

$$\frac{S_{f_1}}{S_{f_0}} = \left(\frac{f_1}{f_0}\right)^{\beta_1}$$

Thus:

$$S_{f_1} = \left(\frac{f_1}{f_0}\right)^{\beta_1} S_{f_0}$$

If we obtain an estimator of S_{f_0}, we can predict S_{f_1}. If S_{f_0} is the mean value of the previous 5 weeks (*baselineSales*), we can estimate λ_{n,f_1}^w as:

$$\lambda_{n,f_1}^w = \left(\frac{f_1}{f_0}\right)^{\beta_1} (baselineSales + 1) - 1$$

To account for the new features, a two-step modification was applied. The original *baselineSales*$_{or}$ was adjusted in the first step to obtain *baselineSales*$_{mod}$:

$$baselineSales_{mod} = baselineSales_{or} \times \left(\frac{prod\_age + 2}{prod\_age + 1}\right)^{\beta_4}$$
$$\times \left(\frac{brok\_ef^w + 1}{brok\_ef^{w-1} + 1}\right)^{\beta_3} \times \left(\frac{norm\_coef^w}{\overline{norm\_coef}}\right)$$

This modified value was then utilized in the second step to predict sales rates:

$$\lambda_{n,f_1}^w = \left(\frac{f_1}{f_0}\right)^{\beta_1} (baselineSales_{mod} + 1) - 1$$

The fixed model incorporating the new features showcased an improvement in MAPE for predicting the first wave of sales of the AW21 markdown for the People's Republic of China (PRC). Simultaneously, MASE values remained comparable to those of the previous models. In Fig. A.1, we present the MAPE and MASE values from the first week of all the forecast models explained in this section.

A.3 THE DATA AGGREGATION WITH CLUSTERING

In addition to employing robust models for reliable predictions, the significance of data preparation cannot be overstated in enhancing predictive power. In this context, data aggregation emerges as a crucial step, and the Data Aggregation with Clustering (DAC) algorithm proposed by Cohen et al. (2019) is explored for its efficacy. The DAC algorithm encompasses three key steps:

1. *Maximum Likelihood Estimation (MLE):* This step involves obtaining distinct coefficient vectors for each item.

2. *Hypothesis Test (t-test):* A hypothesis test is performed on the estimated coefficients to identify the optimal aggregation level.

3. *K-means Clustering:* K-means is applied to the estimated coefficients to delineate the cluster structure.
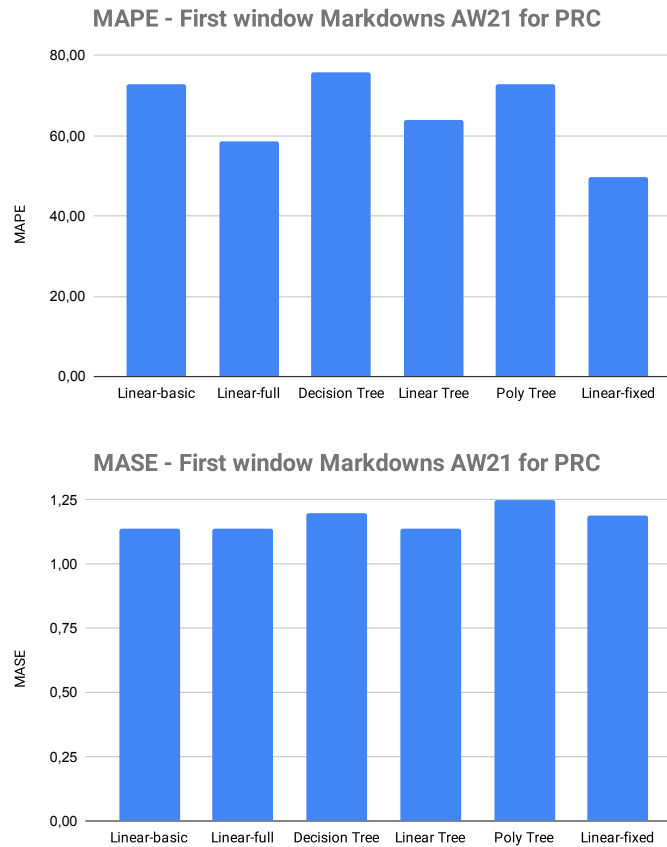
Figure A.1: Error estimators of all the forecast models. Lower values are better.

Following the MLE step, Cohen et al. (2019) generate coefficients for each item using the 'Decentralized model,' as represented by the equation:

$$Y_{i,j} = \sum_{l \in D} X_{i,j}^{l} b_{i,l}, \quad i = 1,...,n \quad \text{and} \quad j = 1,...,m \tag{A.2}$$

Subsequent to obtaining this model, the hypothesis test is conducted to determine the aggregation level of the coefficients. This involves assessing whether the coefficients for different items are essentially the same, vary individually, or change at the group level. This procedure identifies three aggregation levels and three types of features: shared features (common to all items), not shared features (individual for each item), and cluster features (exerting the same impact within a cluster of features).

The final DAC model is then described as follows:

$$Y_{i,j} = \sum_{l \in D_s} X_{i,j}^l \beta_l^s + \sum_{l \in D_n} X_{i,j}^l \beta_{i,l}^n$$
$$+ \sum_{l \in D_c} X_{i,j}^l \beta_{(i,l),l}^c, \quad i = 1, ..., n \quad \text{and} \quad j = 1, ..., m \tag{A.3}$$

Implementing the decentralized model could be the initial approach to enhance prediction power for the Bally data (as well as future models for Camper). Fig. A.2 showcases the performance comparison of different models, revealing that the decentralized model achieves comparable results to the DAC algorithm across various departments.
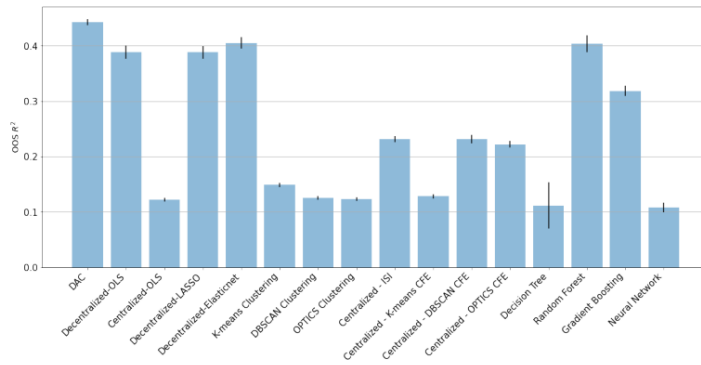
(a) Department 1
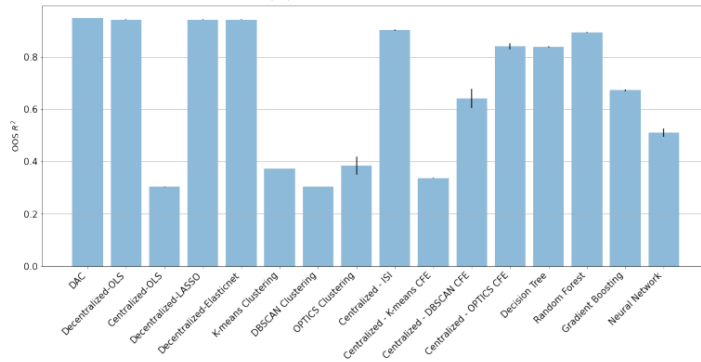
(b) Department 2

Figure A.2: Performance comparison between different models. The Decentralized model provides good predictions compared to DAC, even considering different departments.

If the preference is to apply the DAC algorithm, setting a threshold to determine when two coefficients can be considered equal or not becomes crucial. This enables the estimation of features for the three different levels of aggregation.

A.4 SUMMARY AND OUTLOOK

Prewarp stands as an innovative company leaving its imprint on the fashion industry. With a collaborative team and the ability to attract at-

tention from renowned brands like Bally or Camper, Prewarp, despite its modest size, delivers AI-based recommendations that significantly enhance the benefits of client companies. The hope is for Prewarp's continued growth and contribution to making the fashion industry more sustainable.

Throughout the three-month secondment, the primary focus was on refining the forecast module using Bally data. The experience involved collaborative coding, utilizing GitHub as a version control software and repository, and working extensively with *pandas*. The exploration of algorithms such as Decision Trees, K-means, and PCA has proven beneficial for ongoing Ph.D. projects. The inclusion of more features and novel models is anticipated to bolster the forecast module for upcoming seasons of markdowns.

The secondment also included an in-person workweek in Mallorca, Spain, which provided a unique opportunity to collaborate directly with the team working on a new client project. The experience was enjoyable, and the warm and friendly workspace fostered productive interactions.

Within the framework of the Marie Curie ITN action, this PhD thesis has benefited from the secondment at Prewarp. The exposure to cutting-edge data science and machine learning solutions, coupled with the application of academic skills to real-world business challenges, has significantly enriched the research journey. The acquired transferable skills gained insights into industry practices, and expanded professional network are invaluable assets. Beyond the technical aspects, the secondment has honed project management, team collaboration, agile product development, and communication skills, contributing to a holistic growth experience.

BIBLIOGRAPHY

Abramo, L. Raul et al. (July 2012). «Measuring large-scale structure with quasars in narrow-band filter surveys.» In: *MNRAS* 423.4, pp. 3251–3267. DOI: 10.1111/j.1365-2966.2012.21115.x. arXiv: 1108.2657 [astro-ph.CO].

Abramowicz, Marek A. and P. Chris Fragile (Jan. 2013). «Foundations of Black Hole Accretion Disk Theory.» In: *Living Reviews in Relativity* 16.1, 1. DOI: 10.12942/lrr-2013-1. arXiv: 1104.5499 [astro-ph.HE].

Agüero, E. L., R. J. Díaz, and E. Bajaja (Feb. 2004). «NGC 1566: Spectroscopy of a symmetric system with Seyfert nucleus.» In: *A&A* 414, pp. 453–461. DOI: 10.1051/0004-6361:20031644.

Ahumada, Romina et al. (July 2020). «The 16th Data Release of the Sloan Digital Sky Surveys: First Release from the APOGEE-2 Southern Survey and Full Release of eBOSS Spectra.» In: *ApJS* 249.1, 3. DOI: 10.3847/1538-4365/ab929e. arXiv: 1912.02905 [astro-ph.GA].

Aird, J., A. L. Coil, and A. Georgakakis (Jan. 2018). «X-rays across the galaxy population - II. The distribution of AGN accretion rates as a function of stellar mass and redshift.» In: *MNRAS* 474, pp. 1225–1249. DOI: 10.1093/mnras/stx2700. arXiv: 1705.01132 [astro-ph.HE].

Aird, J., A. L. Coil, A. Georgakakis, K. Nandra, G. Barro, and P. G. Pérez-González (Aug. 2015). «The evolution of the X-ray luminosity functions of unabsorbed and absorbed AGNs out to z~ 5.» In: *MNRAS* 451.2, pp. 1892–1927. DOI: 10.1093/mnras/stv1062. arXiv: 1503.01120 [astro-ph.HE].

Aird, James et al. (Feb. 2012). «PRIMUS: The Dependence of AGN Accretion on Host Stellar Mass and Color.» In: *ApJ* 746.1, 90. DOI: 10.1088/0004-637X/746/1/90. arXiv: 1107.4368 [astro-ph.CO].

Akhlaghi, Mohammad and Takashi Ichikawa (Sept. 2015). «Noise-based Detection and Segmentation of Nebulous Objects.» In: *ApJS* 220.1, 1. DOI: 10.1088/0067-0049/220/1/1. arXiv: 1505.01664 [astro-ph.IM].

Alarie, A. and C. Morisset (Oct. 2019). «Extensive Online Shock Model Database.» In: *Rev. Mexicana Astron. Astrofis.* 55, pp. 377–394. DOI: 10.22201/ia.01851101p.2019.55.02.21. arXiv: 1908.08579 [astro-ph.GA].

Alatalo, Katherine et al. (Jan. 2014). «NGC 1266 as a Local Candidate for Rapid Cessation of Star Formation.» In: *ApJ* 780.2, 186. DOI: 10.1088/0004-637X/780/2/186. arXiv: 1311.6469 [astro-ph.CO].

Alexander, D. M. and R. C. Hickox (June 2012). «What drives the growth of black holes?» In: *New A Rev.* 56.4, pp. 93–121. DOI: 10.1016/j.newar.2011.11.003. arXiv: 1112.1949 [astro-ph.GA].

Alexander, Tal, Eckhard Sturm, Dieter Lutz, Amiel Sternberg, Hagai Netzer, and Reinhard Genzel (Feb. 1999). «Infrared Spectroscopy of NGC 4151: Probing the Obscured Ionizing Active Galactic Nucleus Continuum.» In: *ApJ* 512.1, pp. 204–223. DOI: 10.1086/306751. arXiv: astro-ph/9809094 [astro-ph].

Almeida, Ivan, Rodrigo Nemmen, and Rogemar A. Riffel (Nov. 2023). «Quenching star formation with low-luminosity AGN winds.» In: *MNRAS* 526.1, pp. 217–223. DOI: 10.1093/mnras/stad2673. arXiv: 2303.00826 [astro-ph.GA].

Ananna, Tonima Tasnim et al. (Nov. 2022). «Probing the Structure and Evolution of BASS Active Galactic Nuclei through Eddington Ratios.» In: *ApJ* 939.1, L13. DOI: 10.3847/2041-8213/ac9979. arXiv: 2210.08401 [astro-ph.GA].

Andonie, Carolina et al. (Oct. 2022). «A panchromatic view of infrared quasars: Excess star formation and radio emission in the most heavily obscured systems.» In: *MNRAS*. ISSN: 0035-8711. DOI: 10.1093/mnras/stac2800. URL: https://doi.org/10.1093/mnras/stac2800.

Andonie, Carolina et al. (Jan. 2024). «Obscuration beyond the nucleus: infrared quasars can be buried in extreme compact starbursts.» In: *MNRAS* 527.1, pp. L144–L150. DOI: 10.1093/mnrasl/slad144. arXiv: 2310.02330 [astro-ph.GA].

Annuar, A. et al. (Sept. 2020). «NuSTAR observations of four nearby X-ray faint AGNs: low luminosity or heavy obscuration?» In: *MNRAS* 497.1, pp. 229–245. DOI: 10.1093/mnras/staa1820. arXiv: 2006.13583 [astro-ph.HE].

Antonucci, R. R. J. and J. S. Miller (Oct. 1985). «Spectropolarimetry and the nature of NGC 1068.» In: *ApJ* 297, pp. 621–632. DOI: 10.1086/163559.

Antonucci, Robert (Jan. 1993). «Unified models for active galactic nuclei and quasars.» In: *ARA&A* 31, pp. 473–521. DOI: 10.1146/annurev.aa.31.090193.002353.

Appleton, P. N. et al. (Dec. 2018). «Jet-related Excitation of the [C II] Emission in the Active Galaxy NGC 4258 with SOFIA.» In: *ApJ* 869.1, 61. DOI: 10.3847/1538-4357/aaed2a. arXiv: 1810.12883 [astro-ph.GA].

Asmus, D., P. Gandhi, S. F. Hönig, A. Smette, and W. J. Duschl (Nov. 2015). «The subarcsecond mid-infrared view of local active galactic nuclei - II. The mid-infrared-X-ray correlation.» In: *MNRAS* 454.1, pp. 766–803. DOI: 10.1093/mnras/stv1950. arXiv: 1508.05065 [astro-ph.GA].

Asmus, D., S. F. Hönig, and P. Gandhi (May 2016). «The Subarcsecond Mid-infrared View of Local Active Galactic Nuclei. III. Polar Dust Emission.» In: *ApJ* 822.2, 109. DOI: 10.3847/0004-637X/822/2/109. arXiv: 1603.02710 [astro-ph.GA].

Asmus, D., S. F. Hönig, P. Gandhi, A. Smette, and W. J. Duschl (Apr. 2014). «The subarcsecond mid-infrared view of local active galactic

nuclei - I. The N- and Q-band imaging atlas.» In: *MNRAS* 439.2, pp. 1648–1679. DOI: 10.1093/mnras/stu041. arXiv: 1310.2770 [astro-ph.CO].

Assef, R. J. et al. (Dec. 2011). «Black Hole Mass Estimates Based on C IV are Consistent with Those Based on the Balmer Lines.» In: *ApJ* 742.2, 93. DOI: 10.1088/0004-637X/742/2/93. arXiv: 1009.1145 [astro-ph.CO].

Atek, H. et al. (Dec. 2011). «Very Strong Emission-line Galaxies in the WFC3 Infrared Spectroscopic Parallel Survey and Implications for High-redshift Galaxies.» In: *ApJ* 743.2, 121. DOI: 10.1088/0004-637X/743/2/121. arXiv: 1109.0639 [astro-ph.CO].

Audibert, A., C. Ramos Almeida, S. García-Burillo, F. Combes, M. Bischetti, M. Meenakshi, D. Mukherjee, G. Bicknell, and A. Y. Wagner (Mar. 2023). «Jet-induced molecular gas excitation and turbulence in the Teacup.» In: *A&A* 671, L12. DOI: 10.1051/0004-6361/202345964. arXiv: 2302.13884 [astro-ph.GA].

Aversa, R., A. Lapi, G. de Zotti, F. Shankar, and L. Danese (Sept. 2015). «Black Hole and Galaxy Coevolution from Continuity Equation and Abundance Matching.» In: *ApJ* 810.1, 74. DOI: 10.1088/0004-637X/810/1/74. arXiv: 1507.07318 [astro-ph.GA].

Awaki, Hisamitsu, Katsuji Koyama, Hajime Inoue, and Jules P. Halpern (Apr. 1991). «X-Ray Implications of a Unified Model of Seyfert Galaxies.» In: *PASJ* 43, pp. 195–212.

Baes, Maarten, Joris Verstappen, Ilse De Looze, Jacopo Fritz, Waad Saftly, Edgardo Vidal Pérez, Marko Stalevski, and Sander Valcke (Oct. 2011). «Efficient Three-dimensional NLTE Dust Radiative Transfer with SKIRT.» In: *ApJS* 196.2, 22. DOI: 10.1088/0067-0049/196/2/22. arXiv: 1108.5056 [astro-ph.CO].

Baldi, R. D. et al. (May 2018). «LeMMINGs - I. The eMERLIN legacy survey of nearby galaxies. 1.5-GHz parsec-scale radio structures and cores.» In: *MNRAS* 476.3, pp. 3478–3522. DOI: 10.1093/mnras/sty342. arXiv: 1802.02162 [astro-ph.GA].

Baldi, R. D. et al. (Jan. 2021a). «LeMMINGs - II. The e-MERLIN legacy survey of nearby galaxies. The deepest radio view of the Palomar sample on parsec scale.» In: *MNRAS* 500.4, pp. 4749–4767. DOI: 10.1093/mnras/staa3519. arXiv: 2011.03062 [astro-ph.GA].

Baldi, R. D. et al. (Dec. 2021b). «LeMMINGs III. The e-MERLIN legacy survey of the Palomar sample: exploring the origin of nuclear radio emission in active and inactive galaxies through the [O III] - radio connection.» In: *MNRAS* 508.2, pp. 2019–2038. DOI: 10.1093/mnras/stab2613. arXiv: 2109.06205 [astro-ph.GA].

Baldwin, J. A., M. M. Phillips, and R. Terlevich (Feb. 1981). «Classification parameters for the emission-line spectra of extragalactic objects.» In: *PASP* 93, pp. 5–19. DOI: 10.1086/130766.

Barro, Guillermo, P. G. Pérez-González, J. Gallego, M. L. N. Ashby, M. Kajisawa, S. Miyazaki, V. Villar, T. Yamada, and J. Zamorano

(Mar. 2011). «UV-to-FIR Analysis of Spitzer/IRAC Sources in the Extended Groth Strip. I. Multi-wavelength Photometry and Spectral Energy Distributions.» In: *ApJS* 193.1, 13. DOI: 10.1088/0067-0049/193/1/13. arXiv: 1101.3308 [astro-ph.CO].

Beckert, T. and W. J. Duschl (May 2002). «Where have all the black holes gone?» In: *A&A* 387, pp. 422–428. DOI: 10.1051/0004-6361:20020438. arXiv: astro-ph/0203489 [astro-ph].

Beckmann, Volker and Chris R. Shrader (2012). *Active Galactic Nuclei.*

Benitez, N. et al. (Mar. 2014). «J-PAS: The Javalambre-Physics of the Accelerated Universe Astrophysical Survey.» In: *arXiv e-prints*, arXiv:1403.5237. arXiv: 1403.5237 [astro-ph.CO].

Bennert, Vardha N., Tommaso Treu, Xuheng Ding, Isak Stomberg, Simon Birrer, Tomas Snyder, Matthew A. Malkan, Andrew W. Stephens, and Matthew W. Auger (Nov. 2021). «A Local Baseline of the Black Hole Mass Scaling Relations for Active Galaxies. IV. Correlations Between M_{BH} and Host Galaxy σ, Stellar Mass, and Luminosity.» In: *ApJ* 921.1, 36. DOI: 10.3847/1538-4357/ac151a. arXiv: 2101.10355 [astro-ph.GA].

Bentz, Misty C., Bradley M. Peterson, Hagai Netzer, Richard W. Pogge, and Marianne Vestergaard (May 2009). «The Radius-Luminosity Relationship for Active Galactic Nuclei: The Effect of Host-Galaxy Starlight on Luminosity Measurements. II. The Full Sample of Reverberation-Mapped AGNs.» In: *ApJ* 697.1, pp. 160–181. DOI: 10.1088/0004-637X/697/1/160. arXiv: 0812.2283 [astro-ph].

Bentz, Misty C. et al. (Apr. 2013). «The Low-luminosity End of the Radius-Luminosity Relationship for Active Galactic Nuclei.» In: *ApJ* 767.2, 149. DOI: 10.1088/0004-637X/767/2/149. arXiv: 1303.1742 [astro-ph.CO].

Bertin, E. (July 2006). «Automatic Astrometric and Photometric Calibration with SCAMP.» In: *Astronomical Data Analysis Software and Systems XV*. Ed. by C. Gabriel, C. Arviset, D. Ponz, and S. Enrique. Vol. 351. Astronomical Society of the Pacific Conference Series, p. 112.

Bertin, E. and S. Arnouts (June 1996). «SExtractor: Software for source extraction.» In: *A&AS* 117, pp. 393–404. DOI: 10.1051/aas:1996164.

Bessiere, P. S. and C. Ramos Almeida (May 2022). «Spatially resolved evidence of the impact of quasar-driven outflows on recent star formation: the case of Mrk 34.» In: *MNRAS* 512.1, pp. L54–L59. DOI: 10.1093/mnrasl/slac016. arXiv: 2202.06788 [astro-ph.GA].

Bianchi, Luciana, Alberto Conti, and Bernie Shiao (Mar. 2014). «The ultraviolet sky: An overview from the GALEX surveys.» In: *Advances in Space Research* 53.6, pp. 900–912. DOI: 10.1016/j.asr.2013.07.045. arXiv: 1312.3281 [astro-ph.GA].

Bianchi, S., M. Guainazzi, G. Matt, N. Fonseca Bonilla, and G. Ponti (Feb. 2009). «CAIXA: a catalogue of AGN in the XMM-Newton

archive. I. Spectral analysis.» In: *A&A* 495.2, pp. 421–430. DOI: `10.1051/0004-6361:200810620`. arXiv: `0811.1126 [astro-ph]`.

Bianchi, S. et al. (Dec. 2018). «Fraction of bolometric luminosity absorbed by dust in DustPedia galaxies.» In: *A&A* 620, A112. DOI: `10.1051/0004-6361/201833699`. arXiv: `1810.01208 [astro-ph.GA]`.

Bischetti, M. et al. (Feb. 2017). «The WISSH quasars project. I. Powerful ionised outflows in hyper-luminous quasars.» In: *A&A* 598, A122. DOI: `10.1051/0004-6361/201629301`. arXiv: `1612.03728 [astro-ph.GA]`.

Blandford, R. D. and C. F. McKee (Apr. 1982). «Reverberation mapping of the emission line regions of Seyfert galaxies and quasars.» In: *ApJ* 255, pp. 419–439. DOI: `10.1086/159843`.

Blandford, R. D. and R. L. Znajek (May 1977). «Electromagnetic extraction of energy from Kerr black holes.» In: *MNRAS* 179, pp. 433–456. DOI: `10.1093/mnras/179.3.433`.

Boehringer, H., W. Voges, A. C. Fabian, A. C. Edge, and D. M. Neumann (Oct. 1993). «A ROSAT HRI study of the interaction of the X-ray emitting gas and radio lobes of NGC 1275.» In: *MNRAS* 264, pp. L25–L28. DOI: `10.1093/mnras/264.1.L25`.

Bogdán, Ákos et al. (Nov. 2023). «Evidence for heavy-seed origin of early supermassive black holes from a $z \approx 10$ X-ray quasar.» In: *Nature Astronomy*. DOI: `10.1038/s41550-023-02111-9`. arXiv: `2305.15458 [astro-ph.GA]`.

Bongiorno, A. et al. (Dec. 2012). «Accreting supermassive black holes in the COSMOS field and the connection to their host galaxies.» In: *MNRAS* 427.4, pp. 3103–3133. DOI: `10.1111/j.1365-2966.2012.22089.x`. arXiv: `1209.1640 [astro-ph.CO]`.

Bonoli, S. et al. (Sept. 2021). «The miniJPAS survey: A preview of the Universe in 56 colors.» In: *A&A* 653, A31. DOI: `10.1051/0004-6361/202038841`. arXiv: `2007.01910 [astro-ph.CO]`.

Boquien, M., D. Burgarella, Y. Roehlly, V. Buat, L. Ciesla, D. Corre, A. K. Inoue, and H. Salas (Feb. 2019). «CIGALE: a python Code Investigating GALaxy Emission.» In: *A&A* 622, A103. DOI: `10.1051/0004-6361/201834156`. arXiv: `1811.03094 [astro-ph.GA]`.

Bower, R. G., A. J. Benson, R. Malbon, J. C. Helly, C. S. Frenk, C. M. Baugh, S. Cole, and C. G. Lacey (Aug. 2006). «Breaking the hierarchy of galaxy formation.» In: *MNRAS* 370.2, pp. 645–655. DOI: `10.1111/j.1365-2966.2006.10519.x`. arXiv: `astro-ph/0511338 [astro-ph]`.

Boyle, B. J. and Roberto J. Terlevich (Jan. 1998). «The cosmological evolution of the QSO luminosity density and of the star formation rate.» In: *MNRAS* 293.2, pp. L49–L51. DOI: `10.1046/j.1365-8711.1998.01264.x`. arXiv: `astro-ph/9710134 [astro-ph]`.

Brandt, W. N. and D. M. Alexander (Jan. 2015). «Cosmic X-ray surveys of distant active galaxies. The demographics, physics, and ecology of growing supermassive black holes.» In: *A&A Rev.* 23, 1. DOI: `10.1007/s00159-014-0081-z`. arXiv: `1501.01982 [astro-ph.HE]`.

Brusa, M. et al. (Dec. 2009). «Black hole growth and starburst activity at z = 0.6-4 in the Chandra Deep Field South. Host galaxies properties of obscured AGN.» In: *A&A* 507.3, pp. 1277–1289. DOI: `10.1051/0004-6361/200912261`. arXiv: `0910.1007 [astro-ph.CO]`.

Brusa, M. et al. (Apr. 2018). «Molecular outflow and feedback in the obscured quasar XID2028 revealed by ALMA.» In: *A&A* 612, A29. DOI: `10.1051/0004-6361/201731641`. arXiv: `1712.04505 [astro-ph.GA]`.

Bruzual, G. and S. Charlot (Oct. 2003). «Stellar population synthesis at the resolution of 2003.» In: *MNRAS* 344.4, pp. 1000–1028. DOI: `10.1046/j.1365-8711.2003.06897.x`. arXiv: `astro-ph/0309134 [astro-ph]`.

Bu, De-Fu and Xiao-Hong Yang (Feb. 2019). «Quenching Black Hole Accretion by Active Galactic Nuclei Feedback.» In: *ApJ* 871.2, 138. DOI: `10.3847/1538-4357/aaf807`.

Buat, V., G. Mountrichas, G. Yang, M. Boquien, Y. Roehlly, D. Burgarella, M. Stalevski, L. Ciesla, and P. Theulé (Oct. 2021). «Polar dust obscuration in broad-line active galaxies from the XMM-XXL field.» In: *A&A* 654, A93. DOI: `10.1051/0004-6361/202141797`. arXiv: `2108.07684 [astro-ph.GA]`.

Burgarella, D., V. Buat, and J. Iglesias-Páramo (July 2005). «Star formation and dust attenuation properties in galaxies from a statistical ultraviolet-to-far-infrared analysis.» In: *MNRAS* 360.4, pp. 1413–1425. DOI: `10.1111/j.1365-2966.2005.09131.x`. arXiv: `astro-ph/0504434 [astro-ph]`.

Burtscher, L. et al. (Oct. 2013). «A diversity of dusty AGN tori. Data release for the VLTI/MIDI AGN Large Program and first results for 23 galaxies.» In: *A&A* 558, A149. DOI: `10.1051/0004-6361/201321890`. arXiv: `1307.2068 [astro-ph.CO]`.

Calzetti, Daniela, Lee Armus, Ralph C. Bohlin, Anne L. Kinney, Jan Koornneef, and Thaisa Storchi-Bergmann (Apr. 2000). «The Dust Content and Opacity of Actively Star-forming Galaxies.» In: *ApJ* 533.2, pp. 682–695. DOI: `10.1086/308692`. arXiv: `astro-ph/9911459 [astro-ph]`.

Camps, P. and M. Baes (Mar. 2015). «SKIRT: An advanced dust radiative transfer code with a user-friendly architecture.» In: *Astronomy and Computing* 9, pp. 20–33. DOI: `10.1016/j.ascom.2014.10.004`. arXiv: `1410.1629 [astro-ph.IM]`.

Cao, Xinwu and Jun-Xian Wang (Oct. 2014). «A toy model for the X-ray spectral variability of active galactic nuclei.» In: *MNRAS* 444.1, pp. L20–L24. DOI: `10.1093/mnrasl/slu102`. arXiv: `1406.6442 [astro-ph.HE]`.

Cappi, M. et al. (Feb. 2006). «X-ray spectral survey with XMM-Newton of a complete sample of nearby Seyfert galaxies.» In: *A&A* 446.2, pp. 459–470. DOI: `10.1051/0004-6361:20053893`. arXiv: `astro-ph/0509584 [astro-ph]`.

Carilli, C. L. and F. Walter (Aug. 2013). «Cool Gas in High-Redshift Galaxies.» In: *ARA&A* 51.1, pp. 105–161. DOI: 10.1146/annurev-astro-082812-140953. arXiv: 1301.0371 [astro-ph.CO].

Carnall, A. C., R. J. McLure, J. S. Dunlop, and R. Davé (Nov. 2018). «Inferring the star formation histories of massive quiescent galaxies with BAGPIPES: evidence for multiple quenching mechanisms.» In: *MNRAS* 480.4, pp. 4379–4401. DOI: 10.1093/mnras/sty2169. arXiv: 1712.04452 [astro-ph.GA].

Caro, Felipe and Jérémie Gallien (2012). «Clearance pricing optimization for a fast-fashion retailer.» In: *Operations research* 60.6, pp. 1404–1422.

Carraro, R. et al. (Oct. 2020). «Coevolution of black hole accretion and star formation in galaxies up to z = 3.5.» In: *A&A* 642, A65. DOI: 10.1051/0004-6361/201936649. arXiv: 2007.11002 [astro-ph.GA].

Casey, Caitlin M. (Oct. 2012). «Far-infrared spectral energy distribution fitting for galaxies near and far.» In: *MNRAS* 425.4, pp. 3094–3103. DOI: 10.1111/j.1365-2966.2012.21455.x. arXiv: 1206.1595 [astro-ph.CO].

Cavagnolo, K. W., B. R. McNamara, P. E. J. Nulsen, C. L. Carilli, C. Jones, and L. Bırzan (Sept. 2010). «A Relationship Between AGN Jet Power and Radio Power.» In: *ApJ* 720.2, pp. 1066–1072. DOI: 10.1088/0004-637X/720/2/1066. arXiv: 1006.5699 [astro-ph.CO].

Chabrier, Gilles (July 2003). «Galactic Stellar and Substellar Initial Mass Function.» In: *PASP* 115.809, pp. 763–795. DOI: 10.1086/376392. arXiv: astro-ph/0304382 [astro-ph].

Chang, Heon-Young, Chul-Sung Choi, and Insu Yi (Oct. 2002). «Radio/X-Ray Luminosity Relation for X-Ray-Bright Galactic Nuclei: Implications for Weighing Supermassive Black Holes.» In: *AJ* 124.4, pp. 1948–1953. DOI: 10.1086/342737. arXiv: astro-ph/0207154 [astro-ph].

Charlot, Stéphane and S. Michael Fall (Aug. 2000). «A Simple Model for the Absorption of Starlight by Dust in Galaxies.» In: *ApJ* 539.2, pp. 718–731. DOI: 10.1086/309250. arXiv: astro-ph/0003128 [astro-ph].

Chastenet, Jérémy et al. (Feb. 2023). «PHANGS-JWST First Results: Measuring Polycyclic Aromatic Hydrocarbon Properties across the Multiphase Interstellar Medium.» In: *ApJ* 944.2, L12. DOI: 10.3847/2041-8213/acac94.

Chaves-Montero, J. et al. (Apr. 2022). «Black hole virial masses from single-epoch photometry. The miniJPAS test case.» In: *A&A* 660, A95. DOI: 10.1051/0004-6361/202142567. arXiv: 2111.01180 [astro-ph.GA].

Chiaraluce, E., G. Bruni, F. Panessa, M. Giroletti, M. Orienti, H. Rampadarath, F. Vagnetti, and F. Tombesi (May 2019). «From radio-quiet to radio-silent: low-luminosity Seyfert radio cores.» In: *MNRAS*

485.3, pp. 3185–3202. DOI: 10.1093/mnras/stz595. arXiv: 1902.10670 [astro-ph.GA].

Cohen, Maxime C, Renyu Philip Zhang, and Kevin Jiao (2019). «Data aggregation and demand prediction.» In: *Available at SSRN 3411653*.

Coil, Alison L. et al. (Aug. 2009). «AEGIS: The Clustering of X-Ray Active Galactic Nucleus Relative to Galaxies at z ~1.» In: *ApJ* 701.2, pp. 1484–1499. DOI: 10.1088/0004-637X/701/2/1484. arXiv: 0902.0363 [astro-ph.CO].

Comerón, S., J. H. Knapen, J. E. Beckman, and I. Shlosman (Feb. 2008). «Discovery of ultra-compact nuclear rings in three spiral galaxies.» In: *A&A* 478.2, pp. 403–407. DOI: 10.1051/0004-6361:20078845. arXiv: 0711.4230 [astro-ph].

Conroy, Charlie (Aug. 2013). «Modeling the Panchromatic Spectral Energy Distributions of Galaxies.» In: *ARA&A* 51.1, pp. 393–455. DOI: 10.1146/annurev-astro-082812-141017. arXiv: 1301.7095 [astro-ph.CO].

Costa, T., D. Sijacki, and M. G. Haehnelt (Mar. 2015). «Fast cold gas in hot AGN outflows.» In: *MNRAS* 448, pp. L30–L34. DOI: 10.1093/mnrasl/slu193. arXiv: 1411.0678 [astro-ph.GA].

Cresci, G. et al. (Apr. 2023). «Bubbles and outflows: The novel JWST/NIRSpec view of the z = 1.59 obscured quasar XID2028.» In: *A&A* 672, A128. DOI: 10.1051/0004-6361/202346001. arXiv: 2301.11060 [astro-ph.GA].

Cresci, G. et al. (Oct. 2015). «The MAGNUM survey: positive feedback in the nuclear region of NGC 5643 suggested by MUSE.» In: *A&A* 582, A63. DOI: 10.1051/0004-6361/201526581. arXiv: 1508.04464 [astro-ph.GA].

Croton, Darren J. (July 2006). «Evolution in the black hole mass-bulge mass relation: a theoretical perspective.» In: *MNRAS* 369.4, pp. 1808–1812. DOI: 10.1111/j.1365-2966.2006.10429.x. arXiv: astro-ph/0512375 [astro-ph].

Croton, Darren J. et al. (Jan. 2006). «The many lives of active galactic nuclei: cooling flows, black holes and the luminosities and colours of galaxies.» In: *MNRAS* 365.1, pp. 11–28. DOI: 10.1111/j.1365-2966.2005.09675.x. arXiv: astro-ph/0508046 [astro-ph].

Cutri, RM et al. (2013). «Explanatory supplement to the AllWISE data release products.» In: *Explanatory Supplement to the AllWISE Data Release Products*, p. 1.

Dale, D. A. et al. (July 2006). «Mid-Infrared Spectral Diagnostics of Nuclear and Extranuclear Regions in Nearby Galaxies.» In: *ApJ* 646.1, pp. 161–173. DOI: 10.1086/504835. arXiv: astro-ph/0604007 [astro-ph].

Dale, Daniel A., George Helou, Georgios E. Magdis, Lee Armus, Tanio Díaz-Santos, and Yong Shi (Mar. 2014). «A Two-parameter Model for the Infrared/Submillimeter/Radio Spectral Energy Distributions

of Galaxies and Active Galactic Nuclei.» In: *ApJ* 784.1, 83. DOI: 10.1088/0004-637X/784/1/83. arXiv: 1402.1495 [astro-ph.GA].

Dalla Bontà, Elena et al. (Nov. 2020). «The Sloan Digital Sky Survey Reverberation Mapping Project: Estimating Masses of Black Holes in Quasars with Single-epoch Spectroscopy.» In: *ApJ* 903.2, 112. DOI: 10.3847/1538-4357/abbc1c. arXiv: 2007.02963 [astro-ph.GA].

Davis, M. et al. (May 2007). «The All-Wavelength Extended Groth Strip International Survey (AEGIS) Data Sets.» In: *ApJ* 660.1, pp. L1–L6. DOI: 10.1086/517931. arXiv: astro-ph/0607355 [astro-ph].

de los Reyes, Mithi A. C. and Jr. Kennicutt Robert C. (June 2019a). «Erratum: "Revisiting the Integrated Star Formation Law. I. Non-starbursting Galaxies" (<A href="https://doi.org/10.3847/1538-4357/aafa82">2019 ApJ, 872, 16</A>).» In: *ApJ* 878.1, 74. DOI: 10.3847/1538-4357/ab22af.

– (Feb. 2019b). «Revisiting the Integrated Star Formation Law. I. Non-starbursting Galaxies.» In: *ApJ* 872.1, 16. DOI: 10.3847/1538-4357/aafa82. arXiv: 1901.01283 [astro-ph.GA].

Decarli, R., R. Falomo, A. Treves, M. Labita, J. K. Kotilainen, and R. Scarpa (Mar. 2010). «The quasar MBH-Mhost relation through cosmic time - II. Evidence for evolution from z = 3 to the present age.» In: *MNRAS* 402.4, pp. 2453–2461. DOI: 10.1111/j.1365-2966.2009.16049.x. arXiv: 0911.2988 [astro-ph.CO].

Delvecchio, I. et al. (May 2015). «Mapping the average AGN accretion rate in the SFR-M$_*$ plane for Herschel-selected galaxies at 0 < z ≤ 2.5.» In: *MNRAS* 449.1, pp. 373–389. DOI: 10.1093/mnras/stv213. arXiv: 1501.07602 [astro-ph.GA].

Delvecchio, I. et al. (Apr. 2014). «Tracing the cosmic growth of super-massive black holes to z ∼ 3 with Herschel.» In: *MNRAS* 439.3, pp. 2736–2754. DOI: 10.1093/mnras/stu130. arXiv: 1401.4503 [astro-ph.GA].

Di Matteo, Tiziana, Volker Springel, and Lars Hernquist (Feb. 2005). «Energy input from quasars regulates the growth and activity of black holes and their host galaxies.» In: *Nature* 433.7026, pp. 604–607. DOI: 10.1038/nature03335. arXiv: astro-ph/0502199 [astro-ph].

Diamond-Stanic, Aleksandar M. and George H. Rieke (Nov. 2010). «The Effect of Active Galactic Nuclei on the Mid-infrared Aromatic Features.» In: *ApJ* 724.1, pp. 140–153. DOI: 10.1088/0004-637X/724/1/140. arXiv: 1009.2752 [astro-ph.CO].

Ding, Xuheng et al. (Jan. 2020). «The Mass Relations between Super-massive Black Holes and Their Host Galaxies at 1 < z < 2 HST-WFC3.» In: *ApJ* 888.1, 37. DOI: 10.3847/1538-4357/ab5b90. arXiv: 1910.11875 [astro-ph.GA].

Doi, A., S. Kameno, K. Kohno, K. Nakanishi, and M. Inoue (Oct. 2005). «A high-frequency radio survey of low-luminosity active galactic nuclei.» In: *MNRAS* 363.2, pp. 692–704. DOI: 10.1111/j.1365-2966.2005.09471.x. arXiv: astro-ph/0508598 [astro-ph].

Draine, B. T. and Aigen Li (Mar. 2007). «Infrared Emission from Interstellar Dust. IV. The Silicate-Graphite-PAH Model in the Post-Spitzer Era.» In: *ApJ* 657.2, pp. 810–837. DOI: 10.1086/511055. arXiv: astro-ph/0608003 [astro-ph].

Draine, B. T., Aigen Li, Brandon S. Hensley, L. K. Hunt, K. Sandstrom, and J. -D. T. Smith (Aug. 2021). «Excitation of Polycyclic Aromatic Hydrocarbon Emission: Dependence on Size Distribution, Ionization, and Starlight Spectrum and Intensity.» In: *ApJ* 917.1, 3. DOI: 10.3847/1538-4357/abff51. arXiv: 2011.07046 [astro-ph.GA].

Draine, B. T. et al. (Jan. 2014). «Andromeda's Dust.» In: *ApJ* 780.2, 172. DOI: 10.1088/0004-637X/780/2/172. arXiv: 1306.2304 [astro-ph.CO].

Draine, Bruce T. (2011). *Physics of the Interstellar and Intergalactic Medium*.

Dubois, Yohan, Sébastien Peirani, Christophe Pichon, Julien Devriendt, Raphaël Gavazzi, Charlotte Welker, and Marta Volonteri (Dec. 2016). «The HORIZON-AGN simulation: morphological diversity of galaxies promoted by AGN feedback.» In: *MNRAS* 463.4, pp. 3948–3964. DOI: 10.1093/mnras/stw2265. arXiv: 1606.03086 [astro-ph.GA].

Duras, F. et al. (Apr. 2020). «Universal bolometric corrections for active galactic nuclei over seven luminosity decades.» In: *A&A* 636, A73. DOI: 10.1051/0004-6361/201936817. arXiv: 2001.09984 [astro-ph.GA].

Elitzur, Moshe (Mar. 2012). «On the Unification of Active Galactic Nuclei.» In: *ApJ* 747.2, L33. DOI: 10.1088/2041-8205/747/2/L33. arXiv: 1202.1776 [astro-ph.CO].

– (Nov. 2006). «The obscuring torus in AGN.» In: *New A Rev.* 50.9-10, pp. 728–731. DOI: 10.1016/j.newar.2006.06.027.

– (Aug. 2008). «The toroidal obscuration of active galactic nuclei.» In: *New A Rev.* 52.6, pp. 274–288. DOI: 10.1016/j.newar.2008.06.010. arXiv: 0805.3699 [astro-ph].

Elitzur, Moshe and Luis C. Ho (Aug. 2009). «On the Disappearance of the Broad-Line Region in Low-Luminosity Active Galactic Nuclei.» In: *ApJ* 701.2, pp. L91–L94. DOI: 10.1088/0004-637X/701/2/L91. arXiv: 0907.3752 [astro-ph.CO].

Eracleous, Michael, Jason A. Hwang, and Hélène M. L. G. Flohic (Mar. 2010). «Spectral Energy Distributions of Weak Active Galactic Nuclei Associated with Low-Ionization Nuclear Emission Regions.» In: *ApJS* 187.1, pp. 135–148. DOI: 10.1088/0067-0049/187/1/135. arXiv: 1001.2924 [astro-ph.GA].

Eracleous, Michael, Joseph C. Shields, George Chartas, and Edward C. Moran (Jan. 2002). «Three LINERs under the Chandra X-Ray Microscope.» In: *ApJ* 565.1, pp. 108–124. DOI: 10.1086/324394. arXiv: astro-ph/0109246 [astro-ph].

Esparza-Arredondo, Donaji, Natalia Osorio-Clavijo, Omaira González-Martín, César Victoria-Ceballos, Sinhué A. R. Haro-Corzo, Omar Ulises Reyes-Amador, Jafet López-Sánchez, and Alice Pasetto (Dec.

2020). «Active Galactic Nucleus Ghosts: A Systematic Search for Faded Nuclei.» In: *ApJ* 905.1, 29. DOI: 10.3847/1538-4357/abc425. arXiv: 2010.11962 [astro-ph.GA].

Fabian, A. C. (Sept. 2012). «Observational Evidence of Active Galactic Nuclei Feedback.» In: *ARA&A* 50, pp. 455–489. DOI: 10.1146/annurev-astro-081811-125521. arXiv: 1204.4114 [astro-ph.CO].

Fabian, A. C., A. Lohfink, E. Kara, M. L. Parker, R. Vasudevan, and C. S. Reynolds (Aug. 2015). «Properties of AGN coronae in the NuSTAR era.» In: *MNRAS* 451.4, pp. 4375–4383. DOI: 10.1093/mnras/stv1218. arXiv: 1505.07603 [astro-ph.HE].

Fabian, A. C. et al. (Dec. 2011). «A wide Chandra view of the core of the Perseus cluster.» In: *MNRAS* 418.4, pp. 2154–2164. DOI: 10.1111/j.1365-2966.2011.19402.x. arXiv: 1105.5025 [astro-ph.CO].

Falocco, S., J. Larsson, and S. Nandi (June 2020). «Accretion and jets in a low-luminosity AGN: the nucleus of NGC 1052.» In: *A&A* 638, A67. DOI: 10.1051/0004-6361/202037516. arXiv: 2004.02305 [astro-ph.GA].

Farber, Ryan J. and Max Gronke (Feb. 2022). «The survival of multiphase dusty clouds in hot winds.» In: *MNRAS* 510.1, pp. 551–567. DOI: 10.1093/mnras/stab3412. arXiv: 2107.07991 [astro-ph.GA].

Feltre, A., E. Hatziminaoglou, J. Fritz, and A. Franceschini (Oct. 2012). «Smooth and clumpy dust distributions in AGN: a direct comparison of two commonly explored infrared emission models.» In: *MNRAS* 426.1, pp. 120–127. DOI: 10.1111/j.1365-2966.2012.21695.x. arXiv: 1207.2668 [astro-ph.CO].

Ferland, G. J., K. T. Korista, D. A. Verner, J. W. Ferguson, J. B. Kingdon, and E. M. Verner (July 1998). «CLOUDY 90: Numerical Simulation of Plasmas and Their Spectra.» In: *PASP* 110.749, pp. 761–778. DOI: 10.1086/316190.

Ferland, G. J., R. L. Porter, P. A. M. van Hoof, R. J. R. Williams, N. P. Abel, M. L. Lykins, G. Shaw, W. J. Henney, and P. C. Stancil (Apr. 2013). «The 2013 Release of Cloudy.» In: *Rev. Mexicana Astron. Astrofis.* 49, pp. 137–163. DOI: 10.48550/arXiv.1302.4485. arXiv: 1302.4485 [astro-ph.GA].

Fernández-Ontiveros, J. A., X. López-López, and A. Prieto (Feb. 2023). «Compact jets dominate the continuum emission in low-luminosity active galactic nuclei.» In: *A&A* 670, A22. DOI: 10.1051/0004-6361/202243547. arXiv: 2211.09828 [astro-ph.HE].

Ferrarese, Laura and David Merritt (Aug. 2000). «A Fundamental Relation between Supermassive Black Holes and Their Host Galaxies.» In: *ApJ* 539.1, pp. L9–L12. DOI: 10.1086/312838. arXiv: astro-ph/0006053 [astro-ph].

Ferrarese, Laura et al. (June 2006). «A Fundamental Relation between Compact Stellar Nuclei, Supermassive Black Holes, and Their Host Galaxies.» In: *ApJ* 644.1, pp. L21–L24. DOI: 10.1086/505388. arXiv: astro-ph/0603840 [astro-ph].

Fiore, F. et al. (May 2017). «AGN wind scaling relations and the co-evolution of black holes and galaxies.» In: *A&A* 601, A143. DOI: 10.1051/0004-6361/201629478. arXiv: 1702.04507 [astro-ph.GA].

Fontanot, Fabio et al. (Aug. 2020). «The rise of active galactic nuclei in the galaxy evolution and assembly semi-analytic model.» In: *MNRAS* 496.3, pp. 3943–3960. DOI: 10.1093/mnras/staa1716. arXiv: 2002.10576 [astro-ph.CO].

Fritz, J., A. Franceschini, and E. Hatziminaoglou (Mar. 2006). «Revisiting the infrared spectra of active galactic nuclei with a new torus emission model.» In: *MNRAS* 366.3, pp. 767–786. DOI: 10.1111/j.1365-2966.2006.09866.x. arXiv: astro-ph/0511428 [astro-ph].

Gandhi, P., H. Horst, A. Smette, S. Hönig, A. Comastri, R. Gilli, C. Vignali, and W. Duschl (Aug. 2009). «Resolving the mid-infrared cores of local Seyferts.» In: *A&A* 502.2, pp. 457–472. DOI: 10.1051/0004-6361/200811368. arXiv: 0902.2777 [astro-ph.GA].

Gao, F., L. Wang, W. J. Pearson, Y. A. Gordon, B. W. Holwerda, A. M. Hopkins, M. J. I. Brown, J. Bland-Hawthorn, and M. S. Owers (May 2020). «Mergers trigger active galactic nuclei out to z ∼ 0.6.» In: *A&A* 637, A94. DOI: 10.1051/0004-6361/201937178. arXiv: 2004.00680 [astro-ph.GA].

García-Bernete, I., D. Rigopoulou, A. Alonso-Herrero, M. Pereira-Santaella, P. F. Roche, and B. Kerkeni (Jan. 2022). «Polycyclic aromatic hydrocarbons in Seyfert and star-forming galaxies.» In: *MNRAS* 509.3, pp. 4256–4275. DOI: 10.1093/mnras/stab3127. arXiv: 2011.10882 [astro-ph.GA].

García-Bernete, I. et al. (Dec. 2016). «The nuclear and extended mid-infrared emission of Seyfert galaxies.» In: *MNRAS* 463.4, pp. 3531–3555. DOI: 10.1093/mnras/stw2125. arXiv: 1608.06513 [astro-ph.GA].

García-Burillo, S., S. Fernández-García, F. Combes, L. K. Hunt, S. Haan, E. Schinnerer, F. Boone, M. Krips, and I. Márquez (Mar. 2009). «Molecular gas in NUclei of GAlaxies (NUGA). XI. A complete gravity torque map of NGC 4579: new clues to bar evolution.» In: *A&A* 496.1, pp. 85–105. DOI: 10.1051/0004-6361/200810640. arXiv: 0810.4892 [astro-ph].

Gaspari, Massimo and Aleksander Sądowski (Mar. 2017). «Unifying the Micro and Macro Properties of AGN Feeding and Feedback.» In: *ApJ* 837.2, 149. DOI: 10.3847/1538-4357/aa61a3. arXiv: 1701.07030 [astro-ph.HE].

Gendron-Marsolais, M. et al. (Dec. 2020). «High-resolution VLA low radio frequency observations of the Perseus cluster: radio lobes, mini-halo, and bent-jet radio galaxies.» In: *MNRAS* 499.4, pp. 5791–5805. DOI: 10.1093/mnras/staa2003. arXiv: 2005.12298 [astro-ph.GA].

Gensior, Jindra, J. M. Diederik Kruijssen, and Benjamin W. Keller (June 2020). «Heart of darkness: the influence of galactic dynamics on quenching star formation in galaxy spheroids.» In: *MNRAS* 495.1,

pp. 199–223. DOI: `10.1093/mnras/staa1184`. arXiv: `2002.01484 [astro-ph.GA]`.

Georgakakis, A., J. Aird, A. Schulze, T. Dwelly, M. Salvato, K. Nandra, A. Merloni, and D. P. Schneider (Oct. 2017). «Observational constraints on the specific accretion-rate distribution of X-ray-selected AGNs.» In: *MNRAS* 471.2, pp. 1976–2001. DOI: `10.1093/mnras/stx1602`. arXiv: `1705.01133 [astro-ph.HE]`.

Georgakakis, A., I. Papadakis, and M. Paolillo (Dec. 2021). «Exploring black hole scaling relations via the ensemble variability of active galactic nuclei.» In: *MNRAS* 508.3, pp. 3463–3473. DOI: `10.1093/mnras/stab2818`. arXiv: `2105.08752 [astro-ph.HE]`.

Gilli, R. et al. (Oct. 2022). «Supermassive black holes at high redshift are expected to be obscured by their massive host galaxies' interstellar medium.» In: *A&A* 666, A17. DOI: `10.1051/0004-6361/202243708`. arXiv: `2206.03508 [astro-ph.GA]`.

Girdhar, A. et al. (Jan. 2024). «Quasar feedback survey: molecular gas affected by central outflows and by 10-kpc radio lobes reveal dual feedback effects in 'radio quiet' quasars.» In: *MNRAS* 527.3, pp. 9322–9342. DOI: `10.1093/mnras/stad3453`. arXiv: `2311.03453 [astro-ph.GA]`.

Girelli, G., L. Pozzetti, M. Bolzonella, C. Giocoli, F. Marulli, and M. Baldi (Feb. 2020). «The stellar-to-halo mass relation over the past 12 Gyr. I. Standard ΛCDM model.» In: *A&A* 634, A135. DOI: `10.1051/0004-6361/201936329`. arXiv: `2001.02230 [astro-ph.CO]`.

Giroletti, Marcello and Francesca Panessa (Dec. 2009). «The Faintest Seyfert Radio Cores Revealed by VLBI.» In: *ApJ* 706.2, pp. L260–L264. DOI: `10.1088/0004-637X/706/2/L260`. arXiv: `0910.5821 [astro-ph.CO]`.

González-Martín, O., J. Masegosa, I. Márquez, M. Guainazzi, and E. Jiménez-Bailón (Nov. 2009). «An X-ray view of 82 LINERs with Chandra and XMM-Newton data.» In: *A&A* 506.3, pp. 1107–1121. DOI: `10.1051/0004-6361/200912288`. arXiv: `0905.2973 [astro-ph.CO]`.

Goold, K. et al. (July 2023). «ReveaLLAGN 0: First Look at JWST MIRI data of Sombrero and NGC 1052.» In: *arXiv e-prints*, arXiv:2307.01252. DOI: `10.48550/arXiv.2307.01252`. arXiv: `2307.01252 [astro-ph.GA]`.

Goulding, Andy D., Jenny E. Greene, Rachel Bezanson, Johnny Greco, Sean Johnson, Alexie Leauthaud, Yoshiki Matsuoka, Elinor Medezinski, and Adrian M. Price-Whelan (Jan. 2018). «Galaxy interactions trigger rapid black hole growth: An unprecedented view from the Hyper Suprime-Cam survey.» In: *PASJ* 70, S37. DOI: `10.1093/pasj/psx135`. arXiv: `1706.07436 [astro-ph.GA]`.

Graham, Alister W. (Jan. 2016). «Galaxy Bulges and Their Massive Black Holes: A Review.» In: *Galactic Bulges*. Ed. by Eija Laurikainen, Reynier Peletier, and Dimitri Gadotti. Vol. 418. Astrophysics and Space Science Library, p. 263. DOI: `10.1007/978-3-319-19378-6_11`. arXiv: `1501.02937 [astro-ph.GA]`.

Graham, Alister W. and Nandini Sahu (Sept. 2022). «Appreciating mergers for understanding the non-linear M_{bh}-$M_{*,spheroid}$ and M_{bh}-$M_{*,galaxy}$ relations, updated herein, and the implications for the (reduced) role of AGN feedback.» In: *arXiv e-prints*, arXiv:2209.14526. arXiv: `2209.14526 [astro-ph.GA]`.

Granato, Gian Luigi, Gianfranco De Zotti, Laura Silva, Alessandro Bressan, and Luigi Danese (Jan. 2004). «A Physical Model for the Coevolution of QSOs and Their Spheroidal Hosts.» In: *ApJ* 600.2, pp. 580–594. DOI: `10.1086/379875`. arXiv: `astro-ph/0307202 [astro-ph]`.

Green, Gregory M. et al. (July 2018). «Galactic reddening in 3D from stellar photometry - an improved map.» In: *MNRAS* 478.1, pp. 651–666. DOI: `10.1093/mnras/sty1008`. arXiv: `1801.03555 [astro-ph.GA]`.

Groves, Brent et al. (Oct. 2012). «The heating of dust by old stellar populations in the bulge of M31.» In: *MNRAS* 426.2, pp. 892–902. DOI: `10.1111/j.1365-2966.2012.21696.x`. arXiv: `1206.2925 [astro-ph.CO]`.

Guo, H., Y. Shen, and S. Wang (Sept. 2018). *PyQSOFit: Python code to fit the spectrum of quasars*. Astrophysics Source Code Library. ascl: `1809.008`.

Haardt, F. and L. Maraschi (Oct. 1991). «A Two-Phase Model for the X-Ray Emission from Seyfert Galaxies.» In: *ApJ* 380, p. L51. DOI: `10.1086/186171`.

Habouzit, Mélanie et al. (Apr. 2022). «Co-evolution of massive black holes and their host galaxies at high redshift: discrepancies from six cosmological simulations and the key role of JWST.» In: *MNRAS* 511.3, pp. 3751–3767. DOI: `10.1093/mnras/stac225`. arXiv: `2201.09892 [astro-ph.CO]`.

Habouzit, Mélanie et al. (May 2021). «Supermassive black holes in cosmological simulations I: M_{BH} - $M_\star$ relation and black hole mass function.» In: *MNRAS* 503.2, pp. 1940–1975. DOI: `10.1093/mnras/stab496`. arXiv: `2006.10094 [astro-ph.GA]`.

Hainline, Kevin N., Ryan C. Hickox, Jenny E. Greene, Adam D. Myers, Nadia L. Zakamska, Guilin Liu, and Xin Liu (May 2014). «Gemini Long-slit Observations of Luminous Obscured Quasars: Further Evidence for an Upper Limit on the Size of the Narrow-line Region.» In: *ApJ* 787.1, 65. DOI: `10.1088/0004-637X/787/1/65`. arXiv: `1404.1921 [astro-ph.GA]`.

Hardcastle, M. J. and J. H. Croston (June 2020). «Radio galaxies and feedback from AGN jets.» In: *New A Rev.* 88, 101539. DOI: `10.1016/j.newar.2020.101539`. arXiv: `2003.06137 [astro-ph.HE]`.

Harrison, C. M. (July 2017). «Impact of supermassive black hole growth on star formation.» In: *Nature Astronomy* 1, 0165. DOI: `10.1038/s41550-017-0165`. arXiv: `1703.06889 [astro-ph.GA]`.

Harrison, C. M., T. Costa, C. N. Tadhunter, A. Flütsch, D. Kakkad, M. Perna, and G. Vietri (Feb. 2018). «AGN outflows and feedback twenty years on.» In: *Nature Astronomy* 2, pp. 198–205. DOI: 10.1038/s41550-018-0403-6. arXiv: 1802.10306 [astro-ph.GA].

Harrison, C. M., A. P. Thomson, D. M. Alexander, F. E. Bauer, A. C. Edge, M. T. Hogan, J. R. Mullaney, and A. M. Swinbank (Feb. 2015). «Storm in a "Teacup": A Radio-quiet Quasar with ≈10 kpc Radio-emitting Bubbles and Extreme Gas Kinematics.» In: *ApJ* 800.1, 45. DOI: 10.1088/0004-637X/800/1/45. arXiv: 1410.4198 [astro-ph.GA].

Harrison, Christopher (Sept. 2014). «Observational constraints on the influence of active galactic nuclei on the evolution of galaxies.» PhD thesis. Durham University, UK.

Hauschild Roier, Gabriel R. et al. (May 2022). «Gas inflows in the polar ring of NGC 4111: the birth of an AGN.» In: *MNRAS* 512.2, pp. 2556–2572. DOI: 10.1093/mnras/stac634. arXiv: 2203.02532 [astro-ph.GA].

Hayes, Matthew, Daniel Schaerer, Göran Östlin, J. Miguel Mas-Hesse, Hakim Atek, and Daniel Kunth (Mar. 2011). «On the Redshift Evolution of the Lyα Escape Fraction and the Dust Content of Galaxies.» In: *ApJ* 730.1, 8. DOI: 10.1088/0004-637X/730/1/8. arXiv: 1010.4796 [astro-ph.CO].

Heckman, T. M. (July 1980). «An Optical and Radio Survey of the Nuclei of Bright Galaxies - Activity in the Normal Galactic Nuclei.» In: *A&A* 87, p. 152.

Heckman, Timothy M. and Philip N. Best (Aug. 2014a). «The Coevolution of Galaxies and Supermassive Black Holes: Insights from Surveys of the Contemporary Universe.» In: *ARA&A* 52, pp. 589–660. DOI: 10.1146/annurev-astro-081913-035722. arXiv: 1403.4620 [astro-ph.GA].

– (Aug. 2014b). «The Coevolution of Galaxies and Supermassive Black Holes: Insights from Surveys of the Contemporary Universe.» In: *ARA&A* 52, pp. 589–660. DOI: 10.1146/annurev-astro-081913-035722. arXiv: 1403.4620 [astro-ph.GA].

Hernán-Caballero, A. et al. (Oct. 2021). «The miniJPAS survey: Photometric redshift catalogue.» In: *A&A* 654, A101. DOI: 10.1051/0004-6361/202141236. arXiv: 2108.03271 [astro-ph.GA].

Hickox, Ryan C. and David M. Alexander (Sept. 2018). «Obscured Active Galactic Nuclei.» In: *ARA&A* 56, pp. 625–671. DOI: 10.1146/annurev-astro-081817-051803. arXiv: 1806.04680 [astro-ph.GA].

Hickox, Ryan C., James R. Mullaney, David M. Alexander, Chien-Ting J. Chen, Francesca M. Civano, Andy D. Goulding, and Kevin N. Hainline (Feb. 2014). «Black Hole Variability and the Star Formation-Active Galactic Nucleus Connection: Do All Star-forming Galaxies Host an Active Galactic Nucleus?» In: *ApJ* 782.1, 9. DOI: 10.1088/0004-637X/782/1/9. arXiv: 1306.3218 [astro-ph.CO].

Higdon, S. J. U., L. Armus, J. L. Higdon, B. T. Soifer, and H. W. W. Spoon (Sept. 2006). «A Spitzer Space Telescope Infrared Spectrograph Survey of Warm Molecular Hydrogen in Ultraluminous Infrared Galaxies.» In: *ApJ* 648.1, pp. 323–339. DOI: 10.1086/505701. arXiv: astro-ph/0605359 [astro-ph].

Hirschmann, Michaela, Klaus Dolag, Alexandro Saro, Lisa Bachmann, Stefano Borgani, and Andreas Burkert (Aug. 2014). «Cosmological simulations of black hole growth: AGN luminosities and downsizing.» In: *MNRAS* 442.3, pp. 2304–2324. DOI: 10.1093/mnras/stu1023. arXiv: 1308.0333 [astro-ph.CO].

Hirschmann, Michaela et al. (Dec. 2023). «Emission-line properties of IllustrisTNG galaxies: from local diagnostic diagrams to high-redshift predictions for JWST.» In: *MNRAS* 526.3, pp. 3610–3636. DOI: 10.1093/mnras/stad2955. arXiv: 2212.02522 [astro-ph.GA].

Ho, L. C. (Sept. 2008). «Nuclear activity in nearby galaxies.» In: *ARA&A* 46, pp. 475–539. DOI: 10.1146/annurev.astro.45.051806.110546. arXiv: 0803.2268 [astro-ph].

Ho, Luis C. (Jan. 1999). «LINERs as low-luminosity active galactic nuclei.» In: *Advances in Space Research* 23.5-6, pp. 813–822. DOI: 10.1016/S0273-1177(99)00211-2. arXiv: astro-ph/9807273 [astro-ph].

– (July 2009). «Radiatively Inefficient Accretion in Nearby Galaxies.» In: *ApJ* 699.1, pp. 626–637. DOI: 10.1088/0004-637X/699/1/626. arXiv: 0906.4104 [astro-ph.GA].

Ho, Luis C. and James S. Ulvestad (Mar. 2001). «Radio Continuum Survey of an Optically Selected Sample of Nearby Seyfert Galaxies.» In: *ApJS* 133.1, pp. 77–118. DOI: 10.1086/319185. arXiv: astro-ph/0102506 [astro-ph].

Ho, Luis C. et al. (Mar. 2001). «Detection of Nuclear X-Ray Sources in Nearby Galaxies with Chandra.» In: *ApJ* 549.1, pp. L51–L54. DOI: 10.1086/319138. arXiv: astro-ph/0102504 [astro-ph].

Hönig, S. F., M. Kishimoto, R. Antonucci, A. Marconi, M. A. Prieto, K. Tristram, and G. Weigelt (Aug. 2012). «Parsec-scale Dust Emission from the Polar Region in the Type 2 Nucleus of NGC 424.» In: *ApJ* 755.2, 149. DOI: 10.1088/0004-637X/755/2/149. arXiv: 1206.4307 [astro-ph.CO].

Hopkins, Philip F., Kevin Bundy, Lars Hernquist, and Richard S. Ellis (Apr. 2007a). «Observational Evidence for the Coevolution of Galaxy Mergers, Quasars, and the Blue/Red Galaxy Transition.» In: *ApJ* 659.2, pp. 976–996. DOI: 10.1086/512091. arXiv: astro-ph/0601621 [astro-ph].

Hopkins, Philip F., Lars Hernquist, Paul Martini, Thomas J. Cox, Brant Robertson, Tiziana Di Matteo, and Volker Springel (June 2005). «A Physical Model for the Origin of Quasar Lifetimes.» In: *ApJ* 625.2, pp. L71–L74. DOI: 10.1086/431146. arXiv: astro-ph/0502241 [astro-ph].

Hopkins, Philip F., Gordon T. Richards, and Lars Hernquist (Jan. 2007b). «An Observational Determination of the Bolometric Quasar Luminosity Function.» In: *ApJ* 654.2, pp. 731–753. DOI: 10.1086/509629. arXiv: astro-ph/0605678 [astro-ph].

Hopkins, Philip F., Rachel S. Somerville, Lars Hernquist, Thomas J. Cox, Brant Robertson, and Yuexing Li (Dec. 2006). «The Relation between Quasar and Merging Galaxy Luminosity Functions and the Merger-driven Star Formation History of the Universe.» In: *ApJ* 652.2, pp. 864–888. DOI: 10.1086/508503. arXiv: astro-ph/0602290 [astro-ph].

Hopkins, Philip F., Paul Torrey, Claude-André Faucher-Giguère, Eliot Quataert, and Norman Murray (May 2016). «Stellar and quasar feedback in concert: effects on AGN accretion, obscuration, and outflows.» In: *MNRAS* 458.1, pp. 816–831. DOI: 10.1093/mnras/stw289. arXiv: 1504.05209 [astro-ph.GA].

Hopkins, Philip F. et al. (Sept. 2004). «Dust Reddening in Sloan Digital Sky Survey Quasars.» In: *AJ* 128.3, pp. 1112–1123. DOI: 10.1086/423291. arXiv: astro-ph/0406293 [astro-ph].

Ichikawa, Kohei, Yoshihiro Ueda, Yuichi Terashima, Shinki Oyabu, Poshak Gandhi, Keiko Matsuta, and Takao Nakagawa (July 2012a). «Mid- and Far-infrared Properties of a Complete Sample of Local Active Galactic Nuclei.» In: *ApJ* 754.1, 45. DOI: 10.1088/0004-637X/754/1/45. arXiv: 1205.5032 [astro-ph.GA].

Ichikawa, Takashi, Masaru Kajisawa, and Mohammad Akhlaghi (May 2012b). «A universal stellar mass-size relation of galaxies in the GOODS-North region.» In: *MNRAS* 422.2, pp. 1014–1027. DOI: 10.1111/j.1365-2966.2012.20674.x. arXiv: 1202.1138 [astro-ph.CO].

Inoue, Akio K. (Aug. 2011). «Rest-frame ultraviolet-to-optical spectral characteristics of extremely metal-poor and metal-free galaxies.» In: *MNRAS* 415.3, pp. 2920–2931. DOI: 10.1111/j.1365-2966.2011.18906.x. arXiv: 1102.5150 [astro-ph.CO].

Inoue, Akio K., Ikuru Iwata, and Jean-Michel Deharveng (Sept. 2006). «The escape fraction of ionizing photons from galaxies at z = 0-6.» In: *MNRAS* 371.1, pp. L1–L5. DOI: 10.1111/j.1745-3933.2006.00195.x. arXiv: astro-ph/0605526 [astro-ph].

Ishibashi, W., M. W. Auger, D. Zhang, and A. C. Fabian (Sept. 2014). «Radio-mode feedback in local AGNs: dependence on the central black hole parameters.» In: *MNRAS* 443.2, pp. 1339–1345. DOI: 10.1093/mnras/stu1236. arXiv: 1406.6209 [astro-ph.GA].

Jahnke, Knud and Andrea V. Macciò (June 2011). «The Non-causal Origin of the Black-hole-galaxy Scaling Relations.» In: *ApJ* 734.2, 92. DOI: 10.1088/0004-637X/734/2/92. arXiv: 1006.0482 [astro-ph.CO].

Jones, A. P., M. Köhler, N. Ysard, M. Bocchio, and L. Verstraete (June 2017). «The global dust modelling framework THEMIS.» In: *A&A* 602, A46. DOI: 10.1051/0004-6361/201630225. arXiv: 1703.00775 [astro-ph.GA].

Just, D. W., W. N. Brandt, O. Shemmer, A. T. Steffen, D. P. Schneider, G. Chartas, and G. P. Garmire (Aug. 2007). «The X-Ray Properties of the Most Luminous Quasars from the Sloan Digital Sky Survey.» In: *ApJ* 665.2, pp. 1004–1022. DOI: 10.1086/519990. arXiv: 0705.3059 [astro-ph].

Kammoun, E. S. et al. (Oct. 2020). «A Hard Look at Local, Optically Selected, Obscured Seyfert Galaxies.» In: *ApJ* 901.2, 161. DOI: 10.3847/1538-4357/abb29f. arXiv: 2007.02616 [astro-ph.HE].

Kaneda, H., T. Onaka, I. Sakon, T. Kitayama, Y. Okada, and T. Suzuki (Sept. 2008). «Properties of Polycyclic Aromatic Hydrocarbons in Local Elliptical Galaxies Revealed by the Infrared Spectrograph on Spitzer.» In: *ApJ* 684.1, pp. 270–281. DOI: 10.1086/590243. arXiv: 0805.3257 [astro-ph].

Karachentsev, Igor D., Dmitry I. Makarov, and Elena I. Kaisina (Apr. 2013). «Updated Nearby Galaxy Catalog.» In: *AJ* 145.4, 101. DOI: 10.1088/0004-6256/145/4/101. arXiv: 1303.5328 [astro-ph.CO].

Kaspi, Shai, Dan Maoz, Hagai Netzer, Bradley M. Peterson, Marianne Vestergaard, and Buell T. Jannuzi (Aug. 2005). «The Relationship between Luminosity and Broad-Line Region Size in Active Galactic Nuclei.» In: *ApJ* 629.1, pp. 61–71. DOI: 10.1086/431275. arXiv: astro-ph/0504484 [astro-ph].

Kaspi, Shai, Paul S. Smith, Hagai Netzer, Dan Maoz, Buell T. Jannuzi, and Uriel Giveon (Apr. 2000). «Reverberation Measurements for 17 Quasars and the Size-Mass-Luminosity Relations in Active Galactic Nuclei.» In: *ApJ* 533.2, pp. 631–649. DOI: 10.1086/308704. arXiv: astro-ph/9911476 [astro-ph].

Kass, Robert E. and Adrian E. Raftery (1995). «Bayes Factors.» In: *Journal of the American Statistical Association* 90.430, pp. 773–795. ISSN: 01621459. URL: http://www.jstor.org/stable/2291091.

Kennicutt Robert C., Jr. (Apr. 1992). «A Spectrophotometric Atlas of Galaxies.» In: *ApJS* 79, p. 255. DOI: 10.1086/191653.

Kennicutt Robert C., Jr. et al. (Aug. 2003). «SINGS: The SIRTF Nearby Galaxies Survey.» In: *PASP* 115.810, pp. 928–952. DOI: 10.1086/376941. arXiv: astro-ph/0305437 [astro-ph].

Kewley, Lisa J., Brent Groves, Guinevere Kauffmann, and Tim Heckman (Nov. 2006). «The host galaxies and classification of active galactic nuclei.» In: *MNRAS* 372.3, pp. 961–976. DOI: 10.1111/j.1365-2966.2006.10859.x. arXiv: astro-ph/0605681 [astro-ph].

King, Andrew (Dec. 2005). «The AGN-Starburst Connection, Galactic Superwinds, and M_{BH}-σ.» In: *ApJ* 635.2, pp. L121–L123. DOI: 10.1086/499430. arXiv: astro-ph/0511034 [astro-ph].

Klindt, L., D. M. Alexander, D. J. Rosario, E. Lusso, and S. Fotopoulou (Sept. 2019). «Fundamental differences in the radio properties of red and blue quasars: evolution strongly favoured over orientation.» In: *MNRAS* 488.3, pp. 3109–3128. DOI: 10.1093/mnras/stz1771. arXiv: 1905.12108 [astro-ph.GA].

Kormendy, John and Luis C. Ho (Aug. 2013). «Coevolution (Or Not) of Supermassive Black Holes and Host Galaxies.» In: *ARA&A* 51.1, pp. 511–653. DOI: 10.1146/annurev-astro-082708-101811. arXiv: 1304.7762 [astro-ph.CO].

Koss, Michael J. et al. (July 2022a). «BASS. XXI. The Data Release 2 Overview.» In: *ApJS* 261.1, 1. DOI: 10.3847/1538-4365/ac6c8f. arXiv: 2207.12428 [astro-ph.GA].

Koss, Michael J. et al. (July 2022b). «BASS. XXII. The BASS DR2 AGN Catalog and Data.» In: *ApJS* 261.1, 2. DOI: 10.3847/1538-4365/ac6c05. arXiv: 2207.12432 [astro-ph.GA].

Koss, Michael J. et al. (Feb. 2021). «BAT AGN Spectroscopic Survey. XX. Molecular Gas in Nearby Hard-X-Ray-selected AGN Galaxies.» In: *ApJS* 252.2, 29. DOI: 10.3847/1538-4365/abcbfe. arXiv: 2010.15849 [astro-ph.GA].

Labrie, Kathleen, Kenneth Anderson, Ricardo Cárdenes, Chris Simpson, and James E. H. Turner (Oct. 2019). «DRAGONS - Data Reduction for Astronomy from Gemini Observatory North and South.» In: *Astronomical Data Analysis Software and Systems XXVII*. Ed. by Peter J. Teuben, Marc W. Pound, Brian A. Thomas, and Elizabeth M. Warner. Vol. 523. Astronomical Society of the Pacific Conference Series, p. 321.

Laigle, C. et al. (June 2016). «The COSMOS2015 Catalog: Exploring the $1 < z < 6$ Universe with Half a Million Galaxies.» In: *ApJS* 224.2, 24. DOI: 10.3847/0067-0049/224/2/24. arXiv: 1604.02350 [astro-ph.GA].

Laird, E. S. et al. (Jan. 2009). «AEGIS-X: the Chandra Deep Survey of the Extended Groth Strip.» In: *ApJS* 180.1, pp. 102–116. DOI: 10.1088/0067-0049/180/1/102. arXiv: 0809.1349 [astro-ph].

Lambrides, Erini L., Andreea O. Petric, Kirill Tchernyshyov, Nadia L. Zakamska, and Duncan J. Watts (Aug. 2019). «Mid-infrared spectroscopic evidence for AGN heating warm molecular gas.» In: *MNRAS* 487.2, pp. 1823–1843. DOI: 10.1093/mnras/stz1316. arXiv: 1808.02035 [astro-ph.GA].

Lang, Dustin, David W. Hogg, Keir Mierle, Michael Blanton, and Sam Roweis (May 2010). «Astrometry.net: Blind Astrometric Calibration of Arbitrary Astronomical Images.» In: *AJ* 139.5, pp. 1782–1800. DOI: 10.1088/0004-6256/139/5/1782. arXiv: 0910.2233 [astro-ph.IM].

Lapi, A., S. Raimundo, R. Aversa, Z. -Y. Cai, M. Negrello, A. Celotti, G. De Zotti, and L. Danese (Feb. 2014). «The Coevolution of Supermassive Black Holes and Massive Galaxies at High Redshift.» In: *ApJ* 782.2, 69. DOI: 10.1088/0004-637X/782/2/69. arXiv: 1312.3751 [astro-ph.GA].

Lapi, A., F. Shankar, J. Mao, G. L. Granato, L. Silva, G. De Zotti, and L. Danese (Oct. 2006). «Quasar Luminosity Functions from Joint Evolution of Black Holes and Host Galaxies.» In: *ApJ* 650.1, pp. 42–56. DOI: 10.1086/507122. arXiv: astro-ph/0603819 [astro-ph].

Larson, Rebecca L. et al. (Aug. 2023). «A CEERS Discovery of an Accreting Supermassive Black Hole 570 Myr after the Big Bang: Identifying a Progenitor of Massive z > 6 Quasars.» In: *ApJ* 953.2, L29. DOI: 10.3847/2041-8213/ace619. arXiv: 2303.08918 [astro-ph.GA].

Lauer, Tod R., Scott Tremaine, Douglas Richstone, and S. M. Faber (Nov. 2007). «Selection Bias in Observing the Cosmological Evolution of the M-σ and M-L Relationships.» In: *ApJ* 670.1, pp. 249–260. DOI: 10.1086/522083. arXiv: 0705.4103 [astro-ph].

Lee, Janice C. et al. (Feb. 2023). «The PHANGS-JWST Treasury Survey: Star Formation, Feedback, and Dust Physics at High Angular Resolution in Nearby GalaxieS.» In: *ApJ* 944.2, L17. DOI: 10.3847/2041-8213/acaaae. arXiv: 2212.02667 [astro-ph.GA].

Leroy, Adam K. et al. (July 2021a). «PHANGS-ALMA Data Processing and Pipeline.» In: *ApJS* 255.1, 19. DOI: 10.3847/1538-4365/abec80. arXiv: 2104.07665 [astro-ph.IM].

Leroy, Adam K. et al. (Dec. 2021b). «PHANGS-ALMA: Arcsecond CO(2-1) Imaging of Nearby Star-forming Galaxies.» In: *ApJS* 257.2, 43. DOI: 10.3847/1538-4365/ac17f3. arXiv: 2104.07739 [astro-ph.GA].

Li, Aigen (Mar. 2020). «Spitzer's perspective of polycyclic aromatic hydrocarbons in galaxies.» In: *Nature Astronomy* 4, pp. 339–351. DOI: 10.1038/s41550-020-1051-1. arXiv: 2003.10489 [astro-ph.GA].

Li, Junyao et al. (Dec. 2021). «Synchronized Coevolution between Supermassive Black Holes and Galaxies over the Last Seven Billion Years as Revealed by Hyper Suprime-Cam.» In: *ApJ* 922.2, 142. DOI: 10.3847/1538-4357/ac2301. arXiv: 2109.02751 [astro-ph.GA].

Liu, Hu and Qingwen Wu (Feb. 2013). «Possible Origin of Radio Emission from Nonthermal Electrons in Hot Accretion Flows for Low-luminosity Active Galactic Nuclei.» In: *ApJ* 764.1, 17. DOI: 10.1088/0004-637X/764/1/17. arXiv: 1212.1994 [astro-ph.HE].

Liu, Teng et al. (Oct. 2020). «The Sloan Digital Sky Survey Reverberation Mapping Project: the XMM-Newton X-Ray Source Catalog and Multiband Counterparts.» In: *ApJS* 250.2, 32. DOI: 10.3847/1538-4365/abb5b0. arXiv: 2009.02193 [astro-ph.HE].

López, I. E. et al. (Apr. 2024). «IRX-CIGALE: a tailored module for Low-Luminosity AGN.» In: *arXiv e-prints*, arXiv:2404.16938. DOI: 10.48550/arXiv.2404.16938. arXiv: 2404.16938 [astro-ph.GA].

López, I. E. et al. (Apr. 2023). «The miniJPAS survey: AGN and host galaxy coevolution of X-ray-selected sources.» In: *A&A* 672, A137. DOI: 10.1051/0004-6361/202245168. arXiv: 2302.01358 [astro-ph.GA].

López-Gonzaga, N., L. Burtscher, K. R. W. Tristram, K. Meisenheimer, and M. Schartmann (June 2016). «Mid-infrared interferometry of 23 AGN tori: On the significance of polar-elongated emission.» In: *A&A* 591, A47. DOI: 10.1051/0004-6361/201527590. arXiv: 1602.05592 [astro-ph.GA].

López-Sanjuan, C. et al. (Nov. 2019). «J-PLUS: photometric calibration of large-area multi-filter surveys with stellar and white dwarf loci.» In: *A&A* 631, A119. DOI: 10.1051/0004-6361/201936405. arXiv: 1907.12939 [astro-ph.IM].

Lu, Ru-Sen et al. (Apr. 2023). «A ring-like accretion structure in M87 connecting its black hole and jet.» In: *Nature* 616.7958, pp. 686–690. DOI: 10.1038/s41586-023-05843-w. arXiv: 2304.13252 [astro-ph.HE].

Lusso, E. and G. Risaliti (Mar. 2016). «The Tight Relation between X-Ray and Ultraviolet Luminosity of Quasars.» In: *ApJ* 819.2, 154. DOI: 10.3847/0004-637X/819/2/154. arXiv: 1602.01090 [astro-ph.GA].

Lusso, E. et al. (Sept. 2012). «Bolometric luminosities and Eddington ratios of X-ray selected active galactic nuclei in the XMM-COSMOS survey.» In: *MNRAS* 425.1, pp. 623–640. DOI: 10.1111/j.1365-2966.2012.21513.x. arXiv: 1206.2642 [astro-ph.CO].

Lusso, E. et al. (Mar. 2010). «The X-ray to optical-UV luminosity ratio of X-ray selected type 1 AGN in XMM-COSMOS.» In: *A&A* 512, A34. DOI: 10.1051/0004-6361/200913298. arXiv: 0912.4166 [astro-ph.CO].

Lyke, Brad W. et al. (Sept. 2020). «The Sloan Digital Sky Survey Quasar Catalog: Sixteenth Data Release.» In: *ApJS* 250.1, 8. DOI: 10.3847/1538-4365/aba623. arXiv: 2007.09001 [astro-ph.GA].

Lynden-Bell, D. (Aug. 1969). «Galactic Nuclei as Collapsed Old Quasars.» In: *Nature* 223.5207, pp. 690–694. DOI: 10.1038/223690a0.

Madau, Piero and Mark Dickinson (Aug. 2014). «Cosmic Star-Formation History.» In: *ARA&A* 52, pp. 415–486. DOI: 10.1146/annurev-astro-081811-125615. arXiv: 1403.0007 [astro-ph.CO].

Mahmoud, Ra'ad D. and Chris Done (Feb. 2020). «Discarding the disc in a changing-state AGN: the UV/X-ray relation in NGC 4151.» In: *MNRAS* 491.4, pp. 5126–5139. DOI: 10.1093/mnras/stz3196. arXiv: 1908.05461 [astro-ph.HE].

Małek, K. et al. (Nov. 2018a). «HELP: modelling the spectral energy distributions of Herschel detected galaxies in the ELAIS N1 field.» In: *A&A* 620, A50. DOI: 10.1051/0004-6361/201833131. arXiv: 1809.00529 [astro-ph.GA].

– (Nov. 2018b). «HELP: modelling the spectral energy distributions of Herschel detected galaxies in the ELAIS N1 field.» In: *A&A* 620, A50. DOI: 10.1051/0004-6361/201833131. arXiv: 1809.00529 [astro-ph.GA].

Maoz, Dan (June 2007). «Low-luminosity active galactic nuclei: are they UV faint and radio loud?» In: *MNRAS* 377.4, pp. 1696–1710. DOI: 10.1111/j.1365-2966.2007.11735.x. arXiv: astro-ph/0702292 [astro-ph].

Maraston, Claudia (Sept. 2005). «Evolutionary population synthesis: models, analysis of the ingredients and application to high-z

galaxies.» In: *MNRAS* 362.3, pp. 799–825. DOI: 10.1111/j.1365-2966.2005.09270.x. arXiv: astro-ph/0410207 [astro-ph].

Marchesi, S. et al. (Jan. 2016a). «The Chandra COSMOS Legacy survey: optical/IR identifications.» In: *ApJ* 817.1, 34. DOI: 10.3847/0004-637X/817/1/34. arXiv: 1512.01105 [astro-ph.GA].

– (Jan. 2016b). «The Chandra COSMOS Legacy survey: optical/IR identifications.» In: *ApJ* 817.1, 34. DOI: 10.3847/0004-637X/817/1/34. arXiv: 1512.01105 [astro-ph.GA].

Marconi, Alessandro and Leslie K. Hunt (May 2003). «The Relation between Black Hole Mass, Bulge Mass, and Near-Infrared Luminosity.» In: *ApJ* 589.1, pp. L21–L24. DOI: 10.1086/375804. arXiv: astro-ph/0304274 [astro-ph].

Marocco, Federico et al. (Mar. 2021). «The CatWISE2020 Catalog.» In: *ApJS* 253.1, 8. DOI: 10.3847/1538-4365/abd805. arXiv: 2012.13084 [astro-ph.IM].

Martig, Marie, Frédéric Bournaud, Romain Teyssier, and Avishai Dekel (Dec. 2009). «Morphological Quenching of Star Formation: Making Early-Type Galaxies Red.» In: *ApJ* 707.1, pp. 250–267. DOI: 10.1088/0004-637X/707/1/250. arXiv: 0905.4669 [astro-ph.CO].

Martin, G., S. Kaviraj, M. Volonteri, B. D. Simmons, J. E. G. Devriendt, C. J. Lintott, R. J. Smethurst, Y. Dubois, and C. Pichon (May 2018). «Normal black holes in bulge-less galaxies: the largely quiescent, merger-free growth of black holes over cosmic time.» In: *MNRAS* 476.2, pp. 2801–2812. DOI: 10.1093/mnras/sty324. arXiv: 1801.09699 [astro-ph.GA].

Martínez-Solaeche, G. et al. (May 2022). «The miniJPAS survey: Identification and characterization of the emission line galaxies down to z < 0.35 in the AEGIS field.» In: *A&A* 661, A99. DOI: 10.1051/0004-6361/202142812. arXiv: 2204.01698 [astro-ph.GA].

Masini, A., J. V. Wijesekera, A. Celotti, and P. G. Boorman (July 2022). «Comprehensive X-ray view of the active nucleus in NGC 4258.» In: *A&A* 663, A87. DOI: 10.1051/0004-6361/202243231. arXiv: 2205.07899 [astro-ph.HE].

Mason, R. E. et al. (July 2012). «The Nuclear Infrared Emission of Low-luminosity Active Galactic Nuclei.» In: *AJ* 144.1, 11. DOI: 10.1088/0004-6256/144/1/11. arXiv: 1205.0029 [astro-ph.CO].

Masoura, V. A., G. Mountrichas, I. Georgantopoulos, A. Ruiz, G. Magdis, and M. Plionis (Oct. 2018). «Disentangling the AGN and star formation connection using XMM-Newton.» In: *A&A* 618, A31. DOI: 10.1051/0004-6361/201833397. arXiv: 1807.01723 [astro-ph.GA].

Matsuoka, Yoshiki, Michael A. Strauss, III Price Ted N., and Matthew S. DiDonato (Jan. 2014). «Massive Star-forming Host Galaxies of Quasars on Sloan Digital Sky Survey Stripe 82.» In: *ApJ* 780.2, 162. DOI: 10.1088/0004-637X/780/2/162. arXiv: 1312.2417 [astro-ph.GA].

Matzeu, G. A. et al. (Feb. 2023). «Supermassive Black Hole Winds in X-rays: SUBWAYS. I. Ultra-fast outflows in quasars beyond the local Universe.» In: *A&A* 670, A182. DOI: 10.1051/0004-6361/202245036. arXiv: 2212.02960 [astro-ph.HE].

McAlpine, Stuart, Chris M. Harrison, David J. Rosario, David M. Alexander, Sara L. Ellison, Peter H. Johansson, and David R. Patton (June 2020). «Galaxy mergers in EAGLE do not induce a significant amount of black hole growth yet do increase the rate of luminous AGN.» In: *MNRAS* 494.4, pp. 5713–5733. DOI: 10.1093/mnras/staa1123. arXiv: 2002.00959 [astro-ph.GA].

McElroy, Rebecca, Scott M. Croom, Michael Pracy, Rob Sharp, I. -Ting Ho, and Anne M. Medling (Jan. 2015). «IFU observations of luminous type II AGN - I. Evidence for ubiquitous winds.» In: *MNRAS* 446.2, pp. 2186–2204. DOI: 10.1093/mnras/stu2224. arXiv: 1410.6552 [astro-ph.GA].

Meenakshi, Moun, Dipanjan Mukherjee, Alexander Y. Wagner, Nicole P. H. Nesvadba, Geoffrey V. Bicknell, Raffaella Morganti, Reinier M. J. Janssen, Ralph S. Sutherland, and Ankush Mandal (Oct. 2022). «Modelling observable signatures of jet-ISM interaction: thermal emission and gas kinematics.» In: *MNRAS* 516.1, pp. 766–786. DOI: 10.1093/mnras/stac2251. arXiv: 2203.10251 [astro-ph.GA].

Menzel, M. -L. et al. (Mar. 2016). «A spectroscopic survey of X-ray-selected AGNs in the northern XMM-XXL field.» In: *MNRAS* 457.1, pp. 110–132. DOI: 10.1093/mnras/stv2749. arXiv: 1511.07870 [astro-ph.GA].

Merloni, A. (Jan. 2008). «Cosmological evolution of supermassive black holes and AGN: a synthesis model for accretion and feedback .» In: *Mem. Soc. Astron. Italiana* 79, p. 1310. arXiv: 0808.0070 [astro-ph].

Merloni, A. et al. (2024). «The SRG/eROSITA all-sky survey: First X-ray catalogues and data release of the western Galactic hemisphere.» In: *Astron. Astrophys.* 682, A34. DOI: 10.1051/0004-6361/202347165. arXiv: 2401.17274 [astro-ph.HE].

Merloni, A. et al. (Jan. 2010). «On the Cosmic Evolution of the Scaling Relations Between Black Holes and Their Host Galaxies: Broad-Line Active Galactic Nuclei in the zCOSMOS Survey.» In: *ApJ* 708.1, pp. 137–157. DOI: 10.1088/0004-637X/708/1/137. arXiv: 0910.4970 [astro-ph.CO].

Merloni, A. et al. (Feb. 2014). «The incidence of obscuration in active galactic nuclei.» In: *MNRAS* 437.4, pp. 3550–3567. DOI: 10.1093/mnras/stt2149. arXiv: 1311.1305 [astro-ph.CO].

Merloni, Andrea (Oct. 2004). «The anti-hierarchical growth of supermassive black holes.» In: *MNRAS* 353.4, pp. 1035–1047. DOI: 10.1111/j.1365-2966.2004.08147.x. arXiv: astro-ph/0402495 [astro-ph].

Merloni, Andrea and Sebastian Heinz (Aug. 2008). «A synthesis model for AGN evolution: supermassive black holes growth and feedback

modes.» In: *MNRAS* 388.3, pp. 1011–1030. DOI: 10.1111/j.1365-2966.2008.13472.x. arXiv: 0805.2499 [astro-ph].

Merloni, Andrea and Sebastian Heinz (2013). «Evolution of Active Galactic Nuclei.» In: *Planets, Stars and Stellar Systems. Volume 6: Extragalactic Astronomy and Cosmology*. Ed. by Terry D. Oswalt and William C. Keel. Vol. 6, p. 503. DOI: 10.1007/978-94-007-5609-0_11.

Merloni, Andrea, Sebastian Heinz, and Tiziana di Matteo (Nov. 2003). «A Fundamental Plane of black hole activity.» In: *MNRAS* 345.4, pp. 1057–1076. DOI: 10.1046/j.1365-2966.2003.07017.x. arXiv: astro-ph/0305261 [astro-ph].

Meyer-Hofmeister, E. and F. Meyer (Mar. 2011). «Broad iron emission lines in Seyfert galaxies - re-condensation of gas onto an inner disk below the ADAF?» In: *A&A* 527, A127. DOI: 10.1051/0004-6361/201015478. arXiv: 1101.4854 [astro-ph.HE].

Mezcua, M., F. Civano, S. Marchesi, H. Suh, G. Fabbiano, and M. Volonteri (Aug. 2018). «Intermediate-mass black holes in dwarf galaxies out to redshift ~2.4 in the Chandra COSMOS-Legacy Survey.» In: *MNRAS* 478.2, pp. 2576–2591. DOI: 10.1093/mnras/sty1163. arXiv: 1802.01567 [astro-ph.GA].

Moles, M. et al. (Sept. 2008). «The Alhambra Survey: a Large Area Multimedium-Band Optical and Near-Infrared Photometric Survey.» In: *AJ* 136.3, pp. 1325–1339. DOI: 10.1088/0004-6256/136/3/1325. arXiv: 0806.3021 [astro-ph].

Monaco, Pierluigi, Fabio Fontanot, and Giuliano Taffoni (Mar. 2007). «The MORGANA model for the rise of galaxies and active nuclei.» In: *MNRAS* 375.4, pp. 1189–1219. DOI: 10.1111/j.1365-2966.2006.11253.x. arXiv: astro-ph/0610805 [astro-ph].

Mountrichas, G., V. Buat, I. Georgantopoulos, G. Yang, V. A. Masoura, M. Boquien, and D. Burgarella (Sept. 2021). «Galaxy properties of type 1 and 2 X-ray selected AGN and a comparison among different classification criteria.» In: *A&A* 653, A70. DOI: 10.1051/0004-6361/202141273. arXiv: 2106.11579 [astro-ph.GA].

Mountrichas, George and Véronique Buat (Nov. 2023). «Link between star formation and the properties of supermassive black holes.» In: *A&A* 679, A151. DOI: 10.1051/0004-6361/202347392. arXiv: 2309.15909 [astro-ph.GA].

Moustakas, John and Jr. Kennicutt Robert C. (May 2006). «An Integrated Spectrophotometric Survey of Nearby Star-forming Galaxies.» In: *ApJS* 164.1, pp. 81–98. DOI: 10.1086/500971. arXiv: astro-ph/0511729 [astro-ph].

Mukherjee, Dipanjan, Geoffrey V. Bicknell, Ralph Sutherland, and Alex Wagner (Sept. 2016). «Relativistic jet feedback in high-redshift galaxies - I. Dynamics.» In: *MNRAS* 461.1, pp. 967–983. DOI: 10.1093/mnras/stw1368. arXiv: 1606.01143 [astro-ph.HE].

Mukherjee, Dipanjan, Geoffrey V. Bicknell, Alexander Y. Wagner, Ralph S. Sutherland, and Joseph Silk (Oct. 2018). «Relativistic jet feedback - III. Feedback on gas discs.» In: *MNRAS* 479.4, pp. 5544–5566. DOI: 10.1093/mnras/sty1776. arXiv: 1803.08305 [astro-ph.HE].

Mutch, Simon J., Darren J. Croton, and Gregory B. Poole (Nov. 2013). «The simplest model of galaxy formation - I. A formation history model of galaxy stellar mass growth.» In: *MNRAS* 435.3, pp. 2445–2459. DOI: 10.1093/mnras/stt1453. arXiv: 1304.2774 [astro-ph.CO].

Nagar, N. M., H. Falcke, and A. S. Wilson (May 2005). «Radio sources in low-luminosity active galactic nuclei. IV. Radio luminosity function, importance of jet power, and radio properties of the complete Palomar sample.» In: *A&A* 435.2, pp. 521–543. DOI: 10.1051/0004-6361:20042277. arXiv: astro-ph/0502551 [astro-ph].

Nandra, K. et al. (Sept. 2015). «AEGIS-X: Deep Chandra Imaging of the Central Groth Strip.» In: *ApJS* 220.1, 10. DOI: 10.1088/0067-0049/220/1/10. arXiv: 1503.09078 [astro-ph.HE].

Narayan, Ramesh and Jeffrey E. McClintock (May 2008). «Advection-dominated accretion and the black hole event horizon.» In: *New A Rev.* 51.10-12, pp. 733–751. DOI: 10.1016/j.newar.2008.03.002. arXiv: 0803.0322 [astro-ph].

Nemmen, Rodrigo S., Thaisa Storchi-Bergmann, and Michael Eracleous (Mar. 2014). «Spectral models for low-luminosity active galactic nuclei in LINERs: the role of advection-dominated accretion and jets.» In: *MNRAS* 438.4, pp. 2804–2827. DOI: 10.1093/mnras/stt2388. arXiv: 1312.1982 [astro-ph.HE].

Nersesian, A. et al. (Apr. 2019). «Old and young stellar populations in DustPedia galaxies and their role in dust heating.» In: *A&A* 624, A80. DOI: 10.1051/0004-6361/201935118. arXiv: 1903.05933 [astro-ph.GA].

Netzer, Hagai (1990). «AGN Emission Lines.» In: *Active Galactic Nuclei*. Ed. by T. J.-L. Courvoisier and M. Mayor. Berlin, Heidelberg: Springer Berlin Heidelberg, pp. 57–160. ISBN: 978-3-662-39816-6. DOI: 10.1007/978-3-662-39816-6_2. URL: https://doi.org/10.1007/978-3-662-39816-6_2.

– (Aug. 2015). «Revisiting the Unified Model of Active Galactic Nuclei.» In: *ARA&A* 53, pp. 365–408. DOI: 10.1146/annurev-astro-082214-122302. arXiv: 1505.00811 [astro-ph.GA].

– (2013). *The Physics and Evolution of Active Galactic Nuclei*.

Newman, Jeffrey A. et al. (Sept. 2013). «The DEEP2 Galaxy Redshift Survey: Design, Observations, Data Reduction, and Redshifts.» In: *ApJS* 208.1, 5. DOI: 10.1088/0067-0049/208/1/5. arXiv: 1203.3192 [astro-ph.CO].

Newville, Matt and et al. (May 2023). *lmfit/lmfit-py: 1.2.2.* DOI: 10.5281/zenodo.8145703. URL: https://doi.org/10.5281/zenodo.8145703.

Niedźwiecki, Andrzej, Agnieszka Stępnik, and Fu-Guo Xie (Feb. 2015). «On the Role and Origin of Nonthermal Electrons in Hot Accretion

Flows.» In: *ApJ* 799.2, 217. DOI: 10.1088/0004-637X/799/2/217. arXiv: 1412.4593 [astro-ph.HE].

Nikutta, Robert, Moshe Elitzur, and Mark Lacy (Dec. 2009). «On the 10 μm Silicate Feature in Active Galactic Nuclei.» In: *ApJ* 707.2, pp. 1550–1559. DOI: 10.1088/0004-637X/707/2/1550. arXiv: 0910.5521 [astro-ph.CO].

Nobuta, K. et al. (Dec. 2012). «Black Hole Mass and Eddington Ratio Distribution Functions of X-Ray-selected Broad-line AGNs at z ~1.4 in the Subaru XMM-Newton Deep Field.» In: *ApJ* 761.2, 143. DOI: 10.1088/0004-637X/761/2/143. arXiv: 1211.0069 [astro-ph.CO].

Noll, S., D. Burgarella, E. Giovannoli, V. Buat, D. Marcillac, and J. C. Muñoz-Mateos (Dec. 2009). «Analysis of galaxy spectral energy distributions from far-UV to far-IR with CIGALE: studying a SINGS test sample.» In: *A&A* 507.3, pp. 1793–1813. DOI: 10.1051/0004-6361/200912497. arXiv: 0909.5439 [astro-ph.CO].

Novak, Gregory S., Jeremiah P. Ostriker, and Luca Ciotti (Aug. 2011). «Feedback from Central Black Holes in Elliptical Galaxies: Two-dimensional Models Compared to One-dimensional Models.» In: *ApJ* 737.1, 26. DOI: 10.1088/0004-637X/737/1/26. arXiv: 1007.3505 [astro-ph.GA].

Novikov, I. D. and K. S. Thorne (Jan. 1973). «Astrophysics of black holes.» In: *Black Holes (Les Astres Occlus)*, pp. 343–450.

O'Dell, C. R. and Kerry D. Handron (Apr. 1996). «Cometary Knots in the Helix Nebula.» In: *AJ* 111, p. 1630. DOI: 10.1086/117902.

Ogle, P. M., L. Lanz, and P. N. Appleton (June 2014). «Jet-shocked H_2 and CO in the Anomalous Arms of Molecular Hydrogen Emission Galaxy NGC 4258.» In: *ApJ* 788.2, L33. DOI: 10.1088/2041-8205/788/2/L33. arXiv: 1405.2040 [astro-ph.GA].

Ogle, Patrick, Robert Antonucci, P. N. Appleton, and David Whysong (Oct. 2007). «Shocked Molecular Hydrogen in the 3C 326 Radio Galaxy System.» In: *ApJ* 668.2, pp. 699–707. DOI: 10.1086/521334. arXiv: 0707.0896 [astro-ph].

Ogle, Patrick, Francois Boulanger, Pierre Guillard, Daniel A. Evans, Robert Antonucci, P. N. Appleton, Nicole Nesvadba, and Christian Leipski (Dec. 2010). «Jet-powered Molecular Hydrogen Emission from Radio Galaxies.» In: *ApJ* 724.2, pp. 1193–1217. DOI: 10.1088/0004-637X/724/2/1193. arXiv: 1009.4533 [astro-ph.CO].

Ogle, Patrick M. et al. (Feb. 2024). «Radio Jet Feedback on the Inner Disk of Virgo Spiral Galaxy Messier 58.» In: *ApJ* 962.2, 196. DOI: 10.3847/1538-4357/ad1242. arXiv: 2312.01936 [astro-ph.GA].

Onori, F. et al. (June 2017). «Detection of faint broad emission lines in type 2 AGN - II. On the measurement of the black hole mass of type 2 AGN and the unified model.» In: *MNRAS* 468.1, pp. L97–L102. DOI: 10.1093/mnrasl/slx032. arXiv: 1703.05167 [astro-ph.GA].

Osorio-Clavijo, N., O. Gonzalez-Martín, S. F. Sánchez, M. Guainazzi, and I. Cruz-González (July 2023). «AGNs in the CALIFA survey:

X-ray detection of nuclear sources.» In: *MNRAS* 522.4, pp. 5788–5804. DOI: 10.1093/mnras/stad1262. arXiv: 2303.18245 [astro-ph.GA].

Osterbrock, Donald E. and Gary J. Ferland (2006). *Astrophysics of gaseous nebulae and active galactic nuclei.*

Owen, Frazer N., Jean A. Eilek, and Namir E. Kassim (Nov. 2000). «M87 at 90 Centimeters: A Different Picture.» In: *ApJ* 543.2, pp. 611–619. DOI: 10.1086/317151. arXiv: astro-ph/0006150 [astro-ph].

Pacifici, Camilla et al. (Feb. 2023). «The Art of Measuring Physical Parameters in Galaxies: A Critical Assessment of Spectral Energy Distribution Fitting Techniques.» In: *ApJ* 944.2, 141. DOI: 10.3847/1538-4357/acacff. arXiv: 2212.01915 [astro-ph.GA].

Padovani, P. et al. (Aug. 2017). «Active galactic nuclei: what's in a name?» In: *A&A Rev.* 25.1, 2. DOI: 10.1007/s00159-017-0102-9. arXiv: 1707.07134 [astro-ph.GA].

Pancoast, Anna, Brendon J. Brewer, Tommaso Treu, Daeseong Park, Aaron J. Barth, Misty C. Bentz, and Jong-Hak Woo (Dec. 2014). «Modelling reverberation mapping data - II. Dynamical modelling of the Lick AGN Monitoring Project 2008 data set.» In: *MNRAS* 445.3, pp. 3073–3091. DOI: 10.1093/mnras/stu1419. arXiv: 1311.6475 [astro-ph.CO].

Pâris, Isabelle et al. (May 2018). «The Sloan Digital Sky Survey Quasar Catalog: Fourteenth data release.» In: *A&A* 613, A51. DOI: 10.1051/0004-6361/201732445. arXiv: 1712.05029 [astro-ph.GA].

Park, Taeyoung, Vinay L. Kashyap, Aneta Siemiginowska, David A. van Dyk, Andreas Zezas, Craig Heinke, and Bradford J. Wargelin (Nov. 2006). «Bayesian Estimation of Hardness Ratios: Modeling and Computations.» In: *ApJ* 652.1, pp. 610–628. DOI: 10.1086/507406. arXiv: astro-ph/0606247 [astro-ph].

Pellegrini, S. (May 2005). «Nuclear Accretion in Galaxies of the Local Universe: Clues from Chandra Observations.» In: *ApJ* 624.1, pp. 155–161. DOI: 10.1086/429267. arXiv: astro-ph/0502035 [astro-ph].

Perley, R. A., J. W. Dreher, and J. J. Cowan (Oct. 1984). «The jet and filaments in Cygnus A.» In: *ApJ* 285, pp. L35–L38. DOI: 10.1086/184360.

Perna, Michele (Nov. 2016). «Starbursting to Quenching: the role of X-ray emission in Active Galactic Nuclei feedback processes.» PhD thesis. University of Bologna, Italy.

Peterson, B. M. et al. (Oct. 2000). «X-Ray and Optical Variability in NGC 4051 and the Nature of Narrow-Line Seyfert 1 Galaxies.» In: *ApJ* 542.1, pp. 161–174. DOI: 10.1086/309518. arXiv: astro-ph/0005433 [astro-ph].

Peterson, Bradley M. (1997). *An Introduction to Active Galactic Nuclei.*

Pier, Edward A. and Julian H. Krolik (Dec. 1992). «Infrared Spectra of Obscuring Dust Tori around Active Galactic Nuclei. I. Calculational Method and Basic Trends.» In: *ApJ* 401, p. 99. DOI: 10.1086/172042.

Pilbratt, G. L. et al. (July 2010). «Herschel Space Observatory. An ESA facility for far-infrared and submillimetre astronomy.» In: *A&A* 518, L1. DOI: 10.1051/0004-6361/201014759. arXiv: 1005.5331 [astro-ph.IM].

Planck Collaboration et al. (Sept. 2016). «Planck 2015 results. XIII. Cosmological parameters.» In: *A&A* 594, A13. DOI: 10.1051/0004-6361/201525830. arXiv: 1502.01589 [astro-ph.CO].

Pogge, Richard W. (Nov. 1989). «Ionized Gas in the Nuclear Regions of Nearby Non-Seyfert Spiral Galaxies.» In: *ApJS* 71, p. 433. DOI: 10.1086/191381.

Poglitsch, A. et al. (July 2010). «The Photodetector Array Camera and Spectrometer (PACS) on the Herschel Space Observatory.» In: *A&A* 518, L2. DOI: 10.1051/0004-6361/201014535. arXiv: 1005.1487 [astro-ph.IM].

Predehl, P. et al. (Mar. 2021). «The eROSITA X-ray telescope on SRG.» In: *A&A* 647, A1. DOI: 10.1051/0004-6361/202039313. arXiv: 2010.03477 [astro-ph.HE].

Ptak, A. (Dec. 2001). «Low-luminosity AGN and normal galaxies.» In: *X-ray Astronomy: Stellar Endpoints, AGN, and the Diffuse X-ray Background*. Ed. by Nicholas E. White, Giuseppe Malaguti, and Giorgio G. C. Palumbo. Vol. 599. American Institute of Physics Conference Series, pp. 326–335. DOI: 10.1063/1.1434645. arXiv: astro-ph/0008459 [astro-ph].

Rakshit, Suvendu, C. S. Stalin, and Jari Kotilainen (July 2020). «Spectral Properties of Quasars from Sloan Digital Sky Survey Data Release 14: The Catalog.» In: *ApJS* 249.1, 17. DOI: 10.3847/1538-4365/ab99c5. arXiv: 1910.10395 [astro-ph.GA].

Ramos Almeida, C., N. A. Levenson, J. M. Rodríguez Espinosa, A. Alonso-Herrero, A. Asensio Ramos, J. T. Radomski, C. Packham, R. S. Fisher, and C. M. Telesco (Sept. 2009). «The Infrared Nuclear Emission of Seyfert Galaxies on Parsec Scales: Testing the Clumpy Torus Models.» In: *ApJ* 702.2, pp. 1127–1149. DOI: 10.1088/0004-637X/702/2/1127. arXiv: 0906.5368 [astro-ph.CO].

Ramos Almeida, Cristina and Claudio Ricci (Oct. 2017). «Nuclear obscuration in active galactic nuclei.» In: *Nature Astronomy* 1, pp. 679–689. DOI: 10.1038/s41550-017-0232-z. arXiv: 1709.00019 [astro-ph.GA].

Reines, Amy E. and Marta Volonteri (Nov. 2015). «Relations between Central Black Hole Mass and Total Galaxy Stellar Mass in the Local Universe.» In: *ApJ* 813.2, 82. DOI: 10.1088/0004-637X/813/2/82. arXiv: 1508.06274 [astro-ph.GA].

Reynaldi, V., M. Guainazzi, S. Bianchi, I. Andruchow, F. García, N. Salerno, and I. E. López (Dec. 2020). «On the origin of X-ray oxygen emission lines in obscured AGN.» In: *MNRAS* 499.4, pp. 5107–5120. DOI: 10.1093/mnras/staa3169. arXiv: 2010.05412 [astro-ph.GA].

Ricci, C. et al. (Dec. 2017a). «BAT AGN Spectroscopic Survey. V. X-Ray Properties of the Swift/BAT 70-month AGN Catalog.» In: *ApJS*

233.2, 17. DOI: 10.3847/1538-4365/aa96ad. arXiv: 1709.03989 [astro-ph.HE].

Ricci, Claudio et al. (Sept. 2017b). «The close environments of accreting massive black holes are shaped by radiative feedback.» In: *Nature* 549.7673, pp. 488–491. DOI: 10.1038/nature23906. arXiv: 1709.09651 [astro-ph.HE].

Ricci, F., F. La Franca, F. Onori, and S. Bianchi (Feb. 2017c). «Novel calibrations of virial black hole mass estimators in active galaxies based on X-ray luminosity and optical/near-infrared emission lines.» In: *A&A* 598, A51. DOI: 10.1051/0004-6361/201629380. arXiv: 1610.03490 [astro-ph.GA].

Ricci, F. et al. (Oct. 2017d). «Detection of faint broad emission lines in type 2 AGNs - III. On the M_{BH}-$\sigma_\star$ relation of type 2 AGNs.» In: *MNRAS* 471.1, pp. L41–L46. DOI: 10.1093/mnrasl/slx103. arXiv: 1706.06110 [astro-ph.GA].

Rich, R. Michael et al. (Dec. 2019). «The haloes and environments of nearby galaxies (HERON) - I. Imaging, sample characteristics, and envelope diameters.» In: *MNRAS* 490.2, pp. 1539–1569. DOI: 10.1093/mnras/stz2106. arXiv: 1907.10706 [astro-ph.GA].

Rigopoulou, D., D. Kunze, D. Lutz, R. Genzel, and A. F. M. Moorwood (July 2002). «An ISO-SWS survey of molecular hydrogen in starburst and Seyfert galaxies.» In: *A&A* 389, pp. 374–386. DOI: 10.1051/0004-6361:20020607. arXiv: astro-ph/0206135 [astro-ph].

Roussel, H., M. Sauvage, L. Vigroux, and A. Bosma (June 2001). «The relationship between star formation rates and mid-infrared emission in galactic disks.» In: *A&A* 372, pp. 427–437. DOI: 10.1051/0004-6361:20010498. arXiv: astro-ph/0104088 [astro-ph].

Roussel, H. et al. (Nov. 2007). «Warm Molecular Hydrogen in the Spitzer SINGS Galaxy Sample.» In: *ApJ* 669.2, pp. 959–981. DOI: 10.1086/521667. arXiv: 0707.0395 [astro-ph].

Ruiz-Lapuente, Pilar (July 1996). «The Hubble Constant from 56Co-powered Nebular Candles.» In: *ApJ* 465, p. L83. DOI: 10.1086/310155. arXiv: astro-ph/9604044 [astro-ph].

Salucci, Paolo, Charu Ratnam, Pierluigi Monaco, and Luigi Danese (Sept. 2000). «The masses of black holes in the nuclei of spirals.» In: *MNRAS* 317.2, pp. 488–496. DOI: 10.1046/j.1365-8711.2000.03622.x. arXiv: astro-ph/9812485 [astro-ph].

Salvato, M. et al. (Jan. 2009). «Photometric Redshift and Classification for the XMM-COSMOS Sources.» In: *ApJ* 690.2, pp. 1250–1263. DOI: 10.1088/0004-637X/690/2/1250. arXiv: 0809.2098 [astro-ph].

Salvato, Mara, Olivier Ilbert, and Ben Hoyle (June 2019). «The many flavours of photometric redshifts.» In: *Nature Astronomy* 3, pp. 212–222. DOI: 10.1038/s41550-018-0478-0. arXiv: 1805.12574 [astro-ph.GA].

Sandage, Allan (May 1965). «The Existence of a Major New Constituent of the Universe: the Quasistellar Galaxies.» In: *ApJ* 141, p. 1560. DOI: 10.1086/148245.

Savorgnan, Giulia A. D., Alister W. Graham, Alessandro Marconi, and Eleonora Sani (Jan. 2016). «Supermassive Black Holes and Their Host Spheroids. II. The Red and Blue Sequence in the M_{BH}-$M_{*,sph}$ Diagram.» In: *ApJ* 817.1, 21. DOI: 10.3847/0004-637X/817/1/21. arXiv: 1511.07437 [astro-ph.GA].

Schaffer, Simon (Jan. 1979). «John Michell and Black Holes.» In: *Journal for the History of Astronomy* 10, p. 42. DOI: 10.1177/002182867901000104.

Schartmann, M., K. Meisenheimer, M. Camenzind, S. Wolf, and Th. Henning (July 2005). «Towards a physical model of dust tori in Active Galactic Nuclei. Radiative transfer calculations for a hydrostatic torus model.» In: *A&A* 437.3, pp. 861–881. DOI: 10.1051/0004-6361: 20042363. arXiv: astro-ph/0504105 [astro-ph].

Schartmann, M., K. Wada, M. A. Prieto, A. Burkert, and K. R. W. Tristram (Dec. 2014). «Time-resolved infrared emission from radiation-driven central obscuring structures in active galactic nuclei.» In: *MNRAS* 445.4, pp. 3878–3891. DOI: 10.1093/mnras/stu2020. arXiv: 1409.7404 [astro-ph.GA].

Schawinski, Kevin et al. (Jan. 2009). «Destruction of Molecular Gas Reservoirs in Early-Type Galaxies by Active Galactic Nucleus Feedback.» In: *ApJ* 690.2, pp. 1672–1680. DOI: 10.1088/0004-637X/690/ 2/1672. arXiv: 0809.1096 [astro-ph].

Schaye, Joop et al. (Jan. 2015). «The EAGLE project: simulating the evolution and assembly of galaxies and their environments.» In: *MNRAS* 446.1, pp. 521–554. DOI: 10.1093/mnras/stu2058. arXiv: 1407.7040 [astro-ph.GA].

Schmidt, M. (Mar. 1963). «3C 273 : A Star-Like Object with Large Red-Shift.» In: *Nature* 197.4872, p. 1040. DOI: 10.1038/1971040a0.

Schulze, A. and L. Wisotzki (Nov. 2011). «Selection effects in the black hole-bulge relation and its evolution.» In: *A&A* 535, A87. DOI: 10.1051/0004-6361/201117564. arXiv: 1109.2787 [astro-ph.CO].

Schulze, A. et al. (Mar. 2015). «The cosmic growth of the active black hole population at 1 <z <2 in zCOSMOS, VVDS and SDSS.» In: *MNRAS* 447.3, pp. 2085–2111. DOI: 10.1093/mnras/stu2549. arXiv: 1412.0754 [astro-ph.GA].

Schwarzschild, Karl (Jan. 1916). «Über das Gravitationsfeld eines Massenpunktes nach der Einsteinschen Theorie.» In: *Sitzungsberichte der Königlich Preussischen Akademie der Wissenschaften*, pp. 189– 196.

Seyfert, Carl K. (Jan. 1943). «Nuclear Emission in Spiral Nebulae.» In: *ApJ* 97, p. 28. DOI: 10.1086/144488.

Shakura, N. I. and R. A. Sunyaev (Jan. 1973). «Black holes in binary systems. Observational appearance.» In: *A&A* 24, pp. 337–355.

Shankar, Francesco (Apr. 2009). «The demography of supermassive black holes: Growing monsters at the heart of galaxies.» In: *New A Rev.* 53.4-6, pp. 57–77. DOI: 10.1016/j.newar.2009.07.006. arXiv: 0907.5213 [astro-ph.CO].

Shankar, Francesco, David H. Weinberg, and Jordi Miralda-Escudé (Jan. 2013). «Accretion-driven evolution of black holes: Eddington ratios, duty cycles and active galaxy fractions.» In: *MNRAS* 428.1, pp. 421–446. DOI: 10.1093/mnras/sts026. arXiv: 1111.3574 [astro-ph.CO].

– (Jan. 2009). «Self-Consistent Models of the AGN and Black Hole Populations: Duty Cycles, Accretion Rates, and the Mean Radiative Efficiency.» In: *ApJ* 690.1, pp. 20–41. DOI: 10.1088/0004-637X/690/1/20. arXiv: 0710.4488 [astro-ph].

Shankar, Francesco et al. (May 2019). «Black hole scaling relations of active and quiescent galaxies: Addressing selection effects and constraining virial factors.» In: *MNRAS* 485.1, pp. 1278–1292. DOI: 10.1093/mnras/stz376. arXiv: 1901.11036 [astro-ph.GA].

Shankar, Francesco et al. (Jan. 2020). «Constraining black hole-galaxy scaling relations and radiative efficiency from galaxy clustering.» In: *Nature Astronomy* 4, pp. 282–291. DOI: 10.1038/s41550-019-0949-y. arXiv: 1910.10175 [astro-ph.GA].

Shankar, Francesco et al. (Aug. 2016). «Selection bias in dynamically measured supermassive black hole samples: its consequences and the quest for the most fundamental relation.» In: *MNRAS* 460.3, pp. 3119–3142. DOI: 10.1093/mnras/stw678. arXiv: 1603.01276 [astro-ph.GA].

Shapiro, Stuart L. (Feb. 2005). «Spin, Accretion, and the Cosmological Growth of Supermassive Black Holes.» In: *ApJ* 620.1, pp. 59–68. DOI: 10.1086/427065. arXiv: astro-ph/0411156 [astro-ph].

Shen, Yue, Jenny E. Greene, Michael A. Strauss, Gordon T. Richards, and Donald P. Schneider (June 2008). «Biases in Virial Black Hole Masses: An SDSS Perspective.» In: *ApJ* 680.1, pp. 169–190. DOI: 10.1086/587475. arXiv: 0709.3098 [astro-ph].

Shen, Yue and Xin Liu (July 2012). «Comparing Single-epoch Virial Black Hole Mass Estimators for Luminous Quasars.» In: *ApJ* 753.2, 125. DOI: 10.1088/0004-637X/753/2/125. arXiv: 1203.0601 [astro-ph.CO].

Shen, Yue et al. (June 2015). «The Sloan Digital Sky Survey Reverberation Mapping Project: No Evidence for Evolution in the $M_\bullet$-σ_* Relation to z∼ 1.» In: *ApJ* 805.2, 96. DOI: 10.1088/0004-637X/805/2/96. arXiv: 1502.01034 [astro-ph.GA].

Shen, Yue et al. (Apr. 2019). «The Sloan Digital Sky Survey Reverberation Mapping Project: Sample Characterization.» In: *ApJS* 241.2, 34. DOI: 10.3847/1538-4365/ab074f. arXiv: 1810.01447 [astro-ph.GA].

Silk, Joseph and Martin J. Rees (Mar. 1998). «Quasars and galaxy formation.» In: *A&A* 331, pp. L1–L4. DOI: 10.48550/arXiv.astro-ph/9801013. arXiv: astro-ph/9801013 [astro-ph].

Silverman, J. D. et al. (May 2008). «The Luminosity Function of X-Ray-selected Active Galactic Nuclei: Evolution of Supermassive Black Holes at High Redshift.» In: *ApJ* 679.1, pp. 118–139. DOI: 10.1086/529572. arXiv: 0710.2461 [astro-ph].

Small, Todd A. and Roger D. Blandford (Dec. 1992). «Quasar evolution and the growth of black holes.» In: *MNRAS* 259, pp. 725–737. DOI: 10.1093/mnras/259.4.725.

Smith, J. D. T., L. Armus, D. A. Dale, H. Roussel, K. Sheth, B. A. Buckalew, T. H. Jarrett, G. Helou, and Jr. Kennicutt R. C. (Oct. 2007a). «Spectral Mapping Reconstruction of Extended Sources.» In: *PASP* 119.860, pp. 1133–1144. DOI: 10.1086/522634. arXiv: 0708.3745 [astro-ph].

Smith, J. D. T. et al. (Feb. 2007b). «The Mid-Infrared Spectrum of Star-forming Galaxies: Global Properties of Polycyclic Aromatic Hydrocarbon Emission.» In: *ApJ* 656.2, pp. 770–791. DOI: 10.1086/510549. arXiv: astro-ph/0610913 [astro-ph].

Soltan, A. (July 1982). «Masses of quasars.» In: *MNRAS* 200, pp. 115–122. DOI: 10.1093/mnras/200.1.115.

Springel, Volker, Tiziana Di Matteo, and Lars Hernquist (Feb. 2005). «Black Holes in Galaxy Mergers: The Formation of Red Elliptical Galaxies.» In: *ApJ* 620.2, pp. L79–L82. DOI: 10.1086/428772. arXiv: astro-ph/0409436 [astro-ph].

Stalevski, Marko (Sept. 2012). «SKIRTOR - database of modelled AGN dusty torus SEDs.» In: *Bulgarian Astronomical Journal* 18.3, p. 3.

Stalevski, Marko, Jacopo Fritz, Maarten Baes, Theodoros Nakos, and Luka Č. Popović (Mar. 2012). «3D radiative transfer modelling of the dusty tori around active galactic nuclei as a clumpy two-phase medium.» In: *MNRAS* 420.4, pp. 2756–2772. DOI: 10.1111/j.1365-2966.2011.19775.x. arXiv: 1109.1286 [astro-ph.CO].

– (Aug. 2011). «AGN Dusty Tori as a Clumpy Two-Phase Medium: the 10 μ m Silicate Feature.» In: *Baltic Astronomy* 20, pp. 490–494. DOI: 10.1515/astro-2017-0326. arXiv: 1112.0570 [astro-ph.CO].

Stalevski, Marko, Claudio Ricci, Yoshihiro Ueda, Paulina Lira, Jacopo Fritz, and Maarten Baes (May 2016a). «The dust covering factor in active galactic nuclei.» In: *MNRAS* 458.3, pp. 2288–2302. DOI: 10.1093/mnras/stw444. arXiv: 1602.06954 [astro-ph.GA].

– (May 2016b). «The dust covering factor in active galactic nuclei.» In: *MNRAS* 458.3, pp. 2288–2302. DOI: 10.1093/mnras/stw444. arXiv: 1602.06954 [astro-ph.GA].

Steffen, A. T., I. Strateva, W. N. Brandt, D. M. Alexander, A. M. Koekemoer, B. D. Lehmer, D. P. Schneider, and C. Vignali (June 2006). «The X-Ray-to-Optical Properties of Optically Selected Active Galaxies over Wide Luminosity and Redshift Ranges.» In: *AJ* 131.6, pp. 2826–2842. DOI: 10.1086/503627. arXiv: astro-ph/0602407 [astro-ph].

Steinborn, Lisa K., Michaela Hirschmann, Klaus Dolag, Francesco Shankar, Stéphanie Juneau, Mirko Krumpe, Rhea-Silvia Remus, and Adelheid F. Teklu (Nov. 2018). «Cosmological simulations of black hole growth II: how (in)significant are merger events for fuelling nuclear activity?» In: *MNRAS* 481.1, pp. 341–360. DOI: 10.1093/mnras/sty2288. arXiv: 1805.06902 [astro-ph.GA].

Stuber, Sophia K. et al. (Sept. 2021). «Frequency and nature of central molecular outflows in nearby star-forming disk galaxies.» In: *A&A* 653, A172. DOI: 10.1051/0004-6361/202141093. arXiv: 2107.11227 [astro-ph.GA].

Suganuma, Masahiro, Yuzuru Yoshii, Yukiyasu Kobayashi, Takeo Minezaki, Keigo Enya, Hiroyuki Tomita, Tsutomu Aoki, Shintaro Koshida, and Bruce A. Peterson (Mar. 2006). «Reverberation Measurements of the Inner Radius of the Dust Torus in Nearby Seyfert 1 Galaxies.» In: *ApJ* 639.1, pp. 46–63. DOI: 10.1086/499326. arXiv: astro-ph/0511697 [astro-ph].

Suh, Hyewon, Francesca Civano, Günther Hasinger, Elisabeta Lusso, Stefano Marchesi, Andreas Schulze, Masato Onodera, David J. Rosario, and David B. Sanders (Feb. 2019). «Multi-wavelength Properties of Type 1 and Type 2 AGN Host Galaxies in the Chandra-COSMOS Legacy Survey.» In: *ApJ* 872.2, 168. DOI: 10.3847/1538-4357/ab01fb. arXiv: 1902.03244 [astro-ph.GA].

Suh, Hyewon, Francesca Civano, Benny Trakhtenbrot, Francesco Shankar, Günther Hasinger, David B. Sanders, and Viola Allevato (Jan. 2020). «No Significant Evolution of Relations between Black Hole Mass and Galaxy Total Stellar Mass Up to $z \sim 2.5$.» In: *ApJ* 889.1, 32. DOI: 10.3847/1538-4357/ab5f5f. arXiv: 1912.02824 [astro-ph.GA].

Sutherland, Ralph S. and Michael A. Dopita (Apr. 2017). «Effects of Preionization in Radiative Shocks. I. Self-consistent Models.» In: *ApJS* 229.2, 34. DOI: 10.3847/1538-4365/aa6541. arXiv: 1702.07453 [astro-ph.IM].

Szanecki, Michał, Andrzej Niedźwiecki, and Rafał Wojaczyński (May 2023). «Hot accretion flows in low-luminosity active galactic nuclei in NGC 4258 and NGC 7213.» In: *MNRAS* 521.2, pp. 2215–2224. DOI: 10.1093/mnras/stad699. arXiv: 2212.10973 [astro-ph.HE].

Szanecki, Michał, Andrzej Niedźwiecki, and Andrzej A. Zdziarski (Mar. 2021). «Relativistic Reflection in NGC 4151.» In: *ApJ* 909.2, 205. DOI: 10.3847/1538-4357/abe380. arXiv: 2010.08358 [astro-ph.HE].

Taam, Ronald E., B. F. Liu, W. Yuan, and E. Qiao (Nov. 2012). «Disk Corona Interaction: Mechanism for the Disk Truncation and Spectrum Change in Low-luminosity Active Galactic Nuclei.» In: *ApJ* 759.1, 65. DOI: 10.1088/0004-637X/759/1/65. arXiv: 1209.4961 [astro-ph.HE].

Tanimoto, Atsushi, Yoshihiro Ueda, Hirokazu Odaka, Toshihiro Kawaguchi, Yasushi Fukazawa, and Taiki Kawamuro (June 2019). «XCLUMPY: X-Ray Spectral Model from Clumpy Torus and Its Application to the Circinus Galaxy.» In: *ApJ* 877.2, 95. DOI: 10.3847/1538-4357/ab1b20. arXiv: 1904.08945 [astro-ph.HE].

Teklu, Adelheid F., Rhea-Silvia Remus, Klaus Dolag, Alexander M. Beck, Andreas Burkert, Andreas S. Schmidt, Felix Schulze, and Lisa K. Steinborn (Oct. 2015). «Connecting Angular Momentum and Galactic Dynamics: The Complex Interplay between Spin, Mass, and

Morphology.» In: *ApJ* 812.1, 29. DOI: 10.1088/0004-637X/812/1/29. arXiv: 1503.03501 [astro-ph.GA].

Theios, Rachel L., Matthew A. Malkan, and Nathaniel R. Ross (May 2016). «Hα Imaging of Nearby Seyfert Host Galaxies.» In: *ApJ* 822.1, 45. DOI: 10.3847/0004-637X/822/1/45. arXiv: 1604.00089 [astro-ph.GA].

Thorne, Jessica, Aaron Robotham, Luke Davies, and Sabine Bellstedt (Mar. 2022). *AGN Unification Diagram*. DOI: 10.5281/zenodo.6381013. URL: https://doi.org/10.5281/zenodo.6381013.

Togi, Aditya and J. D. T. Smith (Oct. 2016). «Lighting the Dark Molecular Gas: H_2 as a Direct Tracer.» In: *ApJ* 830.1, 18. DOI: 10.3847/0004-637X/830/1/18. arXiv: 1607.08036 [astro-ph.GA].

Tombesi, F., M. Meléndez, S. Veilleux, J. N. Reeves, E. González-Alfonso, and C. S. Reynolds (Mar. 2015). «Wind from the black-hole accretion disk driving a molecular outflow in an active galaxy.» In: *Nature* 519.7544, pp. 436–438. DOI: 10.1038/nature14261. arXiv: 1501.07664 [astro-ph.HE].

Torbaniuk, O., M. Paolillo, F. Carrera, S. Cavuoti, C. Vignali, G. Longo, and J. Aird (Sept. 2021). «The connection between star formation and supermassive black hole activity in the local Universe.» In: *MNRAS* 506.2, pp. 2619–2637. DOI: 10.1093/mnras/stab1794. arXiv: 2106.11079 [astro-ph.GA].

Tran, Hien D., J. E. Lyke, and Jeff A. Mader (Jan. 2011). «Indecent Exposure in Seyfert 2 Galaxies: A Close Look.» In: *ApJ* 726.2, L21. DOI: 10.1088/2041-8205/726/2/L21. arXiv: 1012.1865 [astro-ph.CO].

Treister, E., K. Schawinski, C. M. Urry, and B. D. Simmons (Oct. 2012). «Major Galaxy Mergers Only Trigger the Most Luminous Active Galactic Nuclei.» In: *ApJ* 758.2, L39. DOI: 10.1088/2041-8205/758/2/L39. arXiv: 1209.5393 [astro-ph.CO].

Tristram, Konrad R. W., Leonard Burtscher, Walter Jaffe, Klaus Meisenheimer, Sebastian F. Hönig, Makoto Kishimoto, Marc Schartmann, and Gerd Weigelt (Mar. 2014). «The dusty torus in the Circinus galaxy: a dense disk and the torus funnel.» In: *A&A* 563, A82. DOI: 10.1051/0004-6361/201322698. arXiv: 1312.4534 [astro-ph.GA].

Ulrich, Marie-Helene, Laura Maraschi, and C. Megan Urry (Jan. 1997). «Variability of Active Galactic Nuclei.» In: *ARA&A* 35, pp. 445–502. DOI: 10.1146/annurev.astro.35.1.445.

Urry, C. Megan and Paolo Padovani (Sept. 1995). «Unified Schemes for Radio-Loud Active Galactic Nuclei.» In: *PASP* 107, p. 803. DOI: 10.1086/133630. arXiv: astro-ph/9506063 [astro-ph].

van der Kruit, P. C., J. H. Oort, and D. S. Mathewson (Nov. 1972). «The Radio Emission of NGC 4258 and the Possible Origin of Spiral Structure.» In: *A&A* 21, p. 169.

Vaona, L., S. Ciroi, F. Di Mille, V. Cracco, G. La Mura, and P. Rafanelli (Dec. 2012). «Spectral properties of the narrow-line region in Seyfert galaxies selected from the SDSS-DR7.» In: *MNRAS* 427.2, pp. 1266–

1283. DOI: 10.1111/j.1365-2966.2012.22060.x. arXiv: 1210.5201 [astro-ph.CO].

Veilleux, S., D. -C. Kim, D. B. Sanders, J. M. Mazzarella, and B. T. Soifer (May 1995). «Optical Spectroscopy of Luminous Infrared Galaxies. II. Analysis of the Nuclear and Long-Slit Data.» In: *ApJS* 98, p. 171. DOI: 10.1086/192158.

Veilleux, Sylvain, David S. N. Rupke, and Rob Swaters (Aug. 2009). «Warm Molecular Hydrogen in the Galactic Wind of M82.» In: *ApJ* 700.2, pp. L149–L153. DOI: 10.1088/0004-637X/700/2/L149. arXiv: 0907.1422 [astro-ph.CO].

Venturi, G. et al. (Oct. 2023). «Complex AGN feedback in the Teacup galaxy. A powerful ionised galactic outflow, jet-ISM interaction, and evidence for AGN-triggered star formation in a giant bubble.» In: *A&A* 678, A127. DOI: 10.1051/0004-6361/202347375. arXiv: 2309.02498 [astro-ph.GA].

Vestergaard, M. and Patrick S. Osmer (July 2009). «Mass Functions of the Active Black Holes in Distant Quasars from the Large Bright Quasar Survey, the Bright Quasar Survey, and the Color-selected Sample of the SDSS Fall Equatorial Stripe.» In: *ApJ* 699.1, pp. 800–816. DOI: 10.1088/0004-637X/699/1/800. arXiv: 0904.3348 [astro-ph.CO].

Vestergaard, Marianne and Bradley M. Peterson (Apr. 2006). «Determining Central Black Hole Masses in Distant Active Galaxies and Quasars. II. Improved Optical and UV Scaling Relationships.» In: *ApJ* 641.2, pp. 689–709. DOI: 10.1086/500572. arXiv: astro-ph/0601303 [astro-ph].

Vollmer, B., M. Soida, R. Beck, A. Chung, M. Urbanik, K. T. Chyży, K. Otmianowska-Mazur, and J. D. P. Kenney (May 2013). «Large-scale radio continuum properties of 19 Virgo cluster galaxies. The influence of tidal interactions, ram pressure stripping, and accreting gas envelopes.» In: *A&A* 553, A116. DOI: 10.1051/0004-6361/201321163. arXiv: 1304.1279 [astro-ph.CO].

Wagner, A. Y., M. Umemura, and G. V. Bicknell (Jan. 2013). «Ultrafast Outflows: Galaxy-scale Active Galactic Nucleus Feedback.» In: *ApJ* 763.1, L18. DOI: 10.1088/2041-8205/763/1/L18. arXiv: 1211.5851 [astro-ph.CO].

Weedman, D. W. (Jan. 1977). «Seyfert galaxies.» In: *ARA&A* 15, pp. 69–95. DOI: 10.1146/annurev.aa.15.090177.000441.

Weinberger, Rainer et al. (Mar. 2017). «Simulating galaxy formation with black hole driven thermal and kinetic feedback.» In: *MNRAS* 465.3, pp. 3291–3308. DOI: 10.1093/mnras/stw2944. arXiv: 1607.03486 [astro-ph.GA].

Williams, D. R. A. et al. (Mar. 2022). «LeMMINGs - IV. The X-ray properties of a statistically complete sample of the nuclei in active and inactive galaxies from the Palomar sample.» In: *MNRAS* 510.4,

pp. 4909–4928. DOI: `10.1093/mnras/stab3310`. arXiv: `2111.09077 [astro-ph.HE]`.

Wills, B. J., H. Netzer, and D. Wills (Jan. 1985). «Broad emission features in QSOs and active galactic nuclei. II. New observations and theory of Fe II and HI emission.» In: *ApJ* 288, pp. 94–116. DOI: `10.1086/162767`.

Wójtowicz, Anna, Łukasz Stawarz, C. C. Cheung, Norbert Werner, and Dominik Rudka (Feb. 2023). «Radio Emission of Nearby Early-type Galaxies in the Low and Very Low Radio Luminosity Range.» In: *ApJ* 944.2, 195. DOI: `10.3847/1538-4357/acb498`. arXiv: `2209.14638 [astro-ph.GA]`.

Wright, Edward L. et al. (Dec. 2010). «The Wide-field Infrared Survey Explorer (WISE): Mission Description and Initial On-orbit Performance.» In: *AJ* 140.6, pp. 1868–1881. DOI: `10.1088/0004-6256/140/6/1868`. arXiv: `1008.0031 [astro-ph.IM]`.

Xu, Ya-Di (Oct. 2011). «The Relation of Optical/Ultraviolet and X-Ray Emission in Low-luminosity Active Galactic Nuclei.» In: *ApJ* 739.2, 64. DOI: `10.1088/0004-637X/739/2/64`. arXiv: `1107.2979 [astro-ph.HE]`.

Xue, Y. Q., W. N. Brandt, B. Luo, D. A. Rafferty, D. M. Alexander, F. E. Bauer, B. D. Lehmer, D. P. Schneider, and J. D. Silverman (Sept. 2010). «Color-Magnitude Relations of Active and Non-active Galaxies in the Chandra Deep Fields: High-redshift Constraints and Stellar-mass Selection Effects.» In: *ApJ* 720.1, pp. 368–391. DOI: `10.1088/0004-637X/720/1/368`. arXiv: `1007.1453 [astro-ph.CO]`.

Yan, Renbin et al. (Jan. 2011). «AEGIS: DEMOGRAPHICS OF X-RAY AND OPTICALLY SELECTED ACTIVE GALACTIC NUCLEI.» In: *The Astrophysical Journal* 728.1, p. 38. DOI: `10.1088/0004-637x/728/1/38`. URL: `https://doi.org/10.1088/0004-637x/728/1/38`.

Yang, G., M. Boquien, V. Buat, D. Burgarella, L. Ciesla, F. Duras, M. Stalevski, W. N. Brandt, and C. Papovich (Jan. 2020). «X-CIGALE: Fitting AGN/galaxy SEDs from X-ray to infrared.» In: *MNRAS* 491.1, pp. 740–757. DOI: `10.1093/mnras/stz3001`. arXiv: `2001.08263 [astro-ph.GA]`.

Yang, G. et al. (Apr. 2018). «Linking black hole growth with host galaxies: the accretion-stellar mass relation and its cosmic evolution.» In: *MNRAS* 475.2, pp. 1887–1911. DOI: `10.1093/mnras/stx2805`. arXiv: `1710.09399 [astro-ph.GA]`.

Yang, Guang et al. (June 2023). «CEERS Key Paper. VI. JWST/MIRI Uncovers a Large Population of Obscured AGN at High Redshifts.» In: *ApJ* 950.1, L5. DOI: `10.3847/2041-8213/acd639`. arXiv: `2303.11736 [astro-ph.GA]`.

Yang, Guang et al. (Mar. 2022). «Fitting AGN/Galaxy X-Ray-to-radio SEDs with CIGALE and Improvement of the Code.» In: *ApJ* 927.2, 192. DOI: `10.3847/1538-4357/ac4971`. arXiv: `2201.03718 [astro-ph.GA]`.

Yuan, Feng and Ramesh Narayan (Aug. 2014). «Hot Accretion Flows Around Black Holes.» In: *ARA&A* 52, pp. 529–588. DOI: 10.1146/annurev-astro-082812-141003. arXiv: 1401.0586 [astro-ph.HE].

Yuan, Feng, Zhaolong Yu, and Luis C. Ho (Sept. 2009). «Revisiting the "Fundamental Plane" of Black Hole Activity at Extremely Low Luminosities.» In: *ApJ* 703.1, pp. 1034–1043. DOI: 10.1088/0004-637X/703/1/1034. arXiv: 0902.3704 [astro-ph.HE].

Yuan, H. B., X. W. Liu, and M. S. Xiang (Apr. 2013). «Empirical extinction coefficients for the GALEX, SDSS, 2MASS and WISE passbands.» In: *MNRAS* 430.3, pp. 2188–2199. DOI: 10.1093/mnras/stt039. arXiv: 1301.1427 [astro-ph.SR].

Yun, S. B. et al. (Aug. 2022). «Extreme X-Ray Reflection in the Nucleus of the Seyfert Galaxy NGC 5033.» In: *ApJ* 935.1, 12. DOI: 10.3847/1538-4357/ac7f30. arXiv: 2207.06524 [astro-ph.HE].

Zackrisson, E., N. Bergvall, and E. Leitet (Mar. 2008). «The Impact of Nebular Emission on the Broadband Fluxes of High-Redshift Galaxies.» In: *ApJ* 676.1, p. L9. DOI: 10.1086/587030. arXiv: 0802.3696 [astro-ph].

Zappacosta, L. et al. (Oct. 2023). «HYPerluminous quasars at the Epoch of ReionizatION (HYPERION): A new regime for the X-ray nuclear properties of the first quasars.» In: *A&A* 678, A201. DOI: 10.1051/0004-6361/202346795. arXiv: 2305.02347 [astro-ph.GA].

Zhang, Fan and Xue-Bing Wu (Apr. 2006). «Comptonization and Reprocessing Processes in Accretion Disks: Applications to the Seyfert 1 Galaxies NGC 5548 and NGC 4051.» In: *Chinese J. Astron. Astrophys.* 6.2, pp. 165–174. DOI: 10.1088/1009-9271/6/2/4.

Zhang, Lulu, Luis C. Ho, and Aigen Li (Nov. 2022). «Evidence That Shocks Destroy Small PAH Molecules in Low-luminosity Active Galactic Nuclei.» In: *ApJ* 939.1, 22. DOI: 10.3847/1538-4357/ac930f. arXiv: 2212.05686 [astro-ph.GA].

Zhang, Z. T., Y. C. Liang, and F. Hammer (Apr. 2013). «Modelling the narrow-line regions of active galaxies in the Sloan Digital Sky Survey - I. Sample selection and physical conditions.» In: *MNRAS* 430.4, pp. 2605–2621. DOI: 10.1093/mnras/sts713. arXiv: 1302.3013 [astro-ph.CO].